İÇİNDEKİLER / CONTENTS — Sayfa / Page

Amaç/Objective
Isı bilimi ve tekniğinin geliştirilmesini teşvik etmek, ısı bilimi ve tekniği alanında özgün, teorik, sayısal ve deneysel çalışmaların yayınlanmasına olanak sağlamaktır.
To connribute improvement of thermal sciences and technology and publication of original, theoretical, numerical and experimental studies in thermal sciences and technology.

İçerik/Content
Isı bilimi ve tekniği alanındaki özgün ve derleme makaleler.
Original and review articles in thermal sciences and technology.

Değerlendirme/Evaluation
Dergi hakemli bir dergi olup, her bir makale konusunda uzman en az iki hakem tarafından değerlendirilir.
Each article published in this journal is evalutated by at least two referees.

Bu Sayıya Hakem Olarak Katkıda Bulunanlar/The Referees Contributed in This Volume

Prof. Dr. Zekeriya Altaç (Eskişehir Osmangazi Üniversitesi)
Prof. Dr. Burhan Çuhadaroğlu (Karadeniz Teknik Üniversitesi)
Prof. Dr. Fuat Egelioğlu (Doğu Akdeniz Üniversitesi)
Prof. Dr. Nurdil Eskin (İstanbul Teknik Üniversitesi)
Prof. Dr. Hasan Güneş (İstanbul Teknik Üniversitesi)
Prof. Dr. İlhami Horuz (Gazi Üniversitesi)
Prof. Dr. Mustafa İlbaş (Gazi Üniversitesi)
Prof. Dr. İres İskender (Gazi Üniversitesi)
Prof. Dr. Ali Koşar (Sabancı Üniversitesi)
Prof. Dr. Necati Mahir (Eskişehir Osmangazi Üniversitesi)
Prof. Dr. İlhan Tekin Öztürk (Kocaeli Üniversitesi)
Prof. Dr. Beşir Şahin (Çukurova Üniversitesi)
Prof. Dr. Haşmet Türkoğlu (Gazi Üniversitesi)
Prof. Dr. Nazım Usta (Pamukkale Üniversitesi)
Prof. Dr. Bekir Zühtü Uysal (Gazi Üniversitesi)
Prof. Dr. Nuri Yücel (Gazi Üniversitesi)
Prof. Dr. Hüseyin Serdar Yücesu (Gazi Üniversitesi)
Prof. Dr. Hüseyin Yapıcı (Erciyes Üniversitesi)
Doç. Dr. Ünal Akdağ (Aksaray Üniversitesi)
Doç. Dr. Kamil Arslan (Karabük Üniversitesi)
Doç. Dr. Timur Aydemir (Gazi Üniversitesi)
Doç. Dr. Sinan Çalışkan (Hitit Üniversitesi)
Doç. Dr. Ahmet Fertelli (Cumhuriyet Üniversitesi)
Doç. Dr. Nezaket Parlak (Sakarya Üniversitesi)
Doç. Dr. Mesut Tekkalmaz (Eskişehir Osmangazi Üniversitesi)
Doç. Dr. Onur Tuncer (İstanbul Teknik Üniversitesi)
Doç. Dr. Elif Büyük Öğüt (Kocaeli Üniversitesi)
Doç. Dr. Tuba Okutucu Özyurt (Orta Doğu Teknik Üniversitesi)
Doç. Dr. Oğuz Turgut (Gazi Üniversitesi)
Doç. Dr. Sıtkı Uslu (TOBB Üniversitesi)
Yrd. Doç. Dr. Çetin Canpolat (Çukurova Üniversitesi)
Yrd. Doç. Dr. Tolga Demircan (Kırıkkale Üniversitesi)
Yrd. Doç. Dr. Nureddin Dinler (Gazi Üniversitesi)
Yrd. Doç. Dr. Mehmet Doğan (Bozok Üniversitesi)
Yrd. Doç. Dr. Gökhan Kirkil (Kadir Has Üniversitesi)
Yrd. Doç. Dr. Çiğdem Susantez (Trakya Üniversitesi)
Yrd. Doç. Dr. Nihal Uğurlubilek (Osmangazi Üniversitesi)
Dr. Cüneyt Uysal (Karabük Üniversitesi)

Derneğimizin Değerli Üyeleri,

Isı Bilimi ve Tekniği Dergisi'nin (Journal of Thermal Science and Technology) Editörlük görevini 2006 yılından beri sürdüren değerli meslekdaşım Prof. Dr. Nuri Yücel'den devraldım.   Prof. Dr. Nuri Yücel 10 yıldır büyük bir başarı ve özveri ile sürdürdüğü bu görevi süresince sürekli olarak dergimizin daha iyiye gitmesi için çalıştı ve dergimizin uluslararası indekslerce taranması için büyük bir çaba içinde oldu.   Kendisine ve önceki dönemde Editörler Kurulu üyesi olarak görev yapan meslekdaşlarım Prof. Dr. Haşmet Türkoğlu, Doç. Dr. Oğuz Turgut ve Yrd. Doç. Dr. Nureddin Dinler ile derginin çıkarılmasına katkıda bulunan teknik sorumlulara içten teşekkür ediyorum.

Editörler Kurulu üyesi meslekdaşlarımla birlikte Isı Bilimi ve Tekniği Dergisi'ni ulaştığı noktadan daha da ilerilere taşımak için sizlerin de katkılarını bekliyor olacağız.

Saygılarımla,

Zafer Dursunkaya
Editör

HEAT TRANSFER FROM AN OSCILLATED VERTICAL ANNULAR FLUID COLUMN THROUGH A POROUS DOMAIN: A THERMODYNAMIC ANALYSIS OF THE EXPERIMENTAL RESULTS

Ersin SAYAR

Istanbul Technical University, Department of Mechanical Engineering
34437 Beyoğlu, İstanbul, Turkey, ersin.sayar@itu.edu.tr

Abstract: Heat transfer in an oscillating vertical annular fluid column flowing through a porous domain in the single phase or bubbly flow two-phase regime (sub-cooled or saturated nucleate flow boiling) are investigated experimentally and theoretically, in quasi-steady state conditions. Forced oscillations are applied to water via a frequency controlled dc motor and a piston-cylinder device. Heat transfer is from the stationary concentric tubular electric heating element outer surface to the reciprocating flow. The heat transfer in an oscillating vertical annular fluid column flowing in the single phase or in the bubbly flow regime is altered by using stainless steel wool porous medium. For the single phase region of flow, it is understood that, the effective heat transfer mechanism is enhanced and it is due to the hydrodynamic boundary layer which can not follow the core flow. Bubbly (nucleate) flow boiling in oscillating flow is also investigated experimentally and theoretically using a simplified thermodynamic analysis. The onset of boiling temperature is distinctly dropped compared to the pool and flow boiling experiments on polished surfaces due the finned surface effect of the steel porous domain, due to the enhanced mixing of the boundary layer flow and core flow; due to the improvement of apparent surface roughness and due to the alteration of ebullition cycle (bubbles are limited by the cell volume here). The developed correlation predicted cycle-space averaged Nusselt number is shown to be in good agreement with the experimental data. The present investigation has possible applications in moderate sized wicked heat pipes, boilers, compact heat exchangers and steam generators.
Keywords: Oscillating, Heat transfer experiment, Single phase, Boiling, Sub-cooled, Flow boiling, Porous, Annular duct.

GÖZENEKLİ ORTAMDA DİKEY SALINIMLI HALKASAL BİR AKIŞKAN KOLONUNDAN ISI GEÇİŞİ: DENEY SONUÇLARININ TERMODİNAMİK ANALİZİ

Özet: Bu çalışmada gözenekli ortamda bulunan, salınımlı olarak dikey yönde hareket ettirilen, halkasal bir akışkan kolonunda tek fazlı veya iki fazlı habbecikli akışlı ısı geçişi sanki-sürekli durumda, teorik ve deneysel olarak incelenmiştir. Zorlanmış salınımlar suya DC motor ve piston-silindir aracılığıyla uygulanmıştır. Isı geçişi merkezdeki sabit elektrikli ısıtma elemanından salınımlı akışa olmaktadır. Tek fazlı veya iki fazlı akış rejimindeki salınımlı halkasal akıştan ısı geçişi paslanmaz çelik yün gözenekli ortam vasıtasıyla değiştirilmektedir. Tek fazlı akış bölgesinde oluşan hidrodinamik sınır tabakasının merkezdeki akışı takip edemediği için ısı geçişini iyileştirdiği tespit edilmiştir. Basitleştirilmiş bir termodinamik analiz kullanılarak salınımlı akışta habbecikli (kabarcıklı) akış kaynaması da teorik ve deneysel olarak incelenmiştir. Gözenekli ortamın sebep olduğu kanat etkileri; akıştaki sınır tabakalarının karışımı; efektif yüzey pürüzlülüğünün artışı ve habbelerin büyüklüklerinin gözenekli ortam hücre hacmiyle kısıtlı olması gibi kaynama döngüsü değişiklikleri sebebiyle kaynama başlangıcı sıcaklığının parlatılmış metal yüzey üzerindeki havuz kaynaması ve kaynamalı akışa nazaran kaydadeğer derecede düştüğü tespit edilmiştir. Çevrim ortalama Nusselt sayısı için bir korelasyon geliştirilmiş, ve korelasyonun deney sonuçları ile uyumlu olduğu görülmüştür. Kazanlar, kompakt ısı değiştiricileri, ısı boruları ve buhar jeneratörleri yapılan çalışmanın uygulama alanları içerisindedir.
Anahtar kelimeler: Salınım, Isı geçişi deneyi, Tek faz, Kaynama, Kaynamalı akış, Gözenek, Halkasal boru.

NOMENCLATURE

A	Cross-sectional area of water column (m^2)
A_o	Dimensionless oscillation amplitude
A_p	Cross-sectional area of piston (m^2)
d	Hydraulic diameter of test duct (m)
h	Heat transfer coefficient (W/m^2-K)
H_1, H_2	Cycle-averaged enthalpies in Equation 6 (J)
i	Enthalpy (J/kg)
i_{lv}	Enthalpy of vaporization (J/kg)

Ja   Jakob number
L   Distance from probe 1 to probe 2 (m)
l_h Heater length (m)
l_o Distance from probes to heater (m)
Nu_L Space and cycle averaged Nusselt number
Pr   Prandtl Number
R_{men} The radius of the liquid-vapor meniscus (m)
Q_{loss} Total heat loss to environment over a cycle (J)
Q_l Total heat transferred to water over a cycle (J)
q_e Total wall heat transfer (W)
$q_1"$ Heat flux from heater to control volume (W/m^2)
$q_2"$ Heat flux from insulation layer to environment (W/m^2)
R   Flywheel radius (m)
R_b Hemispherical vapor bubble effective radius (m)
Re_ω Kinetic Reynolds number
r   Radial coordinate (m)
r_1 Inner radius of annulus (m)
r_2 Outer radius of annulus (m)
t   Time (s)
T   Temperature
T_0 Average temperature defined in Equation 18 (°C)
T_{10} First probe temperatures (°C)
T_{20} Second probe temperatures (°C)
T_a Ambient temperature (°C)
T_v The temperature of the vapor adjacent to the meniscus (ºC)
T_w Wall temperature (ºC)
T_{wo} Space-cycle averaged wall temperatures (ºC)
u_{AMP} Amplitude of Darcy velocity (m/s)
u_D Local Darcy mean velocity (m/s)
y   Vertical coordinate (the origin is at the bottom of the test set-up, $y=y^++1.0$ m)
y^* Distance from reference to the meniscus (m)
y^+ Vertical coordinate (the origin is at the probe 1)
y_m Amplitude of oscillations (m)
y_i Interface position (m)
y_0 Oscillation axis or filling height (m)

Greek Symbols

ε   Volumetric porosity (m^3 fluid volume/m^3 total volume)
δ   Momentum boundary layer thickness (m)
σ Surface tension (N/m)
ρ   Fluid density (kg/m^3)
ω   Angular frequency (rad/s)
ΔT_{crit} Critical superheat for bubble formation (ºC)

Subscripts

l   Liquid
v   Vapor

INTRODUCTION

Oscillating flows have been a common topic of fundamental investigations in the fields of heat and mass transfer in the recent years. Loop heat pipe (LHP) is a promising application of oscillating flow. LHP is an exceptionally efficient heat transfer device (Wang et al., 2013; Wan et al., 2012). A series of experiments were performed to investigate heat transfer under varying length and inner diameter miniature oscillating heat pipes by Lin et al.(2011). Heat transfer in an oscillating loop heat pipe consisting of three interconnected columns was investigated experimentally by Ozdemir (2007) and also by Arslan and Ozdemir(2008). Chatwin (1975) and Watson (1983) discussed mass transfer in pulsating and oscillating flow, to investigate transport phenomena in organs of the human body. Zhao and Cheng (1998) gave a literature survey on the heat and mass transfer in pulsating and oscillating flow. Kurzweg (1984) investigated the longitudinal heat transfer process. Ozawa and Kawamoto (1991) investigated the heat transfer mechanism experimentally and numerically. The researchers concentrated on the flow of the boundary and bulk regions of the fluid. Zhao and Cheng (1995) carried out a study for forced convection in a long heated pipe subjected to uniform heat flux with a laminar reciprocating flow of air. In another numerical study, Zhao and Cheng (1996) investigated the heat transfer for laminar forced convection of a periodically reversing flow in a pipe heated at constant temperature. Four similarity parameters such as Prandtl number, kinetic Reynolds number, dimensionless oscillation amplitude and the length to diameter ratio of the heated tube were used in their study. Xiaoguo and Cheng (1993) obtained a correlation equation for cycle-averaged Nusselt number in terms of Reynolds number, kinetic Reynolds number and dimensionless fluid displacement. The heat transfer from a vertical wall near an oscillating gas/liquid interface was investigated experimentally by Chen and Chen (1998). An empirical equation for average Nusselt number was recommended. The equation was based on Reynolds number and Prandtl number in the case of oscillating interface without evaporation. Heat transfer from a surface having constant heat flux subjected to oscillating flow in a vertical annular liquid column was investigated experimentally by Akdag and Ozguc (2009). The working fluid was liquid water and the experimental system was open to surrounding atmosphere. Heat removal from the cold surface due to the oscillating liquid column was determined in terms of Nusselt number (Akdag et al., 2008).

The heat transfer mode of boiling in porous media is similar to boiling in wicked surfaces except that evaporation on the top of the porous medium does not have much effect on the formation and growth of the vapor bubbles (Sondergeld, and Turcotte, 1997). Udell (1985) observed boiling in porous media with heat application from above. The vapor bubbles cannot escape from the top of the porous medium as they can in the case of boiling on a wicked surface (Ramesh and Torrence, 1990). Costello and Redeker (1963) investigated the ability of wicking material to adequately supply coolant to a surface in order to sustain boiling. When boiling begins in a fluid-saturated porous medium heated from below, a two layer system is formed with a

liquid region overlying a two-phase region (Nield and Bejan,2013). Experiments by Sondergeld and Turcotte(1977) and Bau et al.(1982) have shown that the liquid regime temperature profile may be conductive or convective, but the two-phase region is essentially isothermal at the saturation temperature (Faghri and Zhang,2006) . Chuah and Carey (1987) studied boiling in an unconfined layer of small spheres on a chrome-plated copper boiling surface. The effect of the particles on heat flux depends on the characteristics of the particles: glass beads delay the onset of pool boiling heat transfer, while copper beads improve it. A numerical study of boiling with mixed convection in a vertical porous layer was made by Najjari and Nasrallah(2002). A three-dimensional simulation of phase-change heat transfer in an asymmetrically heated channel was carried out by Li et al.(2010). Li and Leong(2011) performed an experimental and numerical study of single and two-phase flow and heat transfer in aluminum foams. Damronglerd and Zhang (2006) studied transient fluid flow and heat transfer in a layer with partial heating and evaporation at the upper surface. In general, the boiling characteristics from porous coated surfaces are generally superior when compared to the pool boiling on plain surfaces(Li and Peterson, 2007). The mechanisms of improvement are essentially due to the increase of the wetted area, the number of nucleation sites, the enhanced interaction among bubbles, as well as possible film and capillary evaporation induced through the use of porous coatings. For discussion of some wider aspects of boiling and two-phase flow in porous media, the reader is referred to the reviews by Dhir(Dhir, 1994; Dhir, 1998; Dhir and Cotton,1977;Naik and Dhir 1982). Lipinski(1982) presents a comprehensive review of phase change and two-phase flow phenomena in porous media. Porous coatings with higher thermal conductivity were claimed to perform better than those with lower thermal conductivities, especially at low heat fluxes. Accordingly, different from previous studies the motivation of the present study is to investigate single phase heat transfer and two-phase boiling performance of water in a moderate thermal conductivity (stainless steel, k = 15 W/mK) porous domain where the experimental test section is annular. Enhanced boiling surface may affect boiling characteristics; lowering the temperature at onset of nucleate boiling; improving the heat transfer coefficient in the nucleate boiling regime; increasing the critical heat flux(Furberg, 2011). Lowering the temperature at onset of nucleate boiling indicates that the boiling heat transfer in porous layers occurs within a narrower range of wall superheat and, hence, may be more suitable for applications where precise temperature control is required. The present study primarily focuses and covers the relationship of enhanced surface/volume features and the related heat transfer mechanisms of the nucleate boiling regime in a porous domain. This study reports part of an extensive experimental research on the heat transfer from a surface heated with constant heat flux to an oscillating vertical

annular water column. The analysis is carried out for three different oscillation frequencies and four applied wall heat fluxes while the displacement amplitude and the thermo-physical – material properties of the stainless steel wool porous medium can assumed to be constant for all the cases considered. In the experiments, the heated surface temperature is varied as a result of the amount of electrical power supplied. Power is set to produce four discrete wall heat fluxes and three different frequencies of the forced oscillations are controlled by the external piston-cylinder device. A correlation equation is obtained for the cycle-averaged Nusselt number as a function of kinetic Reynolds number and Jakob number. Annular oscillating water column is driven through a stainless steel wool porous media in order to mix the liquid and vapor phases and hence enhance the hydrodynamic and thermal performance of the system. As opposed to the all the reported works at the best of the authors knowledge, the present study investigates the oscillating flow in an annulus for the first time where the evaporation and boiling are significant (in other words, the closest study, to the present one is Chen and Chen (1998) investigates for oscillating interface without evaporation).
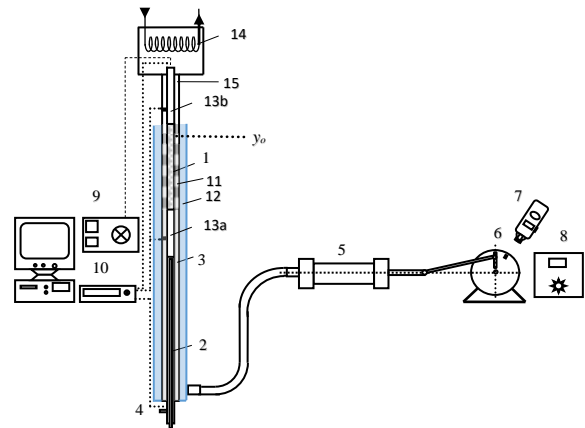
Figure 1 : Experimental setup, 1 Heater, 2 Cooler, 3 Glass pipe, 4 Cooling water inlet and outlet, 5 Piston cylinder apparatus, 6 DC Motor, 7 Digital tachometer, 8 Velocity control, 9 Power supply, 10 Data acquisition system (Keithley-2700), 11 Stainless steel wool porous domain 12 Thermal insulation 13 Teflon parts (a) and (b) 14 Water vapor condenser and 15 Piezoresistive transmitter.

EXPERIMENTAL SETUP

Figure 1 is a schematic diagram of the experimental setup. The outer part of the vertical annular test section is made of tempered glass which is 2.0 m in length, 37.5 mm in inner diameter and 42.0 mm in outer diameter. A layer of thermal insulation (Polyethylene pipe insulation, 0.034 W/mK) is applied to the exterior of the tempered glass test section. The inner and exterior diameters of the insulator are 42.0 mm and 65.0 mm, respectively. A cylinder 18.0 mm in outer diameter consisting of four zones (from top to the bottom: adiabatic (a), heater, adiabatic (b), cooler parts) is anchored precisely and

located at the centerline of the glass tube using three in-house manufactured small positioners. The positioners are located sufficiently far enough from the cooler and heater sections so that they do not significantly disturb the flow or heat transfer. Accordingly, the annuli that the working fluid occupies has inner diameter 18.0 mm and outer diameter 37.4 mm. The heater and cooler are made of concentric copper tubes with lengths of 600.0 and 760.0 mm, respectively. The adiabatic teflon parts (both (a) and (b)) are 300.0 mm in length. One of the adiabatic parts is located between the heater and cooler. The other adiabatic part is screwed smoothly to the top of the heater. The top adiabatic part is in the shape of a hollow tube in order to house the cables of the heater. The axial heat conduction in the teflon cylinder and teflon hollow tube are negligible compared with the copper ones. These four zones are assembled together using threaded joints in order to obtain smooth continuous surfaces among the consecutive sections.

The heater is built by embedding electric resistance wires inside a copper tube. Five thermocouple wires located at the inside of the heater tube are taken out of the test section by passing them through the inside of the heater tube and the adiabatic hollow teflon tube. DC power is used to feed the heater in order to prevent thermocouples from electrical inductance. This is a precaution just because the thermocouple cables are located close to the electrical cables in the heater section. Using five other thermocouple wires, surface temperature of the electrical heater is also recorded. The cooler is made of two concentric copper tubes. The cooling water enters the inner tube which is 6.0 mm / 8.0 mm in inner/outer diameter and leaves from the 16.0 mm / 18.0 mm inner/outer diameter outer tube of the cooler. Seven thermocouples are welded on the cooler surface and the leads are taken out of the test section by passing them through the cooling water.

The heat transfer in an oscillating vertical annular fluid column flowing in the bubbly flow regime is altered by using stainless steel wool (comprises off open-cell, discrete porous cells interconnected to each other geometrically and through a possible contact resistance) which produces a homogeneous porous medium within the system. The porous media has a moderate thermal conductivity (k = 15 W/mK). Porosity, ε (void fraction) of the porous domain is 93.75 % for the volume swept by the oscillating flow and porosity for the entire porous domain is 93.69 %. Accordingly, the porous domain is claimed to be distributed homogenously along the length of the electrical heater.

The thermocouples are placed such that they do not alter the fluid flow i.e. they are placed inside the cooler, heater sections or on the outer surface of the glass tube and insulation layer. There are two thermocouple bundles positioned inside the working fluids and they are called 'probes' in the present study. The first temperature probe is located at the half way of the adiabatic section between heater and cooler in order to measure the variation of water temperature with radius (r). The first temperature

probe location is also the reference position to measure the vertical positions of the surface temperatures and the interface. This first probe consists of four thermocouples located at different radial positions across the same elevation (constant y) of the annular gap. The second probe is similar to the first one but it is positioned at 150.0 mm above the heater section. Each thermocouple signal of the probes is recorded and then the probe temperatures are calculated by area-weighted averaging of the thermocouple data over the cross-sectional area.

The outer surface temperatures of the glass tube are also measured by ten thermocouples. The outer surface temperatures of the pipe exterior insulation are also measured by additional six thermocouples. All thermocouples are calibrated using a constant temperature bath before the experiments. The thermocouples are Omega K-type Nickel-Chromium vs. Nickel-Aluminum with a diameter 0.6 mm.

The pressure at the water vapor condenser is measured by Keller model PAA-23 piezoresistive transmitter. The transmitter was calibrated by the manufacturer. The transmitter is able to measure absolute pressure up to 1.0 bar. The transmitter is connected to a data acquisition system. The transmitter provide 0–10 V electric potential signals, which are converted to actual pressure values using a linear relation between voltage and pressure.

A computer controlled data acquisition system (Keithley 2700) is used to collect temperature, pressure, electrical potential and current data. The reciprocating motion of the water column is generated using a piston-cylinder driven by a 1 kW DC motor with adjustable speed and a piston-cylinder device. The number of revolutions of the motor is measured by an optical digital tachometer (Lutron DT-2234B). The filling height of the water column is kept constant for all the cases (y_0=625 mm). The experiments are conducted at for four different heating powers and three different actuation frequencies.

Uncertainity Analysis

Using the measurable quantities (electric potential, current, temperature and diameter) main error sources were investigated. Applied heat is determined by the product of voltage and current, which are measured with the accuracy of 2 % and 1 %. The temperature values are obtained by thermocouples of 1 °C accuracy, and for each case, 500 values are collected from each thermocouple, when the system is in pseudo-steady state condition. The diameters were measured using a digital caliper with the accuracy of +/-0.03 mm. To ensure if the system is in the pseudo-steady state, temperatures of every 20 minutes are compared, and decision of pseudo-steady state condition is made by obtaining the relative convergence below 1%. It takes up to 6 hours for each experiments to reach pseudo-steady state.

4

MATHEMATICAL MODEL

The Critical Superheat for Bubble Formation in Porous Domain

A surface coated with a porous layer is named a wicked surface in Faghri and Zhang(2006). Some vapor nuclei can always exist within the porous structure, but the superheat is essential for these bubbles to grow. The critical superheat for bubble formation in porous domain given in Faghri and Zhang(2006 is summarized here. Critical superheat for bubble formation in a porous domain is obtained as Faghri(1995):

$$\Delta T_{crit} = T_w - T_v = \frac{2\sigma T_v}{i_{lv}\rho_v}\left(\frac{1}{R_b} - \frac{1}{R_{men}}\right)$$

(1)

which indicates that the required superheat in a porous surface is lower than that for a plain surface.

Working Fluid Velocity

The amplitude of Darcy velocity of the water column is:

$$R\omega A_p/(A\varepsilon) = u_{AMP}$$

where Ap is the piston cross-sectional area, A is the water column cross-sectional area, R is the flywheel radius and ω is the actuation frequency. The temporal variation of the Local Darcy mean velocity can be written as follows:

$$u_D(t) = u_{AMP}\cos\omega t$$

(3)

It can be assumed that the interface is a flat surface once the capillarity and wall effects are neglected. The height yi(t) (represents the approximate position of the interface) can be derived via integration of Equation (3):

$$y_i(t) = y_0 + \frac{RA_p}{A\varepsilon}\sin\theta = y_0 + y_m\sin\omega t$$

(4)

Here, $y_m = RA_p/(A\varepsilon)$ is the amplitude of oscillations and y_0 is the oscillation axis or similarly the initial filling height (both are shown in Figure 2). It is also found that the piston-cylinder device driving motor frequency measured by tachometer is identical to the frequency of the recorded interface motion. The frequency of the recorded interface motion is calculated using the Tracker video analysis and modeling tool (a software developed by Open Source Physics). The Fast Fourier Transform analysis (results are not shown here for brevity) of the measured temperature data points out the

same base frequency with some small kinks at various other frequencies.

Calculation Method of the Cycle-Averaged Heat Transfer

A typical length scale has an order of $\sqrt{2\nu/\omega}$ for the region that inertial and viscous forces in the flow domain are comparable. The momentum diffusion decreases quickly away from the wall and the porous domain. Accordingly, the penetration depth (the depth where the wall effects are in action) is approximately given by Zhao and Cheng (1998) as follows:
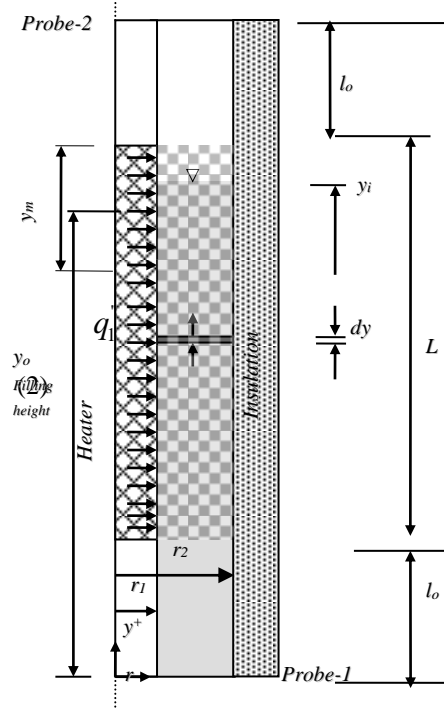
Figure 2. Control volume for the mass, energy and momentum conservation equations

$$\delta \cong 3\sqrt{2\nu/\omega}$$

(5)

This depth is below 1 mm for the frequencies considered in the present study. Thus, the velocity profile can be assumed uniform in the annular channel.

The conservation equations of mass, momentum and energy can be solved for the fluid, porous media and the solid matrix in a coupled algorithm within the system undergoing periodic compression and expansion. Convective heat transfer source term representing the heat transfer from the solid matrix to the fluid should be included in the energy conservation equations for the fluid and for the solid matrix as well. Viscous loss (includes Darcy permeability) and inertial loss (includes Forchheimer number) terms alter the momentum

equation for the porous media zones. Further discussion and solution of the listed governing equations are beyond the scope of the present experimental investigation and that can be conducted in future studies.

Interface position y+ approximately indicates the position of the water–vapor interface in this conjugate heat transfer problem of the water–vapor system. The water–vapor interface is not a flat surface because of the capillary and the water film created by the motion. Thus, the wetted heater surface cannot satisfactorily be identified only by the y+-position. Consideration of the thermal energy for water and vapor regions individually does not give practical results, due to the fact that the shape of the interface surface and the velocity at each point along the interface are presently unknown. Accordingly, the thermal energy equation for the entire system consisting of both water and vapor regions is considered. Once energy equation is integrated over the control volume shown in Figure 2, i.e. $y^+ = 0$ to L and also integrated over a cycle in time domain, the following expression is obtained:

$$H_2 - H_1 = q_1^{"} 2\pi r_1 l_h \left(\frac{2\pi}{\omega} \right) - \iint\int_0^L 2\pi r_2 q_2^{"} dy^+ dt \tag{6}$$

where cycle-averaged enthalpies are
$$H_1 = \iint \varepsilon u_D A \rho_l i_{bl}(0,t) dt = \iint \varepsilon u_D A \rho_l c_l T_{bl}(0,t) dt$$
(thermal energy of the working entering to the control volume) and $H_2 = \iint u_v A \rho_v i_v(y_i,t) dt$ (thermal energy of the working leaving the control volume). Here $i_v(y_i,t)$ is the enthalpy of the two-phase mixture leaving the control volume and $i_v(y_i,t) \approx i_{lv}$ (with the assumption saturated vapor leaves the system and condense enters back to the control volume at the saturated liquid state). q1",q2" are the heat fluxes on the heater surface and the outer surface of the insulation layer, respectively where q2" can assumed to be zero since the exterior of the system is well-insulated. Equation (13) shows the thermal energy balance of the control volume. Enthalpy difference over the control volume (H2-H1) is equal to the heat transfer at the control volume inner and outer surfaces. The heat input from the heater to control volume, $q_1^{"} 2\pi r_1 l_h \left(\frac{2\pi}{\omega} \right)$, is constant over a cycle during the pseudo-steady state of the experiments. The last term on the right hand side of Equation (6) shows the total heat loss from the exterior of the insulation layer to the surrounding room air over a cycle and it is assumed zero. The heat flux from the insulation outer surface to the environment is not constant; it varies with position and time. However, its magnitude is found to be negligible compared to the other terms in the governing equations. Enthalpy

difference over the control volume is rearranged as follows:

$$Q_l = (H_2 - H_1) = q_1^{"} 2\pi r_1 l_h \left(\frac{2\pi}{\omega} \right) - Q_{loss} \tag{7}$$

where $Q_{loss} = \iint\int_0^L 2\pi r_2 q_2^{"} dy^+ dt = 0$. Ql is the total heat transferred to water over a cycle, i.e. the net thermal energy entering to the control volume from the heater. The variation of the measured surface temperatures of the exterior side of insulation with time are neglected according to the observations during the experiments. The surface temperatures of the inner side of the glass tube perhaps vary harmonically with time. Outer surface temperatures have a pretty steady behavior with negligible minor harmonic oscillations which can be attributed to the thermal capacitance effects of the glass wall and exterior insulation layers.

The thermal energy equation for the boiling of two-phase liquid-vapor mixture region over a cycle without flat interface simplification can be written as follows:

$$Q_l = \iint\int_{l_0}^{y^*} 2\pi r_1 q_1^{"} dy^+ dt - \iint\int_0^y 2\pi r_2 q_2^{"} dy^+ dt \tag{8}$$

where, $\iint\int_0^{y_i} 2\pi r_2 q_2^{"} dy^+ dt$ is assumed zero. Here, y* is the distance from probe-1 to the meniscus. The last term on the right hand side of this equation shows the neglected heat loss from the boiling of two-phase liquid-vapor mixture side of the insulation to the environment, so that the Equation (8) can be rearranged to give the total heat transfer to water from the heater over a cycle as:

$$Q_l = \iint\int_{l_0}^{y^*} 2\pi r_1 q_1^{"} dy^+ dt \approx q_1^{"} 2\pi r_1 l_h \left(\frac{2\pi}{\omega} \right) \approx q_e \left(\frac{2\pi}{\omega} \right) \tag{9}$$

RESULT AND DISCUSSION

Cycle-averaged experimental data are given in the Table 1 with varying actuation frequencies of the piston-cylinder driver motor and the applied electrical heater power for each one of experiments.

Temporal variation of temperatures are given in Figures 3a-d (Table 1: Exp-10, $q_e = 180.0W$, $\omega = 1.434rad/s$, ym = 0.10m, $y_0 = 1.625m$), respectively for the heater

outer surface (Figure 3a); glass tube external surface (Figure 3b); insulation outer surface (Figure 3c) and Probe-1 (Figure 3d) (Please also see Figures 1 and 2). Total wall heat transfer, qe and angular frequency ω are kept constant for all figures i.e. temperature versus time and vertical coordinate are shown. As shown in Figure 3a, wall temperatures are slightly above the saturation temperature (97.6 °C) of the working fluid. Saturation temperature is calculated as 97.6 °C using the measured absolute averaged pressure of 95 kPa for all conducted experiments. Boiling starts when the temperature of the liquid near the heaters reaches the saturation temperature of the liquid. The superheat at this state is typically less than 1°C, which is much lower than that for the onset of nucleate boiling during pool boiling on a polished surface. The experiments conducted by Sondergeld and Turcotte (1977) revealed that no significant superheat is required to initiate boiling in porous media. In this regime, the heat flux throughout most of the regime is enhanced compared to pool boiling Rannenberg and Beer (1980) and Rudemiller (1989). In Figure 3b glass wall exterior surface temperatures are shown. Between the heater outer surface temperature and the glass outer surface there are two thermal resistances one is due to convection of internal flow and the outer one is due to the conduction resistance through the glass tube. At similar vertical coordinates the difference between heater outer surface temperature and glass tube outer surface temperatures are insignificant which is a direct result of the following physical mechanism. The vapor rises due to buoyant forces, inertia of the reciprocating flow and vapor pressure gradient, and liquid is pulled down to the heater surface by capillary forces, inertia of the reciprocating flow and gravity. Heat transfer that occurs with the counter-filtration of the vapor and water phases is best described as an evaporation/convection/condensation mechanism. In Figure 3c, insulation outer surface temperatures are given. These temperatures are used to check the consistency between the heat conduction through the pipe insulation and convective-radiative heat transfer to the laboratory where heat loss to the room is found negligible compared to the total heat given to the electrical heater. During the experiments the doors and the windows of the room are kept closed and the velocity of air in the room are measured to be below 1.0 m/s. In Figure 3d, temperatures of Probe 1 is plotted at four radial coordinates where four thermocouples are installed radially at the same y position, y=1000.0mm. The radial distribution of temperatures are insignificant due to the enhanced mixing provided by the steel wool porous domain.

The time-averaged heater outer surface; glass tube external surface and insulation outer surface temperatures at various vertical coordinates at three different actuation frequencies are shown in Figures 4a, 4b and 4c, respectively where the experimental conditions are listed as (Table 1: Exp-1-3), q_e = 115.0W, ω=1.434rad/s; 2.079rad/s or 2.273rad/s,y_m = 0.10m, y_0 = 1.625m. The time-averaged heater outer surface temperatures in Figure

4a are approximately linear a typical case for the fully developed flows. The flow through the heating section can be considered fully developed due to the mixing provided by the porous domain. It decreases slightly at y=1506.5 mm vertical position due to the cooling provided by the condensing vapor and by the heat transfer to the environment. The onset of boiling temperature is distinctly dropped compared to the flow boiling experiments on polished surfaces due the finned surface effect of the steel porous domain, due to the enhanced mixing of the boundary layer flow and core flow; due to the improvement off apparent surface roughness and due to the alteration of ebullition cycle (bubbles are limited by the cell volume here). According to the experimental results, bubbles induce highly efficient heat transfer mechanisms. Experimental study proved that the frequency, and wall temperature are important parameters affecting heat transfer. As shown in Figure 4b, time-averaged glass tube outer surface temperatures increase until saturated boiling (i.e. bulk fluid temperature is 97.6 °C) is reached in the test section (corresponding y=1.375m, here), the temperatures decrease close to the top cooling-condensation part (y=1.750m and y=1.925m). Similar trend to the time-averaged glass exterior surface temperatures, exterior surface temperatures of the insulation increases along the heating section then it decreases along the condenser-cooler section.

Time-averaged probe temperatures (Figures 1 and 2) versus applied electrical power at three different actuation frequencies are shown in Figure 5a (Probe-1) and Figure 5b (Probe-2) for all the cases considered. Experimental conditions and the results are tabulated in Table 1 (Exp-1-12, q_e = 115W-180W, ω=1.434rad/s; 2.079rad/s or 2.273rad/s, y_m = 0.10m, , z_0 = 1.625m). For Probe-1 in Figure 5a, at ω=1.434rad/s (actuation frequency of the piston cylinder device) boiling heat transfer is much prominent as it is compared to single phase heat transfer mechanism at q_e=150W and 180.0W. On the other hand, at q_e=115W and 132.5W single phase heat transfer takes over. At ω=2.079rad/s boiling heat transfer is much prominent as it is compared to single phase heat transfer mechanism at q_e=132.5, 150W and 180.0W. On the other hand, at q_e=115W single phase heat transfer takes over. At ω=2.7227rad/s the vapor bubbles are visually observed to exist perhaps the contribution due to two-phase heat transfer at that comparably high frequency is minor therefore at all wall heat fluxes the single phase heat transfer is the dominant one. For the single phase region of flow, it is understood that, the effective heat transfer mechanism is enhanced and it is due to the hydrodynamic boundary layer which can not follow the core flow. In oscillating flow, the heat transfer coefficient is strongly affected for the single phase flow. In Figure 5b, Probe-2 temperatures are shown at four wall heat fluxes and three actuation frequencies. According to the results in Figure 5b, the temperatures within the cooler-condenser section approach to the condensation temperature as the relative strength of boiling increases relative to the single phase heat transfer within the experimental set-up.

Table 1. Cycle averaged experimental data

	ω (rad/s)	q_e (W)	T_{w0} (°C)	T_{20} (°C)	T_{10} (°C)	Re_ω	Ja	h (W/m2K)	Nu_L (exp)	Nu_L (Corr)	Abs.Error (%)
Exp-1	1.43	115.1	97.6	95.9	83.3	1719.0	5.28E-5	421.6	373.9	395.4	5.7
Exp-2	2.08	114.1	93.3	93.0	82.4	2492.2		598.9	531.1	576.5	8.5
Exp-3	2.72	114.6	85.8	85.7	77.4	3263.9		899.6	797.9	754.9	5.4
Exp-4	1.43	132.1	99.6	99.6	85.2	1719.0	3.70E-3	541.2	480.0	479.7	0.1
Exp-5	2.08	132.6	98.5	98.0	86.6	2492.2	1.70E-3	629.2	558.0	545.8	2.2
Exp-6	2.72	132.7	92.6	92.5	83.3	3263.9		867.4	769.3	754.9	1.9
Exp-7	1.43	150.3	99.9	99.8	85.6	1719.0	4.31E-3	615.4	545.8	538.7	1.3
Exp-8	2.08	150.3	99.9	99.7	88.3	2492.2	3.77E-3	792.5	702.9	704.2	0.2
Exp-9	2.72	150.3	97.9	97.4	88.1	3263.9	6.12E-4	860.2	762.9	718.5	5.8
Exp-10	1.43	178.7	100.3	99.8	86.5	1719.0	5.08E-3	735.6	652.4	632.6	3.0
Exp-11	2.08	180.0	100.1	99.8	89.5	2492.2	4.68E-3	975.9	865.5	842.1	2.7
Exp-12	2.72	178.2	100.4	100.3	90.5	3263.9	4.40E-3	1152.1	1021.8	1042.4	2.0
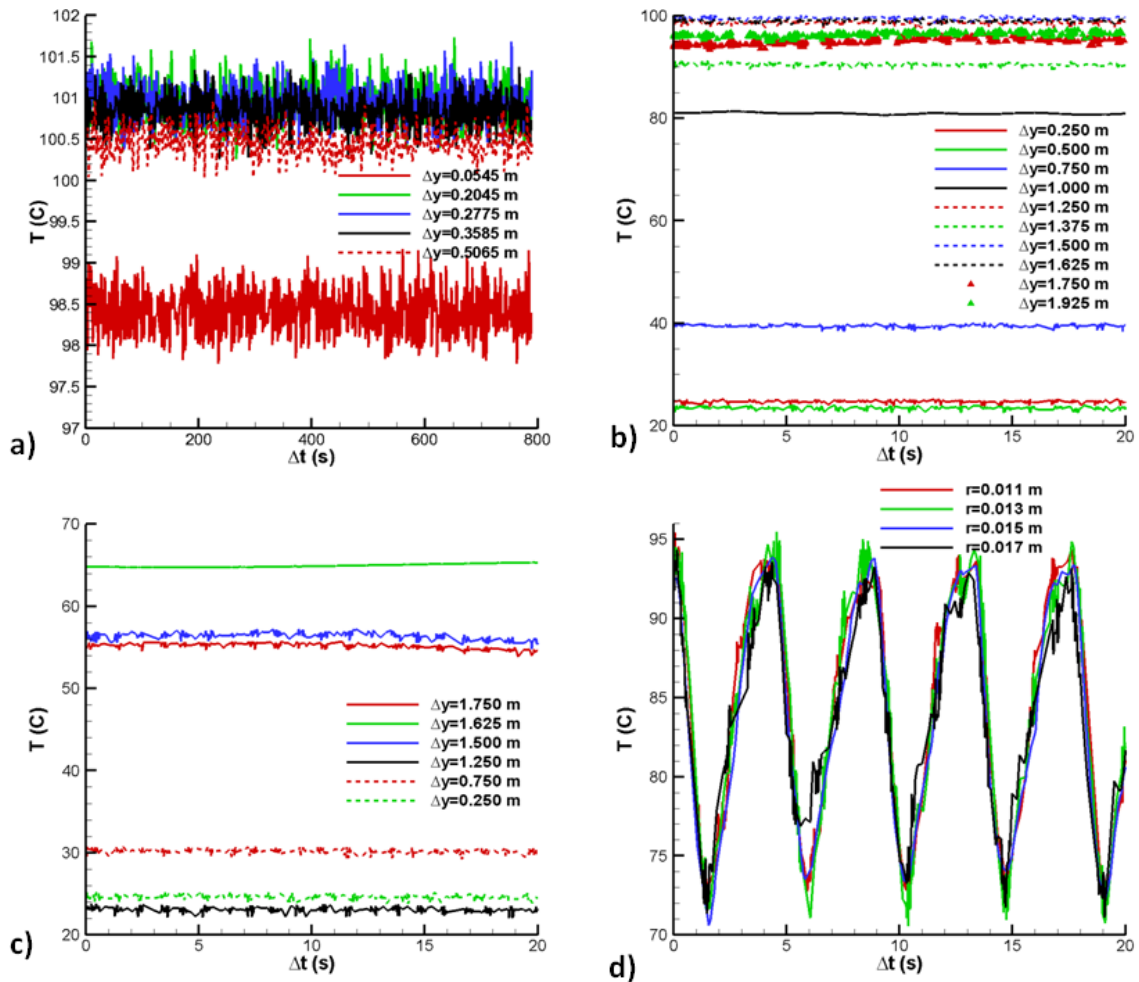
Figure 3. Temperatures versus time (Table 1: Exp-10, q_e = 180.0W, ω=1.434rad/s, y_m = 0.10m, y_0 = 1.625m, Δy, distance from the bottom end of the tubular test section). a) Heater outer surface b) Glass tube external surface c) Insulation outer surface d) Probe-1
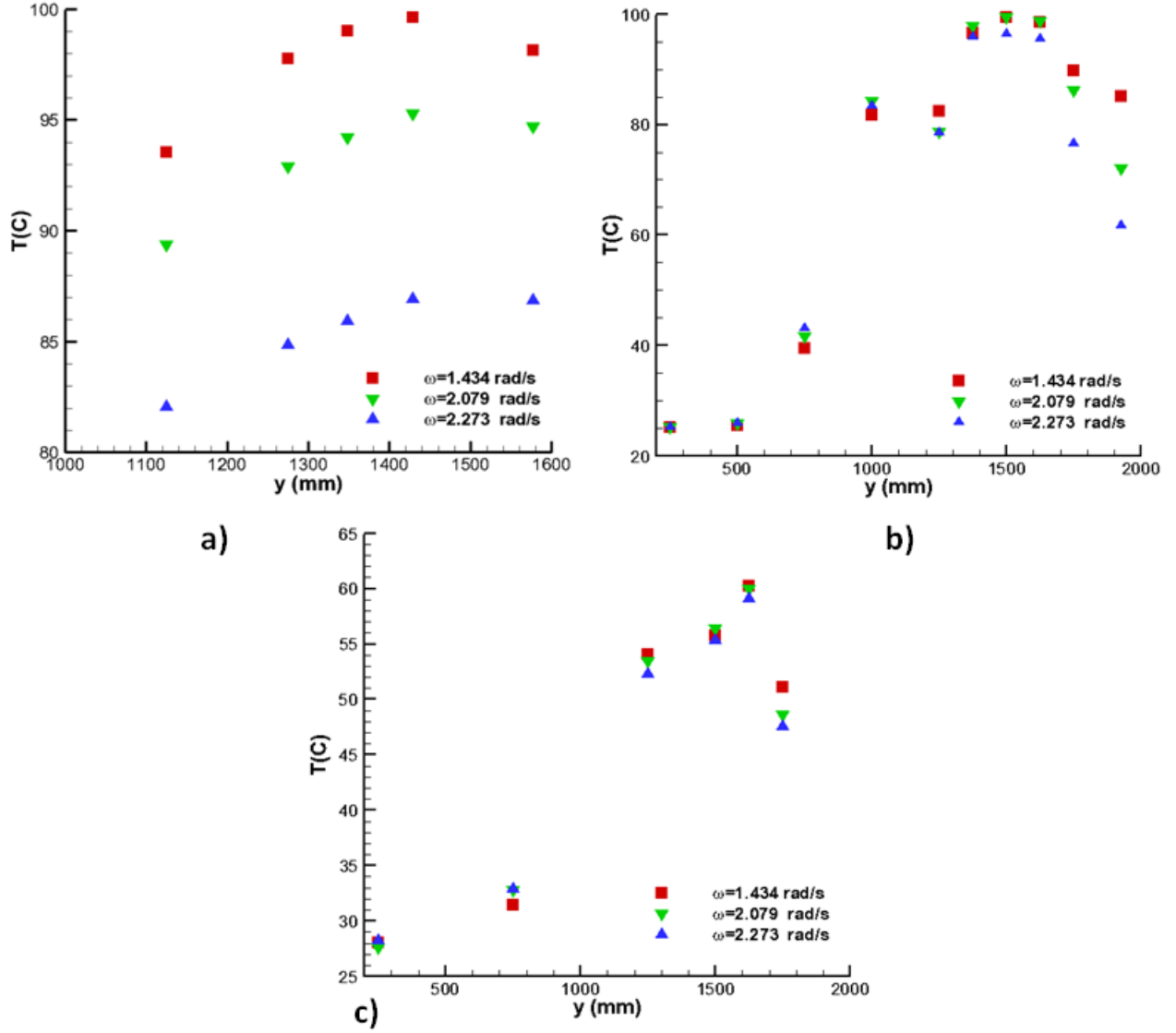
Figure 4. Time-averaged temperatures versus vertical coordinate at three different actuation frequencies (Table 1: Exp-1-3, q_e = 115.0W, ω=1.434rad/s; 2.079rad/s or 2.273rad/s,y_m = 0.10m, y_0 = 1.625m). a) Heater outer surface b) Glass tube external surface c) Insulation outer surface

Prediction of Nusselt Number

The total heat transfer to water from the heater over a cycle Ql can alternatively be written as follows:

$$Q_l = 2\pi r_1 l_h h \left(T_{w0} - T_0\right)(2\pi / \omega) \tag{10}$$

Here, the averaged water temperature can be defined as:

$$T_0 = \frac{T_{10} + T_{20}}{2} \tag{11}$$

T_{10} and T_{20} represent time and space averaged probe temperatures (listed in Table 1). Parallel to the Equation (10), the space and cycle averaged Nusselt number is defined as:

$$Nu_L = \frac{h l_h}{k} = \frac{l_h}{k} \frac{Q_l}{2\pi r_1 l_h (T_{wo} - T_0)(2\pi / \omega)} \tag{12}$$

The calculated Nusselt numbers using Equation (12) are tabulated in Table 1 according to the applied frequencies and heater power. Nusselt number is given as a function of the kinetic Reynolds number $Re_\omega = \omega d^2/\nu$, modified Jakob number,

9
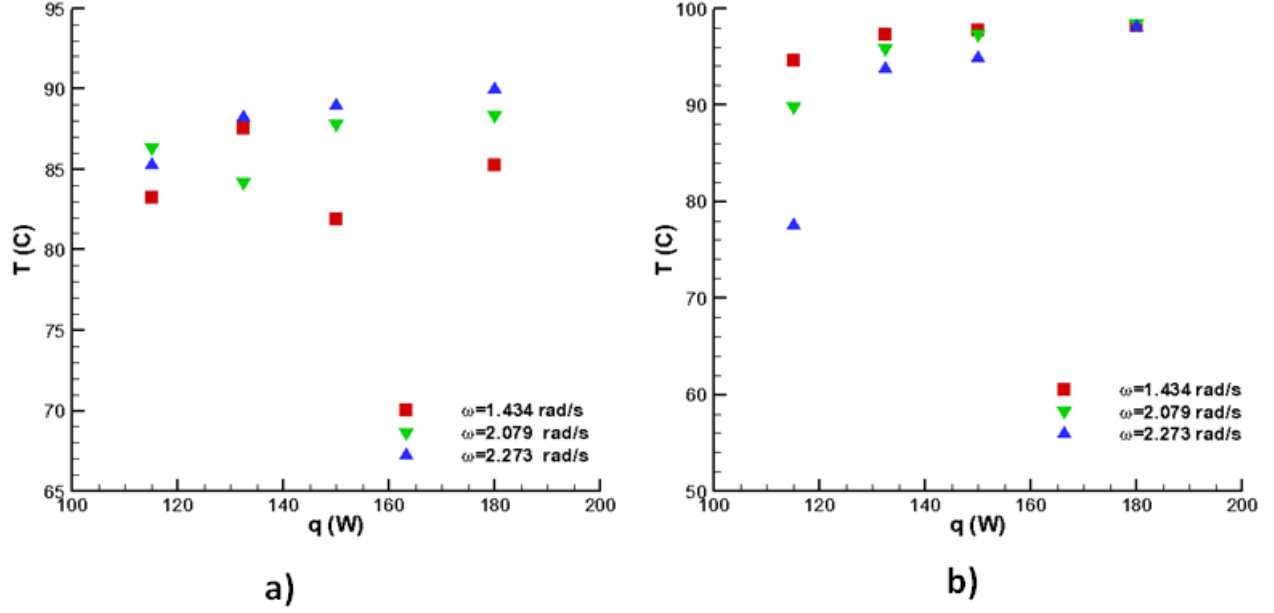
Figure 5. Time-averaged probe temperatures versus applied electrical power at three different actuation frequencies (Table 1: Exp-1-12, q_e = 115W-180W, ω=1.434rad/s; 2.079rad/s or 2.273rad/s, y_m = 0.10m, , y_0 = 1.625m). a) Probe-1 b) Probe-2

$$\left(Ja = \frac{c_{p\,@\,T_0}\left[T_{wo} - T_{sat}\right]}{i_{lv}} \right) \tag{14}$$

dimensionless oscillation amplitude A_o=$2x_m/d$, the aspect (hydraulic diameter to length) ratio of the heater d/l_h and Prandtl number as Zhao and Cheng(1995) :
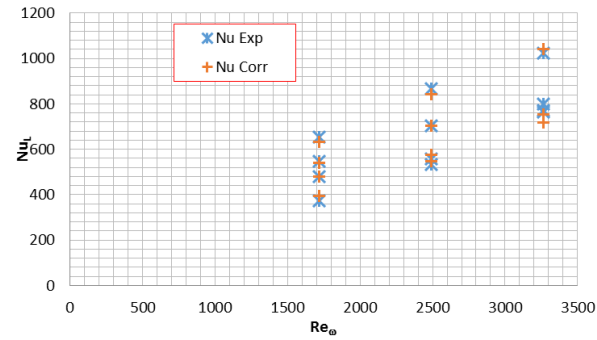
Figure 6. Nusselt number versus kinetic Reynolds number

Nu_L=f($Re\omega$, Ja, A_0, d/l_h,Pr) $\tag{14}$

In this study, the parameters A_0, d/l_h, Pr are kept constant while the kinetic Reynolds number and Jakob number are varied. The correlation equation for Nusselt number is found using the non-linear regression analysis as:

$$Nu_L = \left(10116Ja^2 - 23.408Ja + 0.2306\right)Re_\omega \tag{15}$$

The coefficient of determination is $R^2 = 0.9787$ and the given correlation is applicable in the following range of

kinetic Reynolds numbers according to the the present experiments.

$$1700 < Re\omega < 3300$$

The graphical representation of Equation (15) is shown in Figure 6 together with the experimental data.

CONCLUSION

Nusselt correlation for the single phase and two-phase heat transfer from a forced oscillated vertical annular fluid column through a porous medium is obtained experimentally. Heat transfer is from a surface heated with constant heat flux to an oscillating single phase or boiling vertical annular water column in the present paper. The inner wall of the stationary concentric element is heated and water is oscillated through the annuli by an external piston-cylinder system. The analysis is carried out for the case of three different oscillation frequencies and four different applied wall heat fluxes while the displacement amplitude remains constant. A control volume formulation is introduced in order to investigate the total heat transfer to water over a cycle. The predicted cycle-space averaged Nusselt number (using the kinetic Reynolds number and Jakob number) is shown to be in good agreement with the experimental data where the coefficient of determination is $R^2 = 0.9787$. The experimental results demonstrated that boiling in porous media could occur over a large range heat flux, i.e., from 0 to 5.3 kW/m2, and at the same time, within a much narrower wall superheat, i.e., <2°C, than for plain surfaces. This indicates that the boiling heat transfer in porous layers occur within a narrower range of wall superheat and, hence, may be more suitable for applications where precise temperature control is required.

10

REFERANCES

Akdag, U. and A.F. Ozguc, *Experimental investigation of heat transfer in oscillating annular flow.* International Journal of Heat and Mass Transfer, 2009. **52**(11-12): p. 2667-2672.

Akdag, U., M. Ozdemir, and A.F. Ozguc, *Heat removal from oscillating flow in a vertical annular channel.* Heat and Mass Transfer, 2008. **44**(4): p. 393-400.

Arslan, G. and M. Ozdemir, *Correlation to predict heat transfer of an oscillating loop heat pipe consisting of three interconnected columns.* Energy Conversion and Management, 2008. **49**(8): p. 2337-2344.

Bau, H. and K. Torrance, *Low Rayleigh number thermal convection in a vertical cylinder filled with porous materials and heated from below.* Journal of Heat Transfer, 1982. **104**(1): p. 166-172.

Chatwin, P.C., *Longitudinal Dispersion of Passive Contaminant in Oscillatory Flows in Tubes.* Journal of Fluid Mechanics, 1975. **71**(Oct14): p. 513-527.

Chen, Z.D. and J.J.J. Chen, *A simple analysis of heat transfer near an oscillating interface.* Chemical Engineering Science, 1998. **53**(5): p. 947-950.

Chuah, Y. and V. Carey, *Boiling Heat Transfer in a Shallow Fluidized Particulate Bed.* Journal of Heat Transfer, 1987. **109**(1): p. 196-203.

Costello, C. and E. Redeker. *Boiling heat transfer and maximum heat flux for a surface with coolant supplied by capillary wicking.* in *Chem. Eng. Progr. Symposium Ser.* 1963.

Damronglerd, P. and Y. Zhang, *Transient fluid flow and heat transfer in a porous structure with partial heating and evaporation on the upper surface.* Journal of Enhanced Heat Transfer, 2006. **13**(1).

Dhir, D.V.K., *Boiling and two-phase flow in porous media.* Annual review of heat transfer, 1994. **5**(5).

Dhir, V., *Boiling heat transfer.* Annual review of fluid mechanics, 1998. **30**(1): p. 365-401.

Dhir, V. and I. Catton, *Dryout heat fluxes for inductively heated particulate beds.* Journal of Heat Transfer, 1977. **99**(2): p. 250-256.

Faghri, A. and Y. Zhang, *Transport phenomena in multiphase systems.* 2006: Academic press.

Faghri, A. *Heat pipe science and technology.* in *Fuel and Energy Abstracts.* 1995.

Furberg, R., *Enhanced Boiling Heat Transfer on a Dendritic and Micro-Porous Copper Structure.* 2011.

Kurzweg, U.H. and L. Dezhao, *Heat-Transfer by High-Frequency Oscillations - a New Hydrodynamic Technique for Achieving Large Effective Thermal-Conductivities.* Physics of Fluids, 1984. **27**(11): p. 2624-2627.

Li, H., et al., *Three-dimensional numerical simulation of fluid flow with phase change heat transfer in an asymmetrically heated porous channel.* International Journal of Thermal Sciences, 2010. **49**(12): p. 2363-2375.

Li, C. and G. Peterson, *Parametric study of pool boiling on horizontal highly conductive microporous coated surfaces.* Journal of heat transfer, 2007. **129**(11): p. 1465-1475.

Li, H. and K. Leong, *Experimental and numerical study of single and two-phase flow and heat transfer in aluminum foams.* International Journal of Heat and Mass Transfer, 2011. **54**(23): p. 4904-4912.

Lin, Z.R., et al., *Experimental study on effective range of miniature oscillating heat pipes.* Applied Thermal Engineering, 2011. **31**(5): p. 880-886.

Lipinski, R.J., *Model for boiling and dryout in particle beds.[LMFBR].* 1982, Sandia National Labs., Albuquerque, NM (USA).

Naik, A.S. and V. Dhir, *Forced flow evaporative cooling of a volumetrically heated porous layer.* International Journal of Heat and Mass Transfer, 1982. **25**(4): p. 541-552.

Najjari, M. and S. Ben Nasrallah, *Numerical study of boiling with mixed convection in a vertical porous layer.* International Journal of Thermal Sciences, 2002. **41**(10): p. 913-925.

Nield, D.A. and A. Bejan, *Mechanics of Fluid Flow Through a Porous Medium.* 2013: Springer.

Ozawa, M. and A. Kawamoto, *Lumped-Parameter Modeling of Heat-Transfer Enhanced by Sinusoidal Motion of Fluid.* International Journal of Heat and Mass Transfer, 1991. **34**(12): p. 3083-3095.

Ozdemir, M., *An experimental study on an oscillating loop heat pipe consisting of three interconnected columns.* Heat and Mass Transfer, 2007. **43**(6): p. 527-534.

Ramesh, P. and K. Torrance, *Stability of boiling in porous media.* International journal of heat and mass transfer, 1990. **33**(9): p. 1895-1908.

Rannenberg, M. and H. Beer, *Heat transfer by evaporation in capillary porous wire mesh structures.* Letters in Heat and Mass Transfer, 1980. **7**(6): p. 425-436.

Rudemiller, G.R., *A fundamental study of boiling heat transfer mechanisms related to impulse drying.* 1989.

Sondergeld, C.H. and D. Turcotte, *An experimental study of two-phase convection in a porous medium with applications to geological problems.* Journal of Geophysical Research, 1977. **82**(14): p. 2045-2053.

Udell, K.S., *Heat transfer in porous media considering phase change and capillarity—the heat pipe effect.* International Journal of Heat and Mass Transfer, 1985. **28**(2): p. 485-495.

Xiaoguo, T. and P. Cheng, *Correlations of the cycle-averaged Nusselt number in a periodically reversing pipe flow.* International Communications in Heat and Mass Transfer, 1993. **20**(2): p. 161-172

Wan, Z.P., X.W. Wang, and Y. Tang, *Condenser design optimization and operation characteristics of a novel miniature loop heat pipe.* Energy Conversion and Management, 2012. **64**: p. 35-42

Wang, X.W., Z.P. Wan, and Y. Tang, *Heat transfer mechanism of miniature loop heat pipe with water-copper nanofluid: thermodynamics model and experimental study.* Heat and Mass Transfer, 2013. **49**(7): p. 1001-1007.

Watson, E.J., *Diffusion in Oscillatory Pipe-Flow.* Journal of Fluid Mechanics, 1983. **133**(Aug): p. 233-244.

Zhang, J.G. and U.H. Kurzeg, *Numerical simulation of time-dependent heat transfer in oscillating pipe flow.* Journal of Thermophysics and Heat Transfer, 1991. **5**(3): p. 401-406.

Zhao, T.S. and P. Cheng, *A numerical study of laminar reciprocating flow in a pipe of finite length.* Applied Scientific Research, 1998. **59**(1): p. 11-25.

Zhao, T. and P. Cheng, *A Numerical-Solution of Laminar Forced-Convection in a Heated Pipe Subjected to a Reciprocating Flow.* International Journal of Heat and Mass Transfer, 1995. **38**(16): p. 3011-3022.

Zhao, T.S. and P. Cheng, *Oscillatory Heat Transfer in a Pipe Subjected to a Laminar Reciprocating Flow.* Journal of Heat Transfer, 1996. **118**(3): p. 592-597

DOĞAL GAZ YAKITLI BİR KAZANDA KATI YÜZEY İLAVESİNİN NOx EMİSYONLARINA ETKİSİ

Emre UĞURLUOĞLU*, Y. Erhan BÖKE** ve Özer AYDIN***

*İstanbul Teknik Üniversitesi Fen Bilimleri Enstitüsü, İstanbul, Türkiye, emreugurluoglu@gmail.com
**İstanbul Teknik Üniversitesi Makina Fakültesi, İstanbul, Türkiye, boke@itu.edu.tr
***Dumlupınar Üniversitesi Makine Mühendisliği Bölümü, Kütahya, Türkiye, ozer.aydin@dpu.edu.tr

Özet: Bu çalışmada gaz yakıtlı kazanlarda ışınım ile ısı geçişini arttırmak için yanma odası içerisine yerleştirilen ilave katı yüzeylerin alev sıcaklığına ve NOx emisyonlarına olan etkileri deneysel olarak araştırılmıştır. Yanma odasında katı yüzey ışınımını arttırmak için bu katı yüzeylere kanat ilavesi yapılmıştır. Katı yüzeyler ("kovan" olarak isimlendirilen) et kalınlığı 1 mm, boyları 20 cm olan 25 ve 30 cm çapındaki içi boş silindirik paslanmaz çelik elemanlardır. TS EN 676 standardında tarif edilen alev geri dönüşlü bir kazanın yanma odası içine 2, 4 ve 6 kanata sahip kovanlar yerleştirilmiş ve yanma odasındaki alev sıcaklıkları ile NOx emisyonları ölçülmüştür. Yanma odasına yerleştirilen kovanlar ile kovansız durumlarda yapılan deneylerde 30 cm çaplı kovanın kanat sayısı arttıkça alev geri dönüş bölgesindeki sıcaklıkların ve NOx emisyonların azaldığı tespit edilmiştir. Kazanın baca gazı sıcaklıklığı ve NOx emisyonları kovansız duruma göre daha düşük ölçülmüştür.
Anahtar Kelimler: Doğal gaz yanması, NOx azaltma, Alev sıcaklığı.

THE EFFECT OF ADDITIONAL SOLID SURFACE ON NOx EMISSION IN NATURAL GAS FURNACES

Abstract: In this study, the effect of additional solid surfaces that placed in the combustion chamber on the flame temperature and nitrogen oxide emissions was experimentally investigated. In order to increase the solid surface radiation in the combustion chamber, the wing was added to the solid surface. The solid radiation surface (named as "filling material") was stainless steel tube with a wall of thickness 1 mm and diameters of 25 and 30 cm with lengths of 20 cm. Filling materials with 2, 4, 6 wings were placed in the combustion chamber of a 116 kW fire tube water which is defined in the Turkish Standards TS EN 676, and the flame temperature and NOx emissions were measured in the combustion chamber. According to the experiments, it was seen that the as the number of wing increases on filling material with 30 cm diameter, temperature and NOx emissions in the flame back return region were decreased. The flue gas temperature and NOx emission of the flue gas leaving the boiler were measured lower than the no fill material case.
Keywords: Natural gas combustion, NOx reduction, Flame temperature.

GİRİŞ

Diğer fosil yakıtlarla kıyaslandığında, kirletici emisyonlar bakımından daha temiz bir yakıt olan doğal gazın yanması sonucunda genellikle karbondioksit, karbonmonoksit, su buharı ve azot oksit emisyonları oluşmaktadır. Doğal gaz yanması sonucu oluşan alev sıcaklıkları diğer fosil yakıtlarla karşılaştırıldığında yüksek olduğundan, önlem alınmadığı takdirde azot oksit emisyonları yüksek seviyelere çıkmaktadır. Literatürde doğal gaz yanması sonucu emisyonların azaltılması ve kazan ısıl veriminin arttırılmasını içeren birçok deneysel ve sayısal çalışma mevcuttur. Azot oksit emisyonu azaltma yöntemlerinden biri olan duman gazı geri beslemesi ile yapılan deneylerde daha düşük değerler ölçülmüştür (Hepbaşlı, 1991). İleri alev

bölgesine metan püskürterek ve düşük NOx yakıcılarla (bu yakıcılar üzerinde havanın ve yakıtın kademelenmesini sağlayan konstrüktif değişiklikler yapılarak) farklı karışımlar oluşturup NOx emisyonlarını azaltılması üzerinde çalışılmıştır. Bu çalışma sonucunda ısıl NO oluşumunun reaksiyon sıcaklığına, bölgesel stokiyometriye ve oyalanma zamanına bağlı olduğu tespit edilmiştir. Yakıtsal NO oluşumunda ise yerel oksijen derişiklikleri önemli rol oynamakla beraber, alev sıcaklığı da etkilemektedir (Muzio ve Quartucy, 1997). S. C. Li and F. A. Williams tarafından yapılan ve metanın kullanıldığı farklı bir çalışmada ise farklı ekivalans oranlarında yanma havasına belirli bir miktarda su (CO_2, N_2 ve Argon ile birlikte) ilave edilerek NOx emisyonlarının azaldığı tespit edilmiştir (Li ve Williams, 1999). C. D. Taglia et al. tarafından

Cfc- Tasc programıyla yapılan sayısal çalışmada yakıcıya yakın bölgeye ısı değiştiricisi konularak veya yanmanın gerçekleştiği bölgede konstrüktif değişiklik yapılarak, düşük sıcaklık ve NOx emisyonları elde edilmiştir (Taglia,2001). M. İlbaş, vd., yaptıkları nümerik çalışmada yanma odasına yerleştirilen levhanın sıcaklık ve azotoksit emisyonuna etkisini incelemiştir. FLUENT programının kullanıldığı bu çalışmada ilave ışınım yüzeyinin NOx ve yanma odası sıcaklığını azalttığı saptanmıştır (İlbaş ve diğ.,2006).

K. Onat ise doğal gaz ışınımını arttırarak ocak sıcaklığını düşürmek için alevin içerisine yerleştirilen çeşitli şekildeki katı yüzeylerin uygulamadaki diğer yöntemlere göre etkenliğini araştırmıştır. Doğal gaz ocaklarında tanecik ve is ışınımı bulunmadığından ocak ısıtma yüzeyine geçen ısının katı ve sıvı yakıt ocaklarına göre daha az olacağı ve daha yüksek sıcaklıklar tespit edileceği düşünülmüştür. A. Akgüngör, 35 kW kapasiteli TS EN 676 standardına göre brülör testi için tasarlanmış doğal gaz yakıtlı bir deney kazanına cebri brülör monte ederek laboratuar şartlarında, kazan içerisinde alev özelliklerini ve ortaya çıkan emisyonları incelemiştir. Ş.Yılmaz, A. Abdülkadir Akgüngör tarafından yapılan çalışmadaki deney kazanının hesaplamalı akışkanlar dinamiği programlarıyla modelini oluşturmuş, nümerik ve deneysel verileri karşılaştırmıştır (Yılmaz,2001). S. Tucer doğal gaz yakıtlı bir ocak için yaptığı çalışmada, ocak sıcaklığının yüksek olduğu durumda yakma gazından gelen azotun kimyasal reaksiyona girerek NOx oluşumuna sebebiyet verdiğini belirtmiştir. Sayısal modellemede katı yüzey ışınımını arttırmak amacıyla dolgu maddeleri kullanılmıştır. Dolgu geometrileri için ısı geçiş oranları farklı tespit edilmiştir. Bunun nedeninin farklı geometrilerde dolgunun alanı, dolgu ile ocak duvarları arasındaki şekil faktörleri, eşdeğer tabaka kalınlıkları ve gaz emisivitelerindeki farklılık olduğunu vurgulamıştır. Tezin sonucunda boru kısmı olan dolgularda belirli bir dolgu çapı için kanat sayısı arttıkça ısı geçişinin arttığı görülmüş ve belirli bir kanat sayısı için optimum kovan çap ve boyu değeri bulunmuştur (Tucer, 2005). Ö. Aydın tarafından yapılan deneysel ve nümerik çalışmada TS EN 676 standardına göre imal edilmiş ocak boyu ayarlanabilir alev geri dönüşlü bir brülör test kazanına cebri brülör monte edilerek laboratuar şartlarında doğal gaz yakılmaktadır. Kovansız ve çap x uzunluk değerleri 20x20, 25x20, 25x40, 30x20, 30x40 cm olan kovanlarda, farklı hava fazlalık katsayıları ve ısıl güçlerde bu çalışma yapılmıştır. Deneysel çalışma, FLUENT programı yardımıyla gerçek şartları uygun modellenmiş; deney ve model sonuçları sıcaklık değişimleri (ocak ve bacada), emisyonlar (ocak ve bacada) ve ısıl verim yönünden irdelenmiştir. Yapılan CFD çalışmalarında HFK=1.26 değeri için kazanın yanma odasında katı yüzey bulunmadığı duruma (kovansız) göre katı yüzey alanı arttıkça kazanda ısıtma suyuna aktarılacak enerjinin arttığı hesaplanmıştır.

Tablo 1. Ocak cidarına aktarılan enerji (Aydın, 2005).

Kazanın Yanma Odasındaki Parametreler	Kazanda Suya Aktarılan Enerji (kW)
Kovansız	91.7
25x20	95.0
30x20	95.9

Yanma odasında katı yüzey ışınımını arttırmak amacıyla yapılan çalışmalarda kovan olarak adlandırılan dolgu maddelerinin özellikle kısa boylarında azotoksit ve karbonmonoksit emisyonlarının azaldığı tespit edilmiştir (Aydin ve Boke, 2009; Aydin ve Boke, 2010). Kovan boyları kısaldığı zaman ise katı yüzey ışınımı azaldığı için ocak cidarına olan ısı transferi azalmaktadır. Bu nedenle bu çalışmada boyu 20 cm olan kovanlara kanat ilavesi yapılarak ışınım yüzeylerinin arttırılması sağlanmıştır. Kovan üzerine ilave ışınım yüzeylerinin yanma odası sıcaklığına ve emisyonlara etkisini inceleyen araştırmaların devamı olan bu çalışmada, cebri(üflemeli) brülör ile TS EN 676 standardında alev geri dönüşlü kazanda katı yüzey ışınımını arttırmak amacıyla değişik çap ve boylardaki kovanlara değişik sayılarda (2, 4 ve 6) kanatlar monte edilmiştir.

DENEYSEL ÇALIŞMA

Deney tesisatını oluşturan bileşenler; kazan, pompa, su besleme deposu, hava-su ısı değiştiricisi ve bacadır (Şekil 1). Deneylerde, TS EN 676 standardına göre imal edilmiş, ocak boyu ayarlanabilir, en büyük ocak boyunda (790 mm) ve 400 mm çapında maksimum kazan ısıl kapasitesi 116 kW (100 000 kcal/h) olan alev geri dönüşlü bir kazan kullanılmıştır (Şekil 2). Kazanın yanma odası içerisinde gerçekleşen doğal gazın yanması ile açığa çıkan yanma sonu gazlarının sahip olduğu ısı enerjisi suya aktarılmaktadır. Deneylerde kazana su giriş sıcaklığı 70ºC, kazandan çıkan suyun sıcaklığı ise 90ºC olacak şekilde soğutma sistemi ayarlanmıştır. Deneylerde yapılan ölçümlerin bazıları (sıcaklıklar, gaz ve su debileri) zamana bağlı olarak ölçülerek deney süresince veri toplama ve kayıt cihazına kaydedilmiştir.
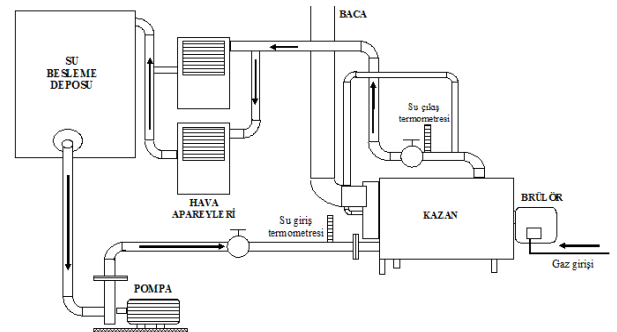
Şekil 1. Deney düzeneği.
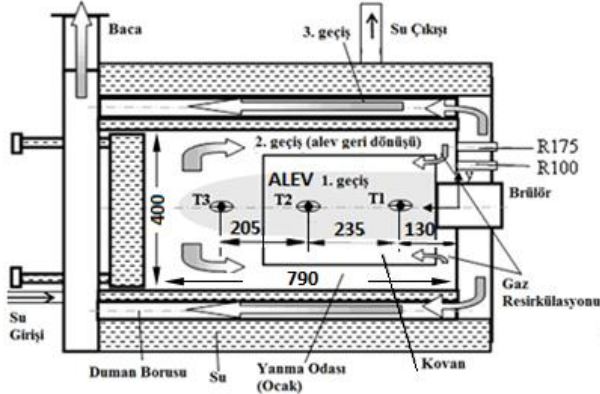
Şekil 2. Deney kazanı ve sıcaklık ölçüm noktaları.

Kazanın yanma odası ekseni boyunca ön, orta ve arka kısımlarındaki alev sıcaklıklarının ölçümü için sırasıyla yüksek sıcaklığa dayanıklı seramik kılıflı S tipi (1800ºC) T1, T2 ve T3 olarak isimlendirilen termoelemanlar yerleştirilmiştir. Kazan kapağından açılan iki farklı noktadan yanma odasında eksenel yönde belli aralıklarda gaz analizi yapılmış ve bu noktalarda sıcaklıklarda ölçülmüştür. Bu noktaların isimleri R100 ve R175 olarak adlandırılmıştır. R100 ölçüm hattı ocak yarıçapının 0.50, R175 ölçüm hattı ise ocak yarıçapının 0.875 oranında yer alacak şekilde ocak içinde oluşturulmuştur. R100 ölçüm hattı kovanların içinden alevin kenarından geçerken, R175 ölçüm hattı ise kovanların dışından ve aynı zamanda alev geri dönüş bölgesinden geçmektedir. Yanma odası içinde gaz analizi seramik gaz örnekleme probu ile yapılmıştır. Bu probun içerisine gaz analizinin yapıldığı noktadaki sıcaklığı ölçmek için termoeleman yerleştirilmiştir. Deneyler bacada karbonmonoksit (CO) değerinin minimum olduğu ve ön deneylerle belirlenen HFK=1.26 değerinde yapılmıştır. Tablo 2'de deneylerin yapıldığı tarihlerde BOTAŞ kurumundan alınan doğal gaz bileşimi görülmektedir.

Tablo 2. Deneylerin yapıldığı tarih itibari ile doğal gaz hacimsel oranları.

Bileşen	Hacimsel oran (%)
Metan	81.25
Etan	8.60
Propan	1.72
Bütan	1.63
Pentan	0.76
Oksijen	0.40
Karbondioksit	1.43
Azot	4.21
TOPLAM	100.00

Deneylerde kazanın yanma odası içerisinde ışınım ile olan ısı geçişini arttırmak için kovan adı verilen kalınlığı 1 mm olan yüksek sıcaklığa dayanıklı çelik malzeme sacdan yapılmış içi boş iki ucu açık silindirik elemanlar kullanılmıştır (Şekil 3). Deneylerde kullanılan kovanların çapları ve boyları, ölçüler cm biriminde

olmak üzere Ø25x20, Ø30x20 olarak verilmiştir. Kovan çaplarının ocak çapına oranı sırasıyla 0.625 ve 0.750 olup, kovan boylarının ocak boyuna oranı 2.53 olarak belirlenmiştir. Yanma odası içerisinde ışınım ile olan ısı geçişini daha da arttırmak için söz konusu bu kovanlara 2, 4 ve 6 kanat ilavesi yapılmıştır. Kanatsız kovanlar ise yanma odasında merkezlemeyi sağlamak için küçük ayaklar ile teçhiz edilmiştir. Yanma odasının boş hali "kovansız" olarak adlandırılmıştır.
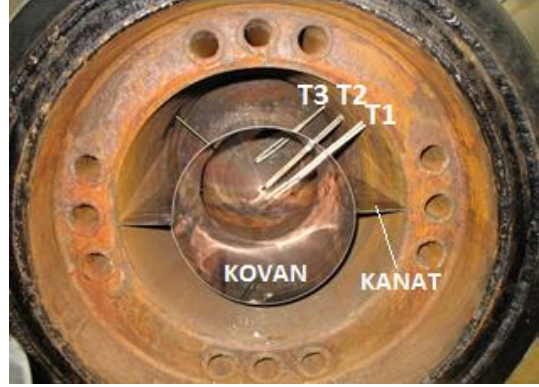
Şekil 3. Yanma odasına içerisine yerleştirilmiş 2 kanatlı kovan.

DENEY SONUÇLARI

Şekil 4'de 2, 4, 6 kanatlı 25x20 kovanları ile kovansız duruma ait HFK=1.26 değeri için yanma odası ekseni boyunca ölçülen alev sıcaklıkları görülmektedir. Kanat sayısının arttıkça yanma odasının merkezinde alev sıcaklıklarının artış gösterdiği görülmektedir. Yanma odası ekseninin baş (T1), orta (T2) ve son (T2) kısmındaki alev sıcaklıkları hemen hemen birbirine yakın değer almıştır.
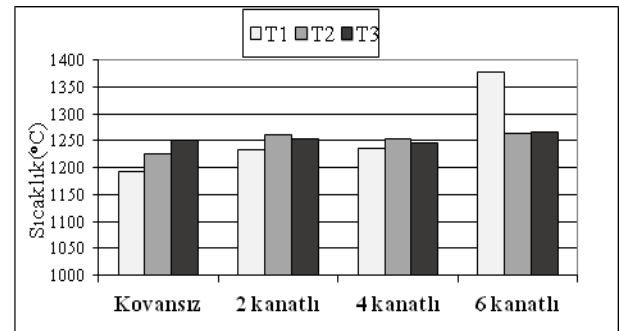
Şekil 4. Kovansız ve 25 x 20 kovanına kanat ilave edilmesi durumunda yanma odası ekseni boyunca ölçülen sıcaklıklar.

Kovansız ve 25 x 20 kovanına kanat ilave edilmesi durumunda R100 ve R175 ölçüm hatlarındaki ocak içi sıcaklık ve NOx değerleri HFK=1.26 değeri için Tablo 3 ve 4'de verilmiştir. R100 ölçüm hattında ölçülen sıcaklıklarda yanma odasının arka tarafına doğru gidildikçe kovanlı ve kovansız durumlar için artış görülmektedir. Bu artışın nedeni alevin ocak arka duvarına çarpmasından dolayı alevin geriye doğru yayılmasından kaynaklanmaktadır. Alevin kovan tarafından baskılanması alevin kazanın arkasına doğru

uzamasına neden olmuştur. Kovan üzerindeki kanatlar bu ölçüm hattı üzerinde bulunmadığından ölçülen sıcaklıklarda kanat sayısının sıcaklıklara etkisinin olmadığı görülmektedir. R100 ölçüm hattında ölçülen NOx emisyonların kovanlı durumlarda daha yüksek oldukları görülmektedir. Kovanlı deneylerde ölçülen alev merkezindeki sıcaklıkların yüksek olması (Şekil 4) NOx emisyonlarında artışa neden olmuştur.

R175 ölçüm hattının alev geri dönüş bölgesi üzerinde olması nedeniyle ocak arkasına gidildikçe sıcaklıklar artmıştır. Yanma odasına kovan konulması durumunda artan kanat sayısı ile birlikte sıcaklıklarda azalmalar görülmektedir. Katı yüzeyler bu bölgede sıcaklıkların azalmasında önemli rol oynamıştır. Fakat bu bölgedeki NOx emisyonları kovansız duruma göre daha yüksek ölçülmüştür. R175 ölçüm hattında ölçülen sıcaklıklar termal NOx oluşumunu tetikleyen sıcaklıklar olmadığı için burada ölçülen NOx emisyonlarının alev bölgesinde oluştukları söylenebilir.

Tablo 3. Kovansız ve 25x20 kovanına kanat ilave edilmesi durumunda R100 ölçüm hattı sıcaklık ve NOx değerleri.

R100	Sıcaklık (ºC)				
Ocak ağzından mesafe (cm)	KOVANSIZ	25X20	25x20 2 kanatlı	25x20 4 kanatlı	25x20 6 kanatlı
0	704	637	625	603	609
10	747	724	706	700	690
20	775	799	793	766	785
30	791	813	795	770	809
40	788	819	800	771	840
R100	NOx (mg/m³)				
0	140	134	146	134	131
10	138	134	144	136	134
20	121	119	138	136	138
30	121	125	142	132	127
40	123	131	148	129	127

Tablo 4. Kovansız ve 25x20 kovanına kanat ilave edilmesi durumunda R175 ölçüm hattı sıcaklık ve NOx değerleri.

R175	Sıcaklık (ºC)				
Ocak ağzından mesafe (cm)	KOVANSIZ	25X20	25x20 2 kanatlı	25x20 4 kanatlı	25x20 6 kanatlı
0	681	697	648	643	668
10	701	715	685	673	688
20	739	733	723	700	719
30	761	736	745	725	743
40	784	741	768	738	765
R175	NOx (mg/m³)				
0	138	131	140	131	144
10	140	134	140	140	146
20	140	134	148	142	146
30	140	134	148	144	148
40	138	134	170	154	150

Şekil 5'de 2, 4, 6 kanatlı 30x20 kovanları ile kovansız duruma ait HFK=1.26 değeri için yanma odası ekseni boyunca ölçülen alev sıcaklıkları görülmektedir. Kovanlı deneylerde alevin baş (T1) bölgesinde sıcaklıkların yüksek değer aldığı görülmüştür. Kovan çapının büyümesinden dolayı alevin bu bölgesine geri dönüşler sıcaklığın artmasına neden olmuştur. Fakat nispeten daha soğuk gazların bir kısmının alev bölgesine geri dönmesi kanatlı kovanlarda alevin orta ve son kısımlarında sıcaklıkların kovansız duruma göre daha düşük değer almasına neden olmuştur. Literatürde mevcut 30x20 kovanlı CFD modelleme çalışmasında yanma odasındaki hız vektörleri, gazların alev bölgesine geri dönüşlerinin olduğunu göstermiştir (Şekil 6), (Aydın, 2005).

Şekil 5. Kovansız ve 30 x 20 kovanına kanat ilave edilmesi durumunda yanma odası ekseni boyunca ölçülen sıcaklıklar.

Şekil 6. 30x20 kovanlı sayısal modelde hız vektörleri (Aydın, 2005; Aydın ve Boke, 2009).

Kovansız ve 30 x 20 kovanına kanat ilave edilmesi durumunda R100 ve R175 ölçüm hatlarındaki ocak içi sıcaklık ve NOx değerleri HFK=1.26 değeri için Tablo 5 ve 6'da verilmiştir. R100 ölçüm hattında ölçülen sıcaklıklarda alevin ocak arka duvarına çarpıp alevin geriye doğru geri dönmesinden (2. geçiş) dolayı kovanlı ve kovansız deneylerde artış olmuştur. Kovanlı deneylerde R100 hattında ölçülen sıcaklıklar daha düşük değerler almıştır. 4 ve 6 sayılı kanatlı kovanlar ile yapılan deneylerde sıcaklıkların azaldığı görülmüştür. Bu ölçüm hattında sıcaklıkların azalmasında kanat etkisinden daha çok artan kovan çapının etkili olduğu söylenebilir. Çünkü kovan çapı artıkça alevin kovan

16

tarafından çevresel baskılanması azalmaktadır. R100 ölçüm hattında NOx emisyonları ise sıcaklıklarda olduğu gibi benzer karakteristik özellik göstermiştir. Fazla kanat sayısına sahip kovanlı deneylerde alev bölgesindeki sıcaklıkların düşük olmasından dolayı R100 hattında NOx emisyonları düşük değerler almıştır.

Tablo 5. Kovansız ve 30x20 kovanına kanat ilave edilmesi durumunda R100 ölçüm hattı sıcaklık ve NOx değerleri.

R100	Sıcaklık (ºC)				
Ocak ağzından mesafe (cm)	KOVANSIZ	30X20	30x20 2 kanatlı	30x20 4 kanatlı	30x20 6 kanatlı
0	704	742	636	594	595
10	747	786	694	630	635
20	775	824	780	693	695
30	791	848	793	750	770
40	788	852	816	800	825
R100	NOx (mg/m³)				
0	140	134	113	107	111
10	138	134	117	105	111
20	121	119	113	119	119
30	121	125	121	123	125
40	123	131	123	127	127

R175 ölçüm hattında kanatların sıcaklıkların azalması üzerinde etkisi daha belirgin olmuştur. Kovanlı deneylerde özellikle kanat sayısının artışı ile sıcaklıkların kovansız deneye göre azaldığı görülmektedir. R175 ölçüm hattında ölçülen NOx emisyonlarında sıcaklıklardaki azalmaya paralel olarak düşüş olmuştur. Kovanlı deneylerin tamamında NOX emisyonları kovansız deneye göre daha düşük değer almıştır. Katı yüzeylerin artması sıcaklıkları azalttığı gibi NOx emisyonlarının da azalmasına neden olmuştur.
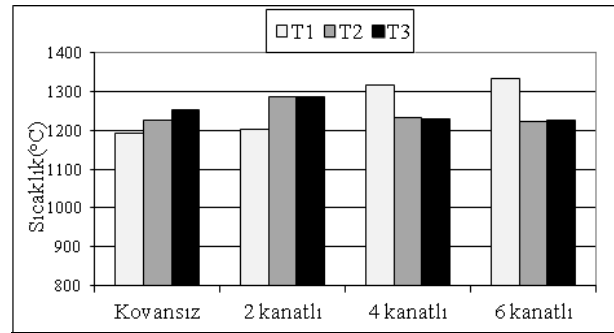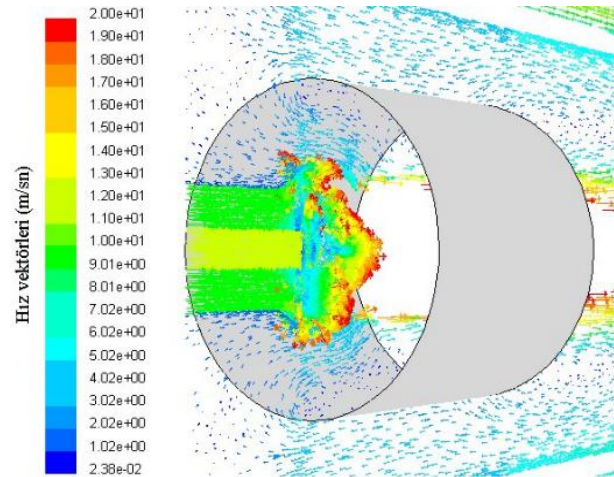
Tablo 6. Kovansız ve 30x20 kovanına kanat ilave edilmesi durumunda R175 ölçüm hattı sıcaklık ve NOx değerleri.

R175	Sıcaklık (ºC)				
Ocak ağzından mesafe (cm)	KOVANSIZ	30X20	30x20 2 kanatlı	30x20 4 kanatlı	30x20 6 kanatlı
0	681	629	623	570	565
10	701	695	650	590	593
20	739	733	700	640	648
30	761	767	735	693	700
40	784	795	755	718	745
R175	NOx (mg/m³)				
0	138	131	117	111	134
10	140	134	117	109	132
20	140	134	121	113	131
30	140	134	125	125	134
40	138	134	131	134	131

25x20 ve 30x20 kovanlarına kanat ilavesi durumunda kazanın bacasından atılan NOx emisyonlarının değişimi

Tablo 7'de verilmiştir. Kovanlara kanat ilavesi durumunda baca sıcaklığında yaklaşık 15⁰C azalma görülmektedir. Baca sıcaklığındaki bu azalma yakıtın yakılması sonucu elde edilen enerjinin daha verimli kullanıldığını göstermektedir. Bacadan atılan enerji azaltılarak yakıt tasarrufu sağlanmış olunmaktadır. Bacadan atılan NOx emisyonlarında da kovansız duruma göre azalma meydana gelmiştir.

Tablo 7. Kovansız, 25x20 ve 30x20 kovanına kanat ilave edilmesi durumunda bacada ölçülen sıcaklık ve NOx değerleri.

KOVANSIZ	25x20 2 kanatlı	25x20 4 kanatlı	25x20 6 kanatlı
Sıcaklık (ºC)			
326	329	308	313
NOx (mg/m³)			
142	150	127	140
KOVANSIZ	30x20 2 kanatlı	30x20 4 kanatlı	30x20 6 kanatlı
Sıcaklık (ºC)			
326	320	322	313
NOx (mg/m³)			
142	119	117	119

SONUÇLAR

Doğal gaz ülkemizde ve dünyada yaygın kullanılan bir yakıt olduğundan doğal gazın enerji dönüşüm veriminin arttırılması ve yanması sonucu çıkan emisyonların azaltılması önemlidir. Bu çalışmada yanma odasına yerleştirilen ilave ışınım yüzeylerinin (farklı ölçülerde kovanlar ve farklı sayılarda kanatlar) alev sıcaklığı ve NOx emisyonlarına etkisi deneysel olarak incelenmiştir. Yanma odasında katı yüzey ışınımını arttırmak amacıyla boyları 20 cm olan 25 ve 30 cm çaplı et kalınlığı 1 mm olan içi boş silindirik dolgu elemanlarına (kovan) kanat ilavesi yapılmıştır. Yanma odasına yerleştirilen farklı çaplar ve kanatlara sahip kovanlar ile kovansız durumda yapılan deneylerde kazan içinden sıcaklık ve emisyonlar ölçülmüştür. Yapılan bu ölçmeler karşılaştırıldığında 30 cm çaplı kovanda alev bölgesine gaz dönüşünün daha fazla olması nedeniyle alev bölgesindeki sıcaklıkların daha düşük olduğu ve dolayısıyla NOx emisyonlarının, 25 cm çaplı kovanla kıyaslandığında, azaldığı görülmüştür. 30x20 kovanının kanat sayısındaki artışa paralel olarak geri dönüş hattında sıcaklıkların ve NOx emisyonların düşük olduğu, akışı bozmadığı tespit edilmiştir. Bu durum R175 ölçüm hattı ocak ağzından mesafenin 0 cm olduğu konumdaki NOx emisyon değerlerinden görülmektedir. R175 ölçüm hattında ocak ağzından 0 cm uzaklıktaki ölçme noktası, yanma sonu gazlarının ocağı terk ettiği yerdir. 25x20 kovanlı deneylerde ise çapın azalması alevi baskılayarak alev boyunun uzamasına neden olmuş ve ocak merkezinde sıcaklık ve NOx emisyonlarının artmasına neden olmuştur. Aynı kovanda kanat ilavesinin arttırılması alev geri dönüş (2. geçiş) sıcaklıkların ve NOx emisyonların, kovansız ve kovanlı kanatsız durumlara kıyasla düşük

değer almasına neden olmuştur. 30x20 kovan kullanılması halinde ocağa yerleştirilmiş olan ilave ışınım yüzey alanı 25x20 kovanlı duruma göre daha fazla olduğundan 30x20 kovan durumundaki ocak içi sıcaklıklarının 25x20 kovan durumundaki sıcaklıklardan ve NOx emisyonlarından daha düşük olduğu görülmektedir. Kovan ilave edilmesi yanma odası merkezindeki sıcaklıkların artmasına sebep olmuştur. Her iki kovan ilavesinde de R100 ve özellikle R175 ölçüm hattında kovansız ve kanatsız kovanlı durumla kıyaslandığında gaz sıcaklığında ve Nox emisyonunda azalma olduğu görülmektedir. Kazanın yanma odasında ışınım yüzeylerinin arttırılması, ışınım ile olan ısı transferini arttırmış ve alev geri dönüş hattı ile bacagazı bölgesindeki NOx emisyonlarını azaltmıştır. Ayrıca yanma odasına konulan bu ilave yüzeyler baca sıcaklığının azalmasına dolayısıyla kazan verimini arttırarak yakıt tasarrufuna neden olmaktadırlar. Kazanın bacasından ölçülen NOx emisyonları da özellikle 30x20 kovanlarında daha düşük değer almıştır.

KAYNAKLAR

Akgüngör, A. A., 2000. Doğal gaz yanması ve emisyon oluşumu, Yüksek Lisans Tezi, İ.T.Ü. Fen Bilimleri Enstitüsü, İstanbul.

Aydın, Ö., 2005, Gaz yakıtlı ocaklarda katı yüzeyin emisyona ve verime etkisi, Doktora Tezi, ESOGÜ Fen Bilimleri Enstitüsü, Eskişehir.

Aydin O, Boke Y. E., 2009, Effect of the radiation surface on temperature and NOx emission in a gas fired furnace, Fuel 88, 1878–1884.

Aydin O, Boke Y. E., 2010, Experimental and numerical modeling of the effect of solid surface on NOx emission in the combustion chamber of a water heater, Computers & Fluids 39, 674–682.

Hepbaşlı, A., 1991, Doğal gaz yakıtlı örnek bir tesiste duman gazı geri beslemesiyle azot oksit emisyonlarının azaltılması, Isı Bilimi ve Tekniği 8. Ulusal Kongresi, Eskişehir, Türkiye.

İlbaş, M., Yılmaz, İ., Özkan, F., 2006, Gaz türbini yanma odasında hidrojen ve hidrokarbon yanmasının modellenmesi ve NOx oluşumunun incelenmesi, Mühendis ve Makina, Cilt:47, Sayı:559.

Li., S. C., Williams, F. A., 1999, NOx Formation in two-stage methane-air flames, Combustion and Flame, 118, 399-414.

Muzio, L. J., Quartucy, G. C., 1997, Implementing NOx control: Research to application, Prog. Energ. Combustion Science, vol.23, 233-266.

Onat, K., 1997, Doğal gaz ışınımının arttırılması için bir öneri, Isı Bilimi ve Tekniği Dergisi, 18, 39-42.

Taglia, C. D., Gass, J., Dreher, H., 2001, Optimization of a low- NOx combustor chamber using CFD simulations, Progress in Computational Fluid Dynamics, vol.1, 117-130.

TS EN 676, 2006, Brülörler–Otomatik üflemeli–Gaz yakıtlar standardı, Türk Standartları Enstitüsü, Ankara.

Tucer, S., 2005. Katı yüzey ışınımı ile gaz yakıtlı ocaklarda ısı geçişinin artırılması, Doktora Tezi, İ.T.Ü. Fen Bilimleri Enstitüsü, İstanbul.

Yılmaz, Ş., 2001. Yanma odasının modellenmesi, Yüksek Lisans Tezi, İ.T.Ü. Fen Bilimleri Enstitüsü, İstanbul.

EFFECTS OF FLOW ROUTING PLATE ON MIXED CONVECTION HEAT TRANSFER FROM PROTRUDED HEAT SOURCES

Burak KURŞUN* and Mecit SİVRİOĞLU**
*Amasya Üniversitesi Teknoloji Fakültesi Makina Mühendisliği Bölümü
Merkez, Amasya, burak.kursun@amasya.edu.tr
** Gazi Üniversitesi Mühendislik Fakültesi Makina Mühendisliği Bölümü
06570 Maltepe, Ankara, mecits@gazi.edu.tr

Abstract: In this study, the effect of the flow routing plates on the laminar mixed convection heat transfer in a horizontal channel that has protruded heat sources at the bottom and top surfaces were investigated numerically and experimentally. The air was used as the cooling fluid, and protruded heat sources were equipped as 4x8 rows into the rectangle channel that has insulated walls. The experimental study was applied for two different Reynolds (Re) numbers. A numerical model complying with the experimental results was created, and numerical investigations were performed in different Reynolds and modified Grashof (Gr*) numbers for the 0°, 30°, 60° values of the plate angles (α). The analyses showed that using flow routing plate only increases the heat transfer from the first four heater rows on the bottom surface, and the first and the last heater rows on the top surface. The findings obtained during the experimental and numerical studies were presented in detail as graphics showing the row averaged Nusselt number (Nu_row ave.), the heater temperatures, velocity vectors, and temperature contours.
Keywords: Flow routing plate, Horizontal channel, Mixed convection, Protruded heat sources

AKIŞ YÖNLENDİRİCİ PLAKANIN ÇIKINTILI ISI KAYNAKLARINDAN KARIŞIK KONVEKSİYONLA ISI TRANSERİNE ETKİSİ

Özet: Bu çalışmada, akış yönlendirici plaka kullanımının alt ve üst yüzeylerinde çıkıntılı ısı kaynakları bulunan yatay bir kanal içerisindeki karışık konveksiyonla laminar ısı transferine etkisi sayısal ve deneysel olarak incelenmiştir. Soğutucu akışkan olarak hava kullanılmış olup ısı kaynakları duvarları yalıtılmış olan dikdörtgen kanal içerisine 8x4'lük diziler halinde yerleştirilmiştir. Deneysel çalışma iki farklı Reynolds sayısı (Re) için yapılmıştır. Deneysel çalışma sonuçları ile uyumlu bir sayısal model oluşturulmuş ve sayısal çalışma 0°, 30°, 60° plaka açıları için farklı Re ve Grashof (Gr) sayılarında gerçekleştirilmiştir. Analizler akış yönlendirici plaka kullanımının yalnızca alt yüzeyde ilk dört ısıtıcı sırası için, üst yüzeyde ise ilk ve son ısıtıcı sıraları için ısı transferini artırdığını göstermiştir. Deneysel ve sayısal çalışma sırasında elde edilen bulgular sıra ortalama Nusselt sayısı (Nu_sıra ort.), ısıtıcı sıcaklıkları, hız vektörleri ve sıcaklık kontörlerini gösteren grafikler halinde ayrıntılı olarak sunulmuştur.
Anahtar Kelimler: Akış yönledirici plaka, Yatay kanal, Karışık konveksiyon, Çıkıntılı ısı kaynakları

NOMENCLATURE

A	heat transfer area, [m²]
A_k	channel cross-sectional area, [m²]
A_{heater}	heater surface area, [m²]
c_p	specific heat, [kJ/kg.K]
D_H	channel hydraulic diameter, [m]
g	gravitional acceleration, [m/s²]
Gr	Grashof number, $[=(g\beta(T_s-T_{inlet})_{ave}.D_H^3)/\nu^2]$
Gr*	modified Grashof number, $[=(g\beta\dot{q}_{conv.ave}.D_H^4)/k\nu^2]$
h	convection heat transfer coefficent, [W/m².K]
k	thermal conductivty, [W/m.K]

L	distance between heater and neighbour temperature, [m]
$L_{glasswool}$	glasswool insulation thickness, [m]
L_P	interplate distance, [m]
$\dot{m}$	mass flow rate of air, [kg/s]
N_{fan}	theoretical fan power, [W]
$Nu_{row\ ave.}$	row average Nusselt number, $[=(\dot{q}_{conv\ row\ ave}D_H)/(k(T_s-T_{inlet})_{row\ ave.})]$
P_{atm}	atmospheric pressure, [Pa]
P_c	channel perimeter, [m]
$\dot{q}_{conv.}$	convection heat flux, [W/m²]
$\dot{q}_{conv\ ave.}$	all heaters average convection heat flux, [W/m²]
$\dot{q}_{conv\ row\ ave}$	row average convection heat flux, [W/m²]
$\dot{Q}_{electric}$	supplied electrical power, [W]

$\dot{Q}_{conv}$	convection heat transfer rate, [W]
$\dot{Q}_{cond.isolation}$	conduction heat transfer rate heater to isolation, [W]
$\dot{Q}_{cond.side}$	conduction heat transfer rate heater to side walls, [W]
$\dot{Q}_{rad}$	radiation heat transfer rate, [W]
R_{heater}	heater electrical resistance, [Ω]
R_{total}	total electrical resistance, [Ω]
Re	Reynolds number, [$=(w_{inlet}D_H)/v$]
Ri	Richardson number, [$=Gr/Re^2$]
T	fluid temperature, [K]
T_s	heater surface temperature, [K]
T_b	bulk temperature, [K]
T_{inlet}	air inlet temperature, [K]
u	x component of air velocity, [m/s]
v	y component of air velocity, [m/s]
V	voltage drop, [V]
w	z component of air velocity, [m/s]
w_{inlet}	air velocity at inlet, [m/s]
ρ	air density, [kg/m^3]
α	angle of plate, [degree]
β	thermal expansion coefficent, [1/K]
v	kinematic viscosity, [m^2/s]
μ	dynamic viscosity, [kg/ms]
ϵ	heater surface emissivity
σ	Stefan-Boltzman constant, [W/m^2.K^4]

INTRODUCTION

The chips on the printed-circuit boards (PCBs) are presented as rectangular heat sources in many numerical and experimental studies in literature over the cooling of the electronic devices and increasing the heat transfer rate. In these studies, the effects of various flow conditions, channels and placement arrays of the heat sources on the temperature distribution and heat transfer were investigated. Wu and Perng (2008) investigated the mixed convection heat transfer from protruded heat sources in a horizontal channel numerically by placing a rectangular plate vertically into the entrance of the channel. The results show that the heat transfer enhancement is provided with the placement of plate for different parameters as Reynolds and Grashof number. The forced convection heat transfer from heat sources on the bottom surface of a horizontal channel, and a triangular shaped plate placed at the entrance of the channel were investigated by Oztop et al. (2009). It is obtained that insertion of triangular plate enhanced heat transfer and the highest heat transfer is observed at the position of the plate with y=3,5. Korichi et al. (2009) made a numerical analysis in a case when plates were placed periodically on the top surface of a channel which had three vertical protruded heat sources on the bottom surface. It is observed that different physical arrangement as plate lengths, angles affect heat transfer. Fu and Tong (2009) investigated the heat transfer from the heat sources in a case when a vibrating cylinder was placed into the entrance of a channel which had four vertical protruded heat sources on the bottom surface. Numerical results show that heat transfer enhancement

occurs with the insertion of the cylinder for the variable cylinder vibration amplitudes and frequencies. The effects of the inclination angle and the thickness of a plate which placed into the channel on the heat transfer and pressure drop for unsteady flow conditions were investigated numerically by Davidson (2001). It is observed that heat transfer is variational for different solution methods. In a numerical study performed by Sohankar (2007), the effects of the plate angle and channel height on heat transfer and pressure drop was investigated by placing a V-shaped plate on the bottom surface of a rectangular and horizontal channel. The study shows that heat transfer and pressure drop increases with V-shaped plate and, DNS and LES simulation results are similar. Literature survey shows that using of flow routing objects (plates, cylinders, etc.) in the channel, affects heat transfer in different ratios based on the parameters as placement order of the heat sources, plate angle, plate length and thickness, Re and Gr numbers, or ratio of channel height to width. (Myrum et al., 1993; Valencia, 1999; Chompookham et al., 2010; Fu et al., 2001; Beig et al., 2011; Perng et al., 2012; Wu and Tao, 2008; Fu et al., 2012; Yang, 2002; Min et al., 2012; Sripattanapipat and Promvonge, 2009; Teamah et al., 2011)

There are not detailed analyses on the effects of the placement of flow routing plates on the mixed convection heat transfer in the channels that have heat sources on the bottom and top surfaces in the literature. In this present research, the heat transfer and the temperature distribution that occur when plates are placed into a horizontal channel which has protruded heat sources on the bottom and top surfaces were investigated numerically and experimentally. Also, the effects of the using of flow routing plate on heat transfer enhancement were analysed by comparing the cases with and without plate in the channel.

EXPERIMENTAL SET-UP

The experimental set-up is seen in Figure 1 mainly consists of a fan, a flow straightener, test zone, damping chamber to separate the test zone from the fan, DC power supply, and control panel, and measurement systems. The test zone has totally 64 protruded heat sources which are equipped with 4x8 rows on lower and upper walls, and there are two plates in the entrance of the test zone.

The test zone is a rectangular-shaped channel in a length of 500 mm with heater blocks and plates. The aluminium heater blocks which have 5 mm thickness, are manufactured by casting method and their surfaces are grinded. Resistance heaters are placed into the each aluminium blocks for heat generating. The parts of the channel that are 850 mm before the test zone and 150 mm after the test zone are composed to maintain the flow to be independent of the effects of the entrance and the exit of the channel respectively. The plates are placed on the line
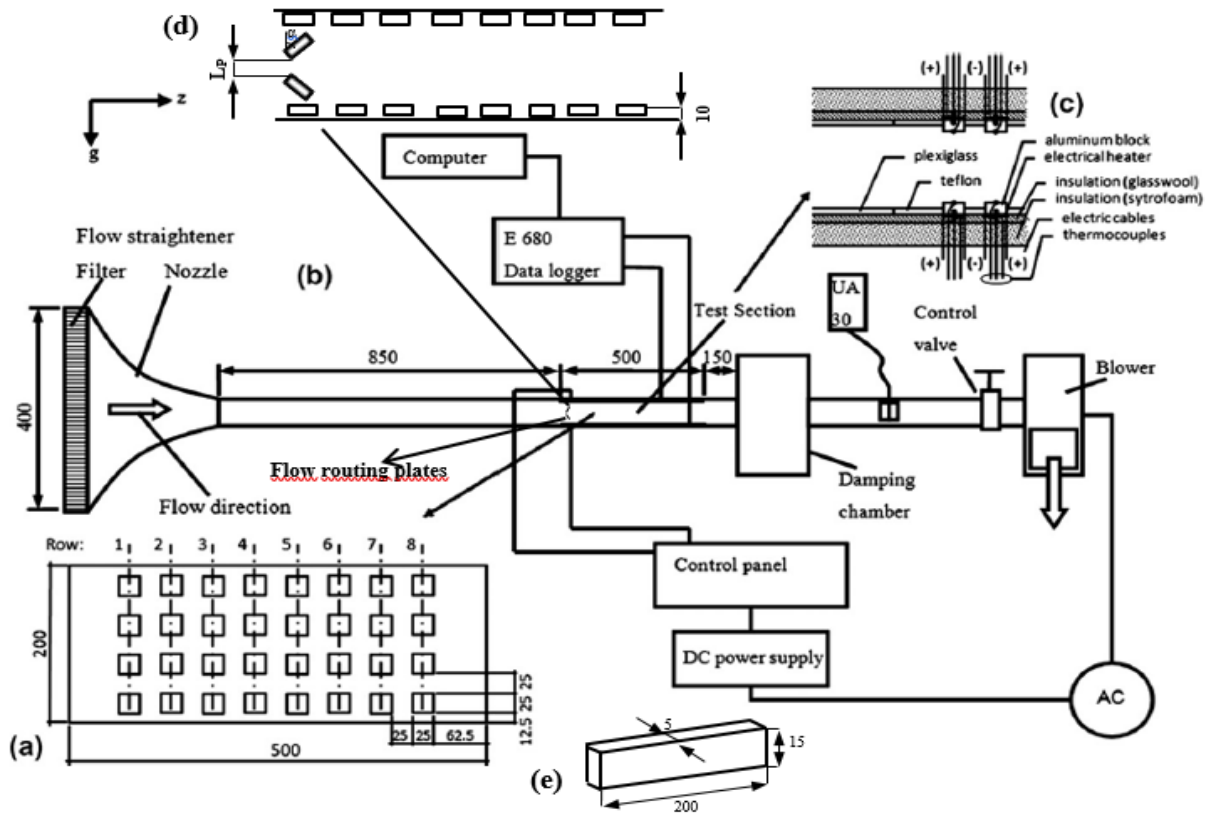
Figure 1. Schematic diagram of the experimental set-up (dimensions in mm.) a) Dimension of test zone (x-z plane), b) Experimental set-up, c) Schematic of heat sources assembly, d) Layout of plates (y-z plane) and e) Dimension of plexiglass plate.

of the first heater rows that are on the lower and upper surfaces. The dimensions of the test zone made from transparent plexiglas are shown in Figure 1.

There are holes which create α=30° angle against the y-axis on the side walls of the channel for the placement of routing. Entire surface is produced from plexiglass material except the test zone where there are the heat sources and plates. Politetrafloroetilen material (PTFE) with a thickness of 5mm however, is used for the test zone. The outer surface of the channel is insulated with foam board that has a thickness of 50 mm. An insulation material (glass wool) with a thickness of 20 mm is placed between the heaters and the foam board to prevent the foam board material from being damaged by the effects of high values of temperature. There are thermocouples in both sides of the insulation material which are in the same alignment with the blocks as shown in Figure 1 to determine the heat transfer from the heater blocks to the insulation material.

A DC power supply and a control panel are used to get the necessary electric current for the heaters in the experiments. The necessary electric current values are obtained by changing the resistance from the control panel. Also, the control panel was equipped with low voltage adjustable regulators. These regulators are used for adjusting heater voltages with an accuracy of ±1%.

The flow straightener which consists of hoses in the diameter of 5 mm and the length of 50 mm is placed at the entrance of the channel to provide uniform velocity distribution in the channel. Also, it consists of a nozzle to eliminate flow separation and provide a uniform velocity profile. The nozzle is made of alloy plates with a thickness of 0,5 mm. The damping chamber is used to separate the test zone from the fan mechanically and acoustically, and to provide the fluid absorption of the fan to be uniform.

Measurement of the electric current, resistance and voltage drop necessary for the calculations, the Protek 506 digital multimeter is used with an accuracy of ±0.1% for the voltage, and of ±0.5% for the resistance. 201 copper-constantan (T-type) thermocouples are used for the measuring of temperatures. All thermocouples are separately calibrated. The outlets of the thermocouples are connected to the ELİMKO 680 series universal data loggers which have computer interaction. The thermocouples are also used in the inlets and outlets of the channel, and on some specific parts of the insulation for the heat transfer calculations. For the measurement of the flow velocity during the experiments, an airflow UA30 ultrasonic anemometer which can measure the speed in the range of 0-30 m/s was used with an accuracy of ±1%. It is observed that experimental conditions reach a steady state after approximately 4-6 h. The steady-state conditions are accepted to have been occurred when the variation of the temperature reaches to a negligible level($\Delta T < 0.1°C$).

Processing of Experimental Data

The nondimensional parameters affecting the heat transfer and temperature distributions are calculated by using the equations given below.
The Re number was determined with Eq. (1),

$$Re = \frac{w_{inlet} D_H}{\nu} \tag{1}$$

In this equation, w_{inlet} shows the inlet velocity of the air entering the channel, and it is measured during the experiments. The kinematic viscosity of the air is shown by ν. D_H, hydraulic diameter is calculated from

$$D_H = \frac{4A_c}{P_c} \tag{2}$$

where A_c shows the cross-sectional area of the channel and P_c shows the channel perimeter.

Grashoff number (Gr) is calculated by the equation below,

$$Gr = \frac{g\beta(T_s - T_{inlet})_{ave.} D_H^3}{\nu^2} \tag{3}$$

where T_s is the surface temperature of the heater, T_{inlet} is the inlet temperature of the air entering the channel, g is the gravitational acceleration, β is the thermal expansion coefficient of the air at inlet conditions. The $(T_s - T_{inlet})_{ave}$ value is determined by considering the average temperature difference of the 64 heaters.

The modified Grashof number (Gr*) is calculated by using Eq. (4).

$$Gr^* = \frac{g\beta \dot{q}_{conv.ave.} D_H^4}{k\nu^2} \tag{4}$$

The $\dot{q}_{conv.\ ave.}$ is the average convection heat flux value for the 64 heaters, and k is the thermal conductivity of the air. The average convection heat flux value is calculated by finding the average value after the calculation of the convection heat flux value ($\dot{q}_{conv.}$) for each heater by using the equation given below.

$$\dot{q}_{conv.} = \frac{\dot{Q}_{conv.}}{A_{heater}} \tag{5}$$

where $Q_{conv.}$ is the convection heat transfer rate from each heater, and A_{heater} is the surface area of each heater.

The row average Nusselt number ($Nu_{row\ ave.}$) is calculated as given below,

$$Nu_{row\ ave.} = \frac{hD_H}{k} \tag{6}$$

where h is the convection heat transfer coefficient of the air and is calculated by Eq. (7).

$$h = \frac{\dot{q}_{conv.row\ ave.}}{(T_s - T_{inlet})_{row\ ave.}} \tag{7}$$

In this equation, $\dot{q}_{konv.row\ ave.}$ is the average convection heat flux that is obtained for each heater row consisting of four heater blocks, and $(T_s - T_{inlet})_{row\ ave.}$ is the average temperature difference. The Eq. (8) for the $Nu_{row\ ave.}$ is obtained by substituting the Eq. (7) into Eq. (6).

$$Nu_{row\ ave.} = \frac{\dot{q}_{conv.row\ ave.} D_H}{k(T_s - T_{inlet})_{row\ ave.}} \tag{8}$$

The Richardson number (Ri) is defined depending upon the Re and Gr numbers with the equation below,

$$Ri = \frac{Gr}{Re^2} \tag{9}$$

The expression of energy balance (Eq. 10) is used to identify the convection heat transfer rate.

$$\dot{Q}_{conv.} = \dot{Q}_{electric} - \dot{Q}_{cond.isolation} - \dot{Q}_{cond.side} - \dot{Q}_{rad.} \tag{10}$$

In the equation, $\dot{Q}_{electric}$ is the supplied electrical power, $\dot{Q}_{cond.insulation}$ is the conduction heat transfer rate from the heater to isolation, $\dot{Q}_{cond.side}$ is the heat transfer rate from heater to other heaters and side walls, and $\dot{Q}_{rad.}$ is the heat transfer from the heaters with radiation.

Supplied electrical power ($\dot{Q}_{electric}$) is calculated with the equation below by using the voltage drop in the heaters (V), and the total resistance (R_{total}) which is the total resistance of the line between the control panel and the heater, and the heater resistance (R_{heater}).

$$\dot{Q}_{electric} = \frac{V^2 R_{heater}}{R_{total}^2} \tag{11}$$

Conduction heat transfer rate from heater to glass wool isolation ($\dot{Q}_{cond.insulation}$) however, is calculated from,

$$\dot{Q}_{cond.isolation} = \frac{k_{isolation} A(T_{top} - T_{bottom})}{L_{isolation}} \tag{12}$$

where $k_{isolation}$ is the thermal conductivity of the glass wool insulation, $L_{isolation}$ is the thickness of the glass wool insulation, and A is the heat transfer area. The expression of $(T_{top} - T_{bottom})$ is the temperature difference for the insulations of the bottom and top surfaces.

The heat transfer rate ($\dot{Q}_{cond.side}$) from the heater to the other heaters or side walls is calculated from

$$Q_{cond.side} = \frac{k_{teflon} A(T_{heater} - T_{neighbour})}{L} \qquad (13)$$

where T_{heater} is the heater temperature measured, $T_{neighbour}$ is the either neighbouring heater temperature when there is heat transfer between the heaters, or is the edge temperature in case there is heat transfer to the edges of the teflon. In calculating the edge temperatures, bulk temperatures, and the temperature distribution in the foamboard are taken into account. The k_{teflon} is the thermal conductivity of the teflon plate, and L is the distance between the heater and the point where the neighbouring temperature value is taken.

Eq. (14) is used to calculate the radiation heat transfer rate ($\dot{Q}_{rad.}$).

$$Q_{rad.} = \sigma \epsilon F A_{heater} (T_s^4 - T_b^4) \qquad (14)$$

where σ is the Stefan-Boltzmann constant, ϵ is the emissivity of the aluminium heater blocks, T_s is the surface temperature of the heaters, and T_b is the average bulk temperature of the fluid. The F shape factor is taken as F=1.

The bulk temperatures T_b can be calculated by applying the principle of the conservation of energy to a selected control volume in the channel (Eq. (15)). The selected control volume includes each four heaters on the lower and upper surfaces for a heater row. Air is used as a cooling fluid and it is accepted as an ideal gas.

$$T_{b2} = \frac{\dot{Q}_{total.c.v.}}{\dot{m} c_P} + T_{b1} \qquad (15)$$

In this equation, $\dot{m}$ is the mass flow rate of the air, c_p is the specific heat, T_{b1} is the inlet temperature of the air before the heater row (it is the inlet temperature of the fluid entering the channel for the first heater row), and T_{b2} is the inlet temperature of the air before the next heater row. $\dot{Q}_{total.c.v.}$ is the total heat energy amount transferred to the fluid from the 8 heaters in the control volume. All the thermophysical properties of the air are defined at the bulk temperature.

The standard calculation methods in the literature are used for uncertainty analysis of the experimental results (Moffat, 1982; Kline, 1985; Smith and Wehofer, 1985). The uncertainty in the Nusselt number is calculated around ±5% depending upon uncertainties of $\dot{q}_{konv.row\,ave.}$, D_H, k and $(T_s-T_{inlet})_{row\,ave.}$. The uncertainties of modified Grashof number and Re number, however, are calculated around ±3% depending upon uncertainties of

D_H, k and $\dot{q}_{conv.\,ave.}$ and around ±2% depending upon uncertainties of D_H and w_{inlet}, respectively.

NUMERICAL STUDY

The problem analysed in the numerical study includes the effects of using of flow routing plates on heat transfer from protruded heat sources in a three-dimensional channel. Numerical analysis is performed by creating a mathematical model, and the numerical findings obtained are compared to the experimental findings to make validation of numerical results. Geometries used in the numerical study for the cases with and without plate are seen in Figure 2. Dimensions of these geometries are identical with Figure 1.

Mathematical Model

The air was used as the cooling fluid, and analyses were performed by assuming the fluid is Newtonian, incompressible, and convection properties of the fluid are constant for the steady-state and laminar flow conditions. Also, the Boussinesq approach was used to determine the effects of the buoyant force. The conservation equations given below were used to calculate the air velocity components (u, v, w), the pressure (P) and temperature (T) values in the study.

The conservation of mass equation is expressed with the Eq. (16).

$$\frac{\partial(\rho u)}{\partial x} + \frac{\partial(\rho v)}{\partial y} + \frac{\partial(\rho w)}{\partial z} = 0 \qquad (16)$$

The conservation of momentum equations is expressed with the equations given below in the directions of x, y and z respectively.

$$u\frac{\partial(\rho u)}{\partial x} + v\frac{\partial(\rho u)}{\partial y} + w\frac{\partial(\rho u)}{\partial z} = -\frac{\partial P}{\partial x} + \mu\left(\frac{\partial^2 u}{\partial x^2} + \frac{\partial^2 u}{\partial y^2} + \frac{\partial^2 u}{\partial z^2}\right) \qquad (17)$$

$$u\frac{\partial(\rho v)}{\partial x} + v\frac{\partial(\rho v)}{\partial y} + w\frac{\partial(\rho v)}{\partial z} = -\frac{\partial P}{\partial y} + \mu\left(\frac{\partial^2 v}{\partial x^2} + \frac{\partial^2 v}{\partial y^2} + \frac{\partial^2 v}{\partial z^2}\right) + \rho g\beta(T - T_{inlet}) \qquad (18)$$

$$u\frac{\partial(\rho w)}{\partial x} + v\frac{\partial(\rho w)}{\partial y} + w\frac{\partial(\rho w)}{\partial z} = -\frac{\partial P}{\partial z} + \mu\left(\frac{\partial^2 w}{\partial x^2} + \frac{\partial^2 w}{\partial y^2} + \frac{\partial^2 w}{\partial z^2}\right) \qquad (19)$$
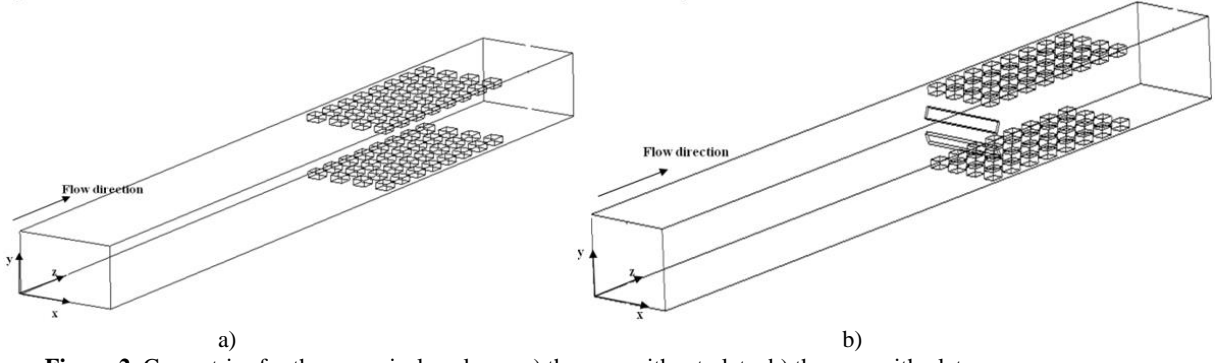
Figure 2. Geometries for the numerical analyses a) the case without plate b) the case with plate

In the differential equations given above u, v and w is the velocity components in the direction of x, y and z respectively, P is the pressure, μ is the dynamic viscosity of the fluid, ρ is the density of the fluid, g is the gravitational acceleration, β is the thermal expansion coefficient of the fluid at inlet temperature, T is the fluid temperature, and T_{inlet} is the inlet temperature of the fluid. The last expression on the right side of the Eq. (18) is used for the purpose of identifying the effects of mass forces (Boussinesq approach).

The conservation of energy equation can be written as follows.

$$u\frac{\partial(\rho T)}{\partial x} + v\frac{\partial(\rho T)}{\partial y} + w\frac{\partial(\rho T)}{\partial z} =$$

$$\frac{k}{c_P}\left(\frac{\partial^2 T}{\partial x^2} + \frac{\partial^2 T}{\partial y^2} + \frac{\partial^2 T}{\partial z^2}\right) \quad (20)$$

where c_p is the specific heat of the fluid, and k is the thermal conductivity of the fluid.

The boundary conditions in the inlet and the outlet of the channel are given in Eq.(21) and (22) respectively.

$u = 0; v = 0; w = w_{inlet}; T_{inlet}=23,5°C;$

$P_{atm}=101325 \text{ Pa}$ (21)

$$\frac{\partial u}{\partial z}=0; \quad \frac{\partial v}{\partial z}=0 \;; \quad \frac{\partial w}{\partial z}=0 \;; \quad \frac{\partial T}{\partial z}=0 \quad (22)$$

The flow is symmetrical to the axis of x. Therefore, the boundary conditions in the symmetrical axis of the channel can be written as follows;

$$u=0; \quad \frac{\partial v}{\partial x}=0 \;; \quad \frac{\partial w}{\partial x}=0 \;; \quad \frac{\partial T}{\partial x}=0 \;; \quad \frac{\partial P}{\partial x}=0 \quad (23)$$

No-slip conditions were defined on the lower, upper and side surfaces of the channel, over the plates and heat sources and all surfaces were assumed to be adiabatic except surface of heat sources;

$u = 0; \quad v = 0; \quad w = 0; \quad \dot{q} =0$ (24)

The boundary condition identified on the heater surfaces is given in Eq. (25);

$\dot{q}=\dot{q}_{conv.}$ (25)

Numerical Method

Creating the geometries and numerical analyses were performed by the ANSYS Fluent (2011) software for the problem. The channel model was created depending upon the measures in Figure 1. As the flow in the channel was symmetrical to the middle of the channel in the direction of x-axis, half of the geometry given in Figure 2 was modelled.

The SIMPLE and Coupled algorithm with the option of Pseudo-Transient were adopted to derive the discretized form of all conservation equations are given Eq. (16)-(20) in the case with and without plate respectively. The Second Order Upwind Differencing scheme was adopted for discretizing terms in Eq. (16)-(20). The iterations were maintained until the residual values became less than 1×10^{-6} for the conservation of mass and momentum, and less than 1×10^{-10} for the energy equations.

Processing of Numerical Data

Numerical analysis was carried out by assuming uniform and constant heat flux values ($\dot{q}_{conv.}$) for each heater block and values of heat fluxes that calculated with Eq.(5) during the experiments, are used for comparing of experimental and numerical results. The Re number, Gr number, modified Gr number (Gr*), row average
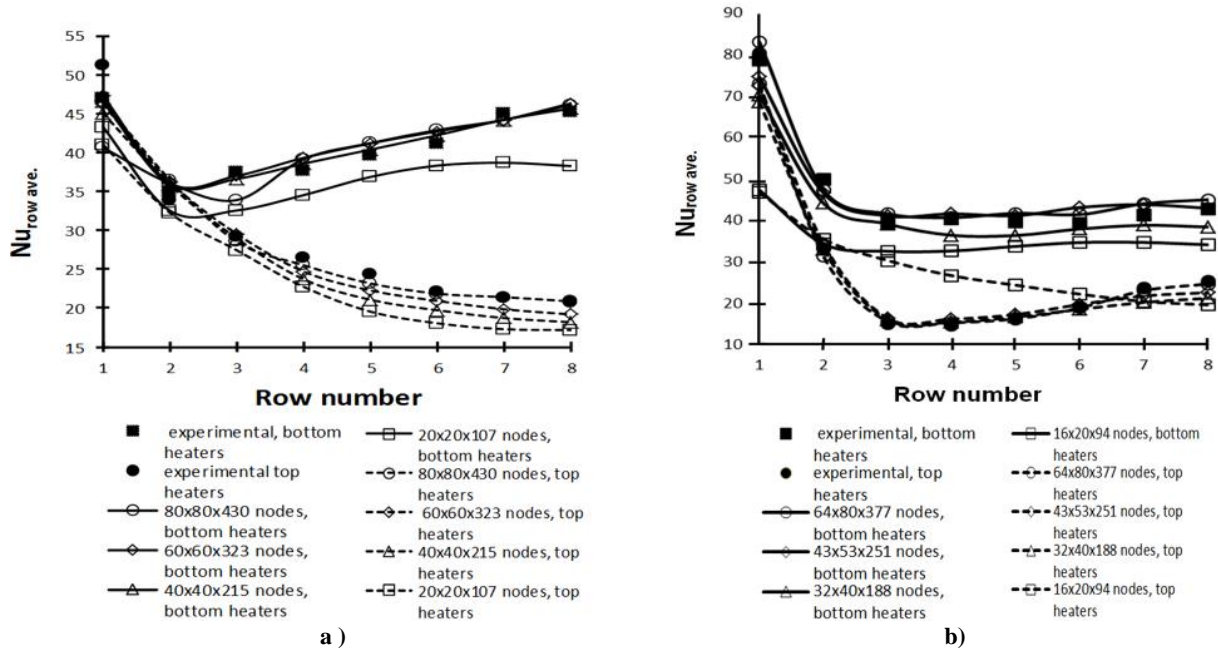
Figure 3. Grid independent test results for different numbers of node (Re=2000, Gr*=3x10^8, α=30˚, L$_P$/H=3/20, H/W=1/2) a) without plate b) with plate
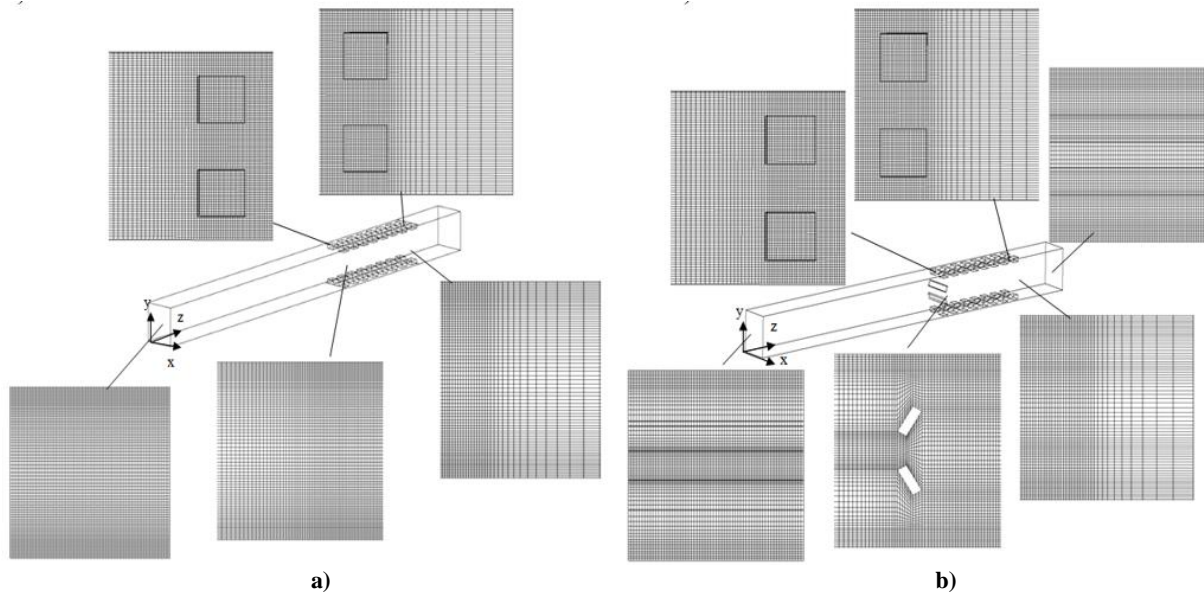
Figure 4. Mesh structure and distribution a) without plate b) with plate(α=30˚)

Nusselt number and Ri number, however, are calculated with Eq. (1),(3),(4), (8) and (9) respectively.

Validation of Numerical Data

In order to obtain grid independent solutions and compatible results with experiments, a grid independent test was carried out. A uniform grid was used for throughout the domain but a fine grid was used near the walls. Grid independent test results for different numbers of node are presented in Figure 3. As seen in Figure 3., it is observed that the mesh structures with 64x80x377 and 80x80x430 nodes on the x, y and z-axes

are in compliance with experimental results for the cases with and without plate, respectively.

The mesh structure and distribution for the cases with and without plate are shown in Figure 4. The comparisons of the experimental and numerical study results for the row average Nusselt numbers in the value of two different Reynolds numbers for the cases without and with plate are shown in Figure 5 and 6 respectively. As can be seen from these figures, there is a very good agreement between the numerical and experimental results. The maximum difference between experimental and numerical values does not exceed 7%. This can be
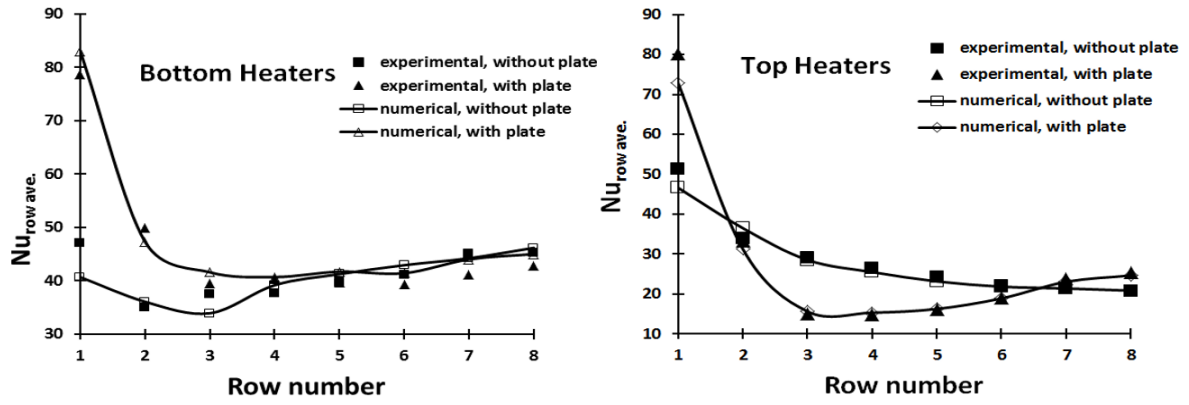
Figure 5. Comparison of experimental and numerical results ($\alpha=30°$, $Gr^*=3 \times 10^8$, Re=2000, H/W=1/2, $L_P/H=3/20$)
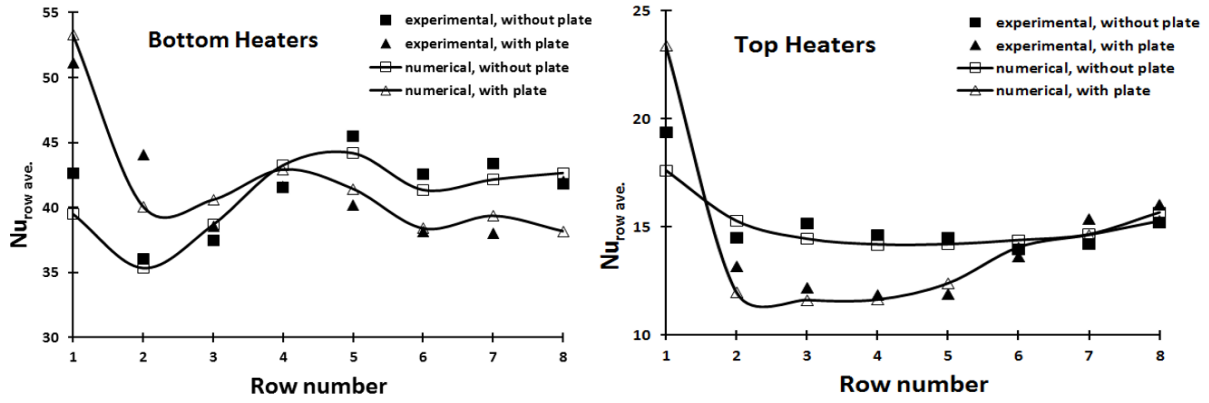
Figure 6. Comparison of experimental and numerical results ($\alpha=30°$, $Gr^*=3 \times 10^8$, Re=930, H/W=1/2, $L_P/H=3/20$)

considered as a sufficient verification of the computational domain and numerical procedures applied in the present study.

RESULTS AND DISCUSSION

The experimental study was performed for certain Re and Gr* number values and compared to the numerical study of the same parametrical values. After this, a parametrical study was performed numerically for the different Re and Gr* numbers, and the values of the plate angles (α). The numerical study parameters are given in Table 1. The comparisons between the cases with and without plates for the row average Nu number and temperature difference at different Gr*, Re numbers and plate angles, are presented in Figures. 7 and 8.

Using plates increases the $Nu_{row\ ave.}$ at the first four heater rows for bottom heaters according to the case

without plate (Figure 7a). As can be seen from Figure 6a, the heat transfer decreases with decrease in Gr* number. At all Gr* number values, the temperatures of the bottom heaters increase until a certain heater row and decrease due to the effect of buoyancy affected secondary flow.

The $Nu_{row\ ave.}$ distributions for the different Re numbers can be seen in Figure 7b. For all the values of Re numbers, it is observed that the heat transfer in the first four heater rows when there are plates is greater, and the heat transfer from other heaters decreases when compared to the case without plates. Using plates is only useful for the first four heater rows since the heat transfer decreases after the fifth heater row. On the other hand, the heat transfer enhancement increases with increase in Re number when all heater rows are taken into account.

Table 1. Numerical study parameters for the cases with and without plate

Re	Gr*	W_{inlet} (m/s)		Ri		L_P/H	H/W	α	Ri	α	Ri	α	Ri
2000	3×10^8	0,24		1,9		3/20	1/2	0°	2,7	30°	2,2	60°	2,3
2000	2×10^8	0,24	Without plate	1,3	With plate	3/20	1/2	0°	1,9	30°	1,4	60°	1,5
2000	1×10^8	0,24		0,76		3/20	1/2	0°	1	30°	0,7	60°	0,8
1400	3×10^8	0,16		5,2		3/20	1/2	0°	6,4	30°	6,3	60°	5,7
930	3×10^8	0,11		13,5		3/20	1/2	0°	15,3	30°	14,9	60°	13,9

26
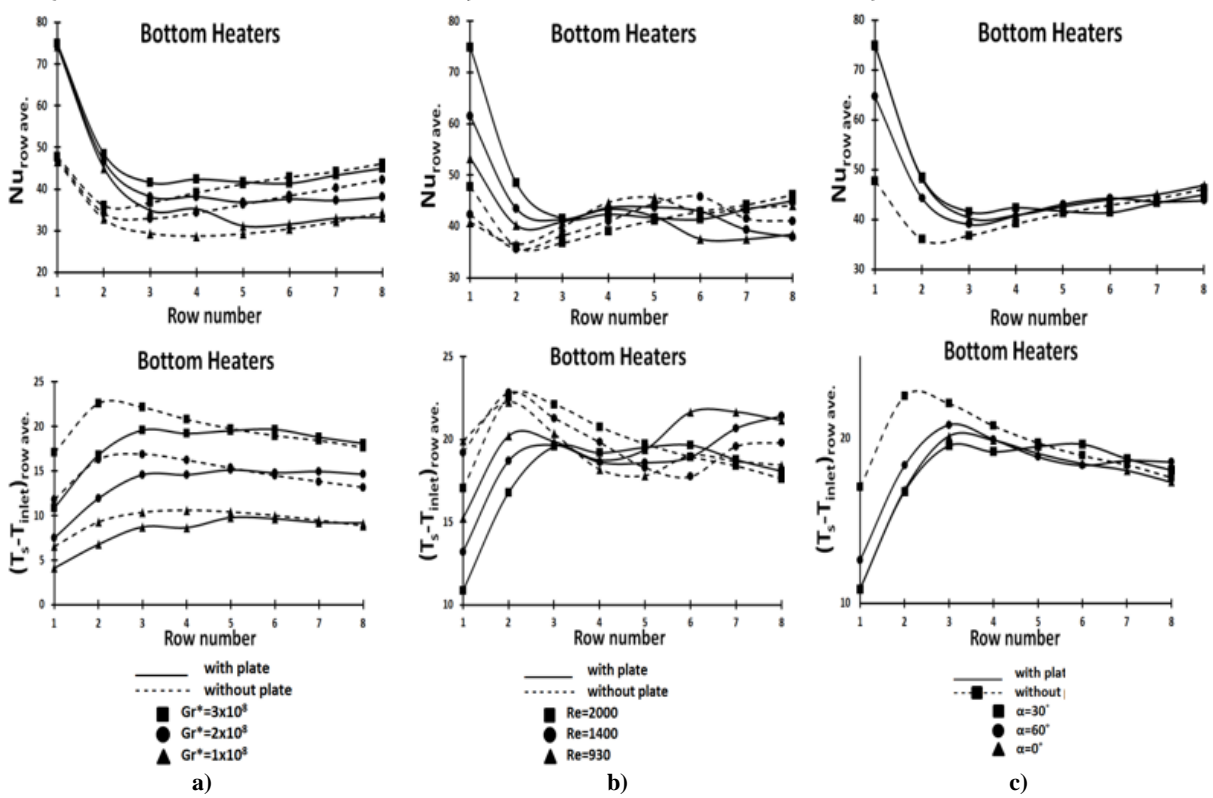
Figure 7. Nu$_{row ave.}$ and (T$_s$-T$_{inlet}$)$_{row ave.}$ distributions at the bottom heaters a) for different Gr* numbers, b) for different Re numbers c) for different plate angles (α)
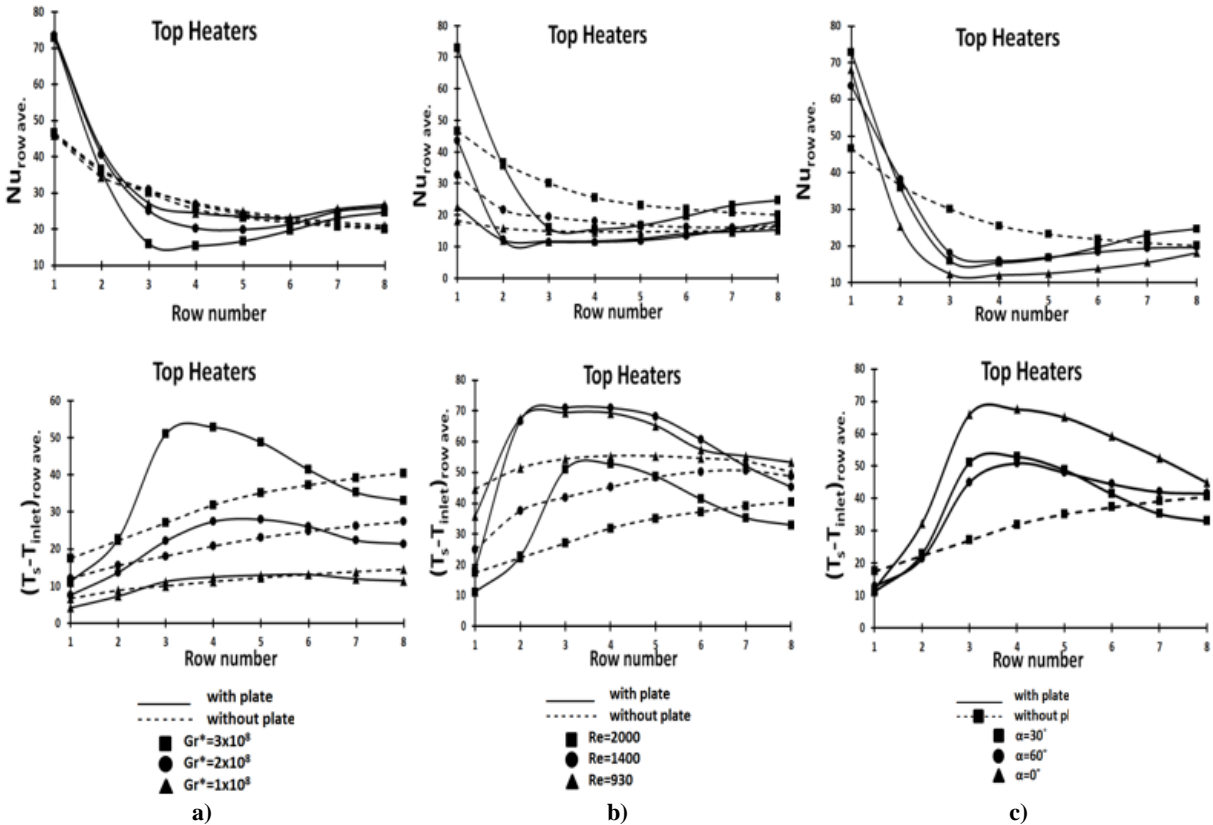
Figure 8. Nu$_{row ave.}$ and (T$_s$-T$_{inlet}$)$_{row ave.}$ distributions at the top heaters a) for different Gr* numbers, b) for different Re numbers c) for different plate angles (α)

The Nu$_{row ave.}$ are higher than those of the case without plate until 5th heater row for the plate angles of α=30˚, 60˚, 0˚ (Figure 7c). After fifth heater row, however, there are not much difference in the heat transfer. When all the bottom heaters are considered, the highest heat transfer enhancement occurs for the plate angle of

α=30˚. When the bottom heater temperatures are considered, the heater temperatures increase until the 3rd heater row and then begin to decrease due to the effect of the natural convection for all plate angles.

$Nu_{row\ ave.}$ and temperature distributions at different Gr* numbers are shown in Figure 8a for the top heaters. Use of plate has only provided heat transfer enhancement at the first and the last heater row. There is a great amount of decrease in heat transfer at the 3rd-6th heater rows compared to the case without plate and the heat transfer increases with the decrease in the Gr* number for the case with plate. Temperatures of heater rows increase starting from the first heater row to the last heater one for the case without plate. Temperatures for the case with plate, however, increase until 4th heater row and then decrease up to the last one.

Effects of the Re number on the $Nu_{row\ ave.}$ and temperature distributions for the top heaters at the case with and without plate is observed in Figure 8b. The heat transfer enhancement for the first heater row and the last heater row occur after the placement of the plates at the Re numbers of Re=2000 and Re=1400. With the decrease of the Re number (Re=930), the heat transfer for the last two heater rows in the case with plate remains nearly the same as for the case without

plate. The heat transfer for other heater rows decreases for the case with plate at all the Re numbers.

Distribution of row average Nu numbers and temperatures at various plate angles for the top heaters are given in Figure 8c. The heat transfer is higher only for the first heater row for the case with plate angle of α=0°. The heat transfer enhancement occurs in different amounts for the first heater row for the cases of α=30°, 60° but for the last two heater rows when the angle is α=30. The heater temperatures increase until the 4th heater row for the plate angles of α=30°, 60° and 0˚, and then decrease after the 3rd heater row.

The velocity vectors and the temperature contours for the case with and without plate are given in Figure 9.The air accelerates while passing between the first heater row and the plates. The air also hits the top and bottom heater surfaces while passing through the between the plate and the heater and then turn towards the middle of the channel. This case causes that the adequate amount of air flow cannot reach to the 3rd – 6th heater rows, and thus the heat transfer decreases. Even though the adequate amount of flow cannot reach to the 3rd – 6th heater rows, the natural convection that occurs on the bottom heaters contributes to the cooling. The air ascends with the effect of buoyancy affected secondary flow and squeezes among the top heaters.
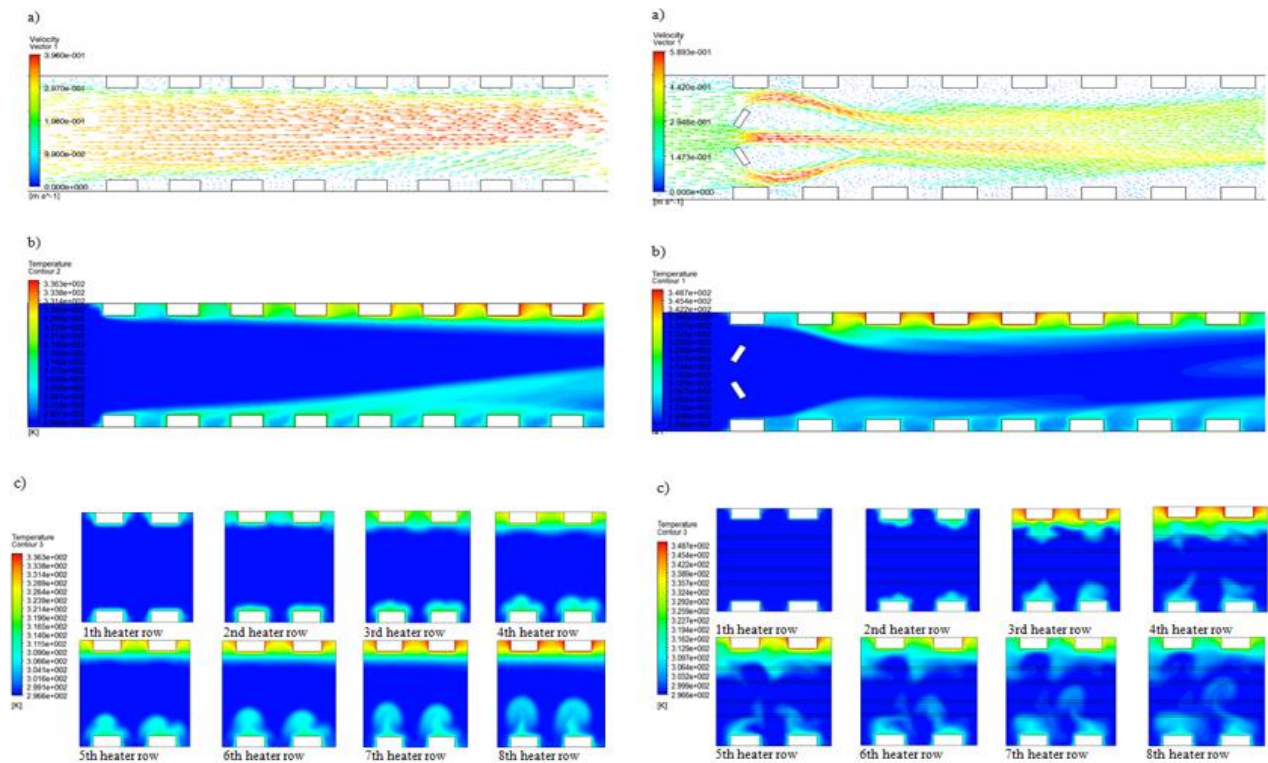

Figure 9. For the cases with and without plate, a) Velocity vectors at y-z plane, x=25mm, b) Temperature contours at y-z plane, x=25mm, c) Temperature contours at x-y plane (Re=2000, Gr*=3x10⁸, α=30˚, H/W=1/2, L_P/H=3/20)

Figure 10. For the cases with and without plate, a) Velocity vectors at y-z plane, x=25mm, b) Temperature contours at y-z plane, x=25mm, c) Temperature contours at x-y plane (Re=2000, Gr*=1x10^8, α=30˚, H/W=1/2, L$_P$/H=3/20)

Therefore, the heater temperatures increase more on the top heater rows. The air flow is more parallel to the bottom and top heater surfaces for the case without plate. This case provides preferable cooling conditions for only the top heaters. The temperatures of the bottom heaters decrease as the effect of buoyancy affected secondary flow increases throughout the last heater rows.

As seen from Figure 10, with the decrease of the Gr* number from Gr*=3x10^8 to Gr*=1x10^8, the Ri number takes the values of Ri=0,76 and Ri=0,7 depending upon the cases with and without plate, respectively and thus the forced convection condition becomes more dominant in the channel. The increase in the effect of forced convection causes a decrease in the effect of buoyancy affected secondary flow on the bottom heaters for both the cases. The top heater temperatures decrease due to the decrease in the amount of hot air that is squeezed among the heaters. Thus, the difference in the temperatures and the heat transfer rates between the cases with and without plate decrease.

The velocity vectors and temperature contours at different Re numbers for a specific Gr* number and plate angle are presented in Figure 11 and 12. Natural convection becomes more dominant with the decrease in the Re number for both cases with and without plate. The air flow passing through between the plate and the heater surface directs more to the middle of the channel

especially for the top heaters by hitting the first heater row for the case with plate (Figure 11 and 12). In this case, the heater temperatures of 2nd -8th heater rows increase more compared to the case without plate. For the bottom heaters, the heat transfer after the 5th heater row at the case without plate is higher than those of the case with plate due to the effect of buoyancy affected secondary flow.

The velocity vectors and temperature contours depending on the variation of the plate angle are presented in Figure 13. For the angle of α=60°, the air that hits the top heater surfaces changes direction slightly since the distance between the plate and the heater surfaces is larger than those of the angle of α=30° and α=0°. This case creates greater cooling conditions for the second heater row on the top surface when compared to the cases which have plate angles of α=30° and 0˚. But because the air velocity in the entrance of the channel decreases in this angle, the heat transfer enhancement decreases for the first and last two heater rows compared the case with plate angle of α=30° and 0˚.

CONCLUSIONS

In the experimental and numerical analyses, it is investigated that using flow routing plates has only provided heat transfer enhancement for the first four
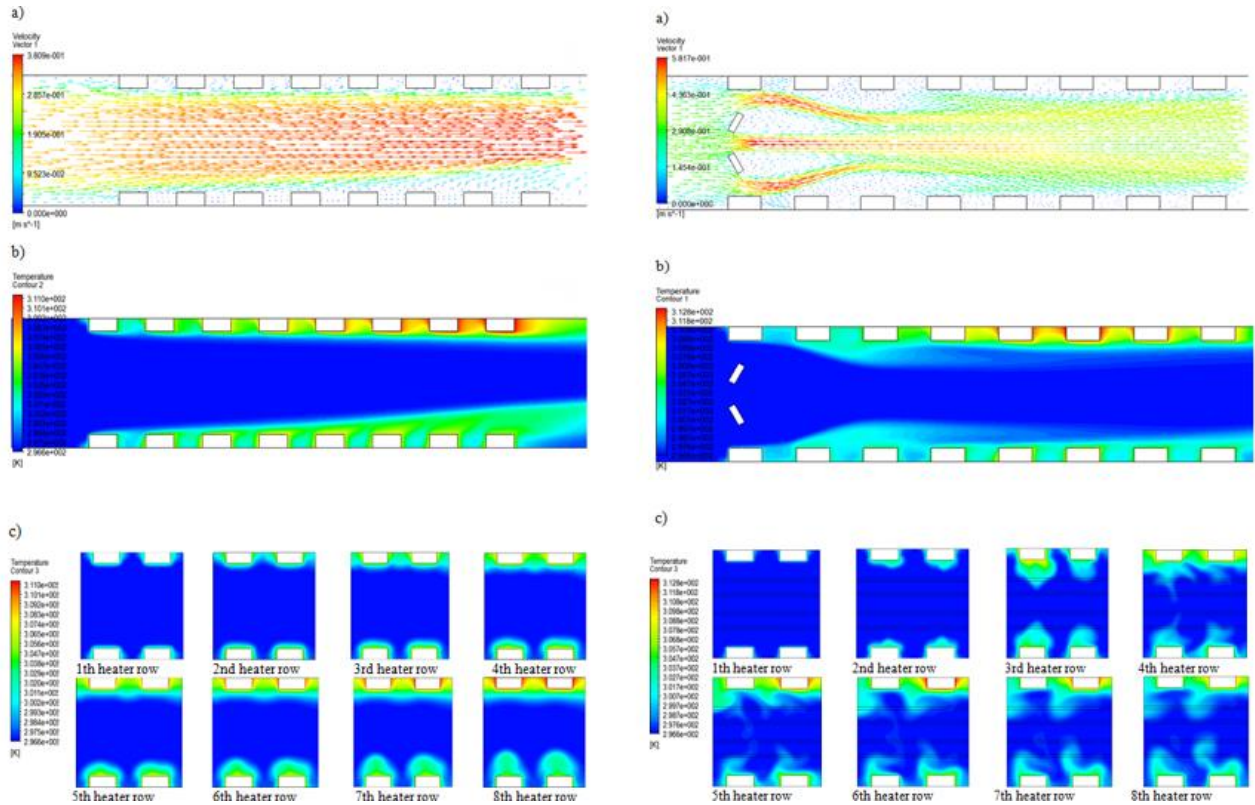
Figure 11. For the cases with and without plate, a) Velocity vectors at y-z plane, x=25mm, b) Temperature contours at y-z plane, x=25mm, c) Temperature contours at x-y plane (Re=1400, Gr*=3x10^8, α=30˚, H/W=1/2, L_P/H=3/20)

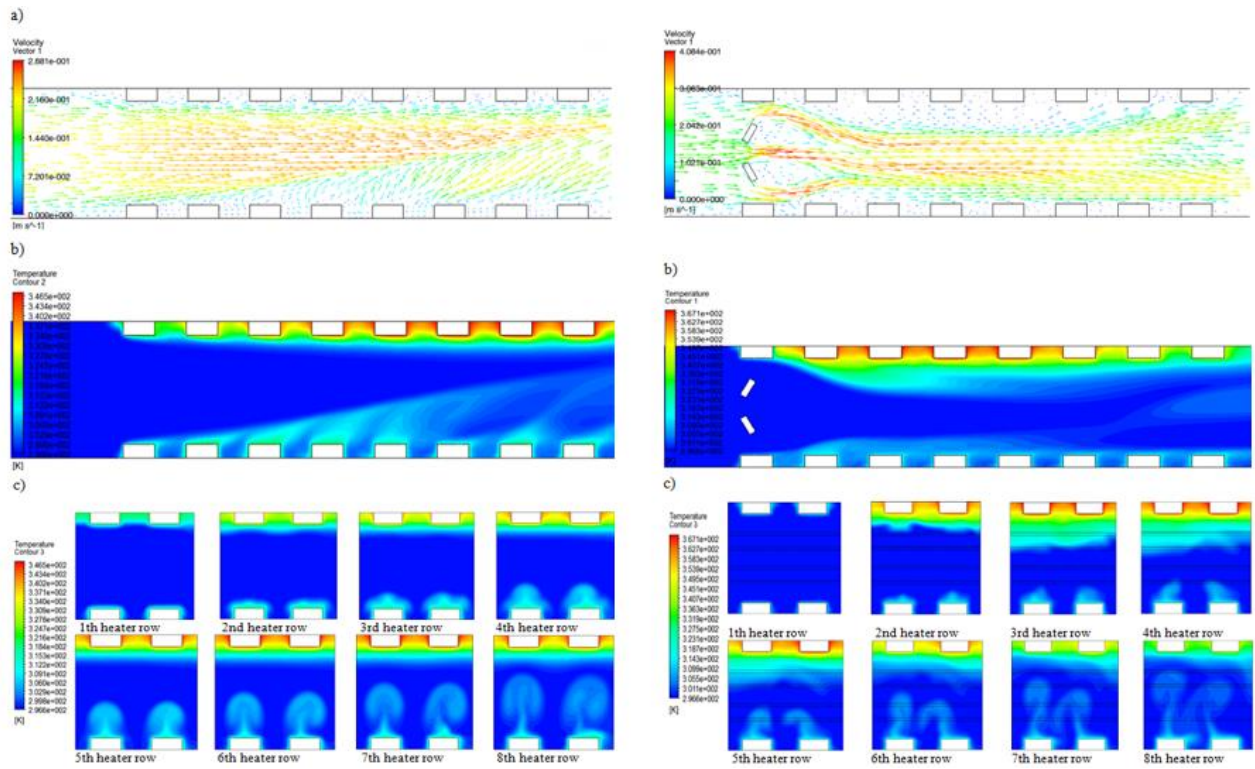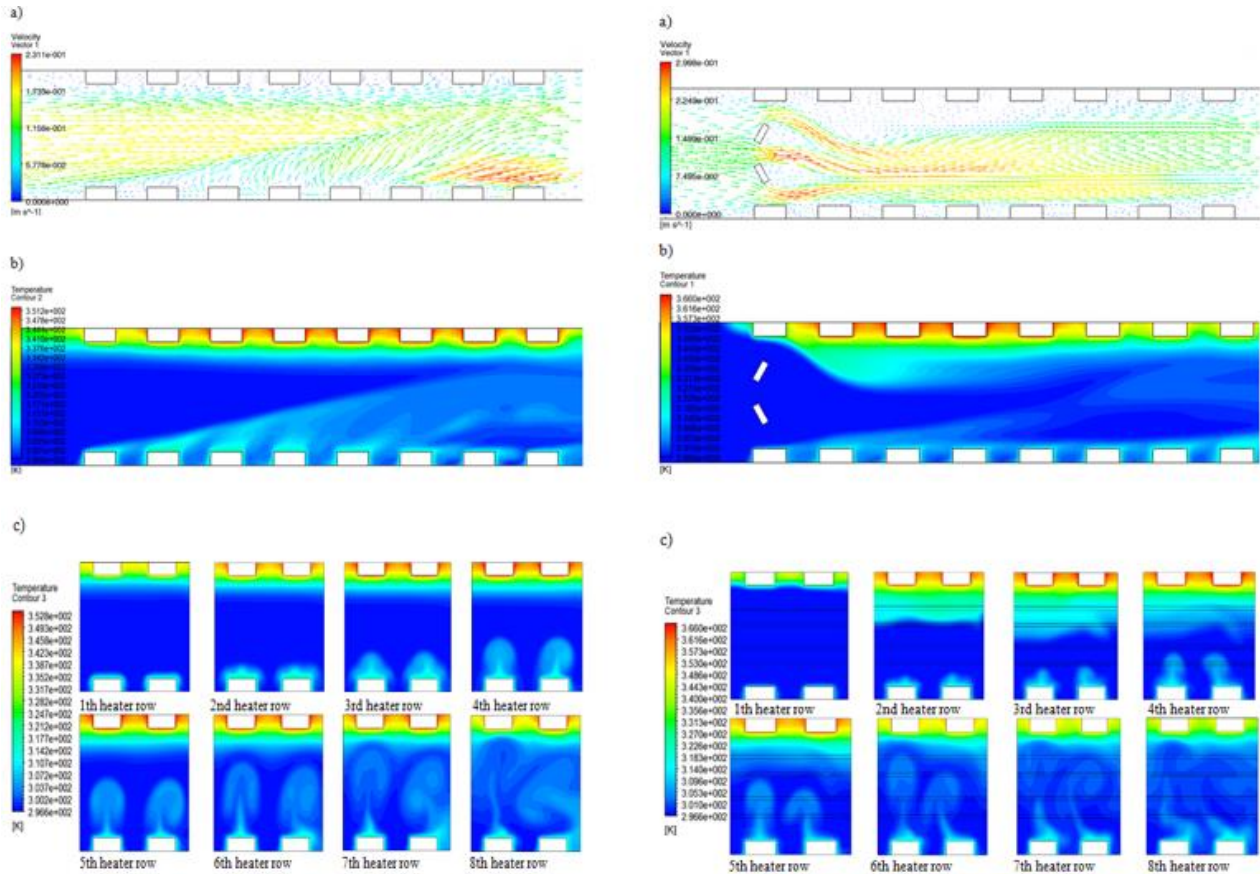**Figure 12.** For the cases with and without plate, a) Velocity vectors at y-z plane, x=25mm, b) Temperature contours at y-z plane, x=25mm, c) Temperature contours at x-y plane (Re=930, Gr*=3x10^8, α=30˚, H/W=1/2, L_P/H=3/20)
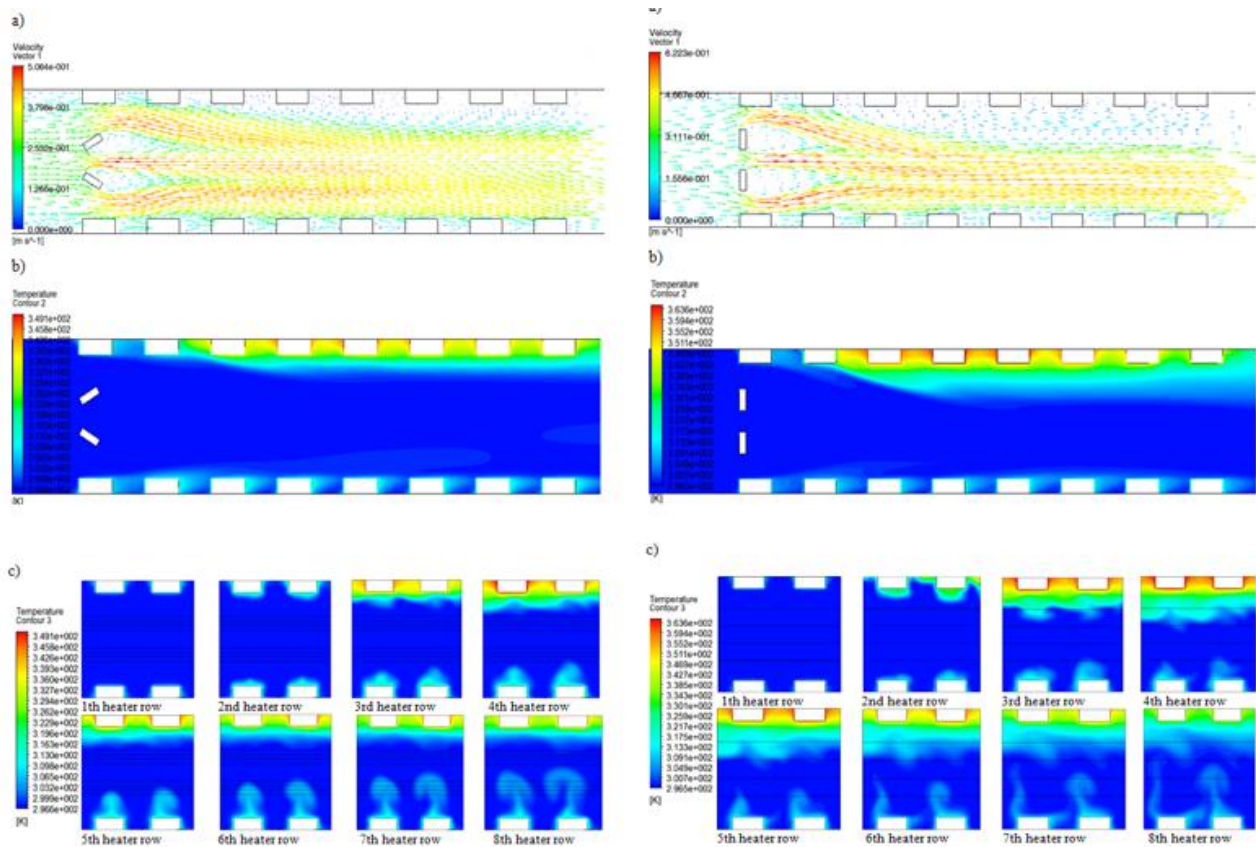
Figure 13. For the cases with plate (α=60˚,and α=0˚) a) Velocity vectors at y-z plane, x=25mm, b) Temperature contours at y-z plane, x=25mm, c) Temperature contours at x-y plane (Re=2000, Gr*=3x10^8, H/W=1/2, L$_P$/H=3/20)

heater rows which are placed at the bottom surface, and the first and the last heater rows which are placed on the top surface. The air passing through between the plates and heaters hits the heater surface and directs to the middle of the channel. This causes the adequate amount of air flow cannot reach to the heater rows of 3rd-6th, and this also causes the decreasing of heat transfer when compared to the case without plate. Also, the air velocity that flowing between plates increases for high Re number and prevents increase in the amount of air that directing to the middle of the channel. For this reason, the air flow more directs to the middle of the channel at low Re number.

The natural convection increases with increase in Gr* number and decrease in Re number. Heated air rises and leaves the channel due to density difference between hot and cold air with increase in natural convection for the bottom heaters. This case increases heat transfer from bottom heaters. Effect of natural convection is different for the top heaters. Ascending hot air with the effect of buoyancy affected secondary flow squeezes among the top heaters. Therefore, the heater temperatures increase more on the top heater rows in regard to bottom heater rows.

Plate angle is the another important parameter and affects heat transfer in different ratios. Variation of plate angle changes the distance between plate and heater surface.

The air accelerates while passing through the region between heater rows and plates. This situation increases heat transfer for certain heater rows. The distance between plate and heater surface is minimum for the angle of α=30˚. Thus, the highest heat transfer enhancement when compared to the case without plate is obtained at an angle of α=30˚.

REFERENCES

Beig, S. A., Mirzakhalili, E. and Kowsari, F., 2011, Investigation of optimal position of a vortex generator in a blocked channel for heat transfer enhancement of electronic chips, *International Journal of Heat and Mass Transfer*, 54(19), 4317-4324.

Chompookham, T., Thianpong, C. and Kwankaomeng, S., and Promvonge, P., 2010, Heat transfer augmentation in a wedge-ribbed channel using winglet vortex generators, *International Communications in Heat and Mass Transfer*, 37(2), 163-169.

Davidson, A. S. L., 2001, Effect of inclined vortex generators on heat transfer enhancement in a three-dimensional channel *Numerical Heat Transfer: Part A: Applications*, 39(5), 433-448.

FLUENT, A. 2011, Release 14.0, User Guide, Ansys. *Inc., Lebanon, US*.

Fu, W. S., Ke, W. W. and Wang, K. N., 2001, Laminar forced convection in a channel with a moving block, *International journal of heat and mass transfer*, 44(13), 2385-2394.

Fu, WS. and Tong, BH., 2004, Numerical investigation of heat transfer characteristics of the heated blocks in the channel with a transversely oscillating cylinder, *International Journal of Heat and Mass Transfer*, 47(2), 341-351.

Fu, W. S., Chen, C. J., Wang, Y. Y. and Huang, Y., 2012, Enhancement of mixed convection heat transfer in a three-dimensional horizontal channel flow by insertion of a moving block, *International Communications in Heat and Mass Transfer*, 39(1), 66-71.

Kline, S. J., 1985, The purposes of uncertainty analysis, *Journal of Fluids Engineering*, 107(2), 153-160.

Korichi, A., Oufer, L. and Polidori, G., 2009, Heat transfer enhancement in self-sustained oscillatory flow in a grooved channel with oblique plates, *International Journal of Heat and Mass Transfer*, 52(5), 1138-1148.

Min, C., Qi, C., Wang, E., Tian, L. and Qin, Y., 2012, Numerical investigation of turbulent flow and heat transfer in a channel with novel longitudinal vortex generators, *International Journal of Heat and Mass Transfer*, 55(23), 7268-7277.

Moffat, R. J., 1982, Contributions to the theory of single-sample uncertainty analysis. ASME, Transactions, *Journal of Fluids Engineering*, 104(2), 250-58.

Myrum, T. A., Qiu, X. and Acharya, S., 1993, Heat transfer enhancement in a ribbed duct using vortex generators, *International journal of heat and mass transfer*, 36(14), 3497-3508.

Oztop, H. F., Varol, Y. and Alnak, D. E., 2009, Control of heat transfer and fluid flow using a triangular bar in heated blocks located in a channel, *International Communications in Heat and Mass Transfer*, 36(8), 878-885.

Perng, S. W. and Wu, H. W. 2008, Numerical investigation of mixed convective heat transfer for unsteady turbulent flow over heated blocks in a horizontal channel, *International Journal of Thermal Sciences*, 47(5), 620-632.

Perng, S. W., Wu, H. W. and Jue, T. C., 2012, Numerical investigation of heat transfer enhancement on a porous vortex-generator applied to a block-heated channel, *International Journal of Heat and Mass Transfer*, 55(11), 3121-3137.

Smith, R. E. and Wehofer, S., 1985, From measurement uncertainty to measurement communications, credibility, and cost control in propulsion ground test facilities. *Journal of Fluids Engineering*, 107(2), 165-172.

Sohankar, A., 2007, Heat transfer augmentation in a rectangular channel with a vee-shaped vortex generator, *International Journal of Heat and Fluid Flow*, 28(2), 306-317.

Sripattanapipat, S. and Promvonge, P., 2009, Numerical analysis of laminar heat transfer in a channel with diamond-shaped baffles, *International Communications in Heat and Mass Transfer*, 36(1), 32-38.

Teamah, M. A., El-Maghlany, W. M. and Dawood, M. M. K., 2011, Numerical simulation of laminar forced convection in horizontal pipe partially or completely filled with porous material, *International Journal of Thermal Sciences*, 50(8), 1512-1522.

Valencia, A., 1999, Heat transfer enhancement due to self-sustained oscillating transverse vortices in channels with periodically mounted rectangular bars, *International Journal of Heat and Mass Transfer*, 42(11), 2053-2062.

Wu, J. M. and Tao, W. Q., 2008, Numerical study on laminar convection heat transfer in a rectangular channel with longitudinal vortex generator. Part A: Verification of field synergy principle, *International Journal of Heat and Mass Transfer*, 51(5), 1179-1191.

Yang, S. J., 2002, A numerical investigation of heat transfer enhancement for electronic devices using an oscillating vortex generator. *Numerical Heat Transfer: Part A: Applications*, 42(3), 269-284.

INVESTIGATION OF COMBINED HEAT TRANSFER AND LAMINAR FLUID FLOW IN TWO AND THREE DIMENSIONAL DUCTS WITH AN OPEN CAVITY

Çisil TİMURALP* and **Zekeriya ALTAÇ****

Department of Mechanical Engineering, Eskisehir Osmangazi University
ESOGU MeselikYerleskesi, Eskisehir 26480, Turkey
E-mail: *cisil@ogu.edu.tr, **zaltac@ogu.edu.tr

Abstract: In this study, developing combined forced and natural convection heat transfer and fluid flow in a duct with an open cavity are numerically studied using two- and three-dimensional models of various cavity size and flow induced parameters. The left wall of the cavity is isothermal while all other walls, including duct walls, are assumed to be adiabatic. Air (Pr=0.71) flows through the duct. The geometrical parameters used in this work are the cavity width to cavity height ratio (0.5≤W/D≤2), and the channel height to cavity height ratio (0.25≤H/D≤2). The flow induced parameters consists of the Reynolds number (Re) and the Richardson number (Ri). Re=10, 100, 200 and Ri=0.01, 0.1, 1 and 10 cases are considered in the study. The effects of the geometrical parameters of the cavity as well as the flow parameters on the fluid flow patterns and the temperature distribution (isotherms) were analyzed. The mean Nusselt number over the isothermal wall of the cavity was computed, and the effects of Richardson and Reynolds numbers, cavity aspect ratio and relative duct dimensions on the heat transfer were investigated. The results show that for all Re numbers, as the Richardson number increases, the air circulation becomes stronger inside the cavity. The flow inside the cavity for Ri>1 and Re>100 becomes three-dimensional. Based on the 2D and 3D numerical simulations, using the computed mean Nusselt numbers, correlations were developed.
Keywords: Natural, Forced convection, Combined flow, Three-dimensional simulation, Open cavity.

AÇIK OYUK İÇEREN KANALLARDA BİLEŞİK ISI TRANSFERİ VE LAMİNAR AKIŞIN İKİ VE ÜÇ BOYUTLU OLARAK İNCELENMESİ

Özet: Bu çalışmada, zorlanmış ile doğal taşınımın birlikte geliştiği, açık oyuk içeren bir kanalda ısı transferi ve akışkan akışı, çeşitli oyuk boyutlarıve akışa etkileyen parametrelerin cinsinden, iki- ve üç-boyutlu modellerle sayısal olarak incelenmiştir.Oyuğun sol duvarı izotermal olarak tutulurken, kanal duvarları da dâhil olmak üzere diğer tüm duvarlar adyabatik kabul edilmiştir. Kanal boyunca hava (Pr = 0.71) akışı sağlanmaktadır. Bu çalışmada kullanılan geometrik parametreler, oyuk genişliğinin ile oyuk yüksekliğine oranı (0.5≤W/D≤2) ve kanal yüksekliğinin oyuk yükseklik oranı (0.25≤H/D≤2)'dır. Akışa bağlı parametreler, Reynolds sayısı (Re) ve Richardson sayısından (Ri) oluşmaktadır. Çalışmada Re=10, 100, 200 ve Ri=0.01, 0.1, 1 ve 10 değerleri göz önüne alınmıştır. Oyuğun geometrik parametrelerinin ve akış parametrelerinin akış üzerindeki etkileri ile sıcaklık dağılımı (izotermler) analiz edilmiştir. Ortalama Nusselt sayısı, oyuğun izotermal duvarı üzerinden hesaplanmış olup; Richardson ve Reynolds sayılarının, oyuk en/boy oranının ve bağıl kanal boyutlarının ısı transferi üzerindeki etkileri araştırılmıştır. Çalışma sonuçları, tüm Reynolds sayıları için, Richardson sayısı arttıkça, oyuk içindeki hava sirkülasyonu daha güçlü hale gelmiştir.2B ve 3B sayısal simülasyonların sonuçlarına dayanarak hesaplanan ortalama Nusselt sayıları kullanılarak korelasyonlar geliştirilmiştir.
Anahtar Kelimeler: Doğal, Zorlanmış taşınım, Birlikte akış, Üç-boyutlu simülasyon, Açık oyuk.

NOMENCLATURE

D	Cavity height [m]	T	Temperature [K]
g	Earth's gravitational acceleration [m/s^2]	T_0	Inlet fluid temperature [K]
Gr	Grashof number [$=g\beta\Delta TH^3/\nu^2$]	T_h	Hot wall temperature [K]
H	Duct height [m]	U_0	Inlet velocity [m/s]
Nu	Nusselt number	V	Dimensionless velocity
P	Pressure [Pa]	W	Cavity width [m]
Pr	Prandtl number [$=\nu/\alpha$]	k	Thermal conductivity [W/mK]
Re	Reynolds number[$=U_0H/\nu$]	h	Convective heat transfer coefficient [W/m²K]
Ri	Richardson number [$=Gr/Re^2$]		

INTRODUCTION

Numerous studies on the convective heat transfer in an enclosure have been studied because of its wide application areas. Investigation of mixed convection of flow and heat transfer in a duct with an open cavity has also attracted attention and studied mostly numerically in recent decades due to its importance in many engineering applications such as cooling of electronic equipment, collection of solar energy, etc.

Most of the studies encountered on mixed natural and forced convection in the literature involve the numerical modeling of the rectangular cavity whose top wall is moving at a constant speed (lid-driven cavity) (Erturk et.al.,2005; Freitas and Street, 1988; Iwatsu and Hyun, 1995; Khanafer and Chamkha,1999; Moallemi and Jang, 1992; Mohamad and Viskanta,1991,1995; Prasad and Koseff,1996; Sharif, 2007); however, the studies which involve cavities heated from vertical or bottom walls placed below a fluid stream are relatively few. Some studies involving open cavity with the presence of discrete heaters, constant heat flux etc. were also pursued to observe the effects of fluid flow and heat transfer on the electronic components (Muftuoglu and Bilgen, 2008; Aminossadati and Ghasemi 2009). Chang and Tsay (2001) numerically studied the natural convection in an enclosure with a heated backward step to investigate the effects of the Rayleigh and Prandtl numbers as well as the size of the enclosure on the flow structure and heat transfer characteristics.The study revealed that the extent of heat transfer enhancement increased with decreasing Rayleigh number. Manca et al. (2006, 2008) experimentally investigated mixed convection and opposing mixed convection in a duct with an open cavity below a horizontal duct. Also some experimental and numerical studies have been conducted with natural convection in two-dimensional enclosures (Calcagnietal., 2005; Das et al., 2002; Ishihara et al., 2002). Aydın et al. (1999) analyzed natural convection of air in enclosure heated from one side and cooling from the top numerically to observe the effects of the Rayleigh number and the aspect ratio on the flow pattern. It was observed that the effect of Rayleigh number on heat transfer was more significant when the enclosure was shallow and the Ra number was high, and when the enclosure was tall, the influence of aspect ratio was stronger. Leong et al. (2005) numerically studied mixed convection in a horizontal channel for $1 \leq Re \leq 200$, $0 \leq Gr \leq 10^6$ and $0.5 \leq D/W \leq 4$. They observed that Reynolds number and Grashof number controlled the flow pattern and the flow became unstable in the mixed convection regime. Manca et al. (2003) investigated numerically the effect of heated wall

position on mixed convection in two-dimensional horizontal channel with an open cavity. They studied streamlines and isotherms for Re=100 and 1000 and Ri=0.1 and 100. The results showed that the mean Nusselt number and the maximum temperature were obtained in the opposing forced flow configuration. Rahman et al. (2012) numerically studied flow and heat transfer in a duct with a cavity heated from different sides subjected to a magnetic field. For specified Pr=0.7 and Re=100 conditions, a constant magnetic field is imposed to the duct. Basak et al. (2009) studied mixed convection flows within a square cavity heated from bottom. They obtained numerical solutions for various values of $1 \leq Re \leq 100$, $10^3 \leq Gr \leq 10^5$ and $0.015 \leq Pr \leq 10$.The flow patterns indicated that the natural or forced convection is based on both the parameters Richardson and Pr numbers. For Pr=7, $1 \leq Gr \leq 4000$, $50 \leq Re \leq 1000$, Sidik et al. (2014) numerically simulated mixed convection for fluid with particle laden flow in an open cavity with an aspect ratio of 4 which is heated from below. This study illustrates the variations in the Grashof number made a remarkable difference in the observed flow pattern and cleaning efficiency. Selimefendigil and Yurddas (2012) investigated using 2D numerical model for the mixed convection in a channel with a cavity heated from below and left vertical walls for pulsating flow for $0.1 \leq Ri \leq 100$, $300 \leq Re \leq 800$ and for Strouhal numbers from 0.25 to 1. Brown and Lai (2005) studied numerically combined heat and mass transfer from a 2D horizontal channel with an open cavity heated from below for Pr =0.7, $1 \leq Re \leq 1000$, $0 \leq Gr \leq 10^6$ and $0.1 \leq Le \leq 10$. Based on the two-dimensional numerical simulations, correlations for the entire convection regime, from natural, mixed, to forced convection, were proposed. Burgos et. al. (2016) numerically studied steady and unsteady laminar flow in a duct with a cavity heated from below for $50 \leq Re \leq 1000$ and $0.01 \leq Ri \leq 10$. They observed that the analysis of the unsteady regime revealed a very rich phenomenology where the geometry of the problem couples with the oscillatory thermal instability.

Recently flow of nanofluids in a duct with an open cavity has attracted some attention due to technological applications. Abdellahoum et al. (2015) numerically studied 2D turbulent forced convection of Al_2O_3 nanofluid over a heated cavity in a horizontal duct and investigated the effects of Re number ($10^4 \leq Re \leq 10^5$) and nanoparticles concentration ($0 \leq \phi \leq 4\%$) on the heat transfer and flow characteristics. As a result, the mean Nusselt number increased with the volume fraction of nanoparticles for the whole range of Re number. And also Pack and Cho viscosity model gave maximum friction and heat transfer. Mehrez et al. (2013) numerically investigated mixed convection and entropy generation of nanofluids flow in an open cavity heated from below for $1 \leq AR \leq 2$, $100 \leq Re \leq 500$, $0.05 \leq Ri \leq 1$ and solid volume fraction of nanoparticles up to 10%. It was found that the heat transfer and the entropy generation increased with increasing Re and Ri numbers, and volume fraction of nanoparticles. In a follow up study, Mehrez et al. (2015) numerically studied entropy

generation and mixed convection heat transfer of Cu–water nanofluid flow in an inclined open cavity uniformly heated from the left wall. The investigation is carried out for a wide range of inclination angles of the cavity and the range of nanoparticle volume fractions up to 6%, for $100 \leq Re \leq 500$ while the Grashof number was fixed at 10^4. The results show that for all inclination angles, the enhancement rate of heat transfer is higher than the increase rate of entropy generation.

Numerical simulations involving three-dimensional models are relatively rare. Stiriba et al. (2010) investigated numerically the effects of mixed convective flow over a three-dimensional cavity which is situated at the bottom of a horizontal channel and heated from right cavity wall. A parametric study is performed for $10^3 \leq Gr \leq 10^6$ and $100 \leq Re \leq 1000$. For high Re and Ri numbers the natural convection was involved in and pushed the recirculation zone further upstream. Pallares et al. (1996) studied natural convection in a cubical cavity heated from below for $3500 \leq Ra \leq 10^4$. They reported that the effect of the Rayleigh number and the type of flow structure on heat transfer rates at the top and bottom plates. The heat transfer and fluid flow characteristics of laminar flow in an open cavity heated from below was carried by Stiriba et al. (2013). The effects of Reynolds and Richardson number on the flow in the duct and inside the cavity are studied for $100 \leq Re \leq 1500$ and $0.001 \leq Ri \leq 10$. It was observed that the flow became steady at both low Ri and Re number, and as Ri number was increased, the buoyancy became stronger and part of the heated fluid moved to the left side wall. Abdelmassih et al. (2016) numerically and experimentally studied 3D steady and unsteady mixed convection in a cubical open cavity heated from below for $100 \leq Re \leq 1500$ and $0.1 \leq Ri \leq 10$. The results show that alternate flow ejections persist for all the Reynolds values analyzed.

The interaction between a flowing external stream and the buoyancy driven flow induced by a heated surface from cavity walls leads to the possibility of complex flows. Therefore it is important to understand the heat transfer characteristics of a mixed convection in such configurations. Correlations involving a wide range of design parameters are practically nonexistent. The objective of this study is to investigate two-dimensional and three-dimensional combined forced and natural convection heat transfer and fluid flow in an open cavity (heated from the left wall) which is located below a horizontally configured duct. The geometrical duct parameters, duct height to cavity height (H/D) and cavity width to cavity height (W/D), and flow parameters, Reynolds and Richardson numbers, are varied in a wide range, and the streamlines as well as isotherms are examined qualitatively. A basic quantitative parameter which is the mean Nusselt number was computed as an average over the heated wall surface area. Finally, based on 2D and 3D numerical trials two correlations are developed.

PHYSICAL PROBLEM AND MATHEMATICAL FORMULATION

A horizontal square duct of H×H in cross section and 8×W in length is considered. A cavity with a width W and height D is placed at bottom at a distance 4×W away from the entrance of the duct. The geometry and the coordinate system as well as the geometric variables used in this study are illustrated in Fig. 1.
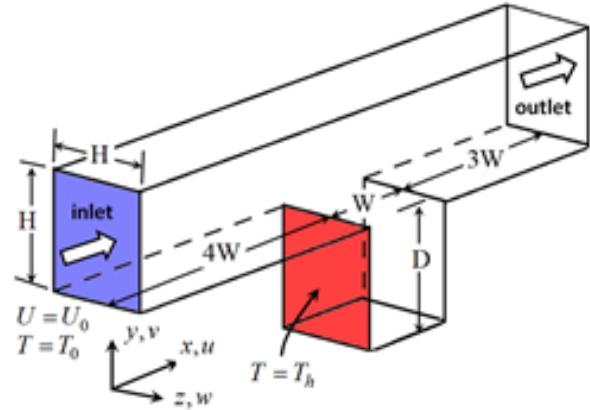
Figure 1. Schematic diagram of the geometry

In this study, the radiative heat exchange is neglected and the thermo-physical properties are assumed to be constant except for the density for which the Boussinesq approximation is used. The working fluid is air (Pr=0.71), and it enters to the duct with a uniform velocity U_0 with ambient temperature T_0. The temperature and flow fields are allowed to develop within the enclosure. Also the flow is assumed to be steady, laminar and incompressible. Constant temperature is applied to the left cavity wall while all other remaining walls, including those of the duct, are assumed to be adiabatic.

Under these assumptions the governing equations can be stated as; for the continuity

$$\nabla \cdot \mathbf{V} = 0 \qquad (1)$$

for the momentum equations

$$(\mathbf{V} \cdot \nabla)\mathbf{V} = -\frac{1}{\rho}\nabla P + \nu\nabla^2\mathbf{V} - g\beta(T - T_0)\mathbf{j} \qquad (2)$$

and for the energy

$$(\mathbf{V} \cdot \nabla)T = \alpha\nabla^2 T \qquad (3)$$

where $\mathbf{V}$ is the velocity, ρ is the density, P is the pressure, ν is the kinematic viscosity, α is the thermal diffusivity, β is the thermal expansion coefficient, T is the temperature and $\mathbf{j}$ is the unit vector depicting y-direction. Due to the physical phenomenon taking place, the dimensionless numbers encountered here are Prandtl, Reynolds, Grashof and Richardson numbers which are defined as $Pr = \nu/\alpha$, $Re = U_0 H/\nu$, $Gr = g\beta\Delta T H^3/\nu^2$ and $Ri = Gr/Re^2$ respectively.

The boundary conditions (for the general 3D model) can be stated as follows:

duct inlet $T = T_0$, $u = U_0$, $v = w = 0$,

duct outlet $\dfrac{\partial u}{\partial x} = \dfrac{\partial v}{\partial x} = 0$, $\dfrac{\partial T}{\partial x} = 0$, $P = 0$

adiabatic walls $\dfrac{\partial T}{\partial n} = 0$, $u = v = w = 0$

heated cavity wall $T = T_h$, $u = v = w = 0$

where T_0 and T_h are the inlet (ambient) and the hot wall temperatures, respectively; P is the gauge pressure at the pressure outlet, U_0 is the fluid velocity at the entry of the duct and **n** denotes the direction normal to the wall.

Once the temperature field is resolved, by equating convection heat flux to that of the conduction heat flux, the local convective heat transfer coefficient at every face nodes are computed. Then the mean heat transfer coefficient and Nusselt number is computed over the isothermal heated surface area according to

$$\bar{h} = \dfrac{1}{A_h} \iint_{A_h} h \, dA$$

(4)

$$\overline{Nu} = \dfrac{\bar{h}H}{k} = \dfrac{1}{A_h} \iint_{A_h} Nu \, dA \tag{5}$$

where k is the conductivity of air, A_h is the heated surface area, $\bar{h}$ and $\overline{Nu}$ are the mean heat convection transfer coefficient and the mean Nusselt number.

NUMERICAL SOLUTION

The continuity, momentum and energy equations are solved using Fluent 6.3®(2003) where Boussinesq approximation is employed for the density variations. In the discretization of the convection terms, the second order upwind and as for the solution algorithm SIMPLE is used. In the numerical simulations, the cavity aspect ratio (W/D) and duct height to cavity height ratio (H/D) are varied for 0.5≤W/D≤2 and 0.25≤H/D≤2 intervals. Richardson number which is a measure of natural convection heat transfer rate to that of forced convection is varied from 0.01 to 10 while, in this study,the Reynolds numbers for 10, 100 and 200 are investigated.

Table 1. Comparison of the computed Nusselt numbers with published results.

Ri=1, Re=10		Ri=0.01, Re=100		Ri=0.1, Re=100		Re=0.1, Re=1000	
Leong, 2005	Present	Leong, 2005	Present	Stiriba 2008	Present	Stiriba 2008	Present
2.209	2.309	3.837	4.006	3.2	2.956	7.8	7.157

Table 2. Grid sensitivity analysis for W/D=1 case.

Grid size	Ri=0.01 Re=100	Ri=0.01 Re=200	Ri=0.1 Re=100	Ri=0.1 Re=10
10^3	2.357	2.744	2.470	1.569
20^3	2.413 (2.3%)	2.806 (2.21%)	2.527 (2.25%)	1.597 (1.75%)
40^3	2.449 (1.47%)	2.830 (0.85%)	2.563 (1.40%)	1.617 (1.24%)
50^3	2.456 (0.28%)	2.822 (0.28%)	2.571 (0.31%)	1.624 (0.43%)

To validate the accuracy of Fluent® solutions with respect to the grid configuration and to ensure grid independent solutions, the numerical solutions are obtained using various grid configurations in the computational domain. First, to determine the accuracy of the present study, the numerical solutions for 2D-model are compared with those of available numerical studies in the literature. The comparative results are presented in Table 1. It is observed that presented solutions fairly agree with the published literature. The numerical simulation results and relative errors with respect to the mean Nusselt numbers for W/D=1 and four different grid configurations (10^3, 20^3, 40^3 and 50^3) are depicted in Table 2 to determine the grid independency. The grid is further clustered near the walls in order accurately to obtain the velocity and temperature gradients. It is determined that with the relative errors below 0.5% as depicted in Table 2,

configuration with 50^3 is the optimum grid configuration. Since flow is laminar, it is observed that the grid structure influences the mean Nusselt results relatively less.

RESULTS AND DISCUSSION

The flow field (streamlines) and temperature distributions (isotherms) for the 2D and 3D studies are produced for each simulation. These distributions are compared and analyzed with respect to the dimension-less parameters (Re and Ri) and geometrical parameters (W/D and H/D) considered.

Two-Dimensional Analysis

For Ri=0.01, H/D=0.5 and Re=10, the variations of streamlines and isotherms with respect to W/D aspect
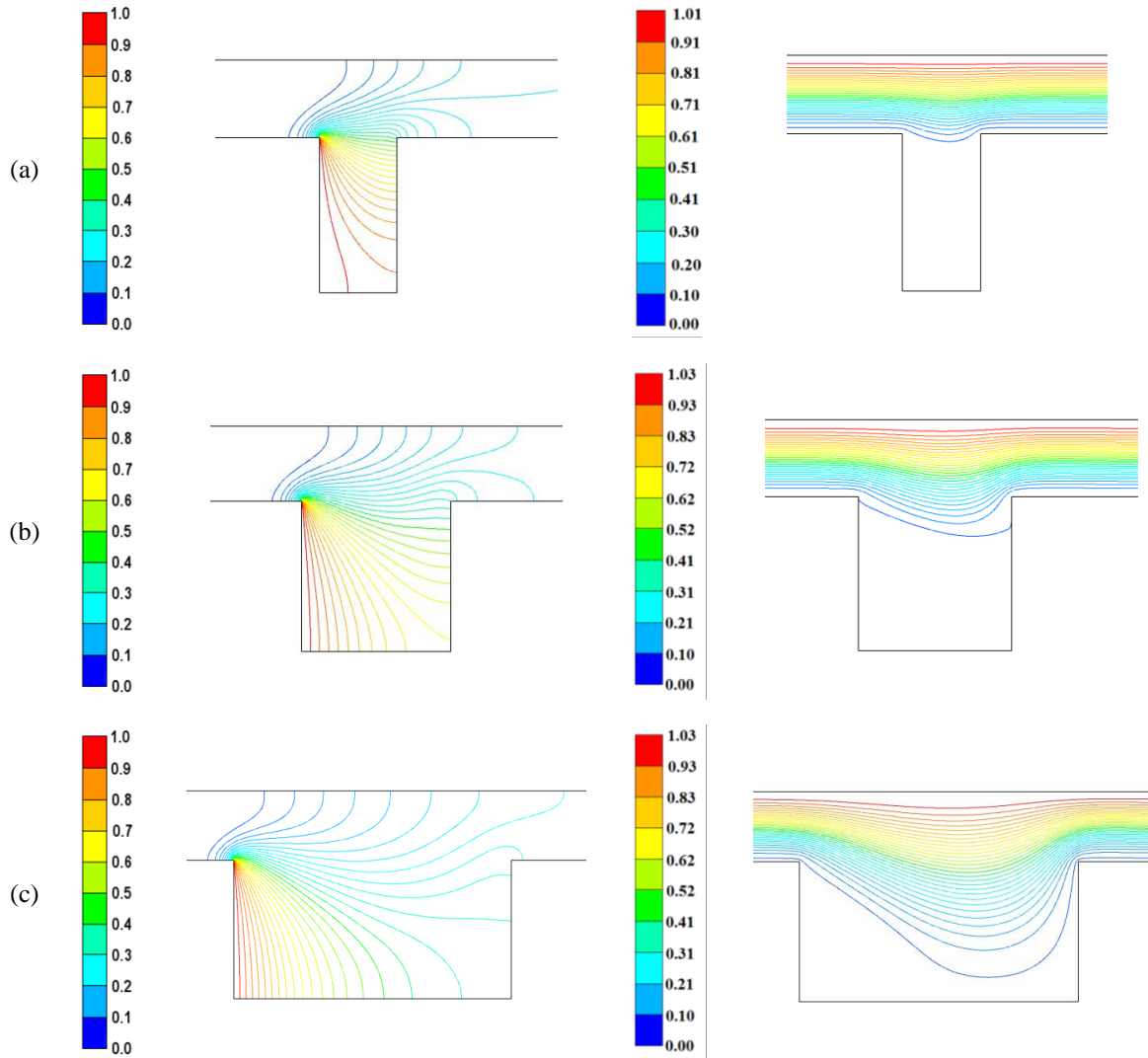
Figure 2. The effect of aspect ratios on isotherms on the left hand side (LHS) and streamlines on the right hand side (RHS) for Ri=0.01, H/D=0.5 and Re=10.(a) W/D=0.5, (b) W/D=1, (c) W/D=2

ratio are depicted in Fig. 2. For a slender cavity (W/D=0.5), the streamlines display almost a linear path on the upper portion of the duct while the moving fluid adjacent to the cavity-top depicts a small dip into the cavity. As a result of this, the fluid inside the cavity remains relatively undisturbed which yields an increase in the temperature of the cavity. The isotherms indicate that the heat transfer mechanism taking place in the cavity is mostly governed by conduction. The thermal boundary layer starting from the top of the cavity encompasses almost the whole cavity. Due to the formation thick thermal boundary layer, hot wall surface yields small temperature gradients as a result the convection heat transfer from the hot cavity wall becomes insignificant. As the aspect ratio W/D increases, the surface area of the cavity open-top surface area facilitates the entrance of the fluid into the cavity (Figs. 2b and 2c) which in turn disturbs relatively inactive fluid. For W/D=1, the region below the bottom streamline in the cavity, the fluid is trapped inside the cavity (Fig. 2c). As W/D increases, the thermal boundary layer shrinks towards the heated wall, the

streamlines are stacked closer thereby the temperature gradients as well as the convection heat transfer rates are increased. However, this increase is still not significant enough to overcome the present conduction mode. For Ri=0.01, W/D=1 and Re=200, the variations of streamlines and isotherms with respect to H/D (0.25≤H/D≤2) ratio are depicted in Fig. 3. In Fig. 3a, the cavity height is 4 times larger than the duct height, the isotherms concentrate on the left wall yielding higher temperature gradients. There is a strong clockwisecirculation inside the cavity which encompasses the entire cavity. The thermal boundary layer is almost symmetrical with respect to central horizontal line where it becomes the thinnest. At the upper portion of the cavity, the isotherms indicate that due to strong clockwise circulations, the fluid escapes the cavity and drifts in the main flow direction along the duct (Fig. 3a) which is consisted with the streamlines.
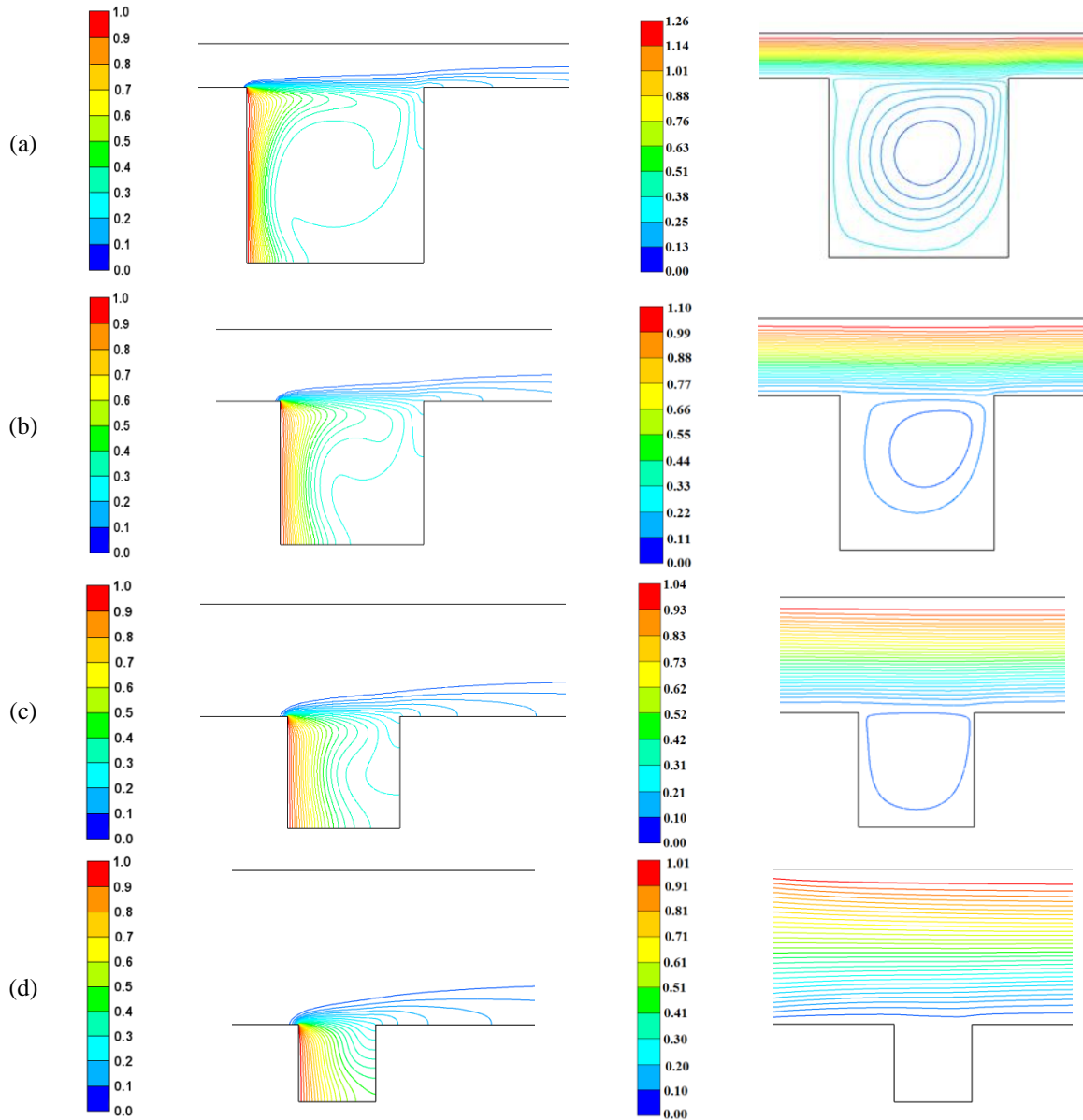
Figure 3. The effect of H/D on isotherms (LHS) and streamlines (RHS) for W/D=1, Ri= 0.01, Re=200, (a) H/D=0.25, (b) H/D=0.5, (c) H/D=1, (d) H/D=2

As H/D is further increased, the strength of the circulation in the cavity is reduced due to fluid volume flowing in the cavity. The circulation center shifts slightly to the northeast of the cavity. As a result of all these, both hydrodynamic and thermal boundary layer thicknesses are increased in comparison to H/D=0.25 case. The fact that some of the hot air escapes and fresh cold air enters the cavity, the natural circulation becomes evident. As H/D is further increased, as depicted in Figs. 3c and 3d, due to smaller cavity height or shallower cavity, the amount of air leaking from the cavity increases leaving no change for natural circulation cycle to be fully completed. Due to strong duct flow (Re=200), as air rises to the top surface level, it is transported away from the cavity in the main flow direction (Fig. 3d).For Ri=0.01, W/D=1 and H/D=0.25, the variations of streamlines and isotherms with respect to Reynolds number (Re=10, 100, 200) are depicted in

Fig. 4. In Fig. 4a, for Re=10, the fluid velocity is considerably small. The rising air due to heat input from the hot wall inthe cavity has the potential to fill the upper portion of the cavity including the corresponding duct section. The streamlines follow a strong curved pattern on the right upper corner of the cavity sweeping the fluid yielding higher fluid temperatures in the downstream of the duct. The thermal boundary layer, due to relatively weak and small circulation, is thick with small temperature gradients at the hot surface, and thus the convection heat transfer rate is significantly small. In Fig. 4b, for Re=100, the fluid velocity is significantly higher than the previous case. Frictional interaction between the fast moving fluid inside the duct and the fluid at the top surface of the cavity creates a stronger clockwise circulation within the cavity. The influence of natural convection is evident. As the circulation gains strength with
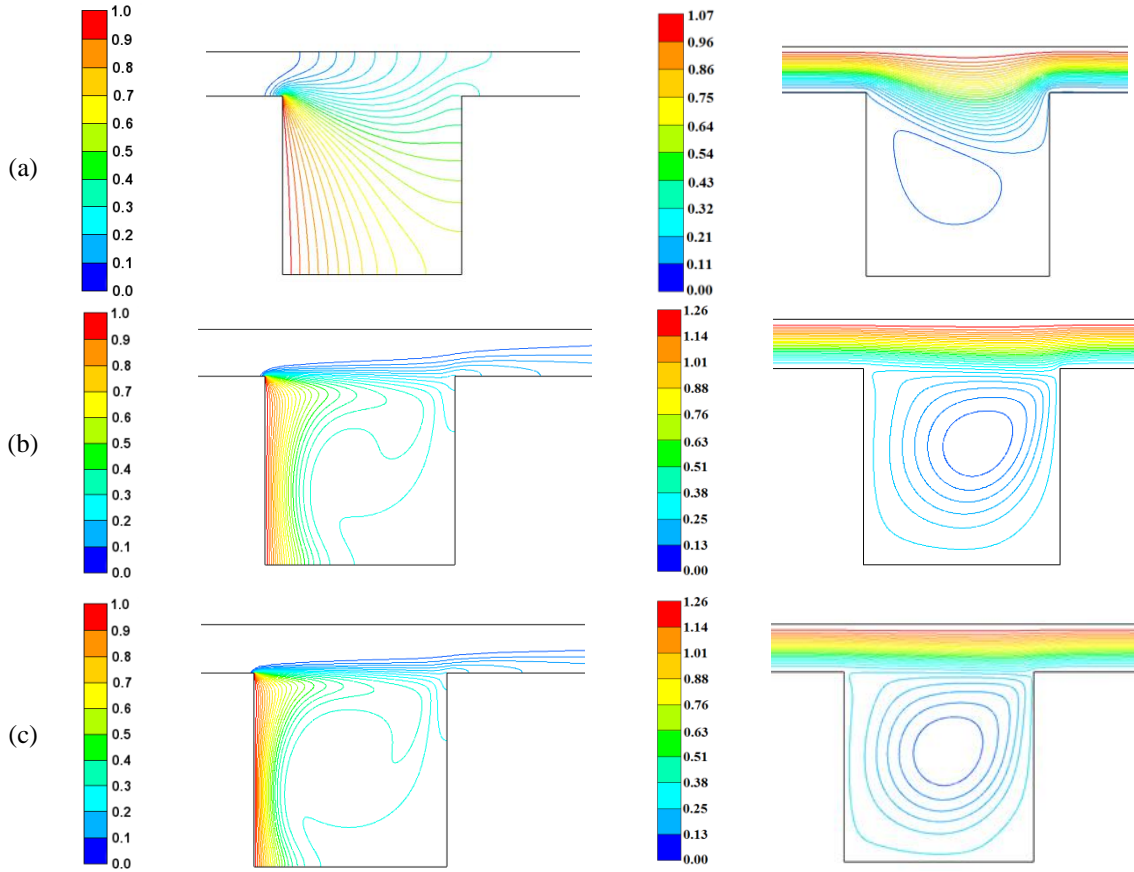
Figure 4. The effect of Reynolds number on isotherms (LHS) and streamlines (RHS) for W/D=1, H/D=0.25 and Ri=0.01, (a) Re=10; (b) Re=100; (c) Re=200.

increasing Re number, the isotherms shrink tighter towards the heated wall yielding increased heat transfer rates; however, during the clockwise circulation of the cavity fluid, some of the rising hot air leak out of the cavity and drifts away along the downstream of the duct. In Fig. 4c, for Re=200, natural circulation caused by buoyant flow expands towards all three walls encompassing the whole cavity. The isotherms are clustered on the hot left wall further squeezing thermal boundary layer yielding steeper temperature gradients in comparison to Re=100 (Fig. 4b) case. Since Re=100 and Re=200 cases involve faster moving duct fluid, the streamlines and isotherms of the two cases are very much similar (Figs. 4b and 4c) in comparison to that of Re=10 which yields much slower axial velocity in the duct.

To observe the effect of Richardson numbers on the flow and heat transfer, computations for Ri=0.01, 0.1, 1 and 10 have been conducted. For Re=10, H/D=0.15 and W/D=1, the variations of streamlines and isotherms with respect to Richardson number are depicted in Fig. 5. In Fig. 5a, Ri=0.01 case, due to small Re number, the air flow into the duct is facilitated mostly from right side of the cavity because of the direction of the velocity vectors. The straight horizontal flow is influenced by rising hot air which penetrates into the cavity slightly.

Conduction heat transfer at two-thirds of the bottom region, where a weak non-uniform circulation occurs, is dominated; therefore, the thermal boundary layer covers almost the entire cavity. The streamlines above the cavity depict deviation towards northeast of the cavity due to relatively small inertia forces. For Ri=0.1 (Fig. 5b), the isotherms are similar to those of depicted in Fig. 5a, but the eddy in the cavity slightly gains strength, and the clockwise circulations spread out to extend the side walls. In Fig. 5c, for Ri=1 where the influence of the buoyancy forces increase, although fluid passing the duct slightly penetrates into the cavity at the top surface, the inertia forces are strong enough to trap most of the fluid inside the cavity. Unicellular circulation becomes stronger covering the entire cavity. It is observed that the shape of the thermal boundary layer is also distorted due to the interactions between the competing buoyancy and inertia forces. This leads to steeper temperature gradients at the bottom half of the heated wall in turn yielding higher heat transfer rates in comparison to previous cases. For Ri=10, in Fig. 5d, the streamlines and isotherms take the form of the flow in a single cavity enclosed by four walls. Natural circulation, a unicellular clockwise roll, is observed within the entire cavity leading to streamlines covering the entire cavity. Due to the flow field, the temperature gradients along the hot wall and thus the heat transfer rate are increased.
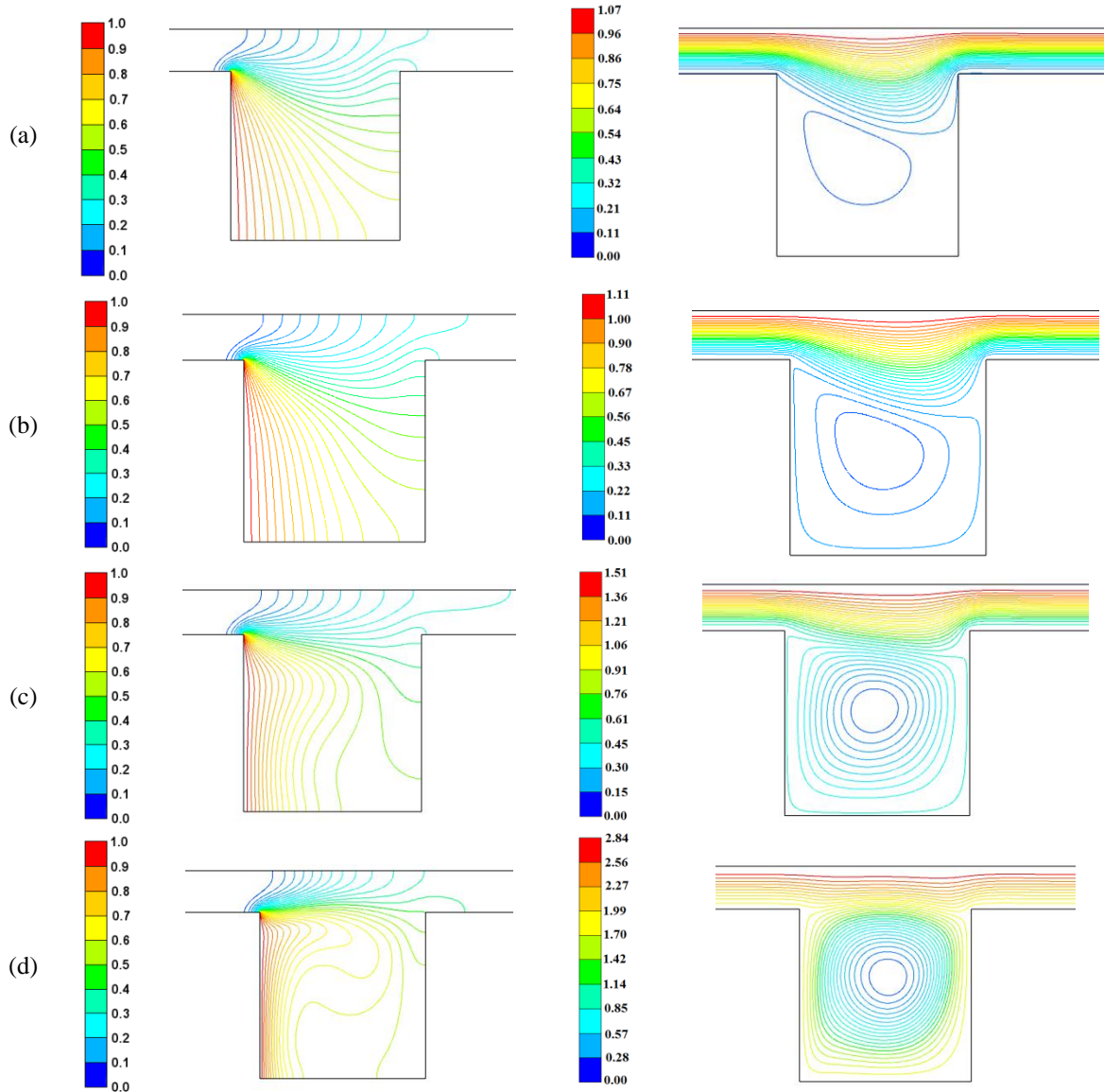
Figure 5. The effect of Richardson Number on isotherms (LHS) and streamlines (RHS) for W/D=1, H/D=0.25 and Re=10, (a) Ri=0.01; (b) Ri=0.1; (c) Ri=1; (d) Ri=10.

Three-Dimensional Analysis

For W/D=0.5 and W/D=1, the pathlines (colored by temperature) are depicted for H/D=1 and Ri=0.1, and for Re=10, 100 and 200 in Fig. 6 to observe the effect of cavity length (W) to cavity height (D) ratio. For W/D=0.5, the cavity is tall having relatively small surface area of interaction between the duct and the cavity in comparison to W/D=1 in which case the surface area is doubled. In Fig. 6a, for Re=10 and W/D=0.5, the fluids lightly penetrates into the cavity from the open top surface. The penetrating fluid is pushed upwards due to buoyancy forces while the bottom of the cavity remains relatively inactive due to a weak circulation. For W/D=1, the cavity's surface is longer or larger along the flow direction. Thus, due to competing forces, the fluid is able to achieve deeper penetration covering most of the cavity. The region occupied by the three-dimensional boundary layer decreases which leads to cooler temperatures inside the cavity because of increased motion of the fluid within the cavity. The flow at the front and back walls of the cavity is hindered due to friction between the fluid and aforementioned cavity walls. The temperature of the fluid passed cavity also increases with respect to afore the cavity due to this interaction. For Re=100 in Fig. 6b, for W/D=0.5 (LHS), the fluid flowing thru the duct does not exhibit significant penetration into the cavity; thus, the circulation in the cavity displays 2-D flow characteristics. The fluid rising from the cavity distorts pathlines above the cavity, but it soon recovers at the downstream of the duct. Relatively weak activity in the cavity, fluid temperature inside the cavity increases yielding small temperature gradients and thus small heat transfer rates.
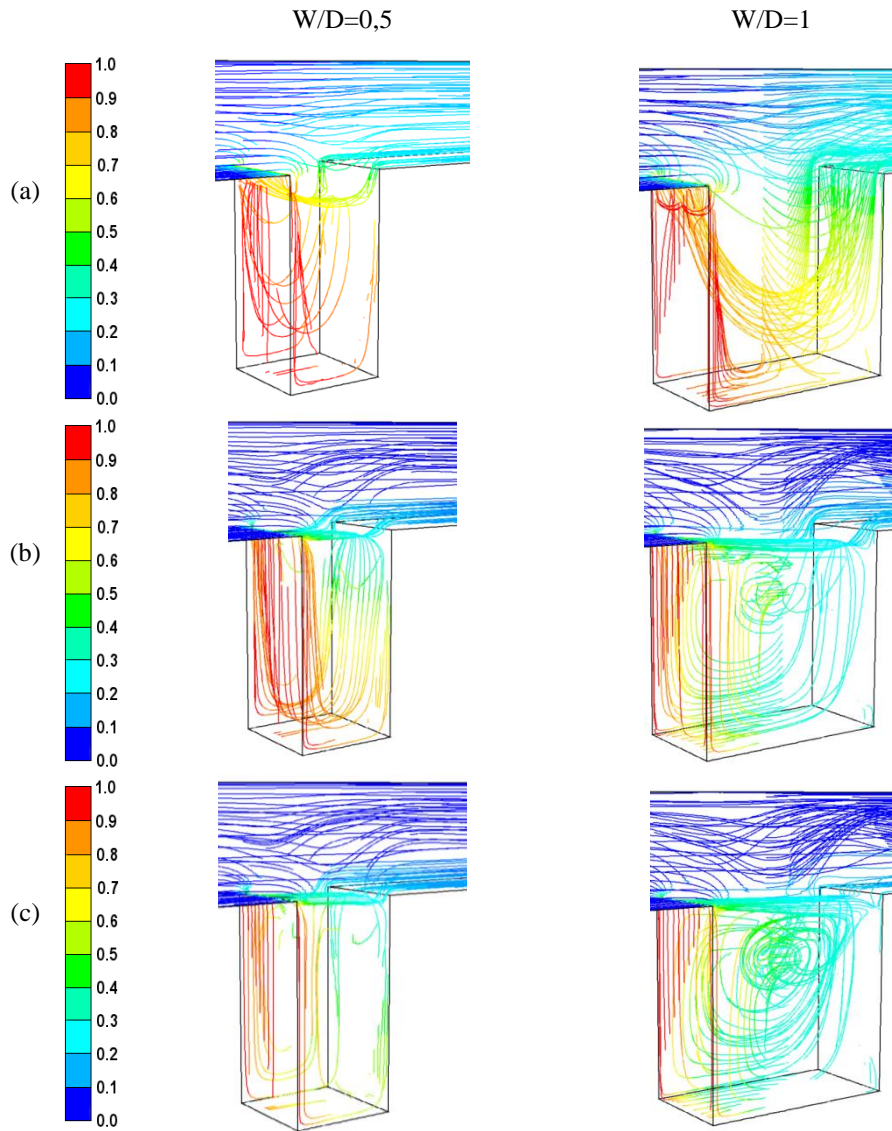
Figure 6. Pathlines (colored by temperature) for H/D=1, Ri=0.1 and W/D=0.5(LHS); W/D=1(RHS) (a) Re=10, (b) Re=100, (c) Re=200

For Re=100 and W/D=1, while the general form of the roll complies with unicellular pattern, the pathlines depict 3-D flow patterns especially at the core of the cavity. In the meantime, the flow above the cavity is further distorted and the flow later recovers to its original horizontal pattern further downstream. The motion of the fluid in the cavity is limited in the zone away from the walls where the friction forces reduce the inertia of the fluid motion. For Re=200 and W/D=0.5 in Fig. 6c, the fluid motion basically resembles those of Fig. 6b; however, the fluid, as the circulation inside the cavity gains strength, expands towards the cavity walls. For W/D=1, the circulation inside the cavity not only maintains its 3-D structure but also expands and becomes more violent leading to a better mixing within the cavity which in turn shrinks the thermal boundary layer region. This physical phenomenon increases the heat transfer rate. For H/D=0.5, 1 and 2, the pathlines (colored by temperature) are depicted for Ri=0.1, W/D=0.5 and for Re=10, 100 and 200 in Fig. 7. In Fig.

7a, for W/D=0.5, the pathlines are depict slight fluid penetration into and out of the cavity at the duct-cavity interface while fluid motion is directed upwards due to occurring density differential which also slightly distorts the flow in the duct above the cavity. The cavity becomes hotter yielding small temperature gradients at the heated wall. When the cavity height is doubled (H/D=1), the inertia forces are increased and the amount of fluid penetration into the cavity is reduced. The weak fluid circulation is basically confined to the upper portion of the cavity. The cavity temperature increases in comparison to H/D=0.5 as a result the temperature gradients at the heated wall surface decrease. This trend is maintained for H/D=2 case as well. In Fig. 7b, for H/D=0.5, the fluid velocity increases with Re number. The clockwise flow pattern in the cavity display 3D characteristics due to the inflow of fluid from the duct flow. As a result of this impact, the duct flow above the cavity is distorted which recovers at the duct downstream. For H/D=1, increased mass and inertial
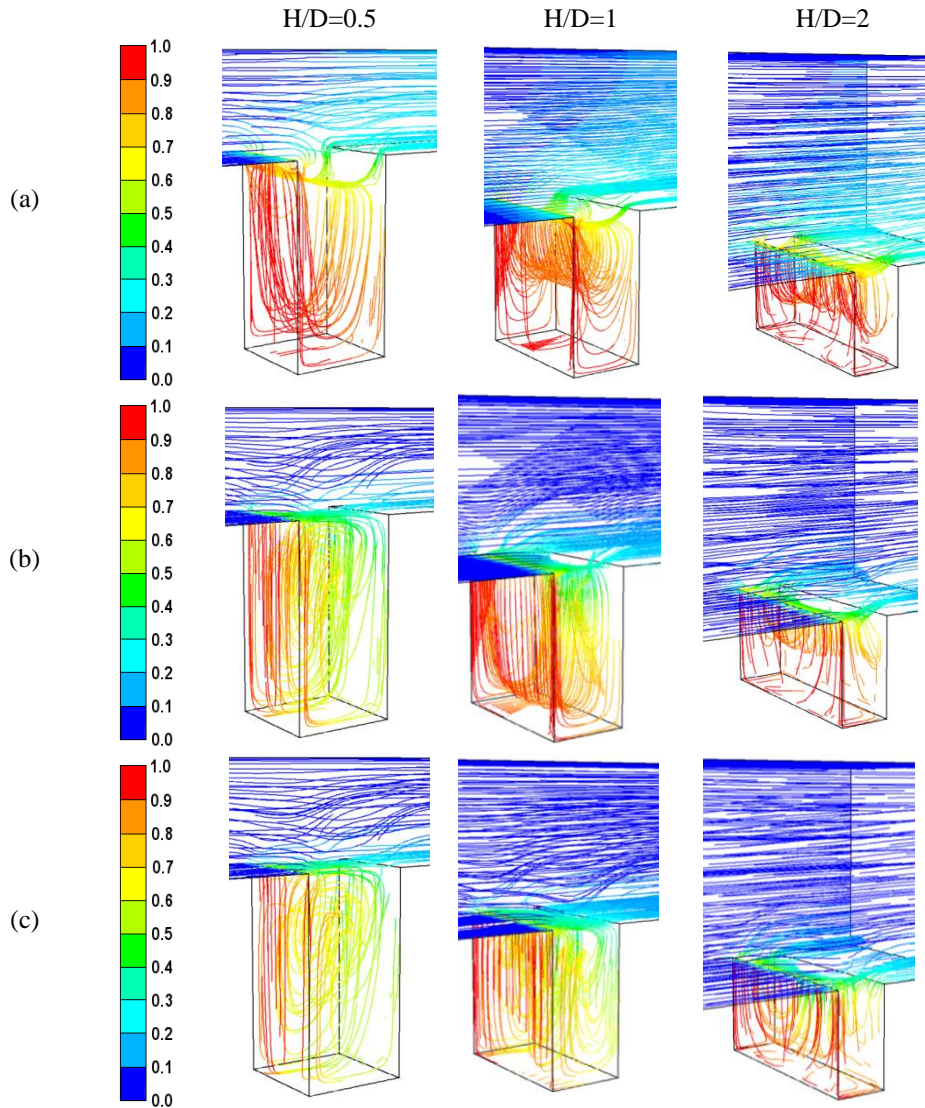
Figure 7. Pathlines (colored by temperature) for W/D=0.5, Ri=1 and H/D=0.5(1st col.); H/D=1(2nd col.); H/D=2(3rd col.) :(a) Re=10, (b) Re=100, (c) Re=200

forces created in the duct lead to smaller distortions in the fluid motion in the duct which confines the fluid inside the cavity. The flow at the interior region of the cavity depicts 2D flow patterns, but the frictional effects are clearly observed near the cavity walls. For H/D=2 in Fig. 7b, the duct height is comparatively much larger than that of the cavity. Thus the mass of the fluid is larger which leads the fluid suppression in the cavity. As a result, a weak circulation confined at the upper half of the cavity is observed. For Re=200 and H/D=0.5 (Fig. 7c), circulations with 3-D mixed-flow structures occupying the entire cavity are formed. For H/D=1, weaker yet 3-D flow patterns are formed at the upper half of the cavity, and it is relatively inactive at the lower half. For H/D=2, the pathlines of the fluid flowing inside the duct is almost linear with slight distortions above the cavity. This means that the fluid in the cavity remains trapped and circulations inside are to be expected.

In Fig. 8, the effects of the Reynolds number on the pathlines are depicted for two cases (1) H/D=0.5,

W/D=0.5, Ri=0.1 (on LHS) and (2) H/D=1, W/D=1, Ri=1 (on RHS). For Re=10 and for Case 1, a weak circulation extending to the duct level is formed. The fluid is relatively motionless at the bottom portion of the cavity. For Re=100, the duct flow partially shifts into the cavity which slams into the wall opposite of the hot wall and continues to circulate in the cavity. The clockwise circulation covers the entire cavity while the circulation generally maintains 2-D flow pattern. As a result, the size of the thermal boundary region is reduced which leads to increased heat transfer rates. For Re=200, the fluid in the cavity is active. For Case 2 in Fig. 8, due to increased top surface area of the cavity, the amount of the inflow fluid up to the top one-third of the cavity increases while creating a cellular (2-D like) fluid motion below this path; however, the circulations are not very strong because of small value of Re number. Since the fluid cannot escape the cavity, the temperatures within the circulation zone which encompasses the hot wall increase yielding small temperature gradients at the surface of the hot wall.
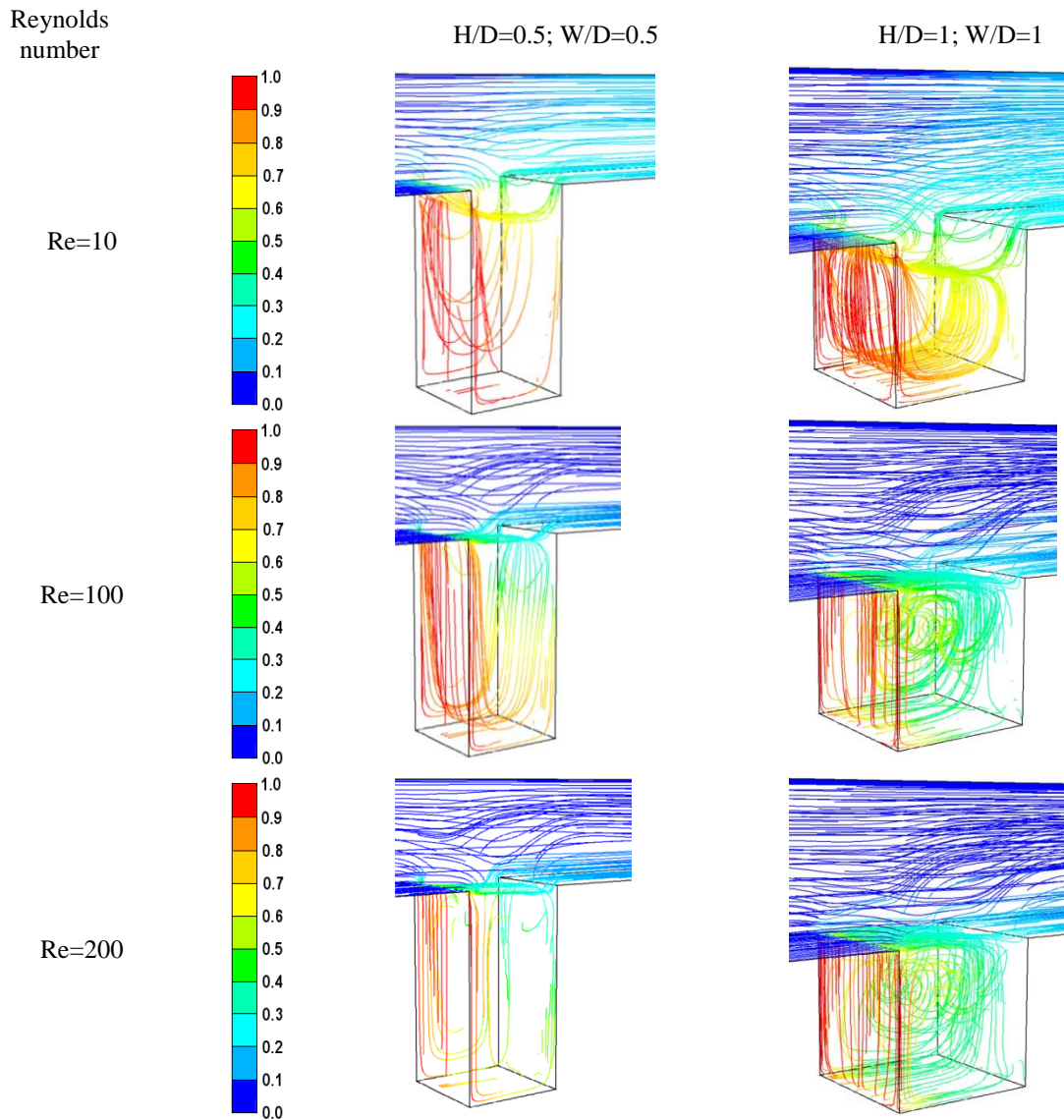
Figure 8. Pathlines (colored by temperature) for different Re numbers (LHS: H/D=0.5; W/D=0.5; Ri=0.1 RHS: H/D=1, W/D=1, Ri=1)

For Re=100, the fluid flow inside the cavity exhibiting 3-D flow patterns is violent. The flow covers the entire cavity; however, the velocity and temperature gradients are observed to be much steeper at the hot wall implying significant increase in the heat transfer rates. For Re=200, basically similar flow and heat transfer patterns are also observed here. Due to higher Reynolds number value, the mixing is more vigorous extending towards enclosing walls, and as a result, the thermal boundary layer region is much smaller.

In Fig. 9, the effects of Richardson number on the flow and heat transfer are depicted for (a) Re=10, (b) Re=200 and for H/D=1 and W/D=0.5. For Re=10, the circulation created at the upper half of the cavity extends towards the bottom wall of the cavity as Richardson number is increased. The flow structure complies with 2D flow patterns, but the effects of the fluid frictions with the walls become more pronounced with increasing Ri number. For Re=200, the flow structures depict 3-D flow patterns with features strengthening by increasing Ri number. It is noted that for Ri=10, the buoyancy

forces are strong enough to overcome inertial forces at the open top of the cavity so that rising cavity fluid causes strong distortions in the region above the cavity.

Fig. 10, using the 3D numerical simulations, the variation of the Nusselt number with the Reynolds number and H/D for Ri=0.1 and 1, and for W/D=0.5 and 1 is depicted. For Ri=0.1 and fluid flow at low Reynolds numbers (Re=10), the change in the mean Nusselt number is insignificant. For Re=10, it is observed that Nu<1 due to stagnant fluid becoming hotter in the cavity which facilitates conduction heat transfer. However, as the Reynolds number is increased, the mean Nusselt number increases with W/D for H/D>0.5 due to strengthening duct flow and increased open surface area of the cavity. For W/D=0.5 and Ri=0.1, the relative increases in mean Nusselt numbers with respect to H/D=0.5 are, respectively for H/D=1 and 2, 59% and 60% for Re=10, 56.5% and 62.1% for Re=100, and 36.3% and 57.3% for Re=200. The relative increases in the mean Nusselt numbers for W/D=1 with respect to

43
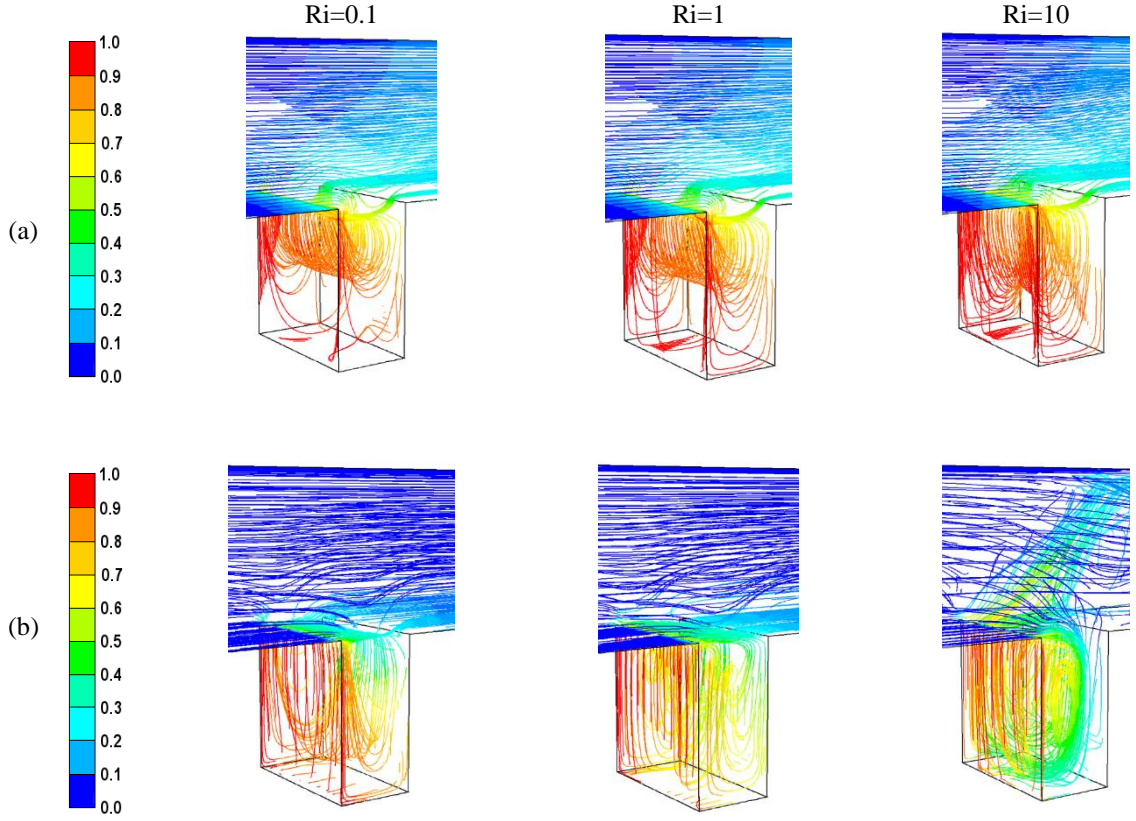
Figure 9. Pathlines (colored by temperature) for different Ri numbers H/D=1, W/D=0.5: (a) Re=10, (b) Re=200.

W/D=0.5 are 25%, 27% and 37% for Re=100 and 21.5%, 22% and 26.5% for Re=200 (Figs. 10a and 10b), respectively, for H/D=0.5, 1 and 2. In Figs.10c and 10d, the mean Nusselt number variations are depicted for Ri=1. The mean Nusselt numbers for Re=10 are identical to Ri=0.1; that is, for duct flows of low Reynolds number, the Richardson number does not have a significant effect on the heat transfer rates. On the other hand, as the Reynolds number is increased, the mean Nusselt number increases with W/D. For W/D=0.5 and Ri=1, the relative increases in mean Nusselt numbers with respect to H/D=0.5 are, respectively for H/D=1 and 2, 59% and 60% for Re=10, 25.5% and 57.1% for Re=100, and 25.5% and 38.2% for Re=200. The relative increases in the mean Nusselt numbers for W/D=1 with respect to W/D=0.5 are 24.8%, 45.1% and 44% for Re=100 and 21.5%, 25% and 35.4% for Re=200 (Figs. 10c and 10d), respectively, for H/D=0.5, 1 and 2.

It is observed that the flow in some cases can be considered two-dimensional. This phenomenon is also observed in the quantitative results depicted by the mean Nusselt numbers tabulated in Table 3. For Ri≤1, the mean Nusselt numbers are almost identical where 3D computations yield slightly larger Nu values. This is also observed for large Reynolds number flows (Re=100 and 200); however, as the Richardson number

is increased, computed Nusselt numbers from the 3D simulations are consistently smaller than those of 2D simulations. It is observed that the deviations in the mean Nusselt numbers increase with the Reynolds number due to aforementioned 3D flow patterns encountered inside the cavity. As a result of momentum losses of the fluid front and back cavity walls as well as complex fluid patterns, the temperature field also becomes three-dimensional.

Table 3. Comparisons of the mean Nusselt numbers computed from 2D and 3D models for W/D=0.5 and H/D=1

Re	Ri	Nu_{2D}	Nu_{3D}
10	0.1	1.13	1.15
10	1	1.13	1.15
10	10	1.14	1.17
100	0.1	1.69	1.72
100	1	1.75	1.79
100	10	3.44	2.49
200	0.1	1.99	2.05
200	1	2.41	2.56
200	10	5.83	3.38
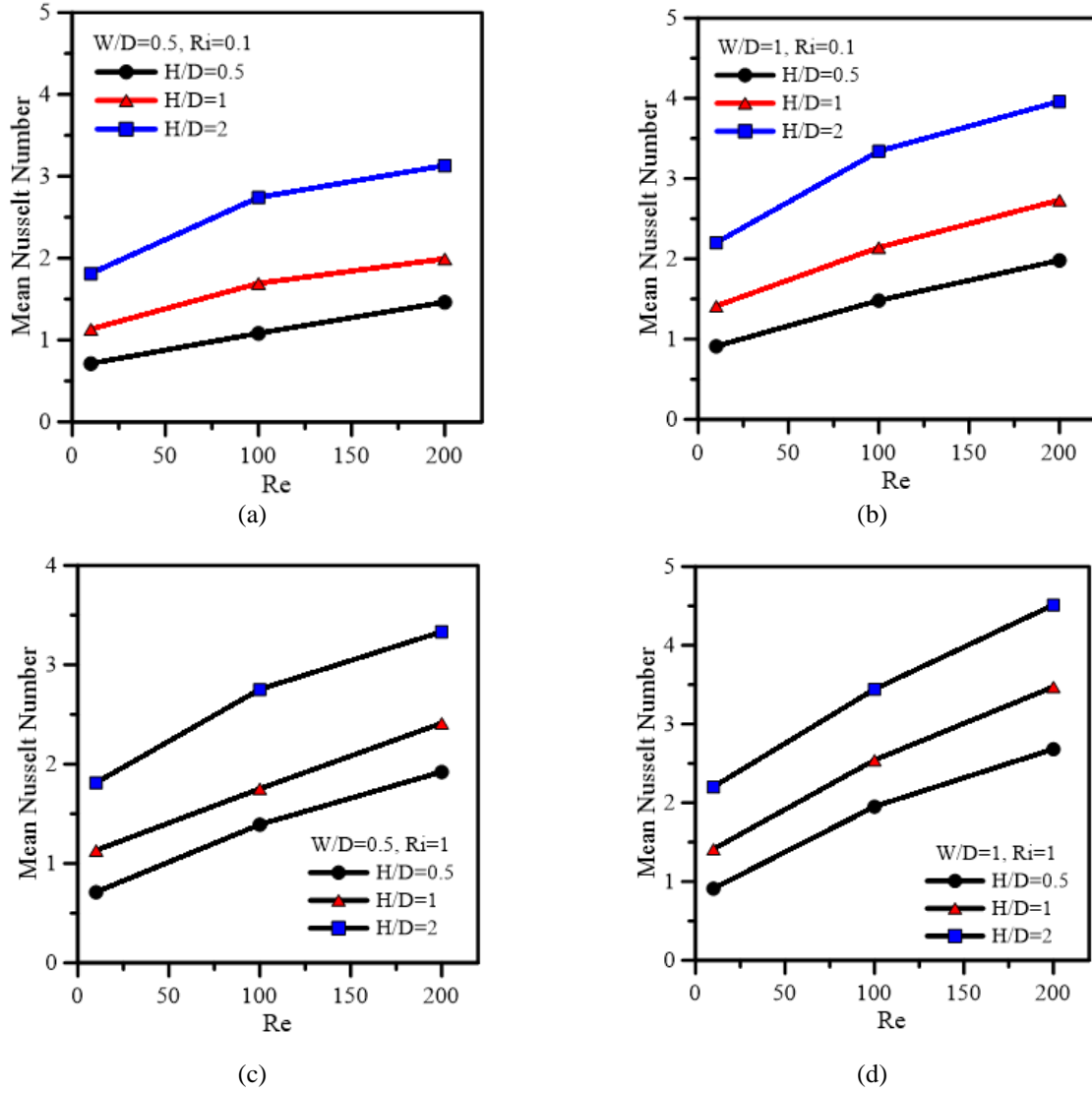
Figure 10. Variation of the computed mean Nusselt number (using 3D models) with the Reynolds number for (a) Ri=0.1, W/D=0.5, (b) Ri=0.1, W/D=1, (c) Ri=1, W/D=0.5, (d) Ri=1, W/D=1.

Heat Transfer Correlations

The mean Nusselt numbers computed from 2D and 3D numerical simulations for all cases and parameters considered in the study were fitted using a regression analysis, and correlations were developed. For 2D simulations, the mean Nusselt number correlation using 144 data sets using four variables led to (Timuralp,2015).

$$\overline{Nu} = 0.674 Re^{0.32} Ri^{0.09} \left(\frac{H}{D}\right)^{0.403} \left(\frac{W}{D}\right)^{0.351}, \quad r^2 = 0.978 \quad (5)$$

for $10 \leq Re \leq 200$, $0.01 \leq Ri \leq 10$, $0.25 \leq \frac{H}{D} \leq 2$, $0.5 \leq \frac{W}{D} \leq 2$

The mean Nusselt number correlation using 54 data sets from three-dimensional numerical simulations using all parameters investigated yields (Timuralp,2015)

$$\overline{Nu} = 0.354 Re^{0.481} Ri^{0.248} \left(\frac{H}{D}\right)^{0.135} \left(\frac{W}{D}\right)^{0.487}, \quad r^2 = 0.949 \quad (6)$$

for $10 \leq Re \leq 200$, $0.1 \leq Ri \leq 10$, $0.5 \leq \frac{H}{D} \leq 2$, $0.5 \leq \frac{W}{D} \leq 1$

CONCLUSIONS

Heat transfer and fluid flow in an open cavity placed below a straight duct are simulated numerically using 2D and 3D models with respect to W/D and H/D, and Richardson and Reynolds numbers. Left surface of the duct is maintained at constant temperature while all other walls, including the duct, are assumed to be adiabatic. The flow through streamlines and/or pathlines and the heat transfer through isotherms and the computed mean Nusselt numbers are studied qualitatively and quantitatively. The study yields the following conclusions:

a) For small W/D cavities, the buoyancy induced circulations are weak, for small Re values, the heat transfer process is dominated by conduction; however, fluid circulations and heat transfer increase with increasing W/D;

b) For large Reynolds numbers and Ri>1, the flow becomes stronger and three-dimensional unstable flow patterns are observed inside the cavity which also

45

effects the mean Nusselt number yielding smaller values than those of computed from 2D models;

    c)   As the Richardson number is increased, either in 2D or 3D simulations, the mean Nusselt number increases and becomes more pronounced at higher Reynolds number values;

    d)   For increasing H/D allowing fluid escape from the cavity yields increase in the mean Nusselt number;

    e)   Two correlations that can be used in practical engineering applications, using 2D and 3D models, were obtained.

REFERENCES

Abdellahoum C., Mataoui A. and Oztop H.F., 2015, Comparison of viscosity variation formulations for turbulent flow of Al2O3-water nanofluid over a heated cavity in a duct, *Advanced Powder Technology*, 26, 1210-1218.

Abdelmassih G., Vernet A. and Pallares J., 2016, Steady and unsteady mixed convection flow in a cubical open cavity with the bottom wall heated, *International Journal of Heat and Mass Transfer*, 101, 682-691.

Aminossadati S.M. and Ghasemi B., 2009, A numerical study of mixed convection in a horizontal channel with a discrete heat source in an open cavity, *European Journal of Mechanics B-Fluid*, 28, 590-598.

Aydin O., Unal A. and Ayhan T., 1999, Natural convection in rectangular enclosures heated from one side and cooled from the ceiling, *International Journal of Heat and Mass Transfer*, 42, 2345-2355.

Basak T., Roy S., Sharma P.K. and Pop I., 2009, Analysis of mixed convection flows within a square cavity with uniform and non-uniform heating of bottom wall, *International Journal of Thermal Sciences*, 48, 891-912.

Brown N.M. and Lai F.C., 2005, Correlations for combined heat and mass transfer from an open cavity in a horizontal channel, *International Communications in Heat and Mass Transfer*, 32, 1000-1008.

Burgos J., Cueta I. and Saluena, C., 2016, Numerical study of laminar mixed convection in a square open cavity, *International Journal of Heat and Mass Transfer*, 99, 599-612.

Calcagni B., Marsili F. and Paroncini M., 2005, Natural convective heat transfer in square enclosures heated from below, *Applied Thermal Engineering*, 25, 2522-2531.

Chang T.S. and Tsay Y.L., 2001, Natural convection heat transfer in an enclosure with a heated backward step, *International Journal of Heat and Mass Transfer*, 44, 3963-3971.

Das S.P., Chakraborty S. and Dutta P., 2002, Natural convection in a two-dimensional enclosure heated symmetrically from both sides, *International Communications in Heat and Mass Transfer*, 29, 345-354.

Erturk E., Corke T.C. and Gokcol C., 2005, Numerical solutions of 2-D steady incompressible driven cavity flow at high Reynolds numbers, *International Journal for Numerical Methods in Fluids*, 48, 747-774.

Fluent, FLUENT 6.3 User's Guide, FLUENT Inc, Lebanon, NH, 2003.

Freitas C.J. and Street R.L., 1988, Non-Linear Transient Phenomena in a Complex Recirculating Flow - a Numerical Investigation, *International Journal for Numerical Methods in Fluids*, 8, 769-802.

Ishihara I., Fukui T. and Matsumoto R., 2002, Natural convection in a vertical rectangular enclosure with symmetrically localized heating and cooling zones, *International Journal of Heat Fluid Flow*, 23, 366-372.

Iwatsu R. and Hyun J.M., 1995, Three-dimensional Driven-Cavity Flows with a Vertical Temperature-Gradient, *International Journal of Heat and Mass Transfer*, 38, 3319-3328.

Khanafer K.M. and Chamkha A.J., 1999, Mixed convection flow in a lid-driven enclosure filled with a fluid-saturated porous medium, *International Journal of Heat and Mass Transfer*, 42, 2465-2481.

Leong J.C., Brown N.M. and Lai F.C., 2005, Mixed convection from an open cavity in a horizontal channel, *International Communications in Heat and Mass Transfer*, 32, 583-592.

Manca O., Nardini S., Khanafer K. and Vafai K., 2003, Effect of heated wall position on mixed convection in a channel with an open cavity, *Numerical Heat Transfer Part a-Applications*, 43, 259-282.

Manca O., Nardini S. and Vafai K., 2006, Experimental investigation of mixed convection in a channel with an open cavity, *Experimental Heat Transfer*, 19, 53-68.

Manca O., Nardini S. and Vafai K., 2008, Experimental investigation of opposing mixed convection in a channel with an open cavity below, *Experimental Heat Transfer*, 21, 99-114.

Mehrez Z., Bouterra M., El Cafsi A. and Belghith A., 2013, Heat transfer and entropy generation analysis of nanofluids flow in an open cavity, *Computers & Fluids*, 88, 363-373.

Mehrez Z., El Cafsi A., Belghith A. and Le Quéré P., 2015,The entropy generation analysis in the mixed convective assisting flow of Cu–water nanofluid in an

inclined open cavity, *Advanced Powder Technology*, 25, 1442-1451.

Moallemi M.K. and Jang K.S., 1992, Prandtl Number Effects on Laminar Mixed Convection Heat-Transfer in a Lid-Driven Cavity, *International Journal of Heat and Mass Transfer*, 35, 1881-1892.

Mohamad A.A. and Viskanta R., 1991, Transient Low Prandtl Number Fluid Convection in a Lid-Driven Cavity, *Numerical Heat Transfer Part A-Applications*, 19, 187-205.

Mohamad A.A. and Viskanta R., 1995, Flow and Heat-Transfer in a Lid-Driven Cavity Filled with a Stably Stratified Fluid, *Applied Mathematical Modelling*, 19, 465-472.

Muftuoglu A. and Bilgen E., 2008, Natural convection in an open square cavity with discrete heaters at their optimized positions, *International Journal of Thermal Sciences*, 47, 369-377.

Pallares J., Cuesta I., Grau F.X. and Giralt F., 1996, Natural convection in a cubical cavity heated from below at low Rayleigh numbers, *International Journal of Heat and Mass Transfer*, 39, 3233-3247.

Prasad A.K. and Koseff J.R., 1996, Combined forced and natural convection heat transfer in a deep lid driven cavity flow, *International Journal of Heat and Fluid Flow*, 17, 460-467.

Rahman M.M., Oztop H.F., Rahim N.A., Saidur R., Al-Salem K., Amin N., Mamun M.A.H. and Ahsan A., 2012, Computational analysis of mixed convection in a channel with a cavity heated from different sides, *International Communications in Heat and Mass Transfer*, 39, 78-84.

Selimefendigil F. and Yurddas A., 2012, Numerical Analysis of Mixed Convection Heat Transfer in Pulsating Flow for a Horizontal Channel with a Cavity Heated from Vertical Side and Below, *Heat Transfer Research*, 43, 509-525.

Sharif M.A.R., 2007, Laminar mixed convection in shallow inclined driven cavities with hot moving lid on top and cooled from bottom, *Applied Thermal Engineering*, 27, 1036-1042.

Sidik N.A.C., Jahanshaloo L. and Safdari A., 2014, The effect of mixed convection on particle laden flow analysis in a cavity using a Lattice Boltzmann method, *Computers & Mathematics with Applications*, 67, 52-61.

Stiriba Y., 2008, Analysis of the flow and heat transfer characteristics for assisting incompressible laminar flow past an open cavity, *International Communications in Heat and Mass Transfer*, 35, 901-907.

Stiriba Y., Ferre J.A. and Grau F.X., 2013, Heat transfer and fluid flow characteristics of laminar flow past an open cavity with heating from below, *International Communications in Heat and Mass Transfer*, 43, 8-15.

Stiriba Y., Grau F.X., Ferre J.A. and Vernet A., 2010, A numerical study of three-dimensional laminar mixed convection past an open cavity, *International Journal of Heat and Mass Transfer*, 53, 4797-4808.

Timuralp C., 2015, Investigation of the two and three dimensional heat transfer and fluid flow in a channel with an open cavity, Ph. D Thesis, Eskisehir Osmangazi University, Eskisehir, Turkey.

AN INDUSTRIAL VAPOR ABSORPTION AIR CONDITIONING APPLICATION

Nazım KURTULMUŞ* and İlhami HORUZ**

*Adana Science and Technology University, Faculty of Engineering and Natural Science, Mech. Eng. Dept., 01180, Adana, nkurtulmus@adanabtu.edu.tr
** Gazi University, Engineering Faculty, Mech. Eng. Dept., 06570, Ankara, ilhamihoruz@gazi.edu.tr

Abstract: In this study, the application of VAR system to an industrial company is investigated. For this purpose, the company which requires an air-conditioning system to its office building was chosen. After determining this company had an industrial furnace, this research aimed to design the VAR system utilizing waste heat from this furnace flue gases to air-condition the office building. Firstly, the physical properties and heat quantity of the flue gases were determined and the cooling load of the office building was calculated. It was found out that the flue gases had enough heat capacity to drive the VAR system. Next, single effect VAR system was introduced and the thermodynamic, energy and exergy analysis were made. The COP of the VAR system is calculated to be 0.64 and the highest exergy destruction was obtained at the generator which is 37.19kW. Finally, the application of the VAR system to this industrial company was analyzed in detail. The capital, maintaining and operating costs of the VAR system were analyzed and compared with alternative systems.
Keywords: Absorption, Water-Lithium bromide solution, Vapor Absorption Refrigeration.

ABSORPSİYONLU SOĞUTMA SİSTEMİNİN SANAYİYE UYGULANMASI

 Özet: Bu çalışmada, Absorpsiyonlu Soğutma (ABS) sistemin bir sanayi firmasına uygulanması incelenmiştir. Bu amaçla, ofis binasında bir klima sistemi ihtiyacı olan bir firma seçilmiştir. Firmada bir endüstriyel fırın bulunduğu belirlendikten sonra, ofis binasının klimalandırılması amacıyla bu endüstriyel fırının baca gazındaki atık ısı ile tahrik olan ABS sisteminin tasarlanması araştırılmıştır. Başlangıç olarak, baca gazının fiziksel özellikleri ve içerdiği atık ısı miktarı tespit edilmiş ve aynı zamanda ofis binasının soğutma yükü hesaplanmıştır. Baca gazının ABS sistemini tahrik edebilecek miktarda atık ısıya sahip olduğu bulunmuştur. Daha sonra, tek kademeli ABS sistemi izah edilmiş ve termodinamik enerji ve ekserji analizleri yapılmıştır. ABS sisteminin Soğutma Tesir Katsayısı (STK) 0.64 olarak hesaplanmış ve en büyük ekserji yıkımının 37.19 kW ile kaynatıcıda meydana geldiği saptanmıştır. Son olarak, ABS sisteminin bu sanayi firmasına uygulanması detaylı bir şekilde analiz edilmiştir. ABS sisteminin yatırım, işletme ve bakım maliyetleri araştırılmış, alternatif sistemler ile karşılaştırılmıştır.
Anahtar Kelimler: Absorpsiyon, Su-Lityum bromür eriyiği, Absorpsiyonlu Soğutma Sistemi.

NOMENCLATURE

a	Characteristic dimension associated with time of spreading [m]	i	Interest rate
		k	Thermal conductivity of tube material, solution thermal conductivity [W/m K]
A	Surface area [m^2]	l	Estimated distance that a drop of solution spreads on the tube [m]
c_p	Specific heat [kJ/kg ºC]		
COP	Coefficient of performance	L	The unwrapped length of the tube length [= $\pi d_o/2$] [m]
d	Diameter [m]		
E	Energy [kW]	m	Mass flow rate [kg/s]
EA	Equivalent annual value	n	The number of sites at which droplets form; time period; efficiency
EAC	Equivalent annual cost		
Ex	Exergy [kW]	Nu	Nusselt number [=$h \cdot d_h/k$]
F	Dry area coefficient	P	Pressure [kPa], present cost
ex	Specific exergy [kJ/kg]	Pr	Prandtl number [$\mu \cdot c_p/k$]
f	Flow ratio	q	Thermal load [kJ/kg]
g	Gravitational acceleration [m/s^2]	Q	Heat transfer [kW]
h	Enthalpy[kJ/kg], heat transfer coefficient [W/m^{2}K]	r	Radius of the tube [m]
		Re	Reynolds number
h*	Modified latent heat of vaporization [kJ/kg]	s	Fin pitch, entropy [kJ/kg K]

t	Thickness [m]
T	Temperature [ºC]
ΔT	Logarithmic temperature difference [ºC]
U	Overall heat transfer coefficient [W/m^2 K]
W	Power [kW]
X	Lithium bromide concentration

Greek symbols

ε	Effectiveness
η	Exergy efficiency
θ	Contact angle at the solution tube interface
μ	Dynamic viscosity [Pa s]
ρ	Density [kg/m^3]
σ	Solution surface tension [N/m]
ϑ	Specific volume of solution [m^3/kg]

Subscripts

AB	Absorber
b	Nucleate boiling
c	Initial cost, convective
ch	Chemical
ci	Cold fluid inlet
co	Cold fluid outlet
conv	Convection
cond	Conduction
CO	Condenser
d	Developing region
dest	Destruction
e	Equivalent
eff	Effective
est	Estimation
EV	Evaporator
f	Fouling, fin
fg	The difference between saturated vapor and liquid
GE	Generator
hi	Hot fluid inlet
ho	Hot fluid outlet
horiz	Horizontal
k	Component
l	Liquid
m	Mean
o	Outer
p	Pump
r	Refrigerant
ref	Reference environment
rtv	Refrigerant throttle valve
sat	Saturation
s	Solution
SHE	Solution heat exchanger
tot	Total
VAR	Vapor Absorption Refrigeration
VCR	Vapor compression system
VRF	Variable refrigerant flow
v	Vapor
w	Wall, wet area
1,2…	State points
0	Reference environment state

INTRODUCTION

Because of the limited fossil fuel sources, ever-increasing energy costs and global warming, people, especially engineers, have to concentrate on both the improvements of the efficiency of the existing systems and the utilization of the waste heat, as well as searching for new energy sources. However, energy consumption of developing counties where the economy and industry grows rapidly increases rapidly. It is claimed that the crude oil and natural gas sources will depleted in next 50 years. As far as the air conditioning and refrigeration are concerned, buildings use quite a lot of energy. The main reason for this is the air conditioning and refrigeration systems mainly use Vapor Compression Refrigeration (VCR) Systems and compressing vapor consumes really a big amount of energy. In cooling season, the consuming electrical energy can reach peak and the brownout situations can be encountered. It is reported that %15 of the generated electricity in whole world is consumed by mostly these systems. For whole buildings, it is estimated that %45 of the consumption is for air-conditioning purposes. The electrical energy consuming by VCR systems is mostly produced by using fossil fuels leads to depletion the fossil fuel sources. Another effect is that the releasing gas during production the electrical energy causes to increase the amount of greenhouse gas emissions. Furthermore, some of the refrigerants using by VCR system as working fluid such as CFCs, HCFC and HFCs which Montreal and Kyoto Protocol limits to use contributes to ozone layer depletion (Choudhury et al.,2010; Kalkan et al., 2012). Utilizing waste heat from industrial process is an effective way in respect of energy efficiency, economy and environment in order to reach sustainable development. As far as the utilization of the waste heat is concerned, Vapor Absorption Refrigeration (VAR) Systems which are devices with the unique capability of producing cold water/air by using the heat sources comes front such as tri-generation applications (Law et al.,2013; Chen et al.,2014). Economical and energy savings by applying VAR systems driven by heat in exhaust gas from industrial process was investigated also. Garimella (2012) investigated the low-grade waste heat recovery for chilled and hot water generation. Heat from waste gas from an industrial process which temperature is 120ºC is supplied to drive the system. They found that annual savings can be achieved up to $1.2 million in such an application. Balaji and Ramkumar (2012) studied the waste heat recovery from steam turbine exhaust for vapor absorption system in sugar industry.

The VAR system performance has been investigated by many researchers. The effect of operating parameters on the system performance for single effect VAR system was investigated. It was found that the solution heat exchanger (SHE) had more effects on the investigated parameters than the refrigerant heat exchanger (RHE)

(Kaynakli and Kilic, 2007). Kilic and Kaynakli (2007) investigated the second law-based thermodynamic analysis of water-lithium bromide VAR system. They analyzed the effect of the temperatures of main system components on the system performance, the irreversibilities in the thermal process and the exergy loss of each component. They found that the increasing heat source temperature is dominant on the exergetic efficiency. The exergy analysis of a single effect VAR system using water-lithium bromide solution is made (Şencan and Yakut, 2005). According to the researcher, the condenser and evaporator has less exergy loss than the generator and absorber because of the heat of mixing in the solution. Kaynakli et al. (2015) investigated the energy and exergy analysis of a double effect VAR system based on different heat sources. Their system used water/lithium bromide as working fluid pair and the refrigeration system run on various heat sources such as hot water, hot air and steam. They concluded that the exergy destruction was maximized when hot air heat source was used and minimized by utilizing hot water heat source.

As can be seen from the literature, the related papers just focused on energy savings by applying VAR systems, but not tried to find the effective way to meet the demands and use energy efficiently. On the other hand, this paper aims to investigate the utilization of the waste heat from an industrial company by using the VAR system for air conditioning purposes and comparing VAR systems with alternative air conditioning systems. Additionally, almost all of the researchers use hot water or steam to drive VAR system while making exergy analysis. Unlike the literature, the exergy analysis for the applied VAR system is applied to show exergy destructions parameters for flue gas fired VAR system in detail.

VAPOR ABSORPTION REFRIGERATION (VAR) SYSTEMS

The VAR system which is quite similar to the vapor compression refrigeration system includes a thermal compressor which consists of an absorber and a generator, instead of a conventional compressor which requires a lot of mechanical energy input. There is no need for the compressor and its compression and maintenance costs in VAR systems. Heat input is enough to operate VAR system except for the small amount of mechanical energy input to the liquid pump. This allows VAR system to be used in utilizing the waste heat and also the solar and geothermal energy (Horuz, 1998).VAR system, shown schematically in Fig. 1, operates in a cycle. The VAR system basically consists of an evaporator, a condenser, a generator, an absorber and a solution heat exchanger. The generator is driven by a heat source, the evaporator takes heat to provide refrigeration and the condenser and absorber release heat to the medium (generally to the ambient air).

The VAR cycle uses a refrigerant-absorbent solution rather than pure refrigerant as the working fluid. The absorbent acts as a secondary fluid to absorb the primary fluid which is refrigerant. This study will concentrate on the VAR system using water-lithium bromide (LiBr) solutions where water is refrigerant and water-lithium bromide is absorbent. The refrigerant-absorbent solution passing through the solution pump is referred to as a weak solution, being relatively weak in LiBr. The solution returning from the generator to the absorber contains only a little more LiBr compared to the solution being pumped from the absorber to the generator and is therefore referred to as rich solution (see Fig.1).
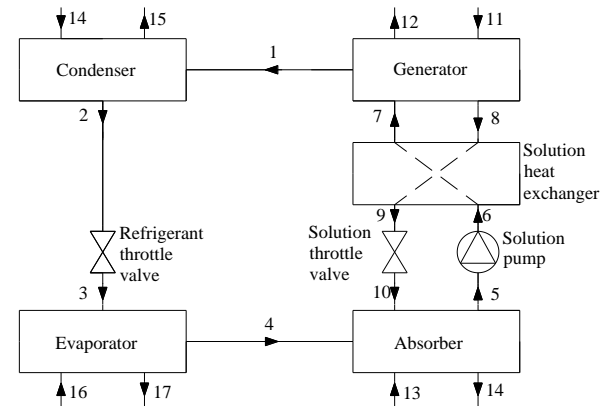
Figure 1. The schematics of the VAR system

The generator, absorber, evaporator, condenser and solution heat exchanger are designed by using heat and mass transfer calculations. The heat transfer capacity of the main components of VAR system is calculated by as follows (Genceli, 1999);

$$\dot{Q} = U \cdot A \cdot \Delta T_m \qquad (1)$$

The overall heat transfer coefficient can be determined as shown below;

$$\frac{1}{U \cdot A} = \sum R_{conv} + \sum R_f + \sum R_{cond} \qquad (2)$$

where thermal resistance is represented by R.

$$\Delta T_m = \frac{\Delta T_1 - \Delta T_2}{\ln(\frac{\Delta T_1}{\Delta T_2})} \qquad (3)$$

where;

$$\Delta T_1 = T_{ho} - T_{ci} \qquad (4)$$

$$\Delta T_2 = T_{hi} - T_{co} \qquad (5)$$

The following assumptions have been made in order to develop the mathematical models for the VAR system analysis (Kilic and Kaynakli, 2007; Şencan and Yakut, 2005; Kaynakli et al., 2015; Dinçer and Rozen, 2007):
1. The temperatures of the VAR system components are constant.
2. Refrigerant leaving the condenser is saturated water at condenser pressure and refrigerant leaving the evaporator is saturated vapor at evaporator pressure.

3. The generator and condenser pressure are equal to the pressure corresponding the refrigerant saturation pressure at the condenser temperature and the evaporator and absorber pressure are equal to the pressure corresponding the refrigerant saturation pressure at the evaporator.
4. The temperature and pressure of superheated vapor leaving the generator is equal to the temperature and pressure of the generator.
5. All the system components are at steady state conditions.
6. Pressure drop in the heat exchangers and piping systems and heat loses and gains in various components and piping system are negligible.
7. Reference environment temperature and pressure are taken as 25ºC and 101.325kPa, respectively. The reference environment enthalpy and entropy used for calculating the exergy of the working fluid are the values for water at an environment temperature and pressure of 25ºC and 101.325kPa, respectively.
8. The kinetic, chemical and potential exergy of all streams at the VAR system are neglected. Chemical exergy of flue gases is considered.
9. The solution pump efficiency is taken as 0.9.

The thermodynamic analysis of an absorption system involves the application of principles of mass conservation, energy and exergy analysis to individual components of the system. The exergy analysis method provides us exergy destruction and exergy efficiency which is an important thermodynamic property. The exergy is represented by "ex" which is defined as the maximum work potential of a matter or a form of energy with respect to its reference environment (Kilic and Kaynakli, 2007).

Mass balance equations are as follows:

$$\dot{m}_7 = \dot{m}_1 + \dot{m}_8 \tag{6}$$

$$\dot{m}_7 \cdot X_7 = \dot{m}_8 \cdot X_8 \tag{7}$$

General energy and exergy balance equations are as follows (Dinçer and Rozen, 2007):

$$E_{in} = E_{out} \tag{8}$$

$$\dot{Ex}_{in} - \dot{Ex}_{out} = \dot{Ex}_{dest} \tag{9}$$

$$\dot{Ex} = \dot{m} \cdot (ex + ex_{ch}) \tag{10}$$

$$ex = h - h_0 - T_0(s - s_0) \tag{11}$$

$$f = \frac{\dot{m}_s}{\dot{m}_r} = \frac{X_7}{X_8 - X_7} \tag{12}$$

Heat capacity and the exergy destructions obtained from exergy balances of each components of VAR system illustrated in Fig. 1 can be expressed as follows:

Condenser:

$$q_{CO} = \frac{\dot{Q}_{CO}}{\dot{m}_1} = h_2 - h_1 \tag{13}$$

$$\dot{Ex}_{dest} = \dot{m}_1 \cdot (ex_1 - ex_2) + \dot{m}_{14} \cdot (ex_{14} - ex_{15}) \tag{14}$$

Evaporator:

$$q_{EV} = \frac{\dot{Q}_{EV}}{\dot{m}_1} = h_4 - h_3 \tag{15}$$

$$\dot{Ex}_{dest} = \dot{m}_3 \cdot (ex_3 - ex_4) + \dot{m}_{16} \cdot (ex_{16} - ex_{17}) \tag{16}$$

Generator:

$$q_{GE} = \frac{\dot{Q}_{GE}}{\dot{m}_1} = h_1 + f \cdot h_8 - (f + 1) \cdot h_7 \tag{17}$$

$$\dot{Ex}_{dest} = \dot{m}_{11} \cdot (ex_{11} - ex_{12}) + \dot{m}_7 \cdot ex_7 - \dot{m}_8 \cdot ex_8 - \dot{m}_1 \cdot ex_1 \tag{18}$$

Absorber:

$$q_{AB} = \frac{\dot{Q}_{AB}}{\dot{m}_1} = (f + 1) \cdot h_5 - h_4 - f \cdot h_{10} \tag{19}$$

$$\dot{Ex}_{dest} = \dot{m}_{14} \cdot (ex_{13} - ex_{14}) + \dot{m}_4 \cdot ex_4 + \dot{m}_{10} \cdot ex_{10} - \dot{m}_5 \cdot ex_5 \tag{20}$$

Solution heat exchanger:

$$q_{she} = \frac{\dot{Q}_{she}}{\dot{m}_1} = f \cdot (h_8 - h_9) = (f + 1) \cdot (h_7 - h_6) \tag{21}$$

$$\dot{Ex}_{dest} = \dot{m}_8 \cdot (ex_8 - ex_9) + \dot{m}_5 \cdot (ex_6 - ex_7) \tag{22}$$

Throttle valve between evaporator and condenser:

$$\dot{Ex}_{dest} = \dot{m}_1 \cdot T_0 \cdot (s_3 - s_2) \tag{23}$$

Solution pump:

$$\dot{W}_p = \dot{m}_5 \cdot (h_6 + h_5) = \frac{\dot{m}_5 \cdot v_s (P_{CO} - P_{EV})}{\eta_p} \tag{24}$$

$$\dot{Ex}_{dest} = \dot{m}_5 \cdot (ex_5 - ex_6) + \dot{W}_p \tag{25}$$

Total exergy destruction can be expressed follows (Dinçer and Rozen, 2007):

$$\dot{Ex}_{dest,tot} = \sum_{j=1}^{N} Ex_{dest,j} \tag{26}$$

where; N is the number of VAR system components and j is jth component.

The exergy efficiency can be expressed as (Dinçer and Rozen, 2007):

$$\eta = \frac{Ex_{16} - Ex_{17}}{Ex_{11} - Ex_{12} + W_p} \tag{27}$$

The coefficient of performance (COP) is a measure of a cycle's ability to transfer heat between various temperature levels (Horuz, 1998)

$$COP_{VAR} = \frac{\dot{Q}_{EV}}{\dot{Q}_{GE} + W_p} \tag{28}$$

Table 1. Assumptions and calculated values of the VAR system

States	Substance	T(ºC)	X(%)	$\dot{m}$ (kg/s)	h(kJ/kg)	s(kJ/kgK)
1	Superheated vapor	90	-	0.0384	2668.27	8.536
2	Saturated water	40	-	0.0384	167.50	0.572
3	Water-vapor	4	-	0.0384	167.50	0.604
4	Saturated vapor	4	-	0.0384	2507.87	9.05
5	Water-LiBr	40	58.43	0.6517	107.80	0.237
6	Water-LiBr	40	58.43	0.6517	107.80	0.237
7	Water-LiBr	61.8	58.43	0.6517	150.86	0.367
8	Water-LiBr	90	62.09	0.6132	221.21	0.494
9	Water-LiBr	65.54	62.09	0.6232	175.45	0.365
10	Water-LiBr	-	62.09	0.6232	-	-
11	Flue gases	270	-	3.1887	-622.02	7.686
12	Flue gases	230.7	-	3.1887	-665.91	7.602
13	Water	29.63	-	7.4661	124.21	0.431
14	Water	33.91	-	7.4661	142.14	0.490
15	Water	37	-	7.4661	155.04	0.531
16	Water	12	-	4.2971	50.45	0.180
17	Water	7	-	4.2971	29.51	0.106

AN INDUSTRIAL APPLICATION

The aim of this section is to apply VAR system to produce chilled water that will be sent to the office building fan coil system by utilizing flue gases from an industrial furnace of an industrial company. Flue gases produced by the natural gas fired industrial furnace is normally not being utilized in this company. The flue gases volume flow rate was measured to be 5.029 m^3/s at 270ºC. To determine the substances in the flue gas, measurements were carried out. It was determined that the flue gas contains 6% H_2O, 2.74% CO_2, and 16.2% O_2. The remaining amount of flue gas content was assumed to be N_2. Normally, the office building does not have any air conditioning system and the company needs their office building to be air conditioned. The office building's comfort cooling load is calculated to be 85 kW. This section aims to investigate an application of the air conditioning system which includes the VAR and fan coil systems. So the necessity of comfort cooling will be met by utilizing the currently available waste heat. In order to do this, the application of the system is analyzed and designed.

The Energy And Exergy Analysis of The Industrial Application

In order to utilize the waste heat at the industrial company, the VAR system's parameters to be applied are needed to be determined. Firstly, the decision is made about which solution will be used. When the manufacturer catalogs of absorption chillers are analyzed, it can be seen that almost all the manufacturers use water-LiBr solution but only a few of them use ammonia-water solution. Additionally it is known that the COP performance of water-LiBr solution is better than the ammonia-water solution. Both have

disadvantages and advantages. The VAR system with water-lithium bromide solutions has higher performance than the VAR system using ammonia-water system. While the VAR system with the water-lithium bromide solution is suitable for air-conditioning applications, the VAR system with the ammonia-water solution is suitable for industrial applications requiring low evaporating temperatures in evaporator. It should be considered that the VAR system using water-LiBr has crystallization risk and limitations on operating in very low temperatures because of water as being the refrigerant (Horuz, 1998). For the reasons mentioned above the VAR system using water-LiBr solution is used to air condition the office building.

The assumptions and calculated values for the VAR system to be applied were summarized in Table 1. Entropy values of the solution are obtained from Kaita (2001).

Table 2. The calculated data of the VAR system

Descriptions	Unit	System
Q_{AB}	kW	133.78
Q_{CO}	kW	96.16
Q_{GE}	kW	139.95
Q_{EV}	kW	90
$Q_{she.}$	kW	28.06
W_P	kW	0.0028
COP_{VAR}		0.64
$Ex_{dest,AB}$	kW	6.35
$Ex_{dest,CO}$	kW	1.59
$Ex_{dest,GE}$	kW	37.19
$Ex_{dest,EV}$	kW	1.89
$Ex_{dest,she}$	kW	1.63
$Ex_{dest,p}$	kW	0.0025
$Ex_{dest,rtv}$	kW	0.37
$Ex_{dest,tot}$	kW	49.04
η_{VAR}		0.082

As it can be seen from Table 2, the COP of the VAR system is 0.64 and exergy efficiency is 8.2%. Because of the large heat capacity and the temperature differences between streams, the generator has the highest exergy destruction. The next biggest exergy destruction occurred at the absorber. The pump has the lowest exergy destruction. Other components exergy destruction values are quite close. Because the exergy destruction value of the generator has the highest value in the total exergy destruction, the special attention is given to decrease it. Fig 2-7 are prepared by the values shown at Table 1.
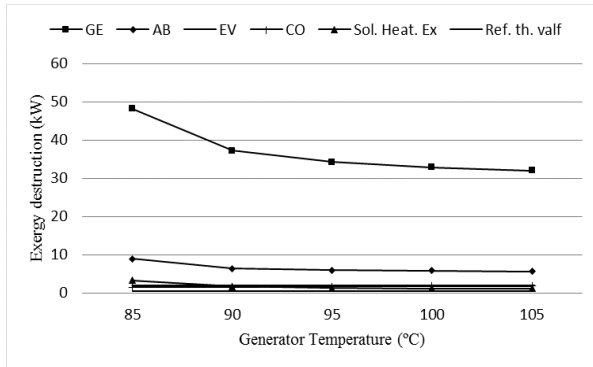

Figure 2. The exergy destruction at the components of VAR system with increasing generator temperature

Fig. 2 shows the variations of exergy destruction of VAR system components against increasing generator temperature. The generator which has the highest exergy destruction and the absorber which has the second highest exergy destruction values decreases with increasing generator temperature. The slope of decrease of the exergy destruction of the generator sharply decreases at 90ºC. The highest exergy destruction value at the generator is 48.16 kW at 85ºC, the lowest exergy destruction value at the generator is 32.06 kW at 105ºC. The same trend is also valid for the absorber. The highest exergy destruction value at the absorber is 8.92 kW at 85ºC, the lowest exergy destruction value at the absorber is 5.65 kW at 105ºC. The other components of VAR system doesn't effects the exergy efficiency and exergy destruction compared to the generator and absorber because of the lower exergy destruction.
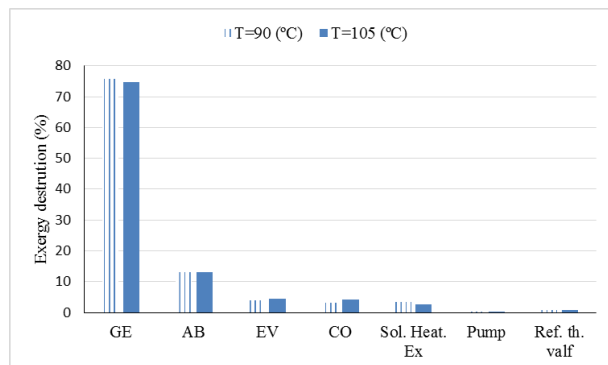

Figure 3. The relative exergy destructions of the components of the VAR system

As seen at Fig. 3 the relative exergy destruction at the generator decreases from 75.83% at $T_{GE}=90$ºC to 74.65% at $T_{GE}=105$ºC. The relative exergy destruction at absorber increases from 12.95% at $T_{GE}=90$ºC to 13.95% at $T_{GE}=105$ºC. When relative exergy destruction at the condenser and evaporator having close values to each other is approximately 3.5% at $T_{GE}=90$ºC, it reaches approximately 4.3% at $T_{GE}=105$ºC. When the solution heat exchanger has 3.33% relative exergy destruction at $T_{GE}=90$ºC, it has 2.67% relative exergy destruction at $T_{GE}=105$ºC. Refrigerant throttle valve has second lowest value like 0.86% at $T_{GE}=105$ºC. And the pump has relatively very low exergy destruction and it can be neglected. The bigger temperature difference between the source and the generator causes the higher relative exergy destruction at the generator. When the generator temperature increases, the relative exergy destruction at the generator decreases because the streams temperature differences and the heat capacity decreases so relative exergy destruction decreases. The mixing of the rich solution coming from the heat exchanger and refrigerant from the evaporator at different temperature at the absorber causes the second highest relative exergy destruction. As increasing the generator temperature, the temperature of rich solution coming from the heat exchanger increases so the temperature difference at the mixing process increases. This causes an increase on relative exergy destruction at the absorber.
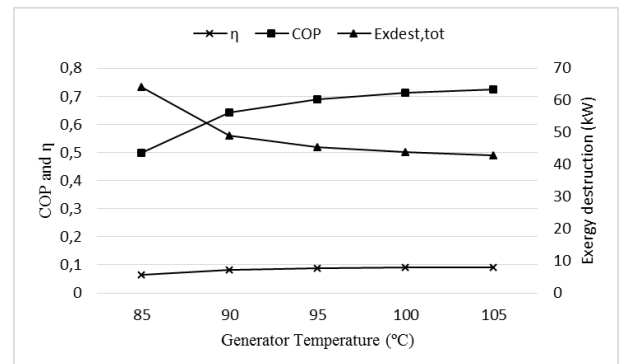
Figure 4. The COP, η and exergy destruction changes with increasing generator temperature

Fig.4 shows the changes of COP, exergy efficiency and exergy destruction versus the generator temperature. It can be observed that COP increases with increasing generator temperature. While the value of COP is 0.49 at $T_{GE}=85$ºC, it reaches to 0.72 at $T_{GE}=105$ºC. The exergy efficiency of VAR system increases with increasing generator temperature. While the value of exergy efficiency is 0.064 at $T_{GE}=85$ºC, it reaches to 0.091 at $T_{GE}=105$ºC. And also it is observed that the total exergy destruction decreases with increasing generator temperature.

Table 3. The VAR system components design parameters

Descriptions	Condenser	Evaporator	Absorber	Generator
Inside of the tube diameter(mm)	17.5	9.55	17.55	17.08
Outside of the tube diameter(mm)	19.05	12.5	19.05	21.3
Horizontal tube number	11	16	10	
Vertical tube number	-	20	19	
Tubes array	-	2x8x20	10x19	3x23
Total number of tubes	104	320	190	69
Tubes length(mm)	2200	1510	1504	1000
Number of pass	2	4	2	1
Pressure(kPa)	7.38	0.81	0.81	7.38
Temperature (ºC)	40	4	40	90
Number of fins	-	-	-	251
Fin height(mm)	-	-	-	10
Fin thickness(mm)	-	-	-	0.5
Fins area(m^2)	-	-	-	46.74
U(W/m^{2}K)	1622.09	952.44	604.5	17.12
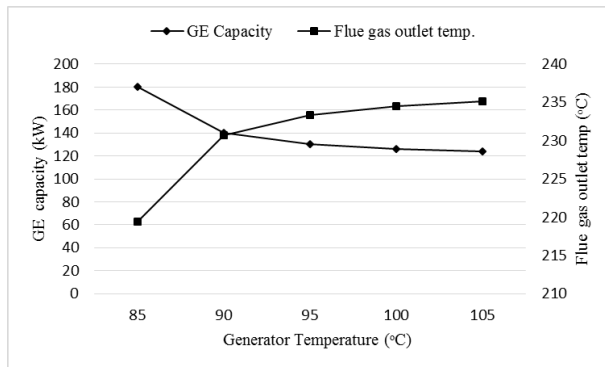
Figure 5. The generator capacity and flue gas outlet temperature variations with increasing generator temperature

Fig. 5 shows us the changes of the flue gas outlet temperature and the generator temperature with increasing the generator temperature. Initially, the generator capacity of the VAR system tends to decrease with increasing generator temperature. It varies between 124 and 180 kW. While the highest capacity of the generator of the VAR system is 180 kW at 85ºC, the lowest capacity of the generator of the VAR system is 124 kW at 105ºC. Also the slope of decrease of the capacity of the generator sharply decreases at 90ºC. The flue gas outlet temperature tends to increase with increasing generator temperature. It varies between 219.36 and 235.18ºC. While the highest flue gas outlet temperature is 235.18ºC for generator temperature at 105ºC, the lowest flue gas outlet temperature is 219.36ºC for generator temperature at 85ºC. The reason of both decrease the generator capacity and increase of the flue gas outlet temperature is the increasing COP of VAR system. This reason shows that the potential energy utilization of waste heat increases with increasing generator temperature.

Fig. 6 shows the changes of total exergy destruction and exergy efficiency with the difference between flue gas inlet temperature and generator temperature which is an important parameter. Total exergy destruction tends to increase with an increase in difference between flue gas inlet temperature and generator temperature. While the highest exergy destruction of the VAR system is 64.07 kW at 185ºC, the lowest exergy destruction of the VAR system is 42.95 kW at 165ºC. The slope of the exergy destruction curve sharply increases when the difference between flue gas inlet temperature and generator temperature reaches at 180ºC. Exergy efficiency of the VAR system tends to decrease with an increase in the difference between flue gas inlet temperature and generator temperature. While the highest exergy efficiency of the VAR system is 0.092 at 165ºC, the lowest exergy efficiency of the VAR system is 0.064 at 185ºC. These changes of total exergy destruction and exergy efficiency show how important parameter the difference between flue gas inlet temperature and generator is.
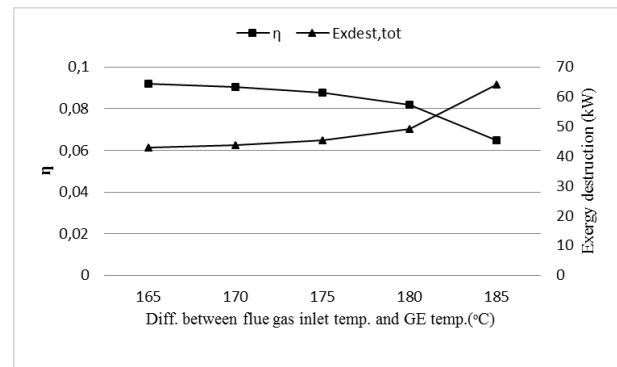
Figure 6. The effect of the difference between flue gas inlet temperature and generator temperature

Fig. 7 shows the exergy efficiency changes with increasing reference environmental temperature. It can be seen that the exergy efficiency increases with increasing reference environment temperature. For T_{GE}=90ºC, the exergy efficiency increases from 0.082 at T_{ref}=25 ºC to 0.122 at T_{ref}=32ºC. And for T_{GE}=105 ºC, the exergy efficiency increases from 0.091 at T_{ref}=25 ºC to 0.137 at T_{ref}=32 ºC. The results at Fig. 7 shows that potential energy to utilize decreases with increasing reference environment temperature and shows that the potential

energy is used better at T_{GE}=105ºC comparing to T_{GE}=90ºC.
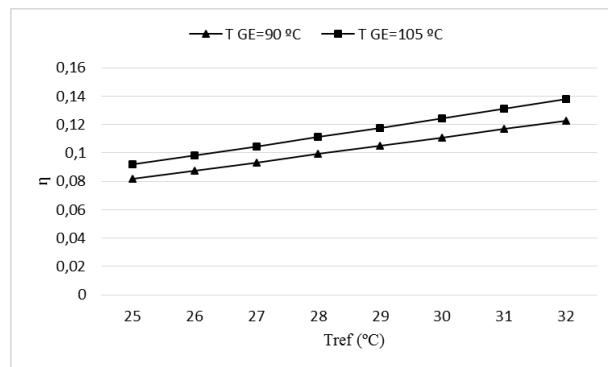
Figure 7. The variation of exergy efficiency with increasing Reference environmental temperature

The VAR System Components Design and Construction

This section aims to show how the VAR system components are designed and constructed. It is expected that the equations at the Appendix and detailed knowledge presented at this section could be a guide for researchers and engineers. To design the components of the VAR system, the equations used to calculate heat and mass transfer coefficient can be found at Appendix (Genceli, 1999; Florides et al.,2003; Seewald and Blanco,1994; Davies and Rideal,1961; Thome, 2009; Cosenza and Vliet, 1990; Lorenz and Yung, 1979; Li et al., 2011; Ribatski and Thome, 2007; Çengel,2002; Wang et al., 2012). All of the VAR system components design parameters are shown at Table 3.

Absorber is chosen to be a shell and tube heat exchanger. In the absorber, the LiBr solution is dripped over the horizontal tubes cooled by water flowing inside by using dripping tray. It drags and absorbs the water vapor coming from the evaporator and flows in a thin film around tubes. And then it is collected at the bottom of the lower shell. The absorber also has feedback system. When the water vapor isn't absorbed by rich solution, a feedback pump start to work and pumps the solution to the dripping tray. So, the more solution drips the more water vapor is dragged and absorbed. When the water vapor is absorbed completely, the solution pump pumps the solution to the solution heat exchanger. These two pumps located at the bottom of the shell are controlled by the control systems. The tubes in the absorber must be resistible to corrosion since water-LiBr solution has corrosion effect. So, CuNi10 is preferred as the tubes material in the absorber. And also the parts of shell which water-LiBr solution contacts with is preferred 316 L stainless steel as the shell material. To design the absorber, the equations used to calculate heat and mass transfer coefficient can be found in Appendix. The thermophysical properties water-LiBr solution was obtained from Florides et al. (2003). Mass transfer must also be considered. A practical model for absorption of vapors into a laminar film of water and LiBr falling along a constant temperature vertical plate

was described. The details of mass transfer coefficient calculation can be found from Florides et al. (2003).

Evaporator is also chosen to be shell and tube heat exchanger. Absorber tubes and evaporator tubes positioned to the same shell. In the evaporator, the saturated water coming from the condenser is dripped over the horizontal tubes. When it flows in a thin film around tubes, it evaporates by rejecting heat from the water flowing inside. Falling film evaporators have dry area problem. When the fluid flows in a thin film around the tubes, the tubes area may not be get wet by the fluid completely. Because of that the heat transfer coefficient may decreases sharply. The refrigerant that couldn't evaporate is collected in the bottom of the lower shell because of the dry area problem. The evaporator also has a feedback system. When the refrigerant accumulates at the bottom of lower shell enough, a feedback pump start to work and pumps the refrigerant to the dripping tray. So, more refrigerant drips and less dry area may occur. When the water evaporates completely, the feedback pump stops. The feedback pump located at the bottom of the shell is controlled by the control systems. Copper is used as tubes material.

Condenser is a water cooled shell and tube heat exchanger. In the condenser, the water vapor coming from generator is condensing over the horizontal tubes cooled by water flowing inside. The cooling water will enter the condenser after it exits from the absorber. Copper is used as tubes material.

In the generator, when the water-LiBr solution flows inside the vertical tubes, the flue gas flows outside the vertical tubes. The tubes are mounted between bottom reservoir and top reservoir. The bottom reservoir is used for collecting the water-LiBr solution coming from the solution heat exchanger and for providing the distribution to tubes properly. The top reservoir is used to send the removed water vapor from the water-LiBr solution to the condenser and to send the water-LiBr solution to the solution heat exchanger. And by mounting the fins to the tubes heat transfer area is increased, so more compact construction is obtained. To protect the corrosion effect of the water-LiBr solution, 316 L stainless steel is used as the generator's tubes material. And the fin's material is selected to be aluminum. The inside heat transfer coefficient is so high relative to the outside heat transfer coefficient because of the boiling, so it is not necessary to calculate it.

When designing the solution heat exchanger, the double-pipe heat exchanger is used. To overcome the corrosion effect of the water-LiBr solution, 316 L stainless steel is used as material. When the solution heat exchanger is designed ε-NTU method was used (Çengel, 2002). The overall heat transfer coefficient is found to be 490 W/m^{2}K.

	P_c (Euro)	EA_c (Euro)	Annual operation cost (Euro)	EAC (Euro)
The fan coil system and the VAR system to be manufactured (1)	49300	5790	233	6023
The fan coil system and the VAR system to be bought (2)	80200	9420	361	9781
The fan coil system and the VCR system to be bought (3)	36300	4269	3108	7377
VRF air conditioning system to be bought (4)	22507	2643	1245	3888

COST ANALYSIS

This section aims to investigate and compare the cost analysis of the system which includes (1) the VAR system to be manufactured and the fan-coil system, (2) the VAR system to be bought and fan-coil system, (3) the vapor compression chiller to be bought and fan-coil system and (4) the Variable Refrigerant Flow (VRF) air conditioning system. During the cost analysis, life cycle cost technique which includes all cost factors as initial cost, operating and maintenance costs. To apply this technique, equivalent annual method is chosen. At this method all the costs taking place over a period are converted to an equivalent uniform yearly amount. The equations below are being used (Elsafty and Al-Daini, 2002). The cost analysis parameters are shown at Table 4. In the cost analysis, it is assumed that the air conditioning systems work 10 hours a day for 120 days which refers to cooling season under full load.

$$EA_c = P_c \frac{(1+i)^n \cdot i}{(1+i)^n - 1} \tag{29}$$

$$EAC = EA_c + \text{annual operating cost} \tag{30}$$

Assumptions are i: 10%, n: 20 year, Electric price: 0.0576 Euro/kWh.

To make the cost analysis, the VAR system to be bought has been chosen to be the single effect hot water driven VAR system because the commercial flue gas fired VAR system which provides the desired cooling capacity is not available in the market on this size. So, the hot water will be obtained by using the heat exchanger mounted to the chimney and run the hot water driven VAR system. The VAR system model HWAR-L 30HH is chosen from World Energy Absorption Chillers Europe Ltd. The VCR system to be bought has been chosen to be air cooled chiller. The VCR system is domestic production by Frigotek and the model is FMC-36. VRF air-conditioning system to be bought is chosen from Samsung. The model of outer unit of VRF air conditioning system is AM260FXVAGH and the inner units of VRF air conditioning system is chosen appropriately from Neo Forte type. The fan coil system has been chosen from domestic productions called Untes. Additionally, the VAR system is planned to be manufactured in Turkey.

As can be seen from the cost analysis, the initial cost of the fan coil system and the VAR system to be manufactured (1) is lower than the initial cost of the fan coil system and the VAR system to be bought (2) because it (2) is not manufactured in Turkey. The system (1) has the lowest operation cost and is third as far as the initial cost is concerned. The system (2) which has the highest initial cost compared with the other systems has quite low operation costs compared to the systems (3) and (4) but not as low as the system (1). The system (3) which has the highest operation cost compared to the other systems has lower initial cost than the systems including the VAR systems. The system (4) which has lowest initial cost compared with the other systems has quite high operation and maintenance costs compared to the systems (1) and (2). Because of the fan coil units and piping system costs, the system (3) has higher initial costs than the system (4). Although the system (1) does not seem to be the most advantageous system, it comes front by utilizing the waste heat and by decreasing the operation costs.

CONCLUSIONS

This study aims to present the investigation of utilization of the waste heat from the chosen industrial company by using VAR systems including energy and exergy analysis and comparing VAR systems with alternative systems.

It is obtained that the flue gas fired VAR system's COP is 64%, and exergy efficiency is 8.2%. The parameters that effect the VAR system are investigated. The COP of the VAR system increases with increasing generator temperature. It increases about 23% with an increase at generator temperature around 20ºC. The highest exergy destruction is found to be at the generator about 75% of the total exergy destruction because of the temperature difference between the inlet and outlet stream properties. And it decreases with increasing generator temperature around 33.4% with the difference of 20ºC at generator temperature. The exergy efficiency increases and total exergy destruction decreases with a decrease at the difference between the source and the generator temperature. Total increase at exergy efficiency is around 2.73% and total decreases at exergy destruction is about 21.13kW with a decrease at the difference of 20ºC. The effect of reference environmental temperature

is also investigated. The exergy efficiency of VAR system increases by increasing reference environmental temperature. When at generator temperature 90ºC, exergy efficiency increases 4.1% with an increase at the difference of 7ºC, at generator temperature 105ºC, exergy efficiency increases 4.6% with an increase at the difference of 7ºC.

It has to be noted that from the cost analysis, the fan coil system and the VAR system to be bought has the highest initial cost like approximately three times higher than the VRF air conditioning system. The fan coil system and the VAR system to be manufactured has the lowest operation cost like approximately thirteen times lower than the fan coil system and the VCR system to be bought. As expected, VAR systems has lower operation cost than VCR and VRF air conditioning systems and VAR systems has higher initial cost than VCR and VRF air conditioning systems. The most advantageous systems are the VRF air conditioning system and the fan coil system and VAR system to be manufactured from the total annual cost. Although the VRF air conditioning system has lower total annual cost, the fan coil system and the VAR system to be manufactured can be more advantageous if the VAR system is manufactured domestically as mass production, also come front by utilizing the waste heat and by decreasing the operation and maintenance costs. Additionally, the other systems use fossil fuels to drive. As known, when the VRF air conditioning system is preferred, the carbon emissions will be released to the atmosphere and it will cause the green house affect that causes global climate change. And also the fluids as CFCs that is being used in the VRF air conditioning system may cause the ozone depletion. In addition to these disadvantages, utilizing the waste energy is so important because the countries like Turkey that do not have enough fossil fuel sources to produce their own energy. But, by preferring VAR systems utilizing waste heat, the total efficiency of industrial furnace integrated to the VAR system will be increased, thermal pollution can be decreased and also total cost of comfort cooling of the office buildings will be minimized.

REFERENCES

Balaji K. and Ramkumar R., 2012, Study of waste heat recovery from steam turbine xhaust for vapour absorption system in sugar industry, *Procedia Engineering, 38*, 1352-1356

Chen Q., Han W., Zheng J., Sui J. and Jin H., 2014, The exergy and energy level analysis of a combined cooling, heating and power system driven by a small scale gas turbine at off design condition, *Applied Thermal Engineering*, 66, 590-602

Choudhury B., Chatterjee P.K. and Sarkar J.P., 2010, Review paper on solar-powered air-conditioning through adsorption route, *Renewable and Sustainable Energy Reviews,* 14, 2189-2195

Cosenza F. and Vliet G.C., 1990, Absorption in falling water/libr films on horizontal tubes, *Conference Proceeding by ASHRAE*, 96, 673-701

Çengel Y.A., 2002, *Heat Transfer: A Practical Approach* (Second edition), McGraw-Hill

Davies J.T. and Rideal E.K., 1961, *Interfacial phenomena*, Academic Press, New York

Dinçer I. and Rozen M., 2007, *EXERGY: Energy, Environment and Sustainable Development,* Elsevier science

Elsafty A. and Al-Daini A.J., 2002, Economical comparison between a solar powered vapour absorption air-conditioning system and a vapour compression system in the Middle East, *Renewable Energy*, 25, 569-583

Garimella S., 2012, Low-grade waste heat recovery for simultaneous chilled and hot water generation, *Applied Thermal Engineering*, 42, 191-198

Genceli O.F., 1999, *Heat exchangers*, Birsen Publishing, İstanbul (in Turkish).

Florides A.G., Kalogirou S.A., Tassou S.A. and Wrobel L.C., 2003, Design and construction of a LiBr-water absorption machine, *Energy Conversion and Management*, 44, 2483-2508

Horuz I., 1998, A comparison between ammonia-water and water-lithium bromide solutions in vapor absorption refrigeration systems, *International Communications Heat Mass Transfer*, 5, 711-721

Kalkan N., Young E.A. and Celiktas A., 2012, Solar thermal air conditioning technology reducing the footprint of solar thermal air conditioning, *Renewable and Sustainable Energy Reviews,* 16, 6352-6383

Kaynakli O. and Kilic M., 2007, Theoretical study on the effect of operating conditions on performance of absorption refrigeration system, *Energy Conversion and Management,* 48, 599-607

Kaynaklı O., Saka K. and Kaynakli F.,2015, Energy and exergy analysis of a double effect absorption refrigeration system based on different heat sources, *Energy Conversion and Management*, 106, 21-30

Kaita Y., 2001, Thermodynamic properties of lithium bromide-water solutions at high temperatures, *International Journal of Refrigeration*, 24, 374-390

Kilic M. and Kaynakli O., 2007, Second law-based thermodynamic analysis of water-lithium bromide absorption refrigeration system, *Energy*, 32, 1505-1512

Law R., Harvey A. and Reay D., 2013, Opportunities for low-grade heat recovery in the UK food processing industry, *Applied Thermal Engineering,* 53, 188-196

Li W., Wu X., Luo Z., Yao S. and Xu J., 2011, Heat transfer characteristics of falling film evaporation on horizontal tube arrays, *International Journal of Heat and Mass Transfer*, 54, 1986-1993

Lorenz J.J. and Yung D., 1979, A note on combined boiling evaporation of liquid films on horizontal tubes, *Journal of Heat Transfer*, 101, 178-180

Ribatski G. and Thome J.R., 2007, Experimental study on the onset of local dryout in an evaporating falling film on horizontal plain tubes, *Experimental Thermal and Fluid Science*, 31, 483-493

Seewald J.S. and Blanco H.P., 1994, A simple model for calculating the performance of a Lithium–Bromide/Water coil absorber, *Conference Proceeding by ASHRAE*, 100, 318–328

Şencan A.,Yakut K.A and Kalogirou S.A., 2005, Exergy analysis of lithium bromide/water absorption systems, *Renewable Energy*, 30, 645-657

Thome J.R., 2009, *Engineering Data Book III,* Wolverine Tube, Inc

Wang C., He B., Sun S., Wu Y., Yan N., Yan L. and Pei X., 2012, Application of a low pressure economizer for waste heat recovery from the exhaust flue gas in a 600 MW power plant, *Energy,* 48, 196-202

Nazım Kurtulmuş has received his bachelor degree from Mechanical Engineering at Selçuk University in 2009. He received his master's degree from Mechanical Engineering at Gazi University. He is currently a Ph.D student at Çukurova University and research assistant at Adana Science and Technology University.

Dr. Ilhami Horuz graduated from Mechanical Engineering Department of Uludag University in the year 1988. Then, he received his M. Sc. degree from the same university and his PhD degree from the University of Strathclyde, U. K. in the years 1990 and 1994, respectively. His principle research interests are heating, refrigeration, air conditioning, renewable energy, energy utilization and fuel cells. He is currently working for the Mechanical Engineering Department of Gazi University as a lecturer.

APPENDIX

The inside heat transfer coefficient for tubes flowing water can be determined as follows [12]

$$Nu = 0.023 \cdot \mathrm{Re}^{0.8} \cdot \mathrm{Pr}^{0.4} \qquad (A1)$$

At the absorber the total area of one tube can be estimated as [16, 17]

$$A_{eff} = 2 \cdot l \cdot n \cdot \pi \cdot r_0 \qquad (A2)$$

$$l = \left(\frac{3 \cdot \rho_s}{32 \cdot g}\right)^{\frac{1}{4}} \cdot \left(\frac{n}{\dot{m}_s \cdot \mu_s}\right)^{\frac{1}{2}} \cdot (\pi \cdot r_0 \cdot a \cdot \sigma \cdot \cos\Theta)^{\frac{3}{4}} \qquad (A3)$$

For absorber, the wavelength can be determined as follows [18]:

$$\lambda = 2 \cdot \pi \cdot \sqrt{\frac{n \cdot \sigma}{\rho \cdot g}} \qquad (A4)$$

At the absorber the outside convective heat transfer coefficient can be determined as follows [19];

$$Nu = \mathrm{Re}^{0.46} \qquad (A5)$$

When the outside heat transfer coefficient is determined, a model for falling film evaporation on horizontal smooth tubes can be used [20].

$$h_o = h_b + h_d \cdot \left(\frac{L_d}{L}\right) + h_c \cdot \left(1 - \frac{L_d}{L}\right) \qquad (A6)$$

Falling film evaporation in a vacuum, the nucleate boiling term can be eliminated [21].
And for wet areas falling film evaporation Nu number can be determined as follows;

$$Nu = 182.1 \cdot \mathrm{Re}^{-1.56} \qquad (A7)$$

At falling film evaporation, for dry areas a coefficient is determined as follows [22];

$$F = 0.0024 \cdot \mathrm{Re}^{0.91} \qquad (A8)$$

For falling film evaporation, the outside convective heat transfer coefficient for developed region is determined by multiplying convective heat transfer coefficient and dry area coefficient as follows;

$$h_c = F \cdot h_w \qquad (A9)$$

The heat transfer for condensation on the outside surface of a horizontal tube gives the outside heat transfer coefficient [23].

$$h_{horiz} = 0.729 \cdot \left[\frac{g \cdot \rho_l \cdot (\rho_l - \rho_v) \cdot h_{fg}^* \cdot k_l^3}{\mu_l \cdot (T_{sat} - T_l) \cdot d_o)} \right]^{\frac{1}{4}} \qquad (A10)$$

$$h_{horiz,Ntubes} = \frac{1}{N^{\frac{1}{4}}} \cdot h_{horiz} \qquad (A11)$$

At the generator, to calculate the outside heat transfer coefficient, the correlation below is used [24]:

$$h_o = 0.134 \cdot \left(\frac{k}{d_e} \right) \cdot \left(\mathrm{Re}^{0.681} \right) \cdot \left(\mathrm{Pr}^{\frac{1}{3}} \right) \cdot \left(\frac{s}{14.85} \right)^{0.2} \cdot$$

$$\left(\frac{s}{t_f} \right)^{0.1134} \qquad (A12)$$

DYNAMIC MASKING TECHNIQUES FOR PARTICLE IMAGE VELOCIMETRY

F. Gökhan ERGİN
Dantec Dynamics A/S
Tonsbakken 16-18, 2740, Skovlunde, Denmark, gokhan.ergin@dantecdynamics.com

Abstract: Objects and surfaces often appear in Particle Image Velocimetry (PIV) images. Unless masked, the features on these contribute to the cross correlation function and introduce an error in the vectors as a result of the PIV analysis in the vicinity of the phase boundary. Digital masking of objects has appeared numerous times in the literature as part of the analysis chain, with a growing focus on isolating moving features using dynamic masks. One aim of this article is to provide a summary of milestones achieved in dynamic masking covering a wide range of applications. Another aim is to show the difference between image masking and vector masking. Finally, two different dynamic masking examples are described in detail and compared. The examples used are selected from swimming microorganisms in small channels. In the first example, a histogram thresholding-based dynamic masking is used, while, in the second example, a novel technique employing a feature tracking-based dynamic masking is used. Results show that histogram thresholding-based masking provides better results for swimmers which randomly change shape and direction; whereas, feature tracking-based masking provides better results for swimmers which do not change shape or direction significantly. In order to show the improvement due to dynamic masking, a comparison is made between PIV results a) with no masking, b) with just image masking and c) with both image and vector masking. Results show that the best approach is to use both image and vector masking.
Keywords: Dynamic masking, Image masking, Vector masking, Histogram thresholding based dynamic masking, Feature tracking-based dynamic masking.

PARÇACIK GÖRÜNTÜLEMELİ HIZ ÖLÇME TEKNİĞİ İÇİN DİNAMİK MASKELEME TEKNİKLERİ

Özet: Cisimlere ve yüzeylere Parçacık Görüntülemeli Hız Ölçümü (PIV) imajlarında sıkça rastlanır. Bunlar maskelenmediği sürece, çapraz korelasyon fonksiyonunu etkiler ve PIV analizi sonucu elde edilen hız vektörlerinde faz sınırına yakın yerlerde hatalı sonuçlar oluşturur. Cisimlerin dijital ortamda maskelenmesi, özellikle hareketli cisimlerin dinamik maske kullanılarak imajlardan çıkarılması hesap zincirinin bir parçası olarak literatürde pek çok kez yayınlanmıştır. Bu yazının bir amacı dinamik maskelemede ulaşılan kilometre taşlarının geniş bir uygulama yelpazesini de kapsayan bir özetini vermektir. Bir diğer amaç ise dinamik imaj ve vektör maskelemenin farklarını göstermektir. En son olarak, iki ayrı dinamik maskeleme örneği ayrıntılı olarak anlatılmakta ve karşılaştırılmaktadır. Kullanılan örnekler küçük kanallarda yüzen mikroorganizmalardan seçilmiştir. İlk örnekte histogram eşikleme ile dinamik maskeleme ve ikincide ise yeni bir teknik olan, özellik takibi ile dinamik maskeleme kullanılmıştır. Sonuçta, histogram eşikleme ile maskelemenin yüzme yönü ve şekli rastgele değişen yüzücülerde; özellik takibi ile maskelemenin ise şekli ve yönü pek değişmeyen yüzücülerde daha iyi sonuçlar verdiği ortaya çıkmaktadır. Dinamik maskelemenin yararını göstermek için maskeleme yapılmadan elde edilmiş PIV sonuçları, sadece imaj maskelemesi yapılarak elde edilmiş PIV sonuçları ve hem imaj hem de vektör maskelemesi yapılarak elde edilmiş PIV sonuçları karşılaştırılmıştır. Sonuçta hem imaj hem de vektör maskelemesinin kullanılmasının daha uygun olduğu ortaya çıkmıştır.
Anahtar Kelimeler: Dinamik maskeleme, İmaj maskeleme, Vektör maskeleme, Histogram eşikleme ile dinamik maskeleme, Özellik takibi ile dinamik maskeleme.

INTRODUCTION

Masking is an important step during PIV processing and, in many cases, manually-drawn static masks are sufficient to remove stationary objects from PIV images. Masking can be a relatively easy process if the unwanted section or object is stationary, however, it

becomes an extremely cumbersome and time-consuming process if the object is moving. Especially in the case of time resolved PIV systems,—where thousands of images can be acquired in an image ensemble—manual masking of moving objects from each image is simply not practical. Static digital masking is rather straightforward and has appeared numerous times in the PIV literature;

therefore, any reference to static masking techniques is omitted here, and the focus will be on dynamic masking.

With the introduction of high-speed PIV systems, time-resolved flow field information has become more readily available. Along with generating large numbers of images, this has also driven a necessity for an effective dynamic masking process when phase separated image processing is required in various multi-phase flow investigations. There are often significant velocity gradients across phase boundaries, which can cause cross-correlation based PIV methods to fail. Ironically, phase boundaries are often the focus of investigations where important fluid dynamics phenomena occur. In interrogation windows which overlap the boundary, the PIV computations are more likely to represent the displacements of the phase with the greater density of particle images. Therefore, it is essential to identify the phase boundary accurately in order to perform phase-separated PIV evaluations for a more accurate representation of the flow field where interesting flow phenomena occur.

To date, many multi-phase flow investigations have used some form of dynamic masking and these cover almost all phase combinations: gas in liquid (e.g. bubbly flow reactors, boiling flows), liquid in gas (e.g. sprays, free surface flows), liquid in liquid (e.g. droplet formation, mixing), gas in gas (e.g. combustion diagnostics, flame front investigations), solid in liquid (e.g. sediment transport, swimming objects), solid in gas (e.g. flapping and flying objects) and solid, liquid and gas (e.g. landslide investigations). Separation of phases can be accomplished using optical methods, digital methods, and using additional hardware components (e.g. a secondary illumination mode, Lindken and Merzkirch, 2002). Phase separation can, of course, also be achieved using a combination of these. Of particular interest—and the focus of the current report—are the digital methods which create dynamic masks of moving objects by applying a number of image processing functions using the original image ensemble. Although a number of different image processing techniques can be used in tandem, digital separation methods can be grouped under three main categories: (i) size-based separation, (ii) greyscale histogram thresholding methods and (iii) boundary detection methods. This study is a first attempt to summarize existing literature on the three digital separation methods. Additionally, two examples are provided of recent dynamic masking applications from bio-micro-fluidics. The first application example demonstrates masking of a uniflagellate microorganism using histogram thresholding and the second details masking of a copepod microorganism using a novel feature tracking-based approach.

Size-based separation

The *first study* using moving masks for phase-separated PIV processing was by Gui and Merzkirch (1996) in a bubbly flow experiment. In their analysis, a digital mask was used to track & separate larger gas phase objects (bubbles) from the smaller seeding particles in the liquid phase for double-frame PIV recordings. The separation technique relied on the existence of a significant difference in size distribution between the bubbles and the seeding particles. In another bubbly flow investigation from the same research group, Lindken and Merzkirch (2000) used a similar digital masking technique. In this study, a secondary high-speed imaging system was added to reconstruct the bubble shape and position in three-dimensions. The light sheets of the two systems were perpendicular to one another, and the 3D bubble shapes were reconstructed using the 2D bubble contours produced by each of the high-speed imaging systems. The use of this secondary imaging system allowed phase-separated *measurements of simultaneous, multiparameter information*: (i) two-component planar velocity field, (ii) bubble positions and (iii) 3D bubble shapes.

Separation of three phases was achieved by Fritz et al. (2003), who performed digital dynamic masking in a landslide wave tank without using additional hardware components. First, the seeding particles in the water phase were separated from the sliding granular matter and air, using image-processing functions. Second, the pixel value fluctuations arising from illumination intensity were removed using a sliding background subtraction. Finally, the water phase was isolated from the other two phases using digital dynamic masks similar to techniques used in Lindken & Merzkirch (2000). The ramp and water surface were masked to avoid biased correlation signals caused by total reflections and light scattering from floating seeding particles. This masking technique was used successfully in un-separated and separated flow conditions, meaning the mask was able to follow *morphological changes* in the two-phase flow.

The size-based separation methods naturally rely on a significant size difference between the phases. If the size difference is small, i.e. if the size of the bubbles are close to the size of the particles, phase separation becomes quite difficult. Histogram thresholding methods, in combination with other image processing functions, have certain advantages in such situations and can be more effective when applied to other challenging flow configurations.

Histogram thresholding methods

Lindken and Merzkirch (2002) improved upon their previous size-based separation method by adding a histogram thresholding-based separation approach. They used the digital mask as an operator in the PIV

evaluation algorithm in which the separation of phases is performed on individual image histograms. Furthermore, a *secondary light source* in transmission mode was used in combination with PIV in order to get distinct background levels between particles and bubble areas. The detailed image processing steps are implemented such that they can be applied to large image ensembles in a systematic fashion (*automated masking*).

In the realm of PIV literature, the term "dynamic masking" was first coined by Sveen and Daziel (2005). In their approach, dynamic masking allowed *simultaneous measurements of velocity and density gradients* by separating PIV and synthetic Schlieren signals in a gravity wave tank. In the experiment, backlit particle shadows were superimposed on synthetic schlieren images. The particle images were removed using a 3-step masking procedure. First, a background subtraction was performed based on pixel maximum to remove static features on the tank walls. Second, a histogram thresholding was performed to locate the particles, and third, an erosion filter was applied to increase the imaged particle size. The resulting image was used for masking the synthetic Schlieren images. Sveen and Daziel (2005) even measured the performance of their dynamic masking technique by comparing the RMS signal of a) a non-seeded measurement, b) a seeded measurement without a mask and c) the seeded measurement with dynamic masking. They observed that the masking technique reduces RMS errors by 7%.

Another performance assessment was made by Seol & Socolofsky (2008) using a PIV/LIF (Laser Induced Fluorescence) experimental setup. In this study, experiments were performed in a bubbly two-phase flow and made a *three-way comparison* between a) optical phase separation, b) digital phase separation (masking) and c) mixed-phase PIV analysis with vector post processing. As a result of the error analysis among the data sets, it was found that the vector post-processing algorithm performed well, but contained small errors in the fluid-phase velocity field around some bubbles. A five-step image processing chain was used to identify the bubble signatures for masking: (i) a 3x3 median filter, (ii) histogram thresholding at 5% of peak pixel value, (iii) binarization, (iv) opening / closing filters and (v) a dilation filter were used to generate the masking algorithm. The binary image mask was then multiplied by the original image to separate the bubbles from the fluorescent particles. In the processed particle image, *the missing* bubble *regions were filled with an average background pixel value* instead of a zero-pixel value so that the PIV algorithm is not biased by the sharp edges created by the masked bubble regions.

Up until 2010, all the histogram thresholding-based techniques used in bubbly flow experiments relied on the use of additional systems or hardware components. In 2010, Deen et al. (2010) and Hammad (2010) reported masking of stationary and moving objects using only image processing functions, i.e. *without the use of additional hardware components*. Deen et al. (2010) described a combined image processing approach that deals with uneven illumination and masking, where a two-phase flow between the filaments of a spiral wound membrane module was digitally separated. The approach consisted of (i) intensity normalization to cope with uneven illumination, (ii) background subtraction to remove stationary objects and (iii) image masking to remove the moving bubbles in two-phase flow. The removal technique of moving bubbles—which appear as bright rings on the image—was similar to what was developed by Seol & Socolofsky (2008). Hammad (2010) performed phase-separated velocity measurements in a two-phase flow experiment in which the turbulent bubbly flow was produced by an impinging water jet on a horizontal air-water interface. Dynamic masking was performed using a sequence of low-pass, high-pass and morphology digital filters to yield background subtraction, bubble detection and phase separation. The liquid-phase containing the seeding particles was produced first by identifying the areas occupied by bubbles using median filtering, and then by subtracting the bubbles from contrast-enhanced images. Each phase was evaluated separately using an adaptive correlation-based PIV algorithm.

In general, the dynamic masks generated in the literature have been accurate down to a single pixel. Wosnik and Arndt (2013) applied a slightly different dynamic masking technique based on a *local threshold filter applied on the interrogation area*. The experiment was performed in a bubbly wake produced by ventilated supercavitation, where only the velocity fields of the gas phase in the cavitating flow were obtained by PIV analysis of the bubbles. In order to retain vectors associated with bubbles, the original PIV image was thresholded not pixel-by-pixel, but by the size of the final interrogation area. The masked and unmasked regions were defined based on a pixel value summation over the final interrogation area compared to a defined threshold value. In other words, if the sum of the pixel values was above a certain threshold, the mask was "on", and if below the mask was "off". Therefore, the 1024x1024 original image was converted to a 63x63 binary image mask for 32x32-pixel final interrogation area and 50% overlap. That approach naturally produced a mask with coarser resolution.

Histogram thresholding-based dynamic masking has also been applied in other challenging applications. Among these are (i) the masking of organisms during locomotion, (ii) the masking of droplets during break-up and (iii) the masking of reactants and products in combustion diagnostics.

Wadhwa et al. (2014) used a dynamic masking algorithm to investigate the flow field around *A. Tonsa*, a sub-millimeter sized microorganism*, during locomotion*. A two-step masking procedure was applied to remove the organism from the particle images: The procedure consisted of a sliding averaging of the pixel intensity values followed by thresholding to remove those pixels from the analysis which corresponded to the organism. The masking process made it "impossible" to get measurements in the close vicinity of the organism, especially around the swimming appendages. As a result, the masking parameters had to be adjusted for each recording manually in order to minimize the loss of useful data. After every pass of the processing and during post-processing, outliers were removed using a median filter and de-noising. Later Ergin et al. (2015a) applied a feature tracking-based dynamic masking approach to achieve better results using the same raw images. This approach will be described in detail in Section 3.

Carrier et al. (2015) used dynamic image and vector masking successfully in a droplet formation experiment where the dynamic mask was used to reject spurious vectors in the non-seeded continuous phase. The first step was to isolate the features in motion (the droplet interface and the seeding particles) from the static background. For this purpose, the harmonic mean was subtracted from the inverted pixel values of the raw shadow images. In addition to this, a static mask was applied to remove residual wall reflections. Finally a suitable histogram threshold level was selected so that only the features in motion had a non-zero pixel value. Then a sufficient number of dilations (bright pixels flooding the dark pixels) were performed to fill the gaps between the particles and the interface entirely. A natural side effect of this dilation is the 'fattening' of the finger, which can be remedied by an equal number of erosions (dark pixels flooding the bright pixels). The masks generated in Carrier et al. (2015) were successful in following the *morphological changes during the droplet formation*, especially during the break-up stage (Fig. 1). A movie of the droplet break-up is available in Ref M1**.**
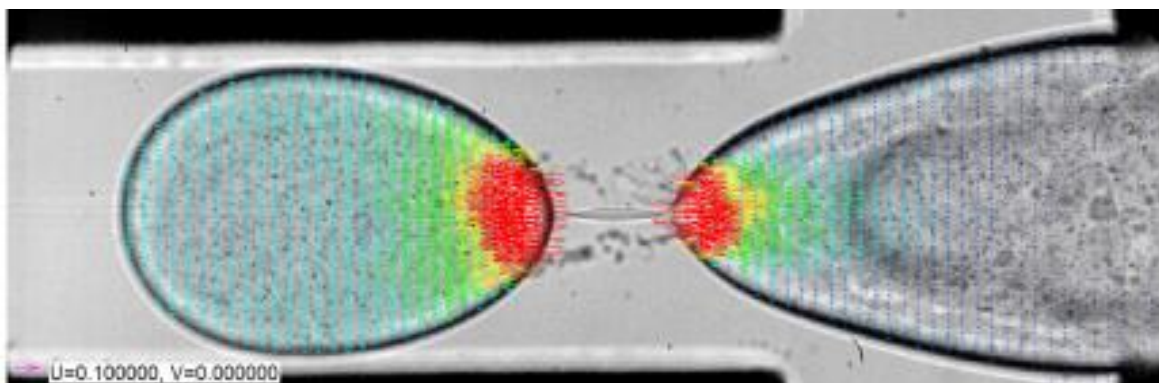
Stevens et al. (1998) performed *phase-separated PIV measurements in a combustion application.* The experiment consisted of a premixed turbulent methane-air flame in a stagnation plate configuration, where a dynamic masking technique was used to improve the PIV results for interrogation areas located along the flame front. In order to separate the reactant and product zones, local seeding density was used as the differentiator. The seeding density is often higher before combustion, and lower afterwards due to a sudden expansion of gases. As a result of the seeding denisty change, local mean pixel intensity in the PIV images is higher in the air-fuel mixture before combustion than after. Stevens et al. (1998) were able to determine the thin flame front using the Light Sheet Tomography technique, which is based on the local intensity of Mie scattering from the seeding particles. A suitable threshold applied on the mean pixel values was used to separate the two zones and a cross-correlation-based PIV algorithm was applied in each zone separately.

The histogram-thresholding techniques seem to be more frequently applied in the literature; particularly for the masking of multiple medium-sized features in the flow field, such as bubbles, microorganisms, and droplets. Due to their flexibility and their ability to handle more challenging situations, they can even produce successful results along more complex phase boundaries such as a flame front in combustion applications.

Boundary detection methods

Boundary detection methods are more suitable for separation of phases across longer, single-phase boundaries such as flame fronts, surface instabilities and liquid free surfaces. For example, Coron et al. (2004) used a boundary detection method for *phase separation in a turbulent premixed flame*, very similar to what is described by Stevens et al. (1998). Both groups were successful in (i) obtaining the phase-separated instantaneous velocity fields simultaneously, and (ii) improving the accuracy of the PIV measurements in the vicinity of the flame front. Additionally, Coron et al. (2004) were able to measure

Figure 1. Snapshot of the flow field at rupture instant during the droplet break-up experiment performed by Carrier et al. (2015). Colors indicate velocity magnitude, max velocity 270 mm/s. Histogram thresholding based dynamic mask is able to follow morphological changes during droplet formation.

the flame front contour location. Coron et al. (2004) also perform a phase separation between fuel and reactants based on the fact that Mie scattering light intensity from the seeding particles is lower in products than in reactants—due to the gas expansion across the flame front. In this study however, the active (deformable) contours technique was used for boundary detection rather than a histogram thresholding method. These deformable contours can be breifly described as curves or surfaces defined within a multi-dimensional domain which can move toward desired features (usually edges). The preferred model for their study employed parametric active contours, which allowed a compact representation of data. The boundary detection technique using active contours is an iterative procedure, in which an initial contour on the image domain is allowed to deform. Coron et al. (2004) used a contour obtained by the reliable averaging windows technique as an initial guess. After the final flame front contour was obtained, a mask was produced on one side of the contour at a time with PIV analysis performed in the fuel mixture phase and the combustion products phase separately. As a result, in regions where the interrogation windows stretch across the flame front, the densely seeded fuel phase did not influence the correlation function in the reactants phase.

Another application where boundary detection methods prove to be more suitable are flows with free liquid surfaces. Sanchis and Jensen (2011) used Radon transformation for automatic boundary detection and performed phase separation in a *stratified two-phase flow* through a circular pipe. The boundary was identified by the seeding particles floating at the free surface, which appeared as a long connected dotted line in PIV recordings. The Radon transform is a mathematical tool well suited for the detection of linear features in noisy images and is commonly applied in computer vision. This technique tends to suppress pixel intensity fluctuations due to noise by the process of integration. A normalization procedure was included to take into account the aspect ratio of rectangular input images. During image processing, segmentation was necessary and an increased number of image segments were used in areas with increased curvature. Hermite cubic interpolation between adjacent segments allowed the reconstruction of the interface piece by piece across the entire image. This technique was able to track the interface with an accuracy of +/- 0.67 pixels under worst-case scenarios; i.e. in low particle density and with a noisy background.

Honkanen and Saarenrinne (2003) provided a good overview of other digital object separation methods and their application in PIV analysis of turbulent bubbly flows. They described four different object separation methods including (i) probability of centre, (ii) convex perimeter, (iii) curvature profile and (iv) Shen's method. The last three are breakpoint detection methods and were found to be more efficient than the probability of centre method for bubbly flows. Their superior performance is due to the fact that they search for connecting points of outlines of individual objects on the perimeter of the segment. Among all four methods the curvature profile method located the connecting points most accurately and most reliably, and it was also the least sensitive to noise. It should be noted that these findings only apply for bubbly flows where smooth contours are normally encountered during PIV recording.

As can be seen in the literature, there are a great number of different masking approaches used by researchers, and it is quite difficult to universally comment whether one approach is better than the other. In the current work, the aim is not to name the best masking technique that works in every scenario. On the contrary, based on previous studies, the dynamic masking approach should be tailored for each application. Regardless of the approach being used, mask definition is the same; information from one or more phases must be suppressed while leaving information from the remaining phase(s). In the next section the mask definition for image masking and vector masking is presented.

Mask definition

The goal of dynamic masking is to get a specific pixel value (such as "0") on the object that is to be masked and retain the pixel value information everywhere else for each image in the ensemble. This can be achieved in a 3-step procedure. In step one; a new image ensemble is produced by filtering, thresholding etc. to obtain a pixel value of 0 on the object and 1 everywhere else (Gui and Merzkirch 1996). In step two, each time step of the new image ensemble is multiplied by the corresponding time step of the original ensemble. If the original image background pixel value is nonzero, this results in a sharp pixel value difference between the mask and the image background. As a remedy, in step three, background subtraction techniques can be used to obtain a 0 pixel value in the masked ensemble's background, or the masked area can be padded with the average pixel value of the background (Seol & Socolofsky 2008). Finally, the mask ensemble can be applied to mask either the raw images (image masking) and/or the PIV results (vector masking). In short, the preferred image masking definition here is following Gui and Merzkirch (1996), where the mask is defined as a binary image and it is applied on the raw images using pixel-by-pixel image multiplication:

Δ (i,j)= 0 if the pixel, p(i,j) belongs to the phase that is to be masked (Phase 1)

Δ (i,j)= 1 if the pixel, p(i,j) belongs to the phase that is subject to PIV evaluation (Phase 2).

A typical phase-separated PIV evaluation of a two-phase flow starts with image masking of phase 1 and PIV evaluation in phase 2. Then the binary mask is inverted to mask phase 2 using a simple pixel inversion and PIV evaluation is performed on phase 1. An additional vector masking step is usually applied after each evaluation in order to clean up the vectors in the masked phase close to the phase boundary (see Fig. 6). The vector masking definition is similar to image masking:

Δ (i,j)= 0 if the vector V(i,j) belongs to the phase that is to be masked (Phase 1)

Δ (i,j)= 1 if the vector V(i,j) belongs to the phase that is subject to PIV evaluation (Phase 2)

Finally, both vector maps are merged to represent the two-phase flow field. For multiphase flows where more than 2 phases are present, the same approach can be used a number of times until each phase is represented in the flow field. In some cases, one of the phases could be a solid boundary in motion (e.g. flapping wing, rotating vane etc.) where PIV evaluation may not be necessary. In the following two sections, different dynamic masking strategies are described using the above mask definition. In the Section 2, flow around a uniflagellate swimmer, *Euglena Gracilis* (*E. Gracilis*), is isolated using histogram thresholding-based dynamic masking. In the Section 3, flow around a breaststroke swimmer, *Acartia Tonsa* (*A. Tonsa*), is isolated using a novel tracking-based dynamic masking technique. Recently, similar dynamic masking procedures for *E. Gracilis* and *A. Tonsa* have been reported in Ergin (2015) and in Ergin et al. (2015a), respectively. The current work uses the same two raw particle image ensembles, but provides improved comparisons and descriptions (including flow charts for data analysis) of masking and velocimetry. In the case of *E. Gracilis*, the importance of dynamic masking is demonstrated by providing a three-way comparison between PIV results with a) no masking, b) image masking and c) vector masking. Similarly for *A. Tonsa*, a comparison between unmasked and masked PIV results is provided.

HISTOGRAM THRESHOLDING-BASED DYNAMIC MASKING

The microorganism *E. Gracilis* is known to use a single whip-like structure, called flagellum, in combination with rolling, stretching and contracting its flexible body. A schematic of this mono-flagellate is shown in Fig. 2. Its body length without the flagellum can vary between 20μm and 100μm. The flagellum is located at the end close to the photoreceptor, and the cell nucleus is centrally located in its body. Although imaging the flagellum is challenging, the photoreceptor and the cell nucleus can be detected easily under a microscope (Fig. 2).
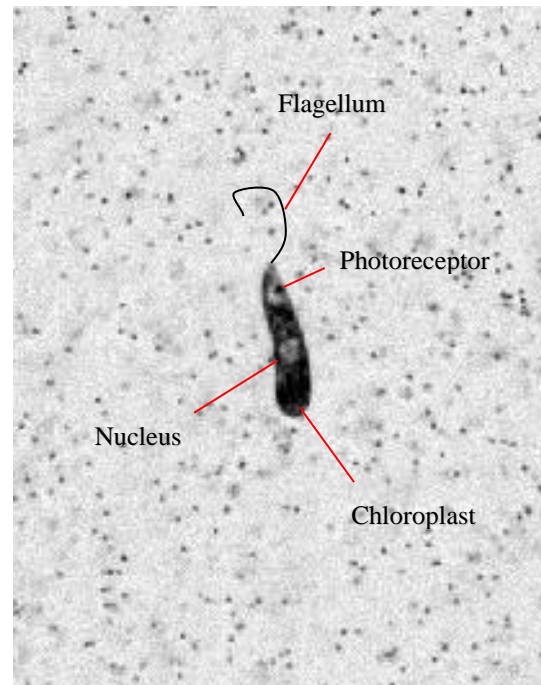

Figure 2. Schematic of *E. Gracilis*. Flagellum is added manually as it cannot be resolved by the optics. The photoreceptor, nucleus and chloroplast are visible under the microscope.

The experimental measurement setup used in this masking example is a MicroPIV system manufactured by Dantec Dynamics. The system components include an inverted fluoresence Microscope (HiPerformance), a sensitive CMOS detector (SpeedSense M310), a synchronization device (80N77 Timer Box), and a pulsed LED illumination system (Microstrobe). In biological flows, high-power pulsed laser illumination is often not preferred as this can disable the organism or influence its normal locomotion behaviour. For this reason, a lower-power LED-based pulsed illumination was used in backlit transmission mode which produced shadow particle images. 1μm-diameter seeding particles were introduced in small quantities until a sufficient seeding density was achieved for PIV. The seeding density was kept at a low level in order to avoid a change in normal swimming behaviour. The particle images were recorded at a frame rate of 12.5 fps, with a resolution of 1280 x 800 pixels. The images were acquired using a 40x magnification objective, producing a 0.64 mm x 0.4mm field of view (FoV). Later a smaller region of interest (ROI) is extracted with a resolution of 323 x 529 pixels, corresponding to 162μm x 265μm in the object space. Single-frame image acquisition was performed with a constant time difference of 80ms. Since the FoV was relatively small (~0,25mm²), it was often necessary to wait until an organism swam through the FoV with the measurement system in operation. The images were continously acquired and stored in a ring buffer with the acquisition stopped manually after the organism had passed through the FoV. 83 consecutive frames were analyzed to produce 82 flow field measurements. Total recording time was 6.56s. Further details can be found in Ergin (2015).
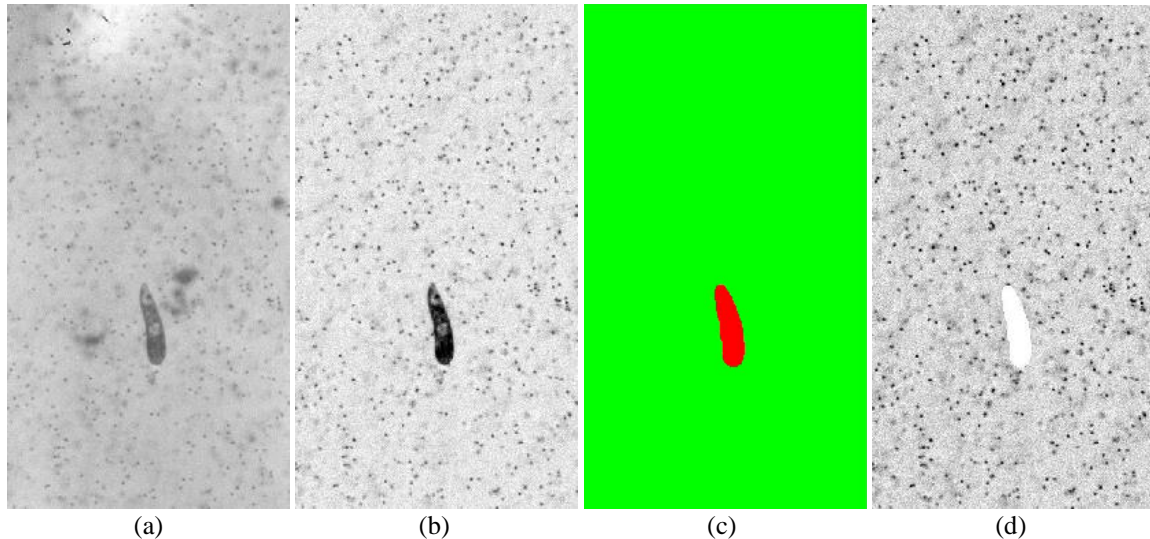
Figure 3. *E. Gracilis* during locomotion in water with 1-μm diameter seeding particles at t=1.92 s. (a) Raw image before background subtraction (b) after pixel inversion and background subtraction (re-inverted) (c) dynamic mask (d) particle image after image masking (re-inverted)

Fig. 3a shows the raw PIV recording of a 47,5μm-tall *E. Gracilis* in the sparsely seeded flow. In the acquired ensemble, *E. Gracilis* meanders upwards through filtered water; covering a net distance of approximately 256μm (Fig. 4). Use of filtered water provides a cleaner, foreign-object-free background in the raw images and allows more precise seeding density adjustments. Furthermore, other marine organisms (predator or prey to *E. Gracilis*) that can change *E. Gracilis*' normal locomotion behaviour are excluded.
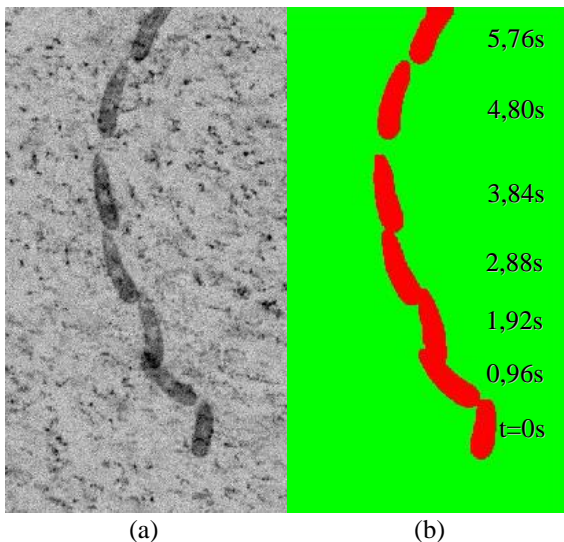

Figure 4. Quality of dynamic masking (a) Recorded position (b) dynamic mask of *E. Gracilis* every 0.96s.

The first step in image pre-processing is pixel inversion in order to work with positive particle images rather than particle shadows. Although working with (inverted) positive particle images during processing, it is preferable to present (re-inverted) shadow particle images for better visibility (Fig. 3b and 3d). In the second step, a background

subtraction is performed using the minimum pixel value found in the inverted ensemble (Fig. 3b). Next, a histogram thresholding-based dynamic mask is produced using the ensemble in the second step (Fig. 3c) and finally image masking is performed (Fig. 3d). A flow chart describing the complete analysis chain for dynamic masking of *E. Gracilis* is shown in Fig. 5.
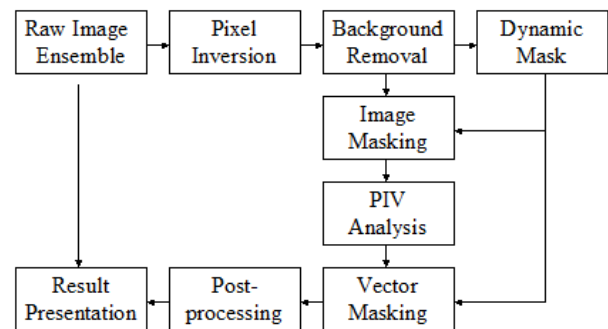
Figure 5. Flow chart describing the analysis chain for dynamic masking of *E. Gracilis*.

In the current study, the following image processing chain produced an acceptable dynamic mask: a 9x9 median filter, a closing filter with 10 iterations, thresholding (min:125 max:4096), pixel inversion, thresholding (min:3970 max:4096), erosion filter with 2 iterations, thresholding (min:0 max:1). The final thresholding step produces the binary image mask. In order to demonstrate the quality of the dynamic mask, position of *E. Gracilis* (Fig. 4a) and the used mask (Fig. 4b) are shown side by side at selected time steps. One immediate observation is that the mask is slightly larger than the organism. This is intentional in order to keep a small margin around the masked object, and the margin thickness can be controlled by the number of erosions and dilations. Another observation is that the used mask may produce non-ideal results around image boundaries (see for example the top of Fig. 4b at t=5,76s). Apart

from these, the dynamic mask captures the position and the shape of *E. Gracilis* in a successful fashion.

For velocity calculations, an adaptive PIV algorithm is used, which is an advanced particle displacement estimator implemented in DynamicStudio (Dantec Dynamics, Skovlunde, Denmark). Briefly, the implementation is a cross-correlation based, adaptive and iterative procedure employing vector validation and deforming windows: First, the displacement is calculated on an initial interrogation area (IA), which is larger in size compared to the final IA. In each step the IA is shifted by the displacement calculated in the previous step. For the case of *E. Gracilis* the final interrogation windows of 32x32 pixel are used with 75% overlap. Window deformation is performed by adapting the IA shape to velocity gradients, with $|du/dx|$, $|dv/dx|$, $|du/dy|$, $|dv/dy| < 0.25$.

Several passes can be made to further shift & deform the windows to minimize the in-plane particle dropout. For each IA size, this procedure is repeated until a convergence limit in pixels or a maximum number of iterations is reached. Then a 9-point, two-dimensional Gaussian fit is performed on the highest correlation peak to obtain the displacement field with subpixel accuracy in each pass. A number of FFT window (Hanning, Hamming etc.) and filter functions can be applied during the analysis. Between passes, spurious vectors are identified and replaced with a number of validation schemes including peak height, peak height ratio, SNR & Universal Outlier Detection (UOD) (Westerweel and Scarano 2005). Following Westerweel and Scarano (2005), UOD is performed between passes in a 5x5 neighbourhood with 0.1 minimum normalization level and a detection threshold of 2.0. The vectors are considered valid if the peak height ratio is larger than 1.25. In other words, the displacement calculation is considered reliable when the highest peak (the assumed signal peak) is at least 1.25 times higher than the second highest peak (assumed to be noise) in the cross-correlation function. This is certainly not the only vector validation method, but it is one of the oldest. A threshold value of 1.2 is often used in the literature, so in this respect the present threshold value of 1.25 is more conservative. The subpixel positioning accuracy of the Adaptive PIV algorithm is reported as 0.06 pixels with 95% confidence (Ergin et al. 2015b). The 0.06 pixels correspond to a 27.5nm displacement in the object space, and the velocity uncertainty is estimated as 0.34µm/s. An average filter in a 5x5 neighbourhood and vector masking is applied after Adaptive PIV computations.

A close up of the flow field around *E. Gracilis* at t=1.92s is shown in Fig. 6. In this figure, vectors represent the u and v components of the flow field and colors represent the magnitude of local velocity, where blue areas represent stagnant flow regions. Figure 6
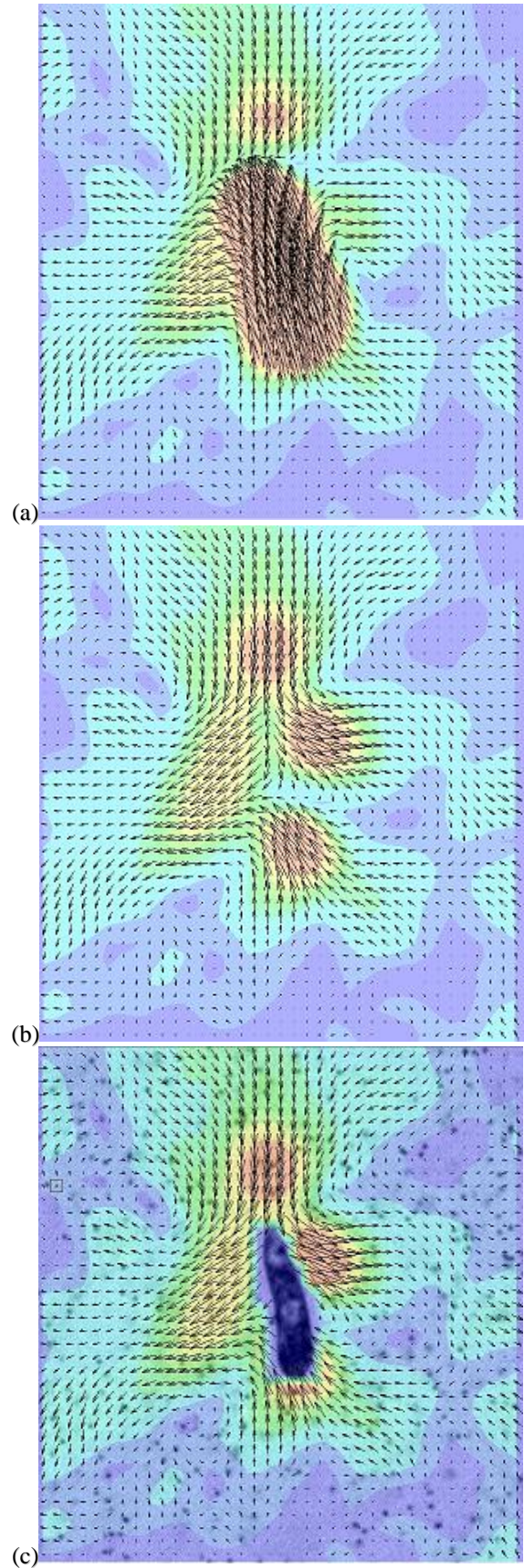

(a)

(b)

(c)

Figure 6. Flow field around *E. Gracilis* at t=1.92s. (a) Without masking, (b) with image masking only, and (c) with both image masking and vector masking. Max velocity is 12µm/s in b and c.

includes three subfigures in order to make a three way comparison of the flow field first without the application of masking (Fig. 6a), second with image masking but without vector masking (Fig. 6b), and third with both image and vector masking (Fig. 6c). The raw particle image is also included in Fig. 6c in order to show the position of *E. Gracilis* with respect to the flow field.

It is clear from Fig. 6a that without any masking the flow field in the immediate vicinity the organism is contaminated by the upward motion of the organism itself. This is simply because the features on the organism produce a strong correlation peak in interrogation areas that overlap the organism and the fluid around it. Application of image masking (Fig. 6b) improves the situation significantly for the liquid phase, but this time some erroneous vectors are registered on the organism; vectors indicate a downward motion while the organism swims upwards. These spurious vectors can be cleaned with the application of vector masking (Fig. 6c), which leaves us with the flow field around *E. Gracilis* where the information is only coming from the liquid phase. The flow field reveals that the fluid is drawn towards the organism upstream and downstream, and fluid is expelled from the organism on the sides. The downstream flow field can be explained as the wake in the aft of the swimmer, and the upstream flow field is produced most likely by the flagellum pulling a stroke, the main source of propulsion. Due to continuity around the organism, the fluid is expelled outwards from the sides. This flow field also produces four small vortices, one at each corner of the image, i.e. due Southwest, Southeast, Northwest and Northeast of the organism.

The histogram thresholding-based dynamic masking example described above proves to be quite powerful as it is able to tackle several important challenges encountered in the image ensemble: uneven illumination (Fig. 3a), random object trajectory, random object shape, and random object velocity (Fig. 4). Although quite powerful, histogram-thresholding based dynamic masking strategies may not work for certain applications. In the following section, the feature tracking-based dynamic masking strategy was used, which proved to be more successful for the application.

FEATURE TRACKING BASED DYNAMIC MASKING

Recently the hydrodynamics of a ~220-μm-long *A. Tonsa* (Fig. 7) nauplius were analyzed in Wadhwa et al. (2014) using time-resolved MicroPIV/PTV (Particle Tracking Velocimetry), in which a two-step masking technique was applied to remove the organism from the particle images.

Figure 7. Schematic of *A. Tonsa* nauplius at the beginning of a power stroke. From Ergin et al. (2015a).

vicinity of the organism, especially around the swimming appendages. As a result, Wadhwa et al. (2014) had to adjust the masking parameters for each recording manually in order to minimize the loss of useful data. Later Ergin et al. (2015a) made some improvements on the masking strategy of Wadhwa et al. (2014) and provided some phase-locked averaged results. In the current study, the same particle image ensemble is used, but a more effective approach for both masking and velocimetry is employed. Although the new strategy is not successful in masking the swimming appendages, it enables more accurate measurements in the close vicinity of the organism without having to adjust masking parameters manually for each image and without having to apply phase-locked averaging. In the current study, an improved tracking algorithm is used, which tracks both the horizontal and the vertical position of *A. Tonsa*, whereas, Ergin et al. (2015a) performed tracking only in the vertical direction. Since *A. Tonsa* is moving slightly to the left (see Fig. 11), a larger mask was used in Ergin et al. (2015a). Second, the analysis consists of 16x16 final IA size with 50% overlap followed by a UOD scheme with a detection threshold of 0.5. This enabled the comparison of masked and unmasked flow fields at any instant, without resorting to phase-locked averaging.

The experimental setup for the second application example is described in Wadhwa et al. (2014) and is summarized here briefly: Copepods *A. Tonsa* were cultured at 18°C and were transferred before experiments to the test aquarium containing filtered seawater. Only a few specimens were transferred in order to avoid possible interactions between them. The test aquarium is a glass cuvette (10x10x40mm) placed on a horizontal stage and kept at room temperature, between 18°C and 20°C.

The experimental measurement setup is a long-distance Micro Particle Image Velocimetry (LDμPIV) system where the light sheet propagation direction and the camera viewing direction are perpendicular. As described in the previous application, high-power visible laser illumination is often not preferred in biological
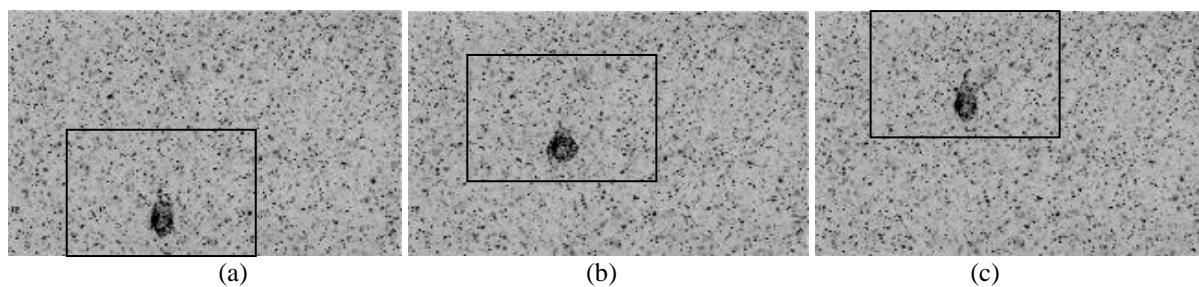
Figure 8. (a) First, (b) 33rd (middle), and (c) 65th (last) frames of the raw particle image ensemble. Boxes show the approximate borders of the ROI extracted around the organism.

flows. For this reason, a low-power, continuous-wave infrared laser (Oxford Lasers Ltd, 808nm wavelength) was used. Sheet forming optics were assembled to produce a 150µm thick light sheet, defining the measurement depth of the experiments. TiO_2 seeding particles smaller than 2µm were introduced in small quantities until a sufficient seeding density was achieved. The particle images were recorded on a high-speed CMOS detector (Phantom v210, Vision Research Inc.) at a resolution of 1280 x 800 pixels. Single frame image acquisition was performed with a constant time difference of 500µs between frames, corresponding to 2000fps. The images were acquired with 11.65x magnification producing a 2.2mm x 1.4mm FoV (approx $3mm^2$). Once again, the images were acquired and stored continuously in a ring buffer and the acquisition was stopped manually after the organism had passed through the FoV. Consecutive frames were used for two-frame PIV processing - quite typical for time-resolved PIV measurements: 65 frames were analyzed to produce 64 flow field measurements. Further details can be found in Ergin et al. (2015a).

The first, middle and last frame of the image ensemble are shown in Fig. 8, where a ~0.22mm tall *A. Tonsa* is in motion. During the experiment, *A. Tonsa* propels itself upwards through filtered seawater by pulling three breaststrokes and covering a distance of approximately 650µm (Average swim speed approx. 20mm/s). It is observed that *A. Tonsa* moves in an almost-vertical straight line and its angular orientation does not change significantly (Fig. 8 and 10). Subsequent image analysis includes feature tracking, image masking, velocity field calculation, vector masking and image masking.

Several different histogram thresholding-based dynamic masking strategies proved unsuccessful in a laboratory-fixed coordinate system; i.e. the "real-life" situation where the fluid is stationary and the microorganism is in motion. Since the microorganism did not rotate around its axis or change shape and moved in a relatively straight trajectory, a pixel-accurate, cross-correlation based tracking method was implemented in order to track its position throughout

the ensemble. The idea behind this tracking technique is to move to an object-fixed coordinate system in which the microorganism is fixed and the surrounding fluid is in motion. When the object is fixed, conventional static masking techniques can be applied on the images and/or on the calculated vectors. This was achieved in three steps: First, a feature was defined using the organism's image in the first frame (Fig. 8a). It was possible to identify the organism throughout the ensemble because some of the seeding particles were stuck on the organism (Fig. 9). For this reason, the tracked feature was selected as the body of the organism, excluding the appendages.
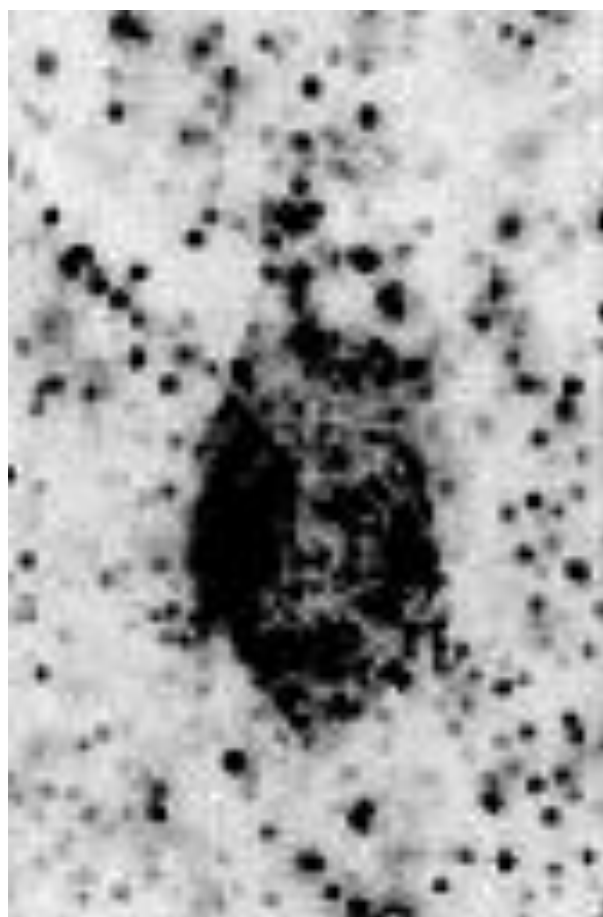

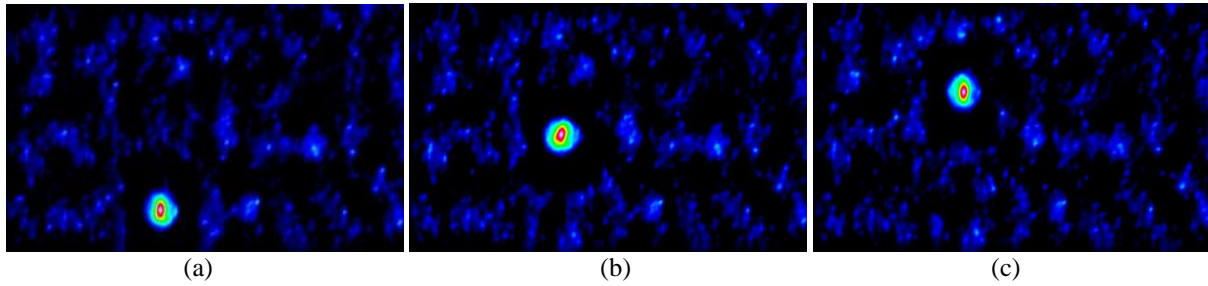**Figure 9.** Close up of the *A. Tonsa* showing particles stuck on its body.

70

Figure 10. Correlation of the organism with itself in the (a) first, (b) 33rd (middle), and (c) 65th (last) frames.

Second, a new pixel-accurate tracking algorithm was implemented in Matlab, which locates the peak of the cross-correlation function between the defined feature and the entire image (Fig. 8). This essentially searches for the defined feature within the entire image. The algorithm is only pixel accurate because no subpixel fitting was performed during the computations. Figure 10 shows the calculated cross correlation function for the first (Fig. 10a), the middle (Fig. 10b) and the last (Fig. 10c) frames in the ensemble, and the position of the cross correlation peak can be compared to the position of the organism in Fig 8a, 8b and 8c. The maximum pixel value of the cross correlation function in the ensemble reveals the nearly-linear trajectory of *A. Tonsa* (Fig. 11).
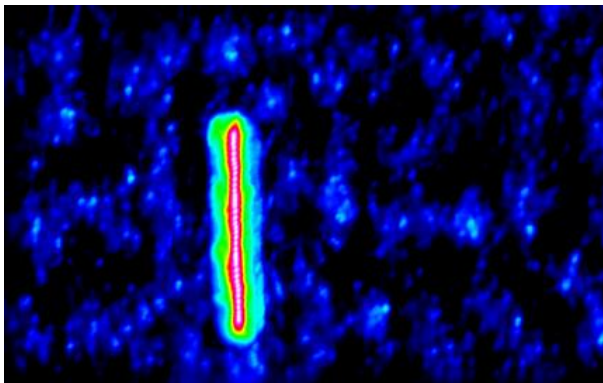

Figure 11. *A. Tonsa*'s nearly linear trajectory during the experiment.

Third, once the organism location was established on all frames, a constant-size ROI, (576x384 pix) was extracted around it (Fig. 8). The vertical ROI dimension (384 pixels) was the maximum value which could be used in all frames. The limitation was due to the first and the last frames, in which the imaged distance fore and aft of the organism must stay within the FoV throughout the ensemble (Fig. 8a and 8c). The horizontal ROI dimension (576 pixels) was a value which fixed the organism approximately in the center of the ROI horizontally, and reached sufficiently far into the flow field. This three-step procedure fixed the coordinate system on the organism and allowed the application of a conventional static masking procedure to remove the organism (image masking) and, eventually, the spurious vectors on the organism (vector masking). In this application, final interrogation windows of 16x16 pixel were used with 50% overlap for PIV processing. Here, the uncertainty of 0.055 pixels corresponds to a 94.4 nm displacement in the object space, and the velocity uncertainty is estimated as 189 μm/s; i.e. 1% compared to the average swim velocity. A flow chart describing the analysis chain for dynamic masking and PIV analysis of *A. Tonsa* is shown in Fig. 12.
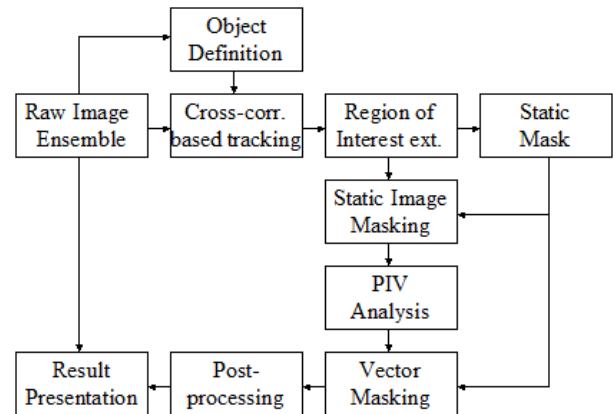
Figure 12. Flow chart describing the analysis chain for dynamic masking of *A. Tonsa*.

The organism's swim velocity history could be measured by probing a vector in the far field, upstream of or beside the organism. A time history of this vector showed that the nauplius is an almost perfectly periodic swimmer, and that three full breaststroke cycles were recorded (Ergin et al. 2015a). Figure 13 shows the flow field around the organism during the power stroke in the vicinity of the maximum swim speed. This figure includes two subfigures in order to make a comparison of the flow field without tracking and masking (Fig. 13a), and with tracking-based image and vector masking (Fig. 13b) at the same time instant. In Fig. 13b, the instantaneous swim velocity value is subtracted to show the flow field details around the organism. Similar to the case for *E. Gracilis*, it is clear from Fig. 13a that, without any masking, the flow field in the immediate vicinity of the organism is contaminated by the upward motion of the organism itself. This error is due to the fact that the features on the organism produce a strong correlation peak in interrogation areas which overlap both the organism and the fluid surrounding it. Application of image and vector masking (Fig. 13b) provides a cleaner picture where the flow field information around *A. Tonsa* is only extracted from the liquid phase.

71

Figure 13. Flow field during the power stroke at t=3.5ms, (a) without masking (b) with image and vector masking. Swim speed at this instant is ~40mm/s. Both subfigures are a result of 16x16 final IA size, 50% overlap followed by UOD scheme with a detection threshold of 0.5.

In both masked and unmasked results, the wake behind the organism and two vortices are detected; one on each side of the organism and each with op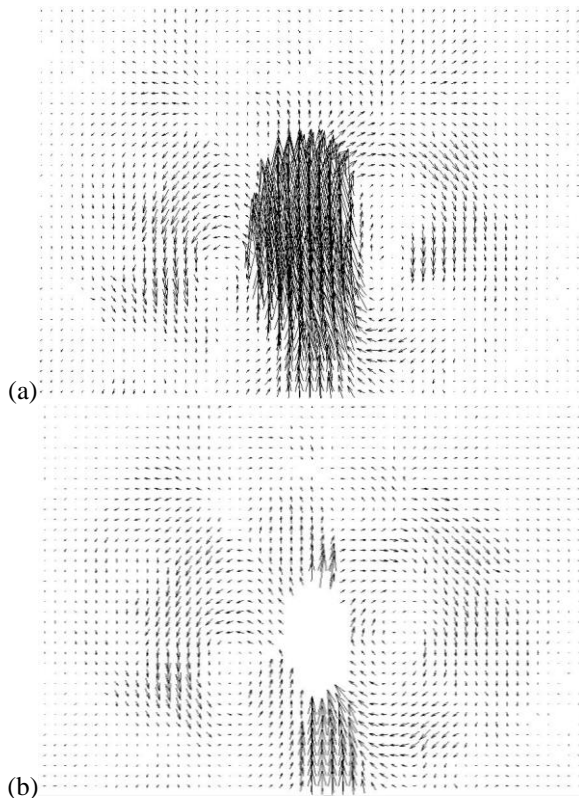posite rotation directions. The counter-rotating vortex system is an indication of a toroidal (ring) vortex system in three-dimensions which is in agreement with the previous findings in Wadhwa et al. (2014). The spatial dimension of the toroidal vortex is similar to the length of the organism. The observed toroidal vortex ring is more clearly visible in Fig. 13b when compared to Fig. 2 in Wadhwa et al. (2014). This is primarily due to the improved image processing functions used here. The masking process successfully removes the contribution of moving particles stuck on the organism.

DISCUSSION, RECOMMENDATIONS & FUTURE WORK

Masking will continue to be an important step in PIV analysis because it allows phase-separated measurements which improve the velocity accuracy along phase boundaries. Phase boundaries are locations where many interesting flow phenomena occur, such as velocity gradients, flow separations, gas expansions, impinging flows and many others. Ironically, this is where masking algorithms often fail and generate the most measurement uncertainty. This necessitates the evaluation of mask quality along the actual phase boundaries and warrants some future investigations into the quantification of mask performance.

It was shown in both application examples that masking improves the accuracy and understanding of the flow field, by removing the swimming object from the analysis. Furthermore, it is shown in the case of *E. Gracilis* that vector masking should almost always be accompanied with image masking for a better representation of flow around the organism. It is described here as "a better representation" of the actual flow field, because the accuracy can still be improved. For instance, there are often sharp velocity gradients in thin boundary layers and the size of the interrogation window where the cross-correlation is applied is relatively large. In such situations, the displacement estimation is often biased towards the faster moving fluid particles which are located away from the wall in the correlation window. Vector repositioning, wall windowing or particle tracking techniques can further improve the accuracy close to these boundaries. Achieving improved accuracy using dynamic masking in conjunction with the above mentioned boundary techniques will be the subject of future investigations.

It is clear that the use of image processing functions is key for dynamic masking. Some image processing functions are more preferrable than others in the literature—median, opening, closing, erosion, dilation and threshold filters—and are widely used for histogram thresholding-based masking algorithms. Since the number of experimental conditions is infinite, it is essential to use these flexible image-processing functions to generate appropriate image masks. Additionally, manual mask generation is a user-dependent process and should be avoided if possible. Instead, masking should be performed based on algorithms in a systematic and traceable fashion. Another recommendation is to work with positive particle images during algorithm development, which can be achieved by a simple pixel inversion in cases with particle shadows.

Based on the results provided here, and in the author's opinion, a histogram thresholding-based dynamic masking is recommended if the object / surface is deforming and changing direction. On the other hand, feature tracking-based dynamic masking should be a better choice for dynamic masking if the object is rigid and does not rotate within the FoV. In practice, this is often not the case, because the object is either deforming or rotating. In order to cope with these situations, future investigations will focus on more advanced feature-tracking techniques where the tracked feature is changing shape and/or orientation from one frame to the next.

Currently, no automated dynamic masking technique is reported which is capable of working globally for every application. There is a general demand for a robust

technique that performs automatic object recognition and phase separation, both for double-frame and for time-resolved acquisitions. This warrants future investigations which focus on a hybrid technique (histogram thresholding + boundary detection + tracking) for automated dynamic masking with minimum input from the user. Edge detection methods are few and far between in the literature, which may indicate more possibilities for better algorithms. In particular, the actively deforming contours technique is interesting for investigation because of its applicability to both smooth and rough contours.

One final remark can be made on the effect of measurement plane thickness and object thickness on the accuracy of the masking techniques described here. (The thickness of the measurement plane is defined by the depth of field of the imaging system in the case for *E. Gracilis* and by the thickness of the light sheet in the case for *A. Tonsa*.) If the thickness of the object was much smaller than the measurement plane thickness, some particles may have been present in the illuminated zone between the object and the objective and could potentially be registered on the PIV images. This would have added some noise on top of the object image and may have had a negative influence on the accuracy for both masking techniques. Fortunately, in both dynamic masking applications presented here, the imaged objects are are thicker than the measurement plane, so noise-free object images were recorded.

ACKNOWLEDGMENTS

REFERENCES

Carrier O, Ergin FG, Li HZ, Watz BB and Funfschilling D "Time-resolved mixing and flow-field measurements during droplet formation in a flow-focusing junction" J. Micromech. Microeng. (2015) 15 084014

M1 - Movie of the droplet break-up experiment performed by Carrier et al. http://www.dantecdynamics.com/microfluidics-category/time-resolved-velocity-measurements-of-droplet-formation-in-a-flow-focusing-junction

Coron X, Champion JL and Champion M: Simultaneous measurements of velocity field and flame front contour in stagnating turbulent premixed flame by means of PIV. In 12th International Symposium on Applications of Laser Techniques to Fluid Mechanics, 2004.

Deen NG, et al. On image pre-processing for PIV of single-and two-phase flows over reflecting objects. Exp Fluids, 2010, 49.2: 525-530.

Ergin FG "Flow field measurements during microorganism locomotion using MicroPIV and dynamic masking" Proc. 11th Int. Symp. on PIV, Santa Barbara, California, September 14-16, 2015

Ergin FG, Watz BB and Wadhwa N "Pixel-accurate dynamic masking and flow measurements around small breaststroke-swimmers using long-distance MicroPIV" Proc. 11th Int. Symp. on PIV, Santa Barbara, California, September 14-16, (2015a)

Ergin FG, Watz BB, Erglis K and Cebers A "Time-resolved velocity measurements in a magnetic micromixer" Exp. Therm. Flu. Sci. (2015b) 67, pp. 6-13

Fritz HM, Hager WH and Minor HE "Landslide generated impulse waves. 1. Instantaneous flow fields" Exp Fluids 35 (2003) 505-519

Gui L and Merzkirch W (1996) Phase-separation of PIV measurements in two-phase flow by applying a digital mask technique. ERCOFTAC Bulletin 30: 45-48

Hammad KJ. "Liquid jet impingement on a free liquid surface: PIV study of the turbulent bubbly two-phase flow." In: ASME 2010 3rd Joint US-European Fluids Engineering Summer Meeting collocated with 8th International Conference on Nanochannels, Microchannels, and Minichannels. American Society of Mechanical Engineers, 2010. p. 2877-2885.

Honkanen M and Saarenrinne P "Multiphase PIV method with digital object separation methods" 5th International Symposium on PIV, Busan Korea, Sept 2003

Lindken R and Merzkirch W (2000) Velocity measurements of liquid and gaseous phase for a system of bubbles rising in water. Exp Fluids 29, 194-201

Lindken R and Merzkirch W (2002) A novel PIV technique for measurements in multiphase flows and its application to two-phase bubbly flows. Exp Fluids 33, 814-825

Sanchis A and Jensen A "Dynamic masking of PIV images using the Radon transform in free surface flows" Exp in Fluids 2011 51(4) 871-880

Seol DG and Socolofsky SA (2008) Vector post-processing algorithm for phase discrimination of two-phase PIV. Exp Fluids 45:223

Stevens EJ, Bray KNC and Lecordier B "Velocity and scalar statistics for premixed turbulent stagnation flames using PIV" Proc. 27th International Symposium on Combustion (1998) pp. 949-955.

Sveen JK and Dalziel SB "A dynamic masking technique for combined measurements of PIV and synthetic schlieren applied to internal gravity waves" Measurement Science and Technology, (2005) 16, 1954-1960

Wadhwa N, Andersen A and Kiørboe T "Hydrodynamics and energetics of jumping copepod nauplii and copepodids" J. Exp. Biol. (2014) 217, pp.3085-3094

Westerweel, J. and & Scarano, F. (2005). Universal outlier detection for PIV data. Experiments in Fluids, 39(6), 1096-1100.

Wosnik, M., and Arndt, R. E. A., (2013), "Measurements in High Void-Fraction Bubbly Wakes Created by Ventilated Supercavitation," ASME J. Fluids Eng. 135(1), pp. 011304-011304-9

A NEW METHOD FOR THE OPTIMIZATION OF INSULATION THICKNESS FOR RADIANT WALL HEATING SYSTEMS

Aliihsan KOCA*, Gürsel ÇETİN** and Eser VELİŞAN***

*Fatih Sultan Mehmet Vakıf Üniversitesi, Mühendislik Fakültesi, 34445 İstanbul, Türkiye, ihsankoca@hotmail.com
** Mir Araştırma ve Geliştirme A.S., 34220 Istanbul, Turkey, mgurselcetin@gmail.com
*** Mir Araştırma ve Geliştirme A.S., 34220 Istanbul, Turkey, velisan.eser@gmail.com

Abstract: In this study we proposed a new modified New Degree-Day Method (NDDM) for the optimization of insulation thickness of the wall where the radiant panels are mounted (WMRP) in which heat generation inside the wall is considered. The existing Standard Degree-Day Method (SDDM) is not applicable to estimate the optimum insulation thickness for the buildings where the WMRP is mounted. Because SDDM method uses indoor air temperature as a base temperature, hence heat generation through the WMRP cannot be taken into account. In the new method, important parameters were obtained from the series of the CFD analysis for different thermal transmittance coefficient (U) and outdoor air temperature (To) values are used to create an empirical equation for the estimation of Tp (new base temperature) with the multiple polynomial regression method. Then the numerical results were validated with experimental results which were obtained from the real-size test chamber. Using the new method optimum insulation thickness, net energy saving and payback periods for radiant wall heating systems were calculated (for Istanbul climate) and compared with the results which were obtained using the standard degree-day method (SDDM). The results showed that, the SDDM significantly lower (85-95%) estimates the optimum insulation thickness and can't be used for the buildings where the WMRP is used. The new method can be used for radiant wall heating systems where the performance of radiant heating systems is significantly affected by the insulation capabilities and has a great importance in the sizing process of the radiant systems.
Keywords: Radiant wall heating; Optimum insulation thickness; New degree-day method.

IŞINIMLA DUVARDAN ISITMA SİSTEMLERİNDE YALITIM KALINLIĞI OPTİMİZASYONUNDA KULLANILABİLECEK YENİ BİR YÖNTEM

Özet: Bu çalışmada ışınım ısıtma panellerin kullandığı duvarlardaki yalıtım kalınlığının optimizasyonu için, duvarlardaki ısı üretimini dikkate alan, yeni bir derece-gün yöntemi (NDDM) geliştirilmiştir. Standard Derece-Gün Yöntemi (SDDM) temel sıcaklık olarak mahal hava sıcaklığını dikkate almakta ve duvara monte edilmiş ışınım panellerindeki ısı üretimini dikkate alamamaktadır. Bu yüzden standart yöntem ile ışınım panellerin bulundugu duvarlar için yalıtım kalınlığı optimizasyonu yapmak imkansızdır. Önerilen yeni metotta kullanılan yeni temel sıcaklık değerinin (Tp) elde edilmesinde kullanılan ampirik ifade (3. dereceden polinom) farklı yapı ısı geçirgenlik katsayısı (U) ve farklı dış hava sıcaklıkları (To) parametreleri için sayısal analizlerden elde edilmiştir. Daha sonra sayısal çalışmaların sonuçları aynı şartlarda yürütülen gerçek ölçekli deney sisteminde doğrulanmıştır. İstanbul iklim şartları için yeni yöntem ve eski yontem kullanılarak ideal yalıtım kalınlıkları, enerji tasarrufları ve geri dönüş süreleri hesaplanmış, iki yöntemden elde edilen sonuçlar kıyaslanmıştır. Sonuçlara göre eski yöntemle hesaplanan ideal yalıtım kalınlığı yeni yöntemden elde edilen değerin çok altında (%85-95) kalmaktadır. Bu yüzden standart yöntemin ısı üretimi olan duvarlarda kullanılmasının mümkün olmadığı görülmüştür. Önerilen yeni yöntem ise, ışınımla ısıtma sistemlerinin projelendirilmesinde önemli bir kriter olan ısı kayıplarının hesaplanması ve ideal yalıtım kalınlığının belirlenmesinde kullanılabilecektir.
Anahtar Kelimler: Işınımla duvardan ısıtma, Optimum yalıtım kalınlığı, Yeni derece-gün yöntemi.

NOMENCLATURE

A	Area [m²]	H_u	Lower heating value of the fuel [j/kg]
C_A	Annular heating cost [TL/yr]	k	Heat conduction coefficient [W/m.K]
C_f	Fuel cost [TL/kg]	m_f	Annular fuel mass [kg]
C_{tins}	Insulation cost per unit area [TL/m²]	R_i	Inside air film thermal resistance [m².K/W]
h_i	Inner heat transfer coefficient [W/m².K]	R_o	Outside air film thermal resist. [m².K/W]
h_o	Outer heat transfer coefficient [W/m².K]	R_w	Total thermal resistance [m².K/W]
		T_b	Base temperature [°C]
		T_i	Indoor air temperature [°C]
		T_o	Outdoor air temperature [°C]

INTRODUCTION

It is a fact that energy consumption is one of the world's biggest problems since energy need is increasing proportionally to the population and conventional sources are diminishing evenly. As a result of this, the International Energy Agency (2013) predicts an increase in global energy consumption by 56% from 2010 to 2040. For the present, fossil fuels are used as major energy sources but they will not able to meet energy requirement in the near future. Thus, it is important to ensure energy efficiency when using fossil fuels and place an emphasis on finding alternative energy solutions. Energy management and efficiency will be an important matter in the coming years. Therefore developing systems which promote energy saving is inevitable. Although the economy has been growing gradually in Turkey as well as energy demand and energy policy is heavily dependent on imported energy. The government invested 25$ billion in energy production between the years 2002 and 2011, but still Turkey has to import 71% of energy needs. According to the Energy and Natural Resources Ministry of Turkey (2013) 31% of Turkey's energy is being used in buildings. This high percentage is due to the fact that most buildings do not meet general energy efficiency criteria such as thermal insulation requirements for external walls. Thermal insulation is an easy and applicable method to increase energy efficiency by means of decreasing the heat flux from indoor to outdoor and vice versa (Çomaklı and Yüksel, 2003).

Insulation thickness is a parameter which balances investment and operational cost. In the literature, there are many studies which have been investigating how to determine optimum insulation thickness (Yıldız et al., 2008; Dikmen, 2011; Bolattürk and Dağıdır, 2013; Kaynaklı, 2013; Kaya et al., 2016; Duman et al., 2015). Çomaklı and Yüksel (2004) used life cycle cost analysis (LCCA) based on the degree day method for calculation of optimum insulation thickness and annual energy savings of some cities from 4th climatic region of Turkey and also they discussed the subject from an

environmental point of view. Optimum insulation thickness of Denizli region for different fuel types and different insulation materials was obtained by Dombaycı et al. (2006) by using the standard degree-day method. Differently, Arslan and Köse (2006) also took into account the effect of condensed vapor within the standard degree day method. Further, Sisman et al. (2007) calculated optimum insulation thickness of roofs for different degree-day regions of Turkey. Kaynaklı (2008) chose Bursa as a model city and evaluated residential energy requirement for heating season and calculated optimum insulation thicknesses for different types of fuels. Bolattürk (2008) calculated the optimum insulation thickness using his method and compared the results with the standard heating degree-hour method. Ucar (2010) determined optimum insulation thicknesses for four different climatic regions of Turkey by using exergy analysis method. Optimum insulation thicknesses and energy savings were also studied by Ucar and Balo (2010) for different regions of Turkey. Ozkan and Onan (2011) considered effects of glazing areas on the optimum insulation thickness. Ozel (2011) determined optimum insulation thickness by using a dynamic method. Kaynaklı (2012) reviewed the existing studies with focusing on reported optimum insulation thickness results. Ekici et al. (2012) calculated optimum insulation thickness using different wall structures and fuels for different regions of Turkey. De Rosa et al. (2014) evaluated energy demand by a method which combines dynamic model based on the lumped capacitance approach and electrical analogy method.

Radiant heating systems are different from typical HVAC systems because they heat surfaces rather than air and can save large amounts of energy while providing higher levels of thermal comfort. The radiant heating system consists of large radiant heat transfer surfaces can be installed on room walls, floors or ceilings. A conditioned surface is called as a radiant system if 50% or more of the designed heat transfer on the temperature-controlled surface takes place by thermal radiation.

Radiant heating systems are quite convenient alternatives to the traditional HVAC systems. They reduce energy consumption because of low-temperature heating and high temperature cooling operations. In the literature heat transfer, thermal comfort performances and energy efficiency capabilities of these kinds of systems have been studied in detailed (Kilkis, 2006; Tye-Gingras and Gosselin, 2012; Seyam et al., 2014; Bojic et al., 2015; Rehee and Kim, 2015; Jeong et al., 2013; Stetiu, 1999; Franc, 1999; Miriel et al., 2002; Koca et al., 2016; Koca et al., 2014; Koca et al., 2013; Koca, 2011; Erikci Çelik et al., 2016; Kanbur et al., 2013; Acikgoz and Kincay, 2015). Therefore this proven technology should be disseminated in Turkey to achieve energy efficiency goals of the country.

In the literature, not many studies available dealt with the optimization of insulation thickness for radiant heating cooling systems. There is only one study (Cvetkovi and Bojic, 2014) available in the literature, in which the investigators used Energy Plus© software to

evaluate the energy consumption of the simulate building. They reported that radiant wall insulation requires a higher insulation thickness when compared with other radiant systems. Moreover the thickness of thermal insulation is the highest for the location where the radiant panels are located. The house with the optimal thermal insulation thickness has significant energy saving compared to house with older customary thermal insulation (Cvetkovi and Bojic, 2014). But in their study, they conducted the simulations according to Serbian climate conditions without any experimental validation. Moreover, they did not compare the classical methods with their newly reported results.

In most of the aforementioned studies researchers dealt only with theoretical examination using either degree-day or hourly-based methods without any experimental validation. As a result of this the results of these studies are not valid for the radiant heating systems, since the indoor air temperatures are taken into account as a heat source (or base temperature). In radiant heating systems there is no indoor heat loss through the walls where the radiant heating panels are mounted. In such cases heat loss occurs through the panel backside surfaces. Therefore, in this study we propose a new method to evaluate the optimum insulation thicknesses of radiant wall heating systems that takes into account the radiant panel backside temperature as a heat source where the huge amount of heat leakage occurs. For this reason, our first goal is to evaluate optimum insulation thicknesses for radiant wall heating systems since the performance of radiant heating systems is significantly affected by the insulation capabilities and has a great importance in the sizing process of the radiant systems. In the new method important parameters, that were obtained from a series of the CFD analysis for different thermal transmittance coefficient (U) and outdoor air temperature (To) values, are used to create an empirical correlation for the estimation of Tp (the new base temperature) with multiple polynomial regression method. A new experimental test set-up which simulates typical conditions of occupancy in an office or residential room was used for the validation of the computational results. Then serial CFD analyses were conducted to create a new correlation for the estimation of the base temperature (Tp) with multiple polynomial regression method (MPR). Based on the new base temperature, LCCA based Standard Degree-Day Method (SDDM) is adjusted for Wall-Mounted Radiant Panel (WMRP) and created a New LCCA based Degree-Day Method (NDDM). Using the new method optimum insulation thickness, net energy saving and payback periods for radiant wall heating systems were calculated for the city of Istanbul and compared with the results which were obtained using the standard degree-day method (SDDM).

NUMERICAL MODEL

In this work, a numerical model was developed using the commercial CFD package ANSYS-FLUENT© Version 15 to simulate the WMRP. Fluent uses a control-volume-based technique to convert an inclusive scalar transport equation to an algebraic equation that is solved numerically. The steady simulations were performed with the software, using the coupled double precision solver.

Physical Model

A 3D model that has the same dimensions as the experimental set-up (1.2 m in height, 0.6 m in length) was used for the simulations. The pipe in the panel which is made of cross-linked polyethylene (PEX) has 10.1 mm outer diameter and 1.1 mm thickness with 150 mm pipe spacing. The gypsum board which is exposed to the inside room has 1.5 cm thickness. EPS (Expanded Polystyrene) was used as an insulation material which has a coefficient of thermal transmittance value of 0.039 W/m.K (at 25˚C). To decrease the mesh number and precisely solve the heat loss from the WMRP, experimental room domain wasn't considered in our numerical model. Instead, average total heat transfer coefficient – comprised of the radiation and convection – was implemented as a surface boundary condition. The implemented average total heat transfer coefficient was obtained experimentally (using the same test chamber in this study) in our previous study (Koca et al., 2014) using different WMRP surface temperatures and which are valid for wide range (25 - 45 °C) of WMRP surface temperature. According to the results of Koca et al. (2014), the measured average values of radiant heat transfer coefficient is about 5.46 $W/m^2.K$ and convection heat transfer coefficient is about 2.32 $W/m^2.K$ resulting in an average total heat transfer coefficient of 8.33 $W/m^2.K$ – which was considered in this study. Obtained average total heat transfer coefficient for wall (8.33 $W/m^2.K$) is compatible with the ones typically shown in standards of EN 15377-1 (2008) and EN 1264-5 (2008).

Computational Domain, Mesh and Mesh Independency Analysis

The computational mesh was generated using tetra and hexahedral elements with ANSYS Meshing tool. In order to accurately resolve the solution fields in the vicinity of the heat transfer surface between pipe and the surrounding interface, the mesh was refined at the area where the heating pipes are embedded. The grid was fine enough for the other areas to solve the simple heat conduction problem. A sample of the computational model and grid was shown in Fig. 1.

Before the computations, a grid independence study was carried out to ensure the results' accuracy. Eight different mesh configurations (varies from 1M to 27M) were analyzed for same boundary conditions and the calculated panel backside surface temperature (T_p) – which is our main parameter – was compared. As shown in Fig. 2, at the range between the first and third configurations of the results slightly vary with the grid resolution but after the fourth mesh configuration, T_p tends towards constant. So after that point the results can be considered grid independent. In regard to this mesh independence results, simulations were carried

out with the mesh configuration which has 6.5M elements and average skewness value of 0.20.
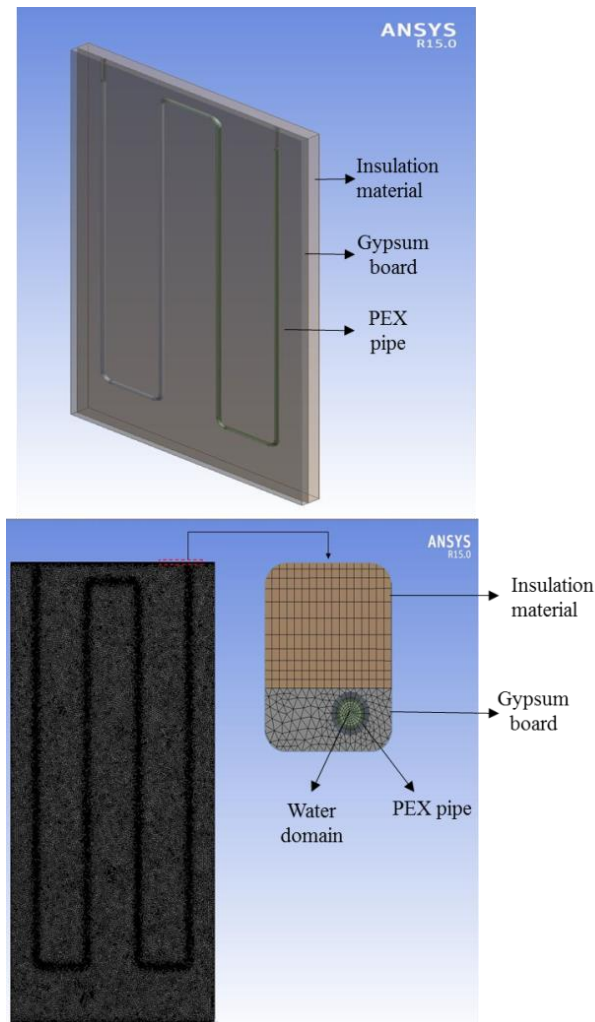

Figure 1. CAD model of the panel (left) and computational mesh grids (right)
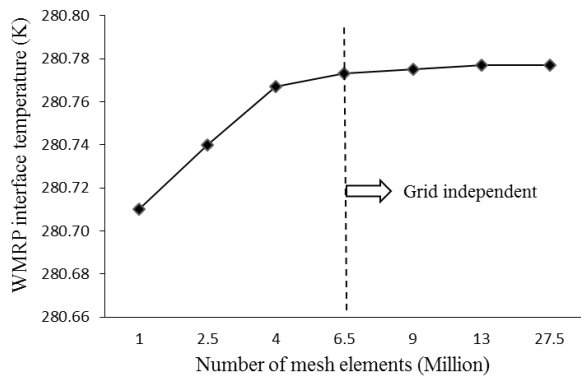

Figure 2. Mesh independence study

Solution Methods and Procedure

3D, steady-state, CFD analysis were performed by using ANSYS FLUENT 15$^{©}$. Mass, momentum and energy conservation equations were solved numerically. As main boundary condition, WMRP surface was set as mixed (radiation and convection) heat transfer surface, where the average total heat transfer coefficient (sum of radiation and convection) was defined as the value of 8.33 W/m^2.K (radiant and convective heat transfer coefficients were obtained from our previous work done by Koca et al., 2014). The other side walls were set as adiabatic boundary conditions. The backside of the panel was set to the convection surface having the certain value of total heat transfer coefficient of 25 W/m^2.K.

The outside air temperature of the WMRP – which is exposed to outside conditions – was set at certain values and studied as a parameter in the simulations. The indoor room temperature (T_i) was defined constant as 15°C for all cases. Inlet water mass flow rate was defined as constant at the value of 0.04 kg/s (Reynolds number is 4200). Therefore a turbulence model (Realizable k-ε model) was chosen for the calculations. Also enhanced wall treatment was implemented for the heat transfer surface where the y$^+$ value is varied between 1 and 5. Among the different code options, Second Order Upwind law interpolation scheme and the discretized equations were chosen and numerically solved by the SIMPLE algorithm. In the present work, all the solutions were considered to be fully converged when the sum of residuals was below 1×10^{-4}.

Multiple simulations were conducted by varying outdoor air temperature (T_o) and insulation thickness (Δ_p) of the WMRP. Outdoor air temperature values between -15 °C and +18 °C (34 different outdoor temperatures increased numerically between -15 °C and +18 °C within a value of around 1 °C) were set as a boundary conditions of the WMRP while the insulation thickness of the panel was varied between 0 - 16 cm (16 different insulation thickness with 1 cm variation). On the basis of the obtained simulations, the backside surface temperatures of WMRP (T_p) were evaluated using area-weighted-average method (cell-centered) and the results are presented in Table 1.

In the table, values of total U (overall coefficient of thermal transmittance of WMRP) and outdoor air temperature (T_o in °C) are the input parameter, WMRP backside temperature (T_p in °C) is the output parameter of the simulations.

Table 1. Result summary of the numerical simulations

T_o	U_{NDDM}	x	T_p	T_o	U_{NDDM}	x	T_p	T_o	U_{NDDM}	x	T_p	T_o	U_{NDDM}	x	T_p
-15	0.23	16	20.7	2	0.23	16	23.1	18	0.23	16	25.8	1	0.23	16	22.9
-14	0.24	15	20	3	0.24	15	23	17	0.24	15	25.6	0	0.24	15	22.5
-13	0.26	14	19.8	4	0.26	14	23	16	0.26	14	25.3	-1	0.26	14	22.1
-12	0.28	13	19.6	5	0.28	13	22	15	0.28	13	24	-2	0.28	13	21.6
-11	0.30	12	19.4	6	0.30	12	22.9	14	0.30	12	24.6	-3	0.30	12	21.1
-10	0.32	11	19.1	7	0.32	11	22.9	13	0.32	11	24.2	-4	0.32	11	20.5
-9	0.35	10	18.8	8	0.35	10	22.8	12	0.35	10	23.8	-5	0.35	10	19.8
-8	0.38	9	18.5	9	0.38	9	22.8	11	0.38	9	23.3	-6	0.38	9	19
-7	0.42	8	18.1	10	0.42	8	22.7	10	0.42	8	22.7	-7	0.42	8	18.1
-6	0.47	7	17.6	11	0.47	7	22.6	9	0.47	7	22	-8	0.47	7	17
-5	0.53	6	17	12	0.53	6	22.5	8	0.53	6	21.2	-9	0.53	6	15.8
-4	0.61	5	16.4	13	0.61	5	22.4	7	0.61	5	20.3	-10	0.61	5	14.3
-3	0.72	4	15.7	14	0.72	4	22.3	6	0.72	4	19.2	-11	0.72	4	12.6
-2	0.88	3	14.7	15	0.88	3	22.1	5	0.88	3	17.7	-12	0.88	3	10.3
-1	1.12	2	13.5	16	1.12	2	21.9	4	1.12	2	15	-13	1.12	2	7.6
0	1.56	1	11.9	17	1.56	1	21.6	3	1.56	1	13.6	-14	1.56	1	3.9
1	2.55	0	9.8	18	2.55	0	21.3	2	2.55	0	10.3	-15	2.55	0	-1.2

METHODOLOGY

A New Degree-Day Calculation Method for Wall-Mounted Radiant Panels

In (SDDM), degree-day value (DD) is calculated using inner and outer air temperatures for a fixed base temperature. This method cannot be applied for buildings heated by WMRP due to the fact that WMRP has different heat transfer characteristic comparing to the conventional systems. Because in these kinds of systems, heat source is part of the wall structure and this causes two-way conduction in the structure. However, as shown in Fig. 3, the temperature gradient from inner surface temperature (T_{si}) to outer air temperature (T_o) in conventional systems is similar to the temperature gradient (from backside temperature, T_p to outer air temperature, T_o) in radiant systems. Therefore, a correlation for the evaluation of T_p which is based on the T_o and overall heat transfer coefficient of wall (U) was obtained using a numeric and statistical methods.
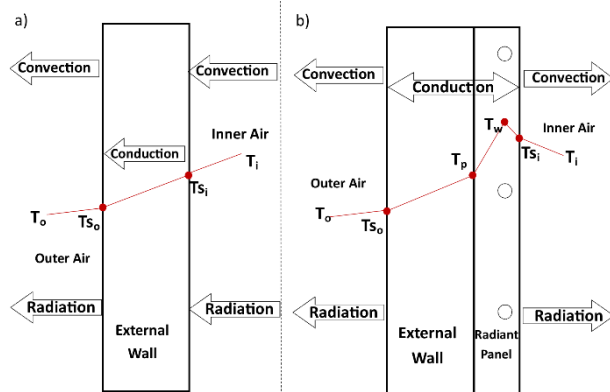

Figure 3. Heat transfer through external wall in a) conventional system b) WMRP system

Moreover base temperature (T_i in Fig. 3) was defined as 15°C for the calculation of degree-day value in SDDM whereas internal heat sources (human, electronic devices etc.) exist. Eqs. 1 and 2 show the general calculation procedure of the DD value:

$$f(D) = \begin{cases} 0 \, , \ T_b < T_o \\ T_p(U, T_o) - T_o \, , \ T_b \geq T_o \end{cases} \tag{1}$$

$$DD = \sum_{D=1}^{N} f(i) \tag{2}$$

25-year averages of daily air temperatures were used to calculate the degree-day value and the degree day value is a series sum of day 1 to day 365 as a function of T_p. Also T_p is a function of x, which was obtained from regression of CFD results.

Multiple Polynomial Regressions

Multiple polynomial regressions, is a statistical approach for modeling of the relationship between a dependent variable and independent variables. WMRP backside temperature (T_p) values were obtained from series of the CFD analysis for different thermal transmittance coefficient (U) and outdoor air temperature (T_o) values were used to create an empirical equation for the estimation of T_p with multiple polynomial regression method (MPR) where the Newton-Raphson method was implemented. In MPR, 3rd degree of the polynomial equation (Eq. 3) was chosen in which the results were best yielded (correlation coefficient (R^2) is 0.998 and Residual Sum of Squares (RSS) is 0.74).

$$T_p = A T_o^3 + BT_o^2 U + CT_o U^2 + DU^3 + ET_o^2 + FT_o U + GU^2 + HT_o + IU + J \tag{3}$$

$$DD = \sum_{D=1}^{N} A T_o^3 + BT_o^2 U + CT_o U^2 + DU^3 + ET_o^2 + FT_o U + GU^2 + (H-1)T_o + IU + J \tag{4}$$

The constant coefficients of the above equations are given in Table 2.

Table 2. Coefficients of the polynomial equation

A	B	C	D	E
$-1.40 \cdot 10^{-4}$	$-2.36 \cdot 10^{-4}$	$-9.61 \cdot 10^{-2}$	-1.27	$1.16 \cdot 10^{-1}$
F	**G**	**H**	**I**	**J**
$6.16 \cdot 10^{-1}$	34	-32	-169.1	3223.15

Calculation of Optimum Insulation Thickness Using New and Standard Degree Day Methods

Eqs. 5-6 and Eqs. 9-15 are common for both new and standard methods. Calculation method of overall heat transfer coefficient (U) is similar both in NDDM and SDDM. Nevertheless in NDDM inner heat transfer coefficient (h_i) and thermal resistance of panel (R_p) are not included into the equation since these parameters have already been taken into account in the CFD calculations and embedded into the proposed equation of T_p (Eq. 3).

The heat loss per unit area of external walls is given by:

$$Q = U(T_b - T_o) \tag{5}$$

Annual heat loss per unit area from external walls (q'') in the terms of degree-days is given by:

$$q'' = 86400 \cdot DD \cdot U \tag{6}$$

Overall heat transfer coefficient (U) and equivalent thermal resistance of wall (R_{tw}) were calculated using the Eqs. 7-8. Whereby, Eq. 8a and Eq. 8b were used to calculate the U values of interest for SDDM and NDDM respectively:

$$R_{tw} = R_w + R_{ins} + R_i + R_o \tag{7}$$

$$U_{SDDM} = \frac{1}{R_w + \frac{x}{k} + \frac{1}{h_o} + \frac{1}{h_i}} \tag{8a}$$

$$U_{NDDM} = \frac{1}{R_w + \frac{x}{k} + \frac{1}{h_o}} \tag{8b}$$

Where, R_o and R_i are the inside and outside air film thermal resistance, R_w is the total thermal resistance of the wall associated with the structural components of the wall and panel, h_i (W/m^2.K) is the inner, h_o (W/m^2.K) is the outer convective heat transfer coefficients, x is the insulation thickness (m) and k (W/m.K) is the heat conduction coefficient of insulation material.

Annual energy requirement (E_A) was calculated by the Eq. 9 and it corresponds to annual heat loss.

$$E_A = m_f \cdot H_u \cdot \eta = \frac{86400 \cdot DD}{\left(R_{tw} + \frac{x}{k}\right)} \tag{9}$$

Where, m_f (kg) is the annular fuel mass consumption, H_u (j/kg) is lower heating value of the fuel and η (%) is the efficiency of the heating system.

Then, the annular fuel mass consumption (m_f) was obtained by dividing the annual heat loss (E_A) by lower heating value (H_u) and efficiency (η) of fuel, yields:

$$m_f = \frac{86400 \cdot DD}{\left(R_{tw} + \frac{x}{k}\right) \cdot H_u \cdot \eta} \tag{10}$$

If we multiply annular fuel mass consumption (m_f) with the fuel cost C_f (TL/kg), we get annular heating cost per unit area (C_A):

$$C_A = m_f \cdot C_f \tag{11}$$

$$C_A = \frac{86400 \cdot DD \cdot C_f}{\left(R_{tw} + \frac{x}{k}\right) \cdot \eta \cdot H_u} \tag{12}$$

The LCCA used in this paper calculates the heating cost over the lifetime of the building. The total heating cost over a lifetime of N years is estimated in present value Turkish Liras using the PWF (Present Worth Factor). The PWF depends on the inflation rate g, and the interest rate i. The PWF, which is dependent on the inflation rate g and the interest rate i, is adjusted for inflation rate as shown below (Hasan A., 1999). The interest rate modified for inflation rate, i^*, is defined by the following equations:

$$i^* = \frac{i-g}{1+g} \qquad (i > g) \tag{13}$$

and

$$PWF = \frac{(1+i^*)^N - 1}{i^*(1+i^*)^N} \tag{14}$$

Where N is the lifetime and which is assumed to be 20 years.

Total cost (C_t) was calculated by multiplying the Present Worth Factor (PWF) into annual heating cost (C_A) and adding the total insulation cost per unit area ($C_{t_{ins}}$).

$$C_t = \frac{86400 \cdot DD \cdot C_f \cdot PWF}{\left(R_{tw} + \frac{x}{k}\right) \cdot \eta \cdot H_u} + C_{t_{ins}} \tag{15}$$

The cost of investment of the insulation material is given by the following equation:

$$C_{t_{ins}} = C_{ins} \cdot x \tag{16}$$

Where, C_{ins} (TL/m^2) is the cost of insulation per unit insulation area. Therefore, the following equation gives the total cost of heating of insulated building in present sum of Turkish Liras:

$$C_t = \frac{86400 \cdot DD \cdot C_f \cdot PWF}{\left(R_{tw} + \frac{x}{k}\right) \cdot \eta \cdot H_u} + C_{ins} \cdot x \tag{17}$$

Then, the optimum insulation thickness was obtained by minimizing the total heating cost (C_t). Therefore, the derivative of C_t with respect to the insulation thickness (x) was taken and set equal to zero, from which the optimum insulation thickness (x_{op}) values were derived for SDDM (Eq. 18a) and NDDM (Eq. 18b) as follows:

$$\frac{dC_t}{dx} = C_{ins} - \frac{86400 \cdot DD \cdot C_f \cdot PWF \cdot k}{\left(k \cdot R_{tw} + x\right)^2 \cdot \eta \cdot H_u} \tag{18a}$$

$$\frac{dC_t}{dx} = \sum_{D=1}^{N} C_{ins} - \left(\frac{86400 \cdot PWF \cdot C_f \cdot U_{NDDM}^3}{k \cdot H_u \cdot \eta} \cdot \left(4 \cdot D \cdot U_{NDDM}^2 + 3 \cdot U_{NDDM} \cdot \left((C \cdot T_o(i)) + G \right) + 2 \cdot \left(I + \left(F \cdot T_o(i) \right) + B \cdot T_o(i)^2 \right) + \frac{A \cdot T_o(i)^3 + E \cdot T_o(i)^2 (H-1) \cdot T_o(i) + J}{U_{NDDM}} \right) \right) \quad (18b)$$

Eqs. 18a and 18b are different in both methods since in the NDDM T_p is a function of U (also U is a function of x). Hence, derivation results of the Eq. 19 are different for NDDM than SDDM.

Despite of the aforementioned differences in the previous steps, the methodology of the last two steps is common for both SDDM and NDDM. A root of Eq. 19 which is the minimum point of the Eq. 18, gives the optimum insulation thickness values.

$$\frac{dC_t}{dx} = 0 \quad (19)$$

For the SDDM, the derivative of the Eq. 18a gives the optimum insulation thickness value, which is obtained as follows:

$$x_{opt} = \sqrt{\frac{86400 \cdot DD \cdot C_f \cdot PWF \cdot k}{C_{ins} \cdot \eta \cdot H_u}} - k \cdot R_{t_w} \quad (20)$$

In Eq. 18a, DD value is constant for SDDM, while the DD value in Eq. 18b for NDDM is a function of U_{NDDM} and accordingly function of x. For this reason in NDDM, optimum insulation thickness values were obtained using the Matlab$^{©}$ code because of the complicity of the dependent variables in the Eq. 18b. In the code, to sum up the series, T_o values were defined as a matrix. Since only the value of x is independent variable in the equation, the solution matrix was equalized to zero and then the values of x obtained.

Parameters used in the optimization calculations are shown in Table 3.

Table 3. Parameters used in the optimization of insulation thickness

Parameters		
Interest rate, i	%	8 %
Inflation rate, g	%	7.49 %
Life cycle, N	yr	20
Present Worth Factor, PWF	-	14.99
h_0	W/m^2.K	25
C_f (N. Gas)	TL/kg	1.003
C_f (Lignite)	TL/kg	0.38
H_u (N. Gas)	j/kg	3.46 x 10^7
H_u (Lignite)	j/kg	2.10 x 10^7
η_u (N. Gas)	%	93
η_u (Lignite)	%	65
C_{EPS}	TL/m^2	300
k_{EPS}	W/m.K	0.4

EXPERIMENTAL VALIDATION

The Arrangement of the Test Chamber

The climatic test chamber was constructed to simulate radiant wall heating system under various boundary conditions which are listed in Table 4. As seen in Fig. 4 and Fig. 5, the test chamber is composed of four zones: Ceiling (volume-4), floor (volume-3), façade (volume-2) and the tested zone (volume-1). WMRP were mounted into the tested zone which is characterized by a floor area of 16 m^2 (4 m × 4 m) and an internal height of 3 m as recommended in EN 1264-5 (2008) and BS EN 14037-5 (2016).

The wall types were chosen as the sandwich type panel with polyurethane insulation between two layers is made out of sheet steel which has engagement and locking mechanism to increase the strength. The coefficients of thermal transmittance of the wall and ceiling were decided according to Turkish Standard TS 825 (thermal insulation requirements for buildings) (2008). The enclosed volumes were conditioned with mechanical air conditioners to ensure relevant boundary conditions in the tested volume. The emissivity of the indoor wall and WMRP surfaces, were estimated by the use of an infrared thermal imaging camera and calibrated thermocouples.

First, the surface temperatures were obtained by using precise temperature sensors, and then the surface emissivity was changed in the pyrometer setup in order to get the same temperature of the analyzed surface as obtained before by the use of the temperature sensors (Olesen et al., 2000). The physical dimensions and the thermo-physical properties of the test chamber and the testing equipment meet the general requirements of the ANSI/ASHRAE Standard 138 (2005). The main difference from the standard is; to ensure appropriate boundary conditions in the tested volume, the inner surfaces in the test zone were conditioned through the surrounded volumes as they are equipped with a mechanical air conditioner whereas the ANSI/ASHRAE Standard 138 (2005) recommends directly conditioning the testing room through pipes embedded in the surfaces.
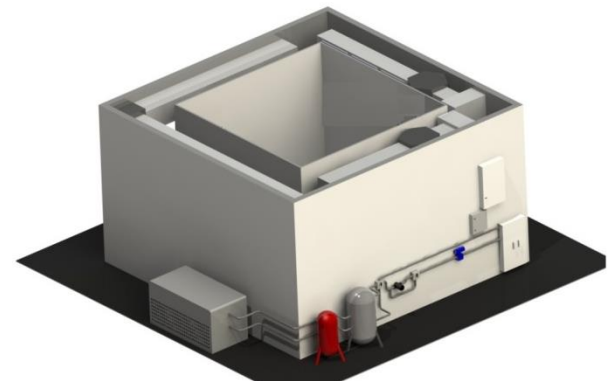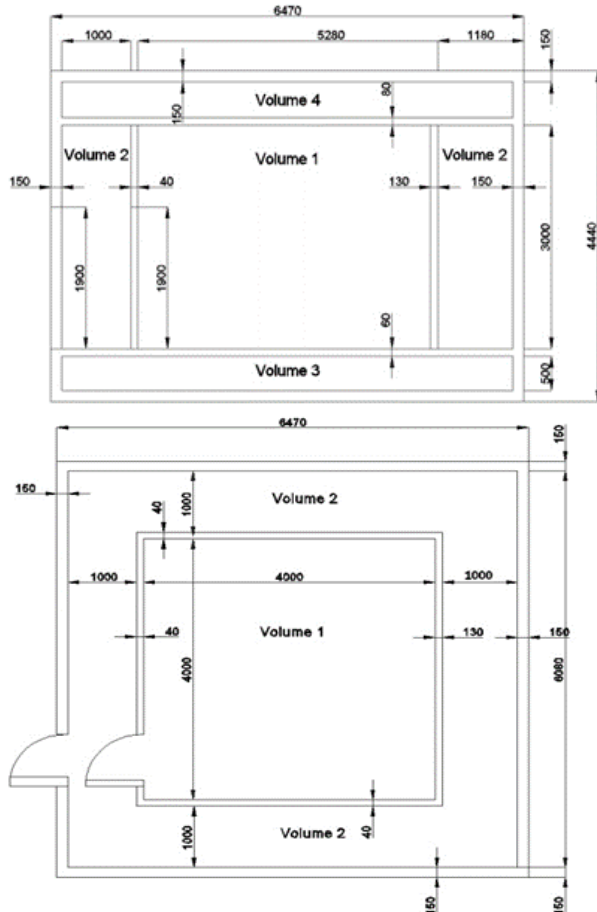

Figure 4. General view of the test room

Table 4. Controlled parameters in the zones

	Ceiling	Floor	Facade	Tested zone
Temperature Range	-10˚C / +40˚C	+0˚C / +30˚C	-10˚C / +40˚C	+0˚C / +30˚C
Temperature Tolerance	± 0.5 ˚C	± 0.5 ˚C	± 0.5 ˚C	± 0.5 ˚C
Humidity Range	n/a	n/a	%35 / %85 RH	n/a
Humidity Control Steps	n/a	n/a	%1	n/a
Humidity Tolerance	n/a	n/a	± % 0.5 RH	n/a
Air Velocity	n/a	n/a	0.5 – 5 m/s	n/a

Figure 5. Dimensions of the test chamber (all units are in millimeters)

The Wall Mounted Radiant Panel

The WMRP's were manufactured for this study consist of three layers which are gypsum board, serpentine heating pipe and insulation material; from inner to outer layers. The pipe serpentine was inserted into the gypsum board. The thickness of the gypsum board is 15 mm while the panel insulation thickness is 30 mm. The serpentine has cross-linked polyethylene (PEX) pipes with a 10.1 mm external diameter and 55 mm pipe spacing. Expanded polystyrene (EPS) was used as a backside thermal insulation material which has a coefficient of thermal transmittance value of 0.040 W/m.K (at 30 °C). WMRP has the standard insulation thickness which is attached during its manufacturing process. It should be noted that, obtained optimum thickness values (x_{opt}) in this study are an additional insulation to be attached to the external walls.

The general dimension of the WMRP was 1.2 m in height and 0.6 m in width (same as the CFD model). The test chamber was configured with six WMRP panels which are shown in Fig. 6 but measurements were performed from one of them. Six WMRP panels were attached to the wall instead of attaching single panel, this more closely simulates typical application allowing for more realistic results.
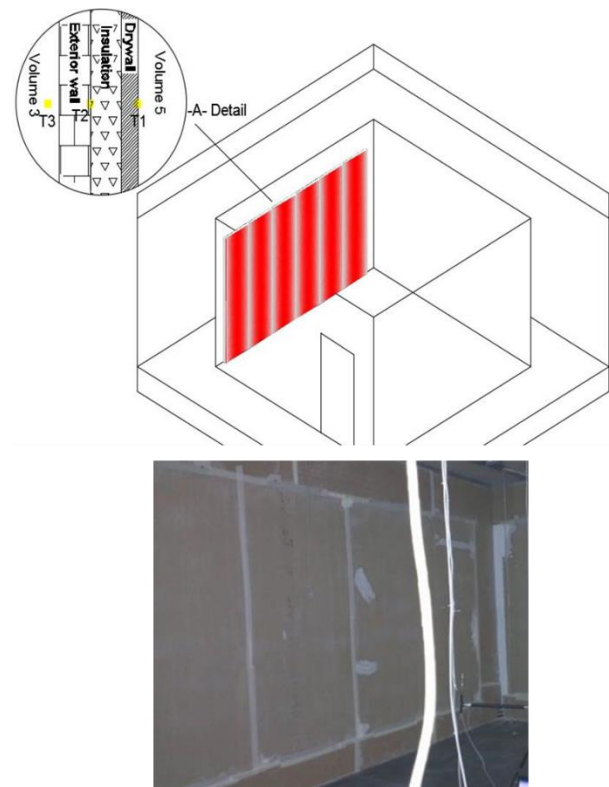
Figure 6. Arrangement of the wall mounted radiant panel

Hydraulic Circuit of WMRP

A water conditioning system was attached to the test chamber. As shown in Fig 7, inlet water accesses the hydraulic line through the buffer tank (the water temperature is maintained by means of electrical resistances), it then comes to the four-way valve. Here, the four-way valve was placed to provide a mixture through the supply and return lines. The mixed water leaves the four-way valve such that it is equal to the desired WMRP inlet temperature and enters the pump to supply the needed pressure. Then, the water comes to the three-way valve where the mass flow rate of the water is maintained at precisely appropriate flow rate. After that, the water passes through the ultrasonic flow meter, where the volumetric flow rate was measured. The data

for the flow rate control was provided from an electromagnetic flow meter. Following the flow meter, the water goes through manifolds and then the WMRP facility to activate the heat transfer mechanism. After finishing the cycle in the hydraulic line, the fluid comes to the four-way valve again through the return pipeline it is mixed with the water that comes from the buffer tank if needed (to adjust the required temperature of the fluid precisely). The pipes in the water circuit are well insulated.
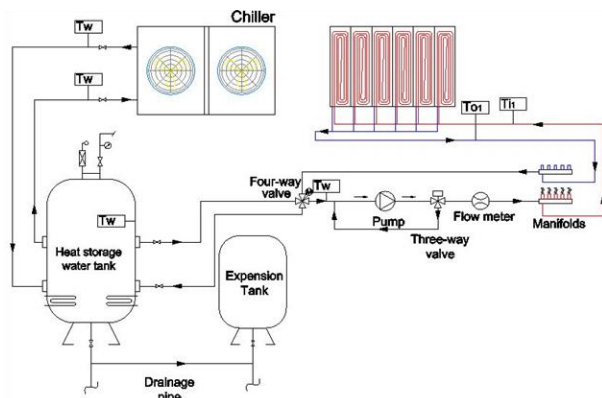

Figure 7. Hydraulic circuit of the test system

The Measurement Equipment and Experimental Method

The main objective of the experimental study was to validate the numerical simulation results. The most reliable analyses are those based on the measurements performed in the full scale test chamber which was described in detailed above. The measurements were carried out for the chosen representative WMRP, where the temperature transducers were inserted as described in the Fig. 3-b. For all cases, the supply water mass flow rate (0.04 kg/s) and the other environmental conditions were fixed at desired conditions. The measurements were carried out under steady conditions for variable outdoor (volume-2) air temperatures (T_o). The water conditioning system was turned on to achieve the desired steady state and initial conditions and heat flow throughout the heated WMRP before collecting the experimental data. Steady state conditions were ensured after about 3-4 h in which supply water temperature and water flow rates, surface temperature of the WMRP (T_{si}), outdoor surface temperature (T_{so}), WMRP backside surface temperature (T_p), outdoor air temperature (T_o) and indoor air temperature (T_i) were nearly constant, only then the tests were begun.

Indoor and surrounding volumes' air temperatures (T_i, T_o), the related surface temperatures (T_p, T_{si}, T_{so}) water mass flow rate, supply and return water temperatures were measured, controlled and stored for each measuring time interval (1 minute). Average test duration took around 8 h so that all important variables reached desired and steady state conditions. The temperatures of T_i, T_o, T_p, T_{si}, T_{so} were evaluated after the system reached a steady state condition (which was characterized by physical properties that were unchanging in time). Results corresponding to average values were stored during the periods of at least 30 min in which stable conditions were observed.

Multiple tests were carried out by varying the outdoor air temperature (T_{o1} = -3 °C, T_{o2} = 3 °C, T_{o3} = 5 °C) in Volume-2. When the air and surface temperatures bands changed less than 0.1 K/min, measurements were started. In terms of the recorded measurements, the panel backside surface temperatures (T_p) were obtained and compared with the numerical results.

RESULTS AND DISCUSSION

The optimum insulation thickness (x_{opt}) values which were calculated by two different methods (NDDM, SDDM) for different fuels in Istanbul climate, are shown in Table 5 and described below.

According to the general outcomes, optimum insulation thickness values which were calculated by NDDM are higher than the ones calculated by SDDM. Because, in SDDM indoor air temperature is used as a base temperature and heat production in the walls is neglected for the buildings heated by WMRP. Therefore, calculated optimum insulation thickness values from SDDM for the walls where the WMRP is mounted will be insufficient from the point of energy saving. On the other hand, optimum insulation thickness values were obtained by NDDM for a building heated by WMRP is lower than the ones obtained for standard building using the SDDM. This is because; backside insulation layer attached to the WMRP provides additional insulation to the walls, resulting in higher energy efficiency. Moreover, the payback periods (PBP) for natural gas and lignite obtained by NDDM were shorter than the ones obtained through SDDM. Accordingly, NDDM ensures better estimation of optimum insulation thickness than the SDDM, resulting in a shorter payback period.

Table 5. Summary results

| | NDDM | | | | | | SDDM | | | | | |
| | x_{opt} | | PBP | | DD | | x_{opt} | | PBP | | DD | |
	N.Gas	Lignite	N.Gas	Lignite	N.Gas	Lignite	N.Gas	Lignite	N.Gas	Lignite	N.Gas	Lignite
WMRP	3.7cm	3.3 cm	3.9yrs.	4.2yrs.	2686	2686	2 cm	1.7 cm	7.2yrs.	7.4yrs.	1865	1865
Standard Heating	5.2cm	4.9 cm	7.9yrs.	9.1yrs.	1865	1865	5.2cm	4.9 cm	7.9yrs.	9.1yrs.	1865	1865

Table 6. Validation of the numerical studies

Outer Air Temperature	U_{NDDM} (W/m^2.K)	T_p (°C)			Error (°C)		
		Experimental	CFD	MPR	CFD-Exp	MPR-CFD	MPR-Exp
-3 °C	0.72	15.9	15.6	15.4	-0.3	0.2	-0.5
3 °C	0.72	17.4	17.9	17.8	0.5	0.1	0.4
5 °C	0.72	18.4	18.7	18.6	0.2	0.1	0.2

Experimental Validation

The numerical model was validated with the experimental results conducted in same conditions. WMRP backside temperatures (T_p) calculated from the simulations were compared with the experimentally evaluated results. Because T_p is the most important, new parameter and affects the NDDM results, this validation of the T_p ensures the accuracy of the numerical results. However to increase the accuracy of the numerical results, comparison study was done for three different outer air temperatures (T_o).

The comparison summary of the numerical and experimental results is shown in Table 6.

According to the comparison results of the simulated and measured T_p values; average deviation is 0.3 °C (~ 1%) which is quite low. The maximum deviation (0.5 °C) was seen in the case where the outer air temperature (T_o) value is about 3 °C. Moreover MPR and CFD results are compatible to each other and average deviation is about 0.15 °C yielded.

Comparison of the NDDM and SDDM Results

Fig. 8 shows the variation of unit cost with respect to the insulation thicknesses (for the fuels of natural gas and lignite) that were obtained using the new (NDDM) and standard methods (SDDM). According to the results, as insulation thickness increases the heating load and accordingly heating cost decreases and vice-versa; when insulation thickness decreases, the heating load and heating cost increases. Furthermore, when the insulation thickness increases, cost of insulation also increases proportionally. When these two curves added together a total cost curve is obtained and the minimum value of this curve gives the optimum insulation thickness (x_{opt}). It can be seen in the Fig. 3a that for the walls where the WMRP is integrated, optimum insulation thicknesses for the usage of natural gas were obtained as 3.7 cm and 2 cm according to the NDDM and SDDM respectively. These values are 3.3 cm and 1.7 cm for the fuel of lignite (Fig 3b). Beyond these values, increasing the thickness of the insulation also increases the total cost. Table 5 shows the optimum insulation thickness results for the Istanbul for the new and standard methods described above.

With respect to the results obtained from both methods, significant difference (~85 %) in optimum insulation thicknesses is seen between the two methods. The main reason of such deviation is; heat source (WMRP) in the wall is not taken into account in the SDDM, while the

NDDM considers the interface temperature (between wall and WMRP) as a base temperature rather than indoor air temperature as well as heat generation (as mentioned above). Thus, SDDM is not convenient to estimate optimum insulation thickness for the walls where the WMRP is implemented. Nevertheless, if one wishes to use the standard method, one should double the obtained insulation thickness result from the SDDM as a safety margin.
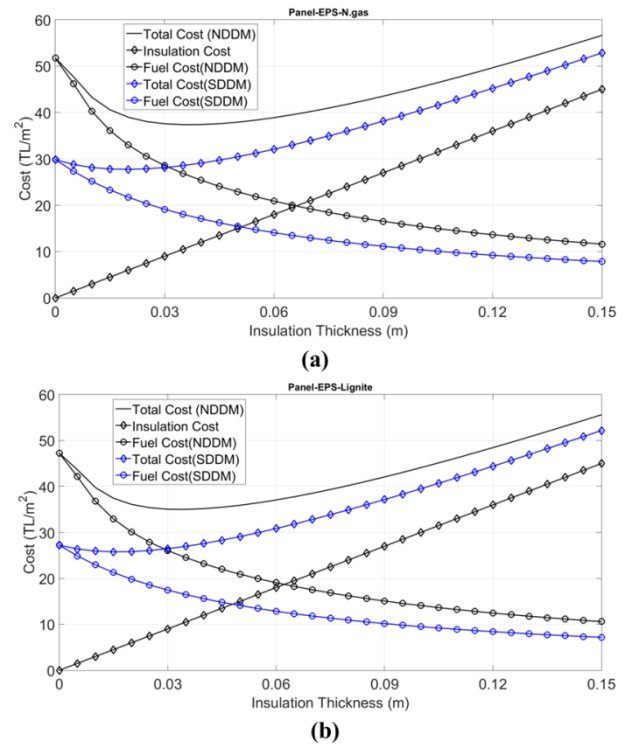

(a)

(b)

Figure 8. Comparison of the SDDM and NDDM methods for the WMRP a) Natural Gas b) Lignite

In Fig. 9, optimum insulation thickness results of SDDM for a standard building conditioned by conventional heating systems are given. As seen in the figure, optimum insulation thickness values for the fuels of natural gas and lignite are 5.2 cm and 4.9 cm respectively. If we compare the optimum insulation thickness results of conventional heating system (in SDDM) with the ones which were obtained from the case of WMRP in SDDM (corresponding to the values of 2 cm 1.6 cm), is significantly higher. Where, it can be stated that WMRP systems increase the insulation capability of buildings by means of providing extra insulation (backside insulation of the WMRP).
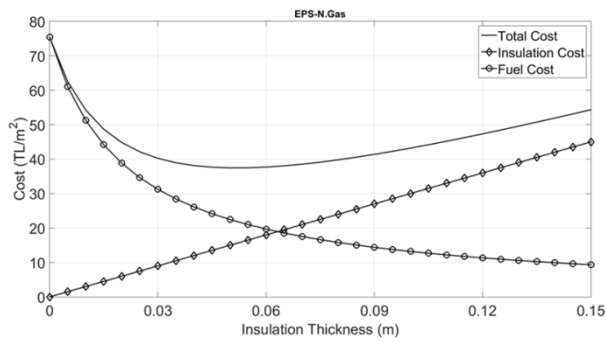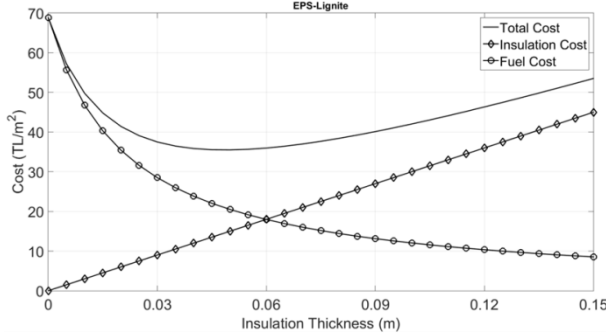
Figure 9. Optimum insulation thickness results of conventional heating systems according to the SDDM a) Natural Gas b) Lignite

Fig. 10 shows the variation of fuel consumption and net saving with respect to the insulation thickness (when the walls are insulated with EPS) which were obtained by the SDDM and NDDM for the Istanbul climate. From Figs. 10a-b it can be stated that, there is a non-linear relation between energy saving and insulation thicknesses – energy savings tend to increase quickly before the optimum point then the increment diminishes. Furthermore, when the insulation thickness increases, net savings gradually increase and reach the maximum value at the optimum thickness; following this point net savings decrease opposite of the trend of the total cost in Fig. 8. Energy savings in the new method (NDDM) is higher than the standard method (SDDM) due to the additional insulation is attached to the WMRP. In the NDDM, energy saving up to 25 TL/m² (average of natural gas and lignite) can be ensured with the calculated optimum insulation thickness, while the calculated insulation thickness by the SDDM provides only 7 TL/m². The effect of insulation thickness on fuel consumption for natural gas and lignite is shown in Figs. 10b-c. The trends are wholly opposite to the energy saving results in Fig. 10a-b. As expected, increasing the insulation thickness decreases the fuel consumption. The maximum decrease in the fuel cost is seen at the region before the optimum insulation thickness point.

CONCLUSION

In this study optimum insulation thickness, net energy saving and payback period were calculated for the Istanbul degree-day region and for two different fuels of natural gas and lignite using the SDDM and NDDM. As
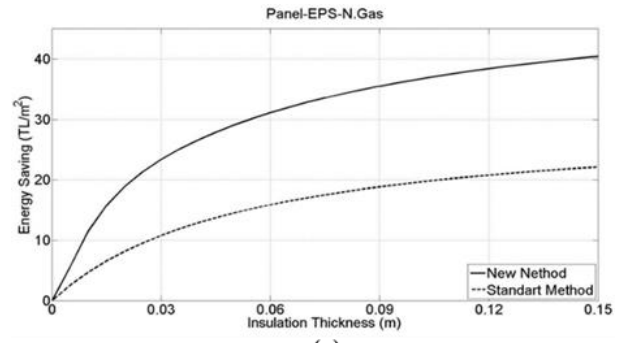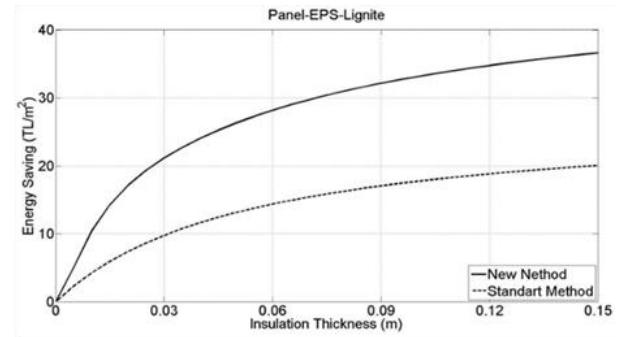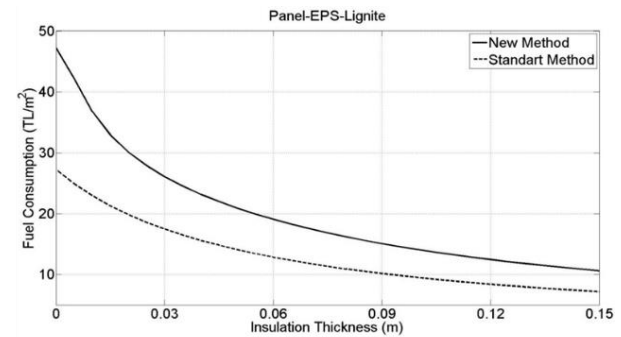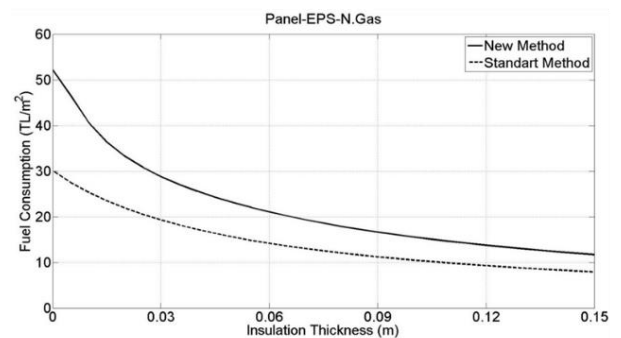
Figure 10. Total energy saving versus insulation thickness for SDDM and NDDM a) Natural Gas b) Lignite, fuel consumption comparison of the methods c) Natural Gas d) Lignite

insulation thickness increases, heating load decreases and accordingly cost of fuel decreases. At the point of optimum insulation thickness, the values of total cost of fuel and insulation material are at a minimum.

Radiant heating systems are quite convenient alternatives to the traditional HVAC systems, ensuring that efficiency requirements are met by producing more

thermally comfortable environments. The existing SDDM is used to estimate the optimum insulation thickness for the buildings where the WMRP is used. For this reason we propose new degree-day method (NDDM) in which base temperature is the interface temperature (backside temperature of the WMRP) between the WMRP and the wall structure. In this way, better estimation of insulation thickness and accordingly higher energy efficiency can be ensured. In the new method, WMRP backside temperature (T_p) was obtained from the series of the CFD analysis for different thermal transmittance coefficient (U) and outdoor air temperature (T_o) values are used to create an empirical equation for the estimation of T_p with multiple polynomial regression method. Then the obtained 3rd degree of the polynomial equation was used to calculate the T_p which is a function of U, also U is a function of x.

According to the results of NDDM; optimum thicknesses of 3.7 cm and 3.3 cm were found for the usage of natural gas and lignite respectively. These values are 2 cm and 1.7 cm for the SDDM. This result shows that, the SDDM significantly lower (85-95%) estimates the optimum insulation thicknesses and the method is not valid for the buildings where the WMRP is used. Therefore, the payback periods of SDDM are higher comparing to the NDDM. So, for the design process of radiant systems, the proposed new method is recommended since it provides an energy savings of 14 TL/m². In such cases, the total investment cost will be returned in the range of 3.9 - 4.2 years.

Moreover for the building where the conventional heating systems are used, SDDM was applied to calculate the optimum insulation thicknesses and the results are found as 5.2 cm and 4.9 cm respectively for the natural gas and lignite. These results confirm the fact that the WMRP systems provide higher energy efficiency comparing to the conventional systems, with respect to the additional backside insulation of the WMRP.

The proposed optimization technique and the evaluated results may lead to a general result for WMRP systems and which may be used to determine the optimum insulation for many different insulation materials and climatic conditions economically and efficiently. Future works should focus on the further numerical and experimental studies to extend our correlation taking into account of the other parameters such as effect of backside insulation of WMRP.

ACKNOWLEDGMENT

REFERENCES

Acikgoz O., Kincay O., 2015, Experimental and numerical investigation of the correlation between radiative and convective heat-transfer coefficients at the cooled wall of a real-sized room, *Energy and Building*, 108, 257-266.

Al-Homoud M.S., 2005, Performance characteristics and practical applications of common building thermal insulation materials, *Build Environment,* 40, 353-66.

ANSI/ASHRAE, 2005, Standard 138: Method of Testing for Rating Ceiling Panels for Sensible Heating and Cooling.

Arslan O., Köse R., 2006, Thermo-economic optimization of insulation thickness considering condensed vapor in buildings*, Energy and Buildings,* 38, 1400-1408.

ASHRAE, 2008, *Handbook-fundamentals Panel heating and cooling*, ASHRAE, Atlanta.

Bojic M., Cvetkovic D., Bojic L., 2015, Decreasing energy use and influence to environment by radiant panel heating using different energy sources, *Applied Energy*, 138, 404-413.

Bolattürk A., 2008, Optimum insulation thicknesses for building walls with respect to cooling and heating degree-hours in the warmest zone of Turkey, *Building and Environment*, 43, 1055-1064.

Bolattürk A., Dağıdır C., 2013, Determination of optimum insulation thickness for buildings in Hot climate regions by considering solar radiation, *J. of Thermal Science and Technology*, 33, 1, 87-99.

BS EN 15377-1 Standard, 2008, Heating systems in buildings. Design of embedded water based surface heating and cooling systems. Determination of the design heating and cooling capacity.

BS EN 14037-5 Standard, 2016, Free hanging heating and cooling surfaces for water with a temperature below 120°C. Open or closed heated ceiling surfaces. Test method for thermal output.

Cvetkovi D., Bojic M., 2014, Optimization of thermal insulation of a house heated by using radiant panels, *Energy and Buildings,* 85, 329-336.

Çomaklı K., Yüksel B., 2003, Optimum insulation thickness of external walls for energy saving, *Applied Thermal Engineering*, 23, 473-479.

Çomaklı K., Yüksel B., 2004, Environmental impact of thermal insulation thickness in buildings, *Applied Thermal Engineering,* 24, 933-940.

De Rosa M., Bianco V., Scarpa F., Tagliafico L.A., 2014, Heating and cooling building energy demand evaluation; a simplified model and a modified degree days approach, *Applied Energy*, 128, 217-229.

Dikmen N., 2011, Performance analysis of the external wall thermal insulation systems applied in residences, *J. of Thermal Science and Technology*, 31, 1, 67-76.

Dombaycı Ö.A., Gölcü M., Pancar Y., 2006, Optimization of insulation thickness for external walls using different energy sources, *Applied Energy*, 83, 921-928.

Duman Ö., Koca A., Acet R.C., Çetin G., Gemici Z., 2015, A study on optimum insulation thickness in walls and energy savings based on degree day approach for 3 different demo-sites in Europe, *Proceedings of International Conference CISBAT 2015 Future Buildings and Districts Sustainability from Nano to Urban Scale*, Lausanne, 155-160 (doi:10.5075/epfl-cisbat2015-155-160).

Ekici B.B., Gulten A.A., Aksoy U.T., 2012, A study on the optimum insulation thicknesses of various types of external walls with respect to different materials, fuels and climate zones in Turkey, *Applied Energy,* 92, 211-217.

Energy and Natural Resources Ministry of Turkey, 2013, Report: General Energy Balance Table.

EN 1264-5 Standard, 2008, Water based surface embedded heating and cooling systems. Part 5: heating and cooling surfaces embedded in floors, ceilings and walls - determination of the thermal output.

Erikci Çelik S.N., Zorer Gedik G., Parlakyildiz B., Koca A., Çetin M.G, Gemici Z., 2016, The performance evaluation of the modular design of hybrid wall with surface heating and cooling system, *A/Z ITU Journal of the Faculty of Architecture*, 13, 12, 31-37 (DOI: 10.5505/itujfa.2016.48658).

Erikci Çelik S.N., Zorer Gedik G., Parlakyildiz B., Koca A., Çetin M.G, Gemici Z., 2016, Yüzeyden ısıtma soğutma sistemli modüler hibrid duvar tasarımı ve performansının değerlendirilmesi, *2. Ulusal yapı fiziği ve çevre kontrolü kongresi*, İstanbul, 243-252.

Franc S., 1999, Economic viability of cooling ceiling systems, *Energy and Building*, 30, 195–201.

Hasan A., 1999, Optimizing insulation thickness for buildings using life-cycle cost. *Appl. Energ.*, 63, 115-124.

International Energy Agency, 2013, Report: World Energy Outlook.

Jeong J.W., Mumma S.A., Bahnfleth W.P., 2003, Energy conservation benefits of a dedicated outdoor air system with parallel sensible cooling by ceiling radiant panels, *ASHRAE Transactions*, 109.

Kanbur B.B., Atayılmaz S.O., Koca A., Gemici Z., Teke İ., 2013, Radyant ısıtma panellerinde açığa çıkan ısı akılarının sayısal olarak incelenmesi, *19. Ulusal Isı Bilimi ve Tekniği Kongresi*, Samsun, 1498-1502.

Kanbur B.B., Atayilmaz S.O., Koca A., Gemici Z., Teke İ., 2013, A study on the optimum insulation thickness and energy savings of a radiant heating panel mounted wall for various parameters, *7. Mediterranean congress of climatization*, İstanbul, 791-797.

Kaya M., İlker F., Comaklı Ö., 2016, Economic analysis of effect on energy saving of thermal insulation at buildings in Erzincan province, *J. of Thermal Science and Technology*, 36, 1, 47-55.

Kaynakli O., 2008, A study on residential heating energy requirement and optimum insulation thickness, *Renewable Energy*, 33, 1164-1172.

Kaynakli O., 2012, A review of the economical and optimum thermal insulation thickness for building applications, *Renewable and Sustainable Energy Reviews*, 16, 415-425.

Kaynakli O., 2013, Optimum thermal insulation thicknesses and payback periods for building walls in turkey, *J. of Thermal Science and Technology*, 33, 2, 45-55.

Kilkis B., 2006, Cost optimization of hybrid HVAC system with composite radiant wall panels, *Applied Thermal Engineering*, 26, 10-17.

Koca A., Atayilmaz O., Agra O., 2016, Experimental investigation of heat transfer and dehumidifying performance of novel condensing panel, *Energy and Building*, 129, 120-137.

Koca A., Gemici Z., Bedir K., 2014, Thermal comfort analysis of novel low exergy radiant heating cooling system and energy saving potential comparing to conventional systems, Book Chapter, *Progress in Exergy, Energy and Environment*, 38, 435-445.

Koca A., Gemici Z., Topacoglu Y., Cetin G., Acet R.C., Kanbur B.B., 2014, Experimental investigation of heat transfer coefficients between hydronic radiant heated wall and room, *Energy and Buildings*, 82, 211-221.

Koca A., Gemici Z., Bedir K., 2013, Thermal comfort analysis of novel low exergy radiant heating cooling system and energy saving potential comparing to conventional systems, *Proceedings of the Sixth International Exergy, Energy and Environment Symposium (IEEES-6)*, Rize, 579-590.

Koca A., Gemici Z., Topaçoğlu Y., Çetin G., Acet R.C., Kanbur B.B., 2013, Radyant ısıtma ve soğutma sistemlerinin ısıl konfor analizleri, *11. Ulusal tesisat mühendisliği kongresi*, İzmir, 2025-2042.

Koca A., 2011, *Duvardan, Yerden, Tavandan Isıtma Soğutma Panellerinin Geliştirilmesi Performans Analizleri ve Örnek Bir Oda Modellenmesi*, Msc Thesis, Istanbul Technical University, Istanbul, Turkey.

Miriel J., Serres L., Trombe A., 2002, Radiant ceiling panel heating-cooling systems: experimental and simulated study of the performances, thermal comfort and energy consumptions, *Applied Thermal Engineering*, 22, 1861-1873.

Olesen B.W., Bonnefoi F., Michel E., De Carli M., 2000, Heat exchange coefficient between floor surface and space by floor cooling – theory or a question of definition, *ASHRAE Transactions,* DA-00-8-2, 684–694.

Ozel M., 2011, Effect of wall orientation on the optimum insulation thickness by using a dynamic method, *Applied Energy*, 88, 2429-2435.

Özkan D.B., Onan C., 2011, Optimization of insulation thickness for different glazing areas in buildings for various climatic regions in Turkey, *Applied Energy*, 88, 1331-1342.

Özel G., Açıkkalp E., Görgün B., Yamık H., Caner N., 2015, Optimum insulation thickness determination using the environmental and life cycle cost analyses based entransy approach, *Sustainable Energy Technologies and Assessments*, 11, 87–91.

Rhee K., Kim W.K., 2015, A 50 year review of basic and applied research in radiant heating and cooling systems for the built environment, *Building and Environment,* 91, 166-190.

Seyam S., Huzayyin A., El-Batsh H., Nada S., 2014, Experimental and numerical investigation of the radiant panel heating system using scale room model, *Energy and Buildings*, 82, 130-141.

Sisman N., Kahya E., Aras N., Aras H., 2007, Determination of optimum insulation thicknesses of the external wall and roof (ceiling) for Turkey's different degree-day regions, *Energy and Policy*, 35, 5151-5155.

Stetiu C., 1999, Energy and peak power savings potential of radiant cooling systems in U.S. commercial buildings, *Energy and Buildings,* 30, 127-138.

TSE 825, 2008, Standard: Thermal Insulation Requirements for Buildings.

Tye-Gingras M., Gosselin L., 2012, Comfort and energy consumption of hydronic heating radiant ceilings and walls based on CFD analysis, *Building and Environment*, 54, 1-13.

Ucar A., 2010, Thermo-economic analysis method for optimization of insulation thickness for the four different climatic regions of Turkey, *Energy,* 35, 1854-1864.

Ucar A., Balo F., 2010, Determination of the energy savings and the optimum insulation thickness in the four different insulated exterior walls, *Renewable Energy*, 35, 88-94

Yıldız A., Gürlek G., Erkek M., Özbalta N., 2008, Economical and environmental analyses of thermal insulation thickness in buildings, *J. of Thermal Science and Technology*, 28, 2, 25-34.

Aliihsan KOCA received his B.S., M.S., Ph.D. degrees in Mechanical Engineering from Yıldız Technical University and Istanbul Technical University, respectively. He worked as research and development engineer and thermo-fluid research department manager in Mir Arastirma ve Gelistirme A.S. between 2009 - 2016. He is currently a post-doctoral researcher at Michigan Technological University.

Gürsel ÇETİN received his BSc in Mechanical Engineering Department from Yıldız Technical University in 2013. He currently continues his MSc at Yıldız Technical University. He has been working as a Research and Development Engineer in Mir Research and Development Company. His research interests are renewable energy, radiant heating & cooling, thermal comfort and experimental analysis of thermal systems.

Eser VELİŞAN received his BSc in Mechatronics Engineering Department from Bahcesehir University in 2014. He currently continues his MSc at Bahcesehir University. He has been working as a Research and Development Engineer in Mir Research and Development Company. His research interests are computational analysis of fluid and thermal systems.

NUMERICAL ANALYSIS OF PULSATING CIRCULAR IMPINGING LAMINAR JET ON A PLANAR DISC

Mitra KAHROBA* and Hasmet TÜRKOĞLU**

Mechanical Engineering Department, Faculty of Engineering, Gazi University, Ankara, Turkey
**Corresponding author: Mechanical Engineering Department, Faculty of Engineering, Çankaya University, Ankara, Turkey,
hasmet@cankaya.edu.tr

Abstract: In this study, the flow and heat transfer characteristics of pulsating circular air jets impinging on a flat surface were numerically analyzed. The jet velocity pulsated in time. The objective of the work is to investigate the influence of the jet Reynolds number, pulsation amplitude and pulsation frequency on the rate of heat transfer from the target hot surface. For the analysis, a computer program, based on the control volume method and SIMPLE algorithm, was developed. Laminar flow with the time averaged jet Reynolds numbers between 300 and 700 were analyzed. The pulsation amplitude is ranged between $0.0V_0$ (steady jet) and $0.8V_0$ (m/s) (V_0 is period averaged jet velocity), and the frequency is ranged between 1 and 6 Hz. The nozzle-to-plate distance was kept constant at H/d=3. From the simulation results, it was observed that at any instant of the pulsation period, the local Nusselt number is maximum at the stagnation point, and it decreases along the plate. This decrease in the local Nusselt number is not monatomic as in the steady jet cases. It has local maximum and minimum values (fluctuations) due to the moving recirculating flow regions along the bottom plate. At low frequencies, the time (period) averaged stagnation point Nusselt numbers are lower than the corresponding steady jet Nusselt numbers. However, with the increasing frequency, the stagnation point Nusselt number increases and become higher than the steady jet Nusselt number.
Keywords: Impinging jet; Pulsating jet; Numerical solution.

DÜZLEM BİR DİSKE ÇARPAN OSİLASYONLU DAİRESEL LAMİNAR JETİN SAYISAL OLARAK İNCELENMESİ

Özet: Bu çalışmada, düzlem bir diske çarpan dairesel osilasyonlu jetlerin akış ve ısı transferi karakteristikleri sayısal olarak incelenmiştir. Çalışmanın amacı, dairesel bir nozuldan çıkıp düzlem bir yüzeye çarpan salınımlı hava jetinin, Reynolds sayısının, salınım genliğinin ve salınım frekansının, hedef yüzeyden akışkana olan ısı transferine etkilerini incelemektir. Bu sayısal çalışmayı yapmak için, kontrol hacmi formülasyonu ve SIMPLE algoritmasına dayanan bir bilgisayar programı geliştirilmiştir. Simülasyonlar, Reynolds sayısı 300 - 700, salınım genliği $0.0V_0$-$0.8V_0$ ve salınım frekansı 1-6 Hz aralığındaki jet akışlar için yapılmıştır. Nozul-çarpma yüzeyi arasındaki uzaklığın, lüle çapına oranı *H/d=3* sabit tutulmuştur. Simülasyon sonuçlarından çarpma periyodunun bütün anlarında durma noktası Nusselt sayısının maksimum olduğu ve durma noktasından uzaklaştıkça Nusselt sayısının azaldığı görülmüştür. Nusselt sayısındaki bu azalma, kararlı jetlerde olduğu gibi monotomik olmayıp yerel maksimum ve minum değerlere sahip olduğu gözlenmiştir. Alt levha üzerinde hareketli akış döngüleri meydana geldiği ve bu döngüler nedeniyle Nusselt sayısında yerel maksimum ve minimum değerlerin oluştuğu görülmüştür. Düşük salınım frekanslarında, Nusselt sayısı aynı Reynolds sayısına sahip kararlı jet Nusselt sayısından daha küçük olduğu, ancak artan frekansla salınımlı jet Nusselt sayısının arttığı ve kararlı jet Nusselt sayısından daha yüksek değere ulaştığı görülmüştür.
Anahtar Kelimeler: Çarpan jet, Salınımlı jet, Sayısal çözüm.

NOMENCLATURE

A   Pulsation amplitude
C_p Specific heat of air, [J/kgK]
D   Diameter of the disc, [m]
d   Jet diameter, [m]
f   Pulsation frequency, [Hz]
h   Heat transfer coefficient at the target surface, [W/m²K]
H   Nozzle-plate spacing, [m]
k   Thermal conductivity of air, [W/mK]

Nu_{max} Instantaneous stagnation point Nusselt number
Nu_r Instantaneous local Nusselt number

$N\overline{u}$ Area and time averaged Nusselt number along the period

$N\overline{u}_A$ Instantaneous area averaged Nusselt number

$N\overline{u}_{max}$ Time averaged stagnation point Nusselt number
p   Pressure, [Pa]
Re   Reynolds number (Re= V_o d/ν)

T_{in}	Temperature of fluid at nozzle exit, [K]
T_H	Temperature of bottom plate, [K]
q''	Heat flux, [W/m^2]
v_r	Velocity component in radial- direction, [m/s]
v_z	Velocity component in axial- direction, [m/s]
V_o	Period averaged jet velocity, [m/s]
r	Radial coordinate, [m]
z	Axial coordinate, [m]

Greek Symbols

Δt	Computational time step, [s]
α	Thermal diffusivity of fluid, [m^2/s]
ρ	Fluid density, [kg/m^3]
τ	Period of pulsation, [s]
ν	Kinematic viscosity, [m^2/s]

INTRODUCTION

Impinging jets are widely used to enhance the heat and mass transfer from surfaces. The widespread usage of impinging jets in cooling and drying applications is attributed to their inherent superior performance over other schemes of single phase heat and mass transfer from a comparatively small surface area. Impinging jets are also used in chemical vapor deposition (CVD) processes.

The flow structure of an impinging jet over a planar target can be divided into three characteristic regions as free jet region, stagnation flow region and wall jet region. The free jet region is formed upon the jet exit with a defined velocity distribution as a function of the jet radius. A shear layer is generated due to the velocity difference between the potential core of the jet and the ambient fluid. However, there is not enough distance for the jet flow to mix with the surrounding fluid in the cases that the distance of jet exit-to-the target wall is short, as in the current study. The stagnation flow region results from the jet impact on the target solid surface. The wall jet region is formed because of re-acceleration of the flow along the target surface. The main part of heat transfer occurs in the proximity of the stagnation point, but a portion of the wall jet region may significantly contribute to the heat exchange, too. In spite of the simple geometry of the jet-plate combination, convective heat transfer coefficient at the target surface is affected by a variety of parameters such as the nozzle to plate distance, Reynolds number (Re), nozzle inclination angle, steadiness of the jet flow, etc.

From the literature review, it is deduced that unsteadiness of the jet flow has been rarely investigated. Studies about the influence of unsteady jet flow on the heat transfer rate via generating a periodic variation in the jet speed are accomplished (Zumbrunnen and Aziz, 1993; Azevedo et al, 1994; Miladin and Zumbrunnen, 1997; Liu and Sullivan, 1996). These studies showed that there is no general trend about the effect of jet unsteadiness on the heat transfer rate, as some researchers found enhanced heat transfer and some do not.

Some researches show significant differences between flow fields with and without unsteady motions. According to existing data, the jets with unsteady velocity show strong mixing of the jet with ambient fluid and hence a rapid reduction in the maximum jet velocity. Considering this phenomenon as a positive result of unsteadiness on heat transfer rate due to the boundary layer renewal in stagnation region, the influence of unsteadiness on the heat transfer rate depends on various parameters. Goppert et al. (2004) pointed out that a threshold-frequency often exists above which the heat transfer augmentation occurs in general. It is obvious from the studies about impinging jets with low jet-to-plate distance normalized by the jet diameter (H/D) that the wall jet undergoes a transition to turbulence, but the mixing turbulence resulted from entrainment doesn't penetrate to the free jet center. Therefore, the stagnation Nusselt number is locally minimum at H/D=2 which is observed by Goldstein and Timmers (1982). Collucci and Viskanta (1996) also reported examples of a couple of Nusselt number peaks. The peak closer to the jet center is due to the thinning of the laminar boundary layer and the secondary one is because of the transition from laminar to turbulent flow in the wall jet. Study by Liu and Sullivan (1996) surveyed the fluctuating heat exchange to an impinging air jet excited acoustically. It was shown that excitation of the jet at certain frequencies leads to enhancement or reduction in both local and area averaged heat transfer. O'Donovan and Murray (2008) have observed the frequency bands growing within the transition region and diminishing as the wall jet transition to the turbulence. They also reported the variation of heat transfer rate as a result of periodic behavior of the flow in the wall jet region.

Demircan and Turkoglu (2010) investigated laminar sinusoidally oscillating rectangular impinging air jet on a planar surface for low Reynolds numbers and observed that the heat transfer increases with increasing Reynolds number and fluctuation amplitude and decreasing H/W ratio where W is width of the rectangular nozzle used in their work. As a result, it was concluded that the optimum values of H/W ratio and oscillation amplitude should be found to make heat transfer maximum.

The focus of the present study is to analyze how convective heat transfer is affected by the unsteady jet velocity. To do this, pulsating circular air jets impinging on a flat surface were numerically analyzed. The jet velocity is pulsated in time. For the analysis, a computer program, based on the control volume method and SIMPLE algorithm, was developed. The objective of the work is to investigate the influence of the jet Reynolds number, pulsation amplitude and pulsation frequency on the rate of heat transfer from the target hot surface.

DESCRIPTION OF THE PROBLEM AND THE MATHEMATICAL FORMULATION

Two parallel, horizontal, infinite planar discs were considered in this study. The geometry of the problem and coordinate system considered are shown in Fig. 1. A pulsating air jet issuing from a circular hole at the center of the upper disc impinges on the bottom disc. The upper disc was insulated and the lower one is kept at constant temperature T_H that is higher than the jet inlet temperature T_{in}.
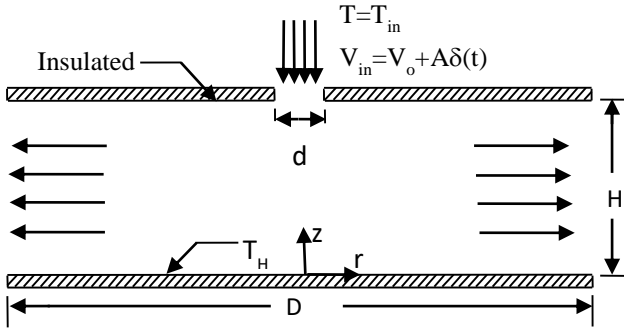

Figure 1. The geometry and the coordinate system of the problem.

The jet velocity over the nozzle exit is uniform but it varies with time periodically according to the function given by Eq. (1) below.

$$V_{in} = V_0 + A\delta(t) \tag{1}$$

where V_0 is the period averaged jet velocity and A is the pulsation amplitude based on the average velocity V_0. $\delta(t)$ is the Dirac function which has a value as

$$\delta(t) = \begin{cases} 1 & \text{for } 0 < t \le \tau/2 \\ -1 & \text{for } \tau/2 < t < \tau \end{cases}$$

where τ is the pulsation period. It is assumed that the flow is laminar and incompressible. Since the temperature difference in the flow field is small, the variation in the fluid properties such as density, viscosity and heat conduction coefficient are assumed to be negligible. Also, the variations in all variables in the angular direction can be neglected. So, the basic equations of the problem in cylindrical coordinate system can be written as follows:

Continuity Equation

$$\frac{1}{r}\frac{\partial}{\partial r}(rv_r) + \frac{\partial}{\partial z}(v_z) = 0 \tag{2}$$

Conservation of linear Momentum Equations

In the axial direction (z-direction):
$$\rho\left(\frac{\partial v_z}{\partial t} + v_r\frac{\partial v_z}{\partial r} + v_z\frac{\partial v_z}{\partial z}\right) = \\ -\frac{\partial p}{\partial z} + \mu\left[\frac{1}{r}\frac{\partial}{\partial r}\left(r\frac{\partial v_z}{\partial r}\right) + \frac{\partial^2 v_z}{\partial z^2}\right] \tag{3}$$

In radial direction (r-direction):
$$\rho\left(\frac{\partial v_r}{\partial t} + v_r\frac{\partial v_r}{\partial r} + v_z\frac{\partial v_r}{\partial z}\right) = \\ -\frac{\partial p}{\partial r} + \mu\left[\frac{1}{r}\frac{\partial}{\partial r}\left(r\frac{\partial v_r}{\partial r}\right) + \frac{\partial^2 v_r}{\partial z^2}\right] \tag{4}$$

Energy equation

$$\rho c_p\frac{\partial T}{\partial t} + \rho c_p v_z\frac{\partial T}{\partial z} + \rho c_p v_r\frac{\partial T}{\partial r} = \\ k\left[\frac{1}{r}\frac{\partial}{\partial r}\left(r\frac{\partial T}{\partial r}\right) + \frac{\partial^2 T}{\partial z^2}\right] \tag{5}$$

Boundary Conditions

The fluid temperature at nozzle outlet T_{in} is constant and the vertical component of velocity is defined by the expression $V_{in} = V_0 + A\delta(t)$. The flow is assumed to be symmetric about the nozzle axis. The upper disc is insulated and the lower disc is kept at a prescribed constant temperature, T_H. On the solid surfaces no-slip condition applies and hence the velocity components are zero. At the surface, at $r=D/2$, through which the fluid leaves the flow domain, the variations of the velocity components and temperature were neglected.

Calculation of Nusselt Number

The temperature and velocity fields vary with the time and the position in the flow domain. Hence, to characterize the heat transfer rate from the bottom plate, instantaneous local, instantaneous area averaged, area and time (period) averaged, instantaneous stagnation and time (period) averaged stagnation point Nusselt numbers are calculated. For the definition of these Nusselt numbers, Nozzle diameter d is considered as the characteristic length. The calculation of all these five different Nusselt numbers is formulated below.

The temperature distribution obtained by the numerical solution of the energy equation is used to calculate the Nusselt number along the hot bottom plate. The local instantaneous heat flux from the hot bottom plate to the fluid can be expressed as;

$$q'' = h(T_H - T_{in}) = -k\frac{\partial T}{\partial z}\bigg)_{z=0} \tag{6}$$

In this equation, T_H and T_{in} are temperatures at the bottom wall and jet inlet, respectively. From this equation, the instantaneous local Nusselt number can be determined. Using the nozzle diameter d as the characteristic length, the above equation can be rearranged as,

$$Nu_r = \frac{hd}{k} = -\frac{d}{(T_H - T_{in})}\frac{\partial T}{\partial z}\bigg)_{z=0} \tag{7}$$

The instantaneous area averaged Nusselt number on the hot bottom plate can be calculated by integrating the

instantaneous local Nusselt number over the bottom surface.

$$N\overline{u}_A = \frac{1}{A}\int_A Nu_r\, dA \qquad (8)$$

The area and time averaged Nusselt number along the period of injection can be calculated by integrating Eq. (8) over the injection period τ.

$$N\overline{u} = \frac{1}{\tau}\int_\tau \frac{1}{A}\int_A Nu_r\, dA dt \qquad (9)$$

where A is the area of the target surface and τ is the period of the pulsation. The instantaneous local Nusselt number at the stagnation point is equal to the Nusselt number at $r=0$ and it is the maximum Nusselt number. Hence, it can be expressed as

$$Nu_{max} = Nu_r\big)_{r=0} \qquad (10)$$

The period averaged stagnation point Nusselt number is calculated by integrating the instantaneous stagnation point Nusselt number along the period of injection as,

$$\left(N\overline{u}\right)_{max} = \frac{1}{\tau}\int_\tau Nu_{max}\, dt \qquad (11)$$

NUMERICAL SOLUTION

The continuity, momentum and the energy equations have to be solved together with the relevant boundary conditions to determine the velocity and temperature distributions in the flow field. These equations are linked with each other. Hence, the solution of this set of equations is only possible by using a numerical method. The numerical method used in this study is based on the control volume approach and SIMPLE algorithm. The governing equations were discretized by integrating them over finite control volumes. The hybrid scheme was used for the discretization. The time dependent terms were discretised using the fully implicit scheme. Gauss-Seidel iteration technique was used for solving the algebraic equations. A computer program developed in our one of previous study was modified to solve the present problem. Using the computer program developed, the velocity, pressure and temperature distributions were obtained for all grid points at different instants of the injection period.

To minimize the numerical errors and optimize the solution time, a non-uniform grid system was used. Near the top and bottom plates and also around the axis of the jet, finer grid spacing was utilized. To determine the optimum size of the mesh, by keeping all other parameter constant, the simulation of the problem was repeated with different grid systems and time steps. Comparing the area averaged and stagnation point Nusselt numbers obtained

with different mesh sizes and time steps, the optimum mesh size and time step were determined.

To obtain periodically fully developed results, the computations were repeated successively until the difference between Nusselt numbers for two successive periods is negligibly small. The validity of the numerical scheme and the computer program used in this study was checked by Demircan and Turkoglu (2010) in a previous study. Based on the comparison of the results obtained using the computer program developed with the results in the literature, it was shown that the developed model and computer code simulate the unsteady impinging jet flow and heat transfer with a satisfactory accuracy.

RESULTS AND DISCUSSIONS

In this study, the heat transfers and flow characteristics of impinging air jets which have a periodically pulsating velocity in time were analyzed. The jet velocity was changed according to the expression given by Eq. (1). In Fig. 2, the variations of the jet velocity along the pulsation period are shown for different pulsation amplitudes. As seen in this figure, during the first half of the injection period, the jet velocity is at its maximum value, and during the second half of the pulsation period, the jet velocity assumes its minimum value. Computations were performed for different Reynolds numbers ($Re=V_0d/\nu=100$, 300, 500 and 700), the jet velocity amplitudes ($A=0.2V_0$, $0.4V_0$, $0.6V_0$ and $0.8V_0$) and the jet oscillation frequencies ($f=1$ Hz, 2 Hz, 3 Hz, 4 Hz, 5 Hz and 6 Hz) with fixed geometrical dimensions of $H/d=3$ and $D/d=8.33$.

The simulations show that the flow and the temperature fields of the pulsating impinging jets have the similar general characteristics of the steady impinging jets at all instants of the period. As in the steady jet cases, the free jet region, the impingement region and the wall jet region form. In the steady jet case, there is no change in both temperature and velocity fields with time, however, when the jet is pulsating along the injection period, in all these regions, the velocity and temperature fields change in time. As a result, the jet renews itself continuously, and hence a higher heat removal rate from the hot bottom surface is expected in comparison with the steady impinging jet cases.
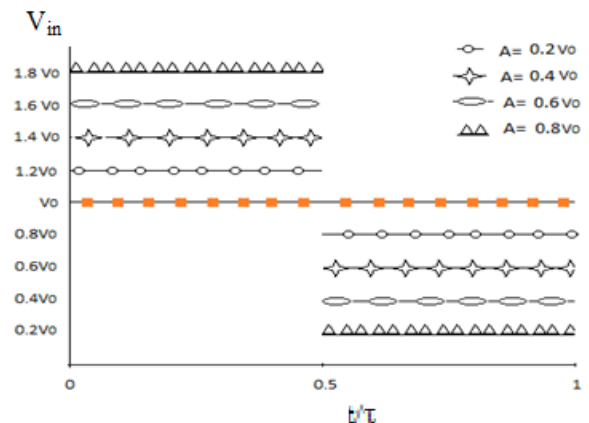

Figure 2. Variation of the jet velocity over a pulsation period.

The velocity vector distributions for the jets with Reynolds number 500, pulsation amplitude $A=0.2V_0$ and oscillation frequency of 1 Hz at four different instants of the period ($t=0.0\tau$, 0.25τ, 0.5τ and 0.75τ) are shown in Fig. 3. In Fig. 4, the velocity vector distributions are shown for the jets with Reynolds number 500, pulsation amplitude $A=0.2V_0$ and pulsation frequency $f=3$ Hz. Analysis of these figures shows that the flow fields exhibit the general behavior of a steady impinging jets. However, due to the pulsation of the jet velocity, secondary recirculating flow regions form and their location changes during the period.

In Fig. 3a, it is seen that in the beginning of the injection period ($t=0.0\tau$), the ambient fluid entrains the free jet near the exit of the nozzle and a recirculating flow region forms. In time, as seen in Fig. 3 a, b, c and d, eye of the circulation moves towards the impingement point and then toward the outlet of the flow domain. As seen in these figures, the velocity vectors vary in the impingement region, more than other regions of the flow area. After hitting the plate, the flow accelerates again and starts to flow along the plate toward the exit. However, it is also seen that, in some parts, the fluid flows in the opposite direction, so that a number of circulations are formed. One circulation forms close to the free jet, and the other, within the wall jet region. The formation of these circulations can cause changes in heat transfer rate, thus, the secondary local maximums form in Nusselt number along the plate. Figure 3b depicts the flow field at the instant $t=0.25\tau$ of the pulsation period. The analogous descriptions about the flow field as the previous can also be drawn from this figure but, it is notable that the circulation formed have widened. Figure 3c and 3d show the flow field at two instants of the second half of the pulsation period. Considering the impingement region at all instants of the pulsation period, it can be seen that the magnitudes of the velocity vectors in the first part of the period are higher than those of the second part. This is an expected result, since the jet exit velocity in the first half of the period is higher than that in the second half.

Figure 4, shows the flow fields at the same instants of the pulsation period as in Fig. 3, for the case of $Re=500$, A= $0.2V_0$ and $f=3$ Hz. Comparison of velocity fields given in Figs 3 and 4 shows that with changing pulsation frequency from 1 to 3, the flow fields changes considerable as everything else is kept the same. As seen in these figures, in the impingement and wall jet regions, the flow field changes, more than all other parts of the flow domain so that two circulations form. There is also another circulations forming in the wall jet region. Another thing that should be pointed out is that two small eddies formed in the first half of the period merge and create a bigger circulation. The wall jet zone circulation also enlarges within the second half of the period, and becomes more obvious.
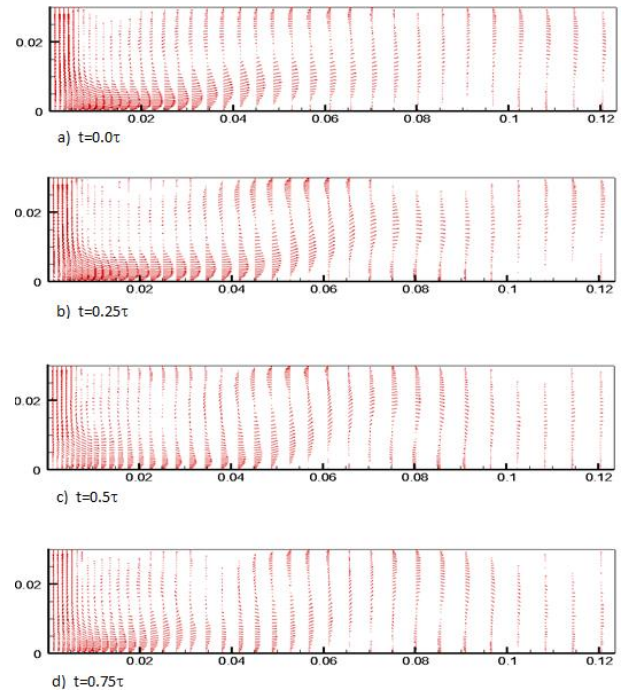

Figure 3. Velocity vector distributions at four different instants of pulsation period for *Re=500*, *A=0.2V₀* and *f=1 Hz*.
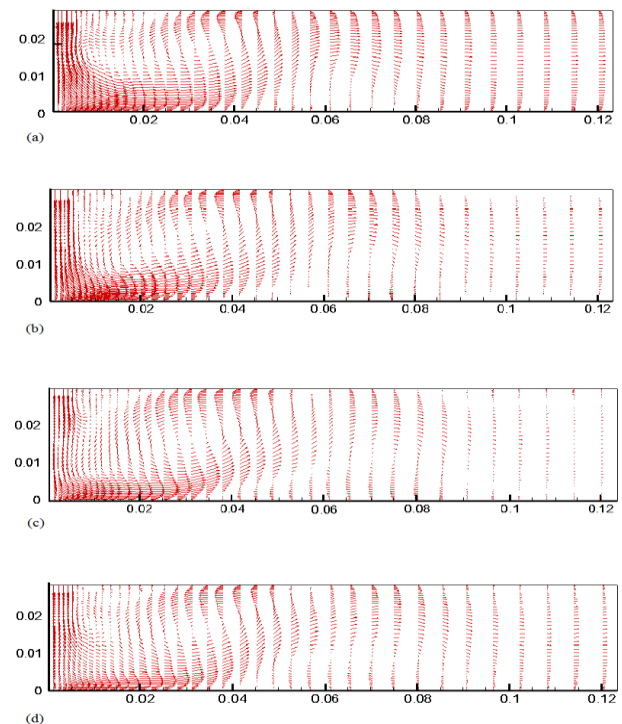

Figure 4. Velocity vector distribution at four different instants of pulsation period when *Re=500*, *A=0.2V₀* and *f=3 Hz*. a) *t=0.0τ*, b) *t=0.25τ*, c) *t=0.5τ*, d) *t=0.75τ*.

Figures 5 and 6 show the temperature fields at different instants of the pulsation period for the cases considered in Figs 3 and 4. It is seen in these figures that for both cases, the thermal boundary layer has its smallest thickness and the temperature gradients are very high around the impingement point. Hence, the heat transfer rate reaches its maximum value. This provides a means for efficient local cooling. It should be pointed out that

the boundary layer thickness increases toward the end of the injection period. This is the result of the variation of the jet exit velocity along the pulsation period.

To investigate the effects of Reynolds number, pulsation frequency and pulsation amplitude on the heat transfer rate from the bottom plate, the instantaneous local, time (period) averaged local, instantaneous stagnation point and period averaged stagnation point Nusselt numbers were calculated using Eqs. (7) through (11). Some of these results are discussed below.
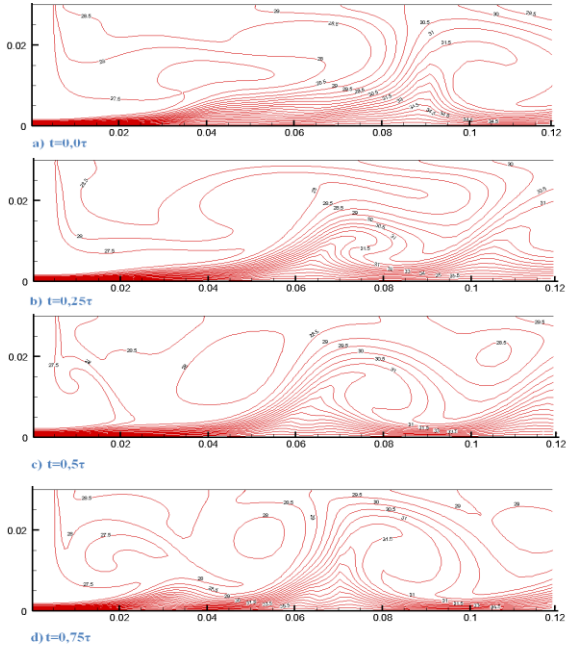

Figure 5. Temperature contours at four different instants of pulsation period when $Re=500$, $A= 0.2V_0$ and $f=1$ Hz.
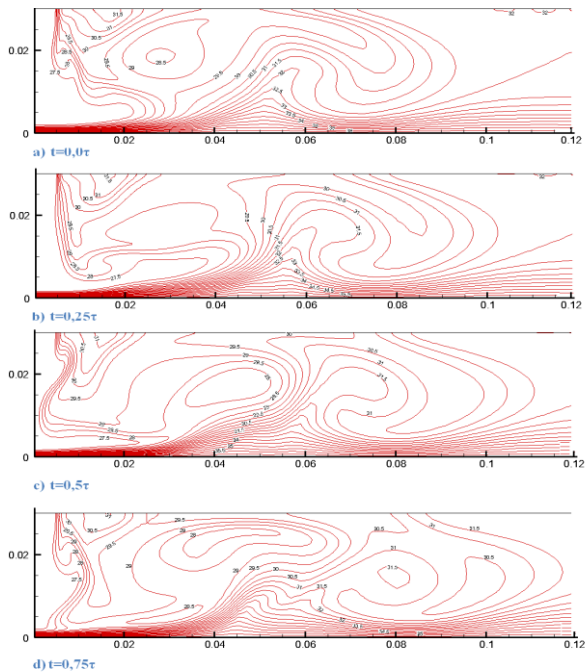

Figure 6. Temperature contours at four different instants of oscillation period when $Re=500$, $A= 0.2V_0$ and $f=3$ Hz.

In order to see the variation of the heat transfer rate compared to that of the steady jet flow, Nusselt number variations along the bottom plate at different moments of the pulsation period were analyzed and compared with the steady jet Nusselt number. In this regard, in Fig. 7 the local Nusselt number variation curves over the bottom plate are given for two different amplitudes ($A= 0.4V_0$ and $0.6V_0$) when $Re=500$ and $f=2$ Hz. In Fig. 8, the similar results are given for $f=6$ Hz. In these figures, it is seen that the instantaneous Nusselt number curves are around the Nusselt number of the steady jet. Since the flow is pulsating, the impingement velocity of the fluid is different at different instants of the pulsation period. Hence, it is expected that the instantaneous Nusselt number changes with both position and time. Also, Nusselt number changes with both the pulsation amplitude and frequency. It is seen in Fig. 7 (a) and (b) that the highest stagnation point Nusselt number is attained at the instant $t= 0.375\tau$ in both cases shown in these figures. It is also seen that, at all instants of the period, Nusselt number curves have local maximum and minimum values at different locations. However, toward the exit of the flow domain, the Nusselt number curves at different instants converge to each other. Analysis of the results given in in Fig. 7 and 8 shows that at a given jet Reynolds number, the difference between steady jet Nusselt number and the pulsating jet Nusselt number increases with the increasing pulsation amplitude. With the increasing pulsation frequency, this difference decreases at all pulsation amplitudes.

a) f=2, A=0.4V_0

b) f=2, A=0.6 V_0

Figure 7. Variation of instantaneous local Nusselt number along the bottom plate for Re=500 and oscillation frequency f=2 Hz at different oscillation amplitudes.

CONCLUSIONS

In this study, pulsating impinging jets confined by two circular discs were considered. The bottom disc was kept at constant temperature, and the top disc was insulated. A pulsating air jet, issuing from a circular hole on the top

disc, was impinged on the bottom hot disc. The jet velocity was pulsated in time. A computer code based on control volume approach and SIMPLE algorithm was developed. The jet Reynolds number was varied between 100 and 700. The effects of the amplitude and frequency of the jet pulsation on the flow and temperature fields, and on the heat transfer rate from the bottom plate were numerically investigated.
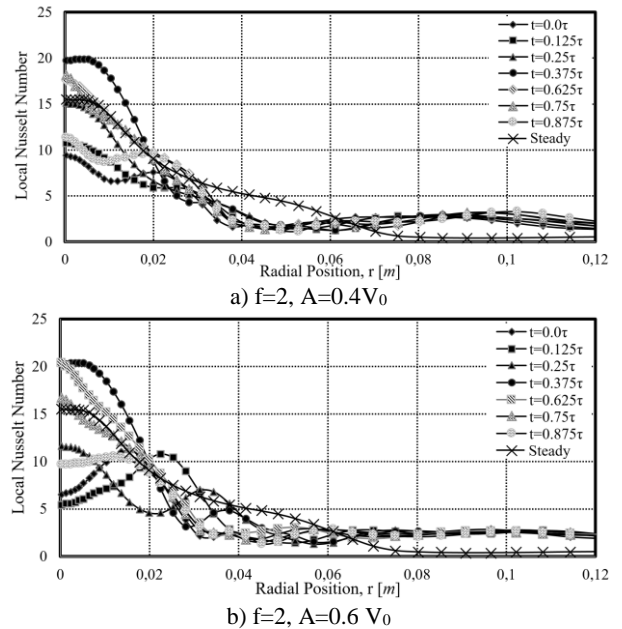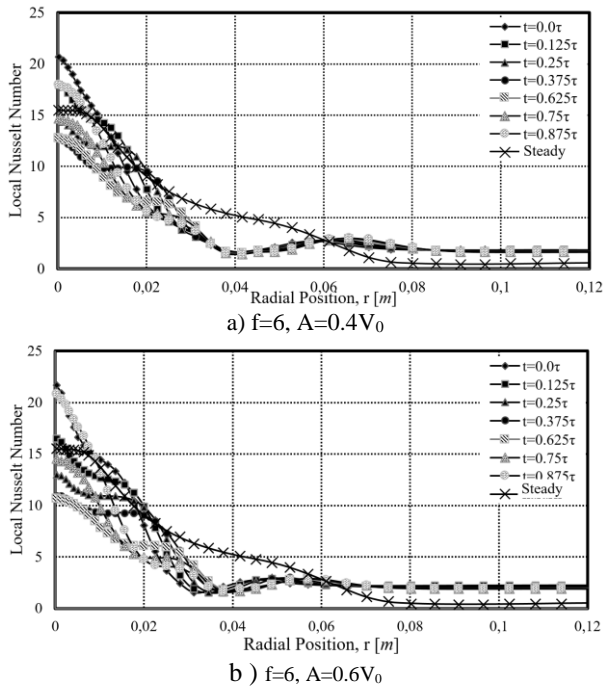

Figure 8. Variation of instantaneous local Nusselt number along the bottom plate for Re=500 and oscillation frequency f=6 Hz at different oscillation amplitudes.

It was observed that the general structures of the flow and temperature fields of pulsating jets are similar to the flow field of the steady jets. However, in the pulsating jet cases, circulating and moving flow regions form in the flow. These circulating flow regions become more apparent with increasing Reynolds number and pulsation amplitude.
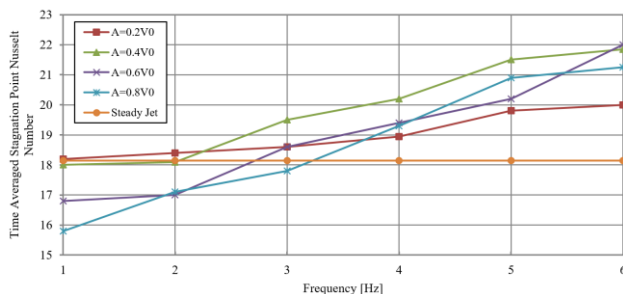

Figure 9. Period averaged stagnation point Nusselt number variation with the pulsation frequency and pulsation amplitude at *Re=700* and different.

At a given instant of the pulsation period, the local Nusselt number is maximum at the stagnation point and it decreases along the plate. This decrease in the local Nusselt number is not monatomic as in the steady jet case. It has local maximum and minimum values

(fluctuations) due to the moving recirculating flow regions along the bottom wall. At low frequencies, the time (period) averaged stagnation point Nusselt numbers for all the pulsating jets considered are lower than the corresponding steady jet Nusselt numbers, However, with the increasing frequency, the stagnation point Nusselt number increases and become higher than the steady jet Nusselt number. With the increasing pulsation frequency, the impingement point Nusselt number increases up to a certain value of the frequency, after that value of the frequency, the impingement point Nusselt number approximately stays the same.

REFERENCES

Azevedo, L. F. A., Webb, B.W. and Queiroz, M., 1994, Pulsed Air Jet Impingement Heat Transfer, *Exp. Thermal Fluid Sci.*, 8, 206–213.

Collucci, D. W. and Viskanta, R., 1996, Effect of Nozzle Geometry on Local Convective Heat Transfer to a Confined Impinging Air Jet, *Experimental Thermal and Fluid Science*, 13, pp. 71 – 80.

Demircan, T. and Turkoglu, H., 2010, The Numerical Analysis of Oscillating Rectangular Impinging Jets, *Numerical Heat Transfer, Part A*, 58, 146-161.

Goldstein, R. J. and Timmers, J. F., 1982, Visualization of Heat Transfer from Arrays of Impinging Jets, *International Journal of Heat and Mass Transfer,* 25, 1857 – 1868.

Goppert S., Gourtler T., Mocikat H. and Herwig, H., 2004, Heat Transfer Under a Precessing Jet: Effects of Unsteady Jet Impingement. *International Journal of Heat and Mass Transfer,* 47, 2795–2806.

Liu T. and Sullivan J.P., 1996, Heat Transfer and Flow Structures in an Excited Circular Impinging Jet, *Int. J. Heat Mass Transfer* 39 (17), 3695–3706.

Miladin, E.C. and Zumbrunnen, D. A., 1997, Local Convective Heat Transfer to Submerged Pulsating Jets, *Int. J. Heat Mass Transfer,* 40 (14), 3305–3321.

O'Donovan T. S. and Murray. B., 2008, Fluctuating Fluid Flow and Heat Transfer of an Obliquely Impinging Air Jet, *International Journal of Heat and Mass Transfer,* 51, 25-26.

Poh H. J, Kumar K. and Majumdar A. S., 2005, Heat transfer from a pulsed laminar impinging jet, *International Communications in Heat and Mass Transfer,* 32, 1317–1324.

Zumbrunnen, D. A. and Aziz, M., 1993, Convective Heat Transfer Enhancement Due to Intermittency in an Impinging Jet, *J. Heat Transfer,* 115 91–98.

EXPERIMENTAL INVESTIGATION OF SOLAR STILLS INTEGRATED WITH SOLAR WATER HEATING COLLECTORS

Emin EL*, Gülşah ÇAKMAK**, Zeki ARGUNHAN*** and Cengiz YILDIZ**

*Vocational School of Technical Sciences, Bitlis Eren University, 13000 Bitlis, Turkey
**Corresponding author: Department of Mechanical Engineering, Firat University, 23119 Elazig, Turkey,
zeki.argunhan@batman.edu.tr, Phone: +90 488 2173670, Fax: +90 488 217 36 01
***Department of Mechanical Engineering, Batman University, 72100 Batman, Turkey

Abstract: Solar still is a more practical way of obtaining clean water. In this study, we aimed to improve the efficiency of solar still systems and obtain distilled water at the same time. For this purpose, 5 different solar still systems were designed. Type 1; conventional solar still, Type 2; conventional solar still integrated with solar water heating collector and run via natural convection, Type 3; conventional solar still integrated with solar water heating collector and tubular heat exchanger and run via natural convection, Type 4; conventional solar still placed with plate heat exchanger and integrated with solar water heating collector and run via natural convection, Type 5; conventional solar still placed with plate heat exchanger and integrated with solar water heating collector and run via forced convection. In this study, the experiments were carried out on the parameters influencing the performance, the amount of distilled water obtained, and the efficiency of experiment settings designed in different types; and finally the results were presented. The amount of distilled water and efficiency of conventional solar still were 2389 ml and 51.47%, respectively. Maximum total amount of water and efficiency from natural convection systems were obtained from Type 4, and the values calculated were found as to be 5788 ml and 55.91%. Maximum amount of distilled water and the efficiency were obtained by utilizing forced convection system were found as to be 6068 ml and 58.99%, respectively.
Keywords: Solar water heater, Solar water distillation, Efficiency.

GÜNEŞ ENERJİLİ SU ISITICI KOLLEKTÖRLERLE BİRLEŞTİRİLMİŞ GÜNEŞ ENERJİLİ DAMITICILARIN DENEYSEL İNCELENMESİ

Özet: Güneş enerjili damıtıcı temiz su elde etmenin daha pratik bir yöntemidir. Bu çalışmada, güneş enerjili damıtıcı sistemlerin verimini arttırmayı ve aynı anda damıtılmış su elde etmeyi amaçladık. Bu amaçla 5 farklı güneş enerjili damıtıcı sistem tasarlandı. Tip 1; geleneksel güneş enerjili damıtıcı, Tip 2; doğal taşınım yoluyla çalıştırılan ve güneş enerjili sıcak su kollektörü ile birleştirilmiş geleneksel güneş enerjili damıtıcı Tip 3;doğal taşınım yoluyla çalıştırılan, boru tipi ısı değiştirgeci ve güneş enerjili sıcak su kollektörü ile birleştirilmiş geleneksel güneş enerjili damıtıcı, Tip 4; doğal taşınım yoluyla çalışan, plaka tipi ısı değiştirgeci ve güneş enerjili sıcak su kollektörü ile birleştirilmiş geleneksel güneş enerjili damıtıcı, Tip 5; zorlanmış taşınımla çalışan plaka tipi ısı değiştirgeci ve güneş enerjili sıcak su kollektörü ile birleştirilmiş geleneksel güneş enerjili damıtıcı. Bu çalışmada deneyler, farklı tiplerde tasarlanan deney düzeneklerinin performansı etkileyen parametreler, elde edilen damıtık su miktarları ve verimleri ile ilgili yürütüldü. Ve nihayetinde sonuçlar sunuldu. Geleneksel güneş enerjili damıtıcının damıtılmış su miktarı ve verimi sırasıyla 2389 ml ve %51.47 'dir. Doğal taşınım sistemlerde, maksimum toplam damıtık su eldesi ve verim Tip 4'te elde edildi ve hesaplanan değerler 5788 ml ve %55.91 olarak bulundu. Maksimum damıtık su miktarı ve verim zorlanmış taşınım sisteminden faydalanarak elde edilmiş sırasıyla 60698 ml ve %58.99 olarak bulunmuştur.
Anahtar Kelimeler: Güneş enerjili su ısıtıcısı, Güneş enerjili su damıtma, Verim.

NOMENCLATURE

h	Heat transfer coefficient [W/m^2°C]
I	Total solar energy [W/m^2]
L	Water's heat of vaporization [J/g]
P	Vapor pressure [kPa]
m	The amount of distilled water [ml]
T	Temperature [°C]
V	Wind speed [m/s]
Wp	Consumed electric power [W]

ε_{eff}	Effective permittivity
η	Efficiency
σ	Stefan-Boltzmann constant

Subscripts

e	evaporation
w	water
g	glass
r	radiation
c	convection

s   surrounding
b   bottom
v   vapor
ig   internal surface of glass
og   outer surface of glass

INTRODUCTION

Since the fresh surface waters sources cannot sufficiently meet the water requirement, many researches are being carried out on alternative solutions. For instance; within the scope of use of underground waters, the studies are carried out on using the precipitation waters and recycling waste waters. The insufficient time for preventing the irreversible depletion of natural resources forces humans to develop and utilize the technologies in order to protect and save these resources.

It is a very old method to obtain potable water by distilling saltwater and underground and aboveground waters containing excessive level of minerals (Sampathkumar, at al, 2010). The process of obtaining clean water is divided into 2 main categories based on the type of energy used. These are energy-supported methods and mechanically-supported methods. The main input of thermal energy-supported distillation is the thermal energy, while the reverse-osmosis and electrolysis methods require mechanical or electrical energy. Since the reverse osmosis and electrolysis methods are the processes requiring high level energy, it is essential to establish large systems in order to utilize them effectively. On the other hand, the small-scaled thermal systems are also very suitable for the places, where the central water mains cannot be reached, or if it is not possible to make investment for central water main.

The places, where clean water is needed mostly, are also the places receiving the most intense solar energy. For this reason, the solar energy distillation method is the most effective method to be implemented. The production of clean water via distillation is a simple, effective, and also a reliable method. This process requires energy, and solar energy can be used as a very effective source of heat in this process. During this process; firstly, water vaporizes, and the matters it includes are separated, and then potable water condenses. Solar energy distillation pools remove salt and heavy metals from the water and prevent water-related diseases. The potable waters obtained from these systems are much healthier than great many bottled waters.

In general, constructing and operating the solar energy distillation systems are not too expensive. However, their most important disadvantage is low productivity. For this reason, large surfaces are required for achieving successful results. This significantly increases the initial investment costs. The scientists carrying out research on this topic have designed various types of distillation systems in order to achieve better efficiency values. As a result, various models of solar energy distillation systems have been introduced.

Rajaseenivasan et al. (2014) examined the performance of conventional solar still by pre-heating saltwater via integrated flat plate solar collector. They examined the system by using various water depths, wick and energy storage equipment. Under the same conditions, they achieved 60% higher distillation than the classic distillers. The maximum productivity of conventional solar and integrated system were 3.62 and 5.82 kg/m²·day, respectively.

Xiong et al. (2013) designed a new-type solar distiller system via increased condensation surface. In this system, heating was performed with both vacuum-piped collected at bottom and the coating at the top of tank. The trays placed inside the tank were wrinkled in order to decrease the condensation resistance. In that system, they have examined the temperature changes and fresh water efficiency. As a result of their study, they reached fresh water productivity up to 40%.

Morad et al., (2015) performed thermal analyses via energy balance equations by using internal and external heat transfers in order to estimate the performance of bilateral solar distiller system with integrated glass cover cooler. They utilized active and passive distillers for thermal analyses. For both distiller systems, the performance was found to be the function of change in glass coverage thickness and pool depth under cooled and non-cooled conditions.

Appadurai and Velmurugan (2015) performed experimental analysis and theoretical performance examination of flapped-type solar pool integrated with solar distiller, flapped-type solar distiller and classic solar distiller. In order to improve the performance of classic solar distiller, the flaps were placed into the distiller. Then the same operation was also performed in the pool. With using a larger surface for solar radiation, 50% higher productivity was achieved than the conventional solar still.

Alaudeen et al., (2014) utilized a multi-stage solar distiller in order to improve the productivity of solar distiller. In order to establish the new system, they combined the multi-stage solar still with a sloped plate collector. In order to increase the vaporization rate, the experiments were performed at various depths allowing additional space, and 3% increase was achieved at 2 cm depth in proportion to the classic distiller.

The aim of this study is to obtain drinkable and usable clean water by using this four newly-developed solar stills. For this purpose, a conventional solar still system integrated with solar collector was designed. In this system, in order to enlarge the surface area, the tubular and plate heat exchangers were placed into the distiller integrated with solar water heating collector, and the

daily production and the system efficiency values were recorded and then compared.

EXPERIMENTAL DESIGN AND METHOD

In this experimental study, the solar still was integrated with solar water heating collector, and the experiments were performed by placing tubular and plate heat exchangers into the distiller. In the experiments, the parameters affecting the performance of solar still integrated with plate solar collector under the conditions of Elazığ city were examined as shown in Figure 1. Within this scope, 5 different experimental settings, equipment and the working principles of these settings are specified below in Figure 2-4.


**Figure 1.** Photograph of the experiment set

Type 1; Conventional solar still was designed. Distilling pool was manufactured from stainless sheet iron in dimensions of 1000x1000x250 mm. The base area was 1m², and the slope of cover was 38°. The basement and internal parts were painted with epoxy filler and mat black paint. In order to prevent leakage from the cover, the solar, heat, and moisture-resistant sealing components were utilized. The sloped top of distiller allowed gathering the condensed waters into a tank, which was placed out of the distiller, through natural convection. Distilled water collection channel, which was placed in the distillation pool, was made of stainless material in 50mm width, 25mm height and 7° slope. The transparent cover conveying the solar radiation but preventing the thermal loss protected the surface from external effects such as rain, hail and heat loss from the top. For this purpose, a 4mm-thick glass was used as cover of this system. Moreover, in order minimize the heat loss from sides, bottom and rear parts were isolated with a 4cm-thick polyurethane material.

Type 2; the conventional solar still was integrated with solar water heating collector and then operated via natural convection. The system consisted of planar solar water heating collector, a solar still distiller, table, and connectors. For the experiments, the setting had the

dimensions of 930x1930x87.5 mm, and with covering gross surface area of 1.8 m² and net surface area of 1.6 m² and consisting of aluminium oval pipes, flapped and painted in black, planar solar water heating collector. In this system, the heat of water within the solar still was increased via solar energy.
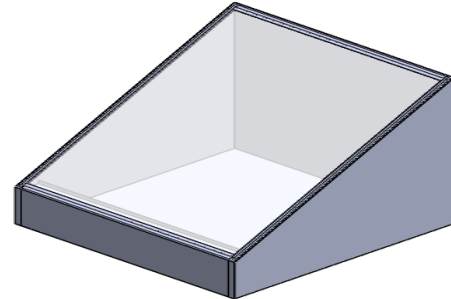
Type 1
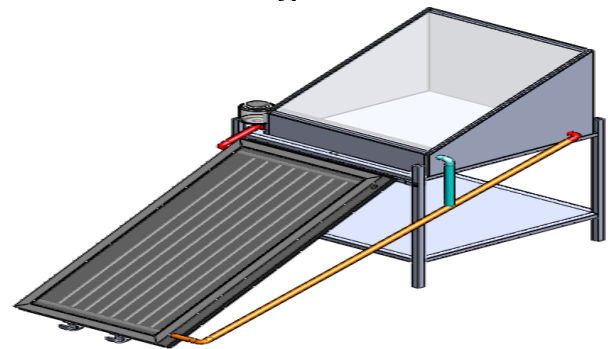
Type 2
Figure 2. Type 1; Conventional solar still Type 2; Conventional solar still was integrated with solar water heating collector

As a result of increased temperature, the vaporized water reached at the colder top-cover and then condensed. Then, due to the slope of top condensation cover, the distilled water condensed, dropped onto the bottom surface and then flowed into the collection channel place on the front side. The distilled water gathering in collection channel was conveyed out by means of slope, and collected in the distilled water tank.

Type 3; By placing tubular heat exchanger into the conventional solar still, it was integrated with the solar water heating collector and then run via natural convection. In this system, there was a planar solar water heating collector, a solar still distiller, a tubular heat exchanger placed into the distiller, table, and connectors. In this experimental setting, different from Type-2, there is a tubular heat exchanger placed within the distiller, and the hot water from planar solar water heating collector passes through the tubular heat exchanger without mixing with the water in hot water distiller, and then returns. In this system, the water increasing its temperature in planar solar water heating collector passes through the tubular heat exchanger within the solar still and then conveys its heat to the water within the solar still distiller. So, the effect of water with increased temperature on the vaporization and condensation is

determined, and then compared to other experimental settings.

Type 4; By placing plate heat exchanger into the conventional solar still, it was integrated with the solar water heating collector and then run via natural convection. In this system, a plate heat exchanger was placed into the solar still. By employing the plate heat exchanger, it was aimed to enlarge the areas of both heat transfer surface and absorber surface. In this system, the water having increased temperature in planar solar water heating collector passes through the plate heat exchanger within the solar still distiller, and then conveys its heat to the water within the solar still.

Type 5; By placing a plate heat exchanger into the conventional solar still, it was integrated with the solar water heating collector and then run via forced convection. In this system, different from Type-4, a circulation pump was added into the setting, the system was run at 50 kg/h flowrate as forced convection. Rotameter was utilized in order to measure the flowrate.
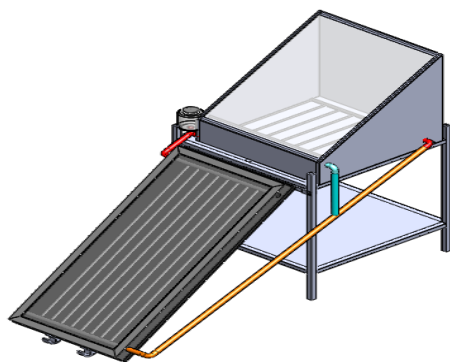
Type 3
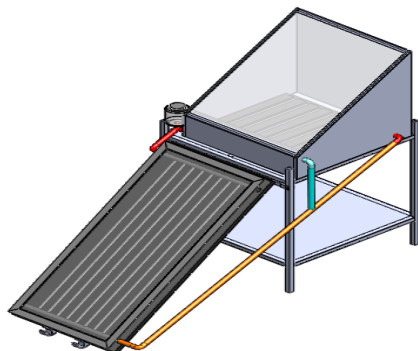
Type 4

Figure 3. Type 3; Conventional solar still integrated with solar water heating collector and tubular heat exchanger Type 4; Conventional solar still integrated with solar water heating collector and tubular heat exchanger.

In present study, 2 different heat exchangers were designed in order to improve the amount of distilled water production and increase the efficiency of distillers, and then they were placed into the solar still (Figure 5). One of the designed heat exchangers was tubular, while

other had the advanced plate design. Hence, the tubulars and advanced plates were placed into the conventional solar still, and the amounts of distilled water obtained from the solar still distillers, and the efficiency values were compared to each other.

Of the heat exchangers used for this purpose; the plate and tubular ones were made of copper and their dimensions were 900x900 mm, the number of tubulars was 8, the manifold material was copper, manifold diameter was 25mm, and the welding method was ultrasonic welding, and the copper tubulars and plates were painted in black.
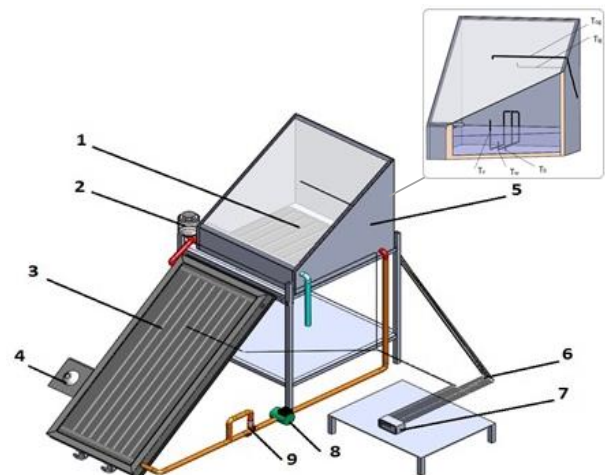
Figure 4. Type 5; Conventional solar still integrated with solar water heating collector and tubular heat exchanger. (1. Heat exchanger, 2.Glass jar, 3.Solar water heating collector, 4. Pyranometer, 5.Solar still , 6. Thermocouple, 7. Digital thermometer, 8. Circulation pump, 9. Rotameter.)

(a)

(b)
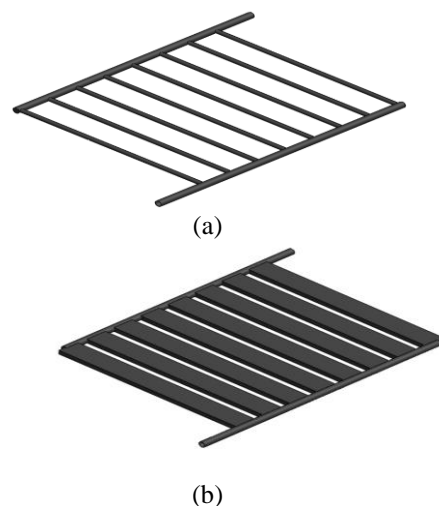
Figure 5. (a). Tubular heat exchanger (b). Advanced plate heat exchanger

After the designed experimental settings were established, by adding 100L water into the solar still distiller, the angle of planar solar water heating collectors in systems was set to 38˚. And then, the inlet and outlet temperatures of water into and out of the planar solar water heating collectors, internal temperatures of

distillers, and ambient temperature were measured by placing J-type thermocouples at the required points. By using digital thermometer, the temperature of places, where the thermocouples were placed, were hourly measured between 08:00 and 16:00.

Considering the parameters leading to error during the distillation experiments, the total error was determined in accordance with the following formula (Holman, 1971).

$$W_{th} = \left[(x_1)^2 + (x_2)^2 + ...(x_\infty)^2 \right]^{\frac{1}{2}} \qquad (1)$$

The error parameters arising from different independent variables are different and the parameters resulting from temperature and speed measurement are listed below.

Errors Made in Temperature Measurement
(X_1) Error due to thermo couple pairs = $\pm$ 0.25-0.5 ° C,
(X_2) Error due to digital thermometer = $\pm$ 0.1 ° C,
(X_3) Error due to connectors and points = $\pm$ 0.1 ° C,
(X_4) Mean error that can be done with temperature measurement = $\pm$ 0.25 ° C,

Errors Caused by Speed Measurement
(X_5) Error due to sensitivity of anemometry = $\pm$ 0.1 m /s
(X_6) Measuring error = $\pm$ 0.1 m / s
During the experiments, the total errors were calculated and are presented in Table 1.

Table 1. Total errors occurring during the distillation experiments

Parameters Leading to Error	Total Error
Total error in measuring the temperature at collector inlet	$\pm$ 0.173 °C
Total error in measuring the temperature at collector outlet	$\pm$ 0.173 °C
Total error in measuring the water temperature in the solar still	$\pm$ 0.173 °C
Total error in measuring the glass surface temperature	$\pm$ 0.173 °C
Total error in measuring the air temperature	$\pm$ 0.173 °C
Total periodical error in measuring the wind speed	$\pm$ 0.104 m/s
Total periodical error in reading the temperature values	$\pm$ 0.1 min
Total periodical error in measuring the air temperature	$\pm$ 0.1 min
Total periodical error in measuring the radiation	$\pm$ 0.1 min
Total periodical error in measuring the fresh water produced	$\pm$ 4.062 ml
Total periodical error in measuring the flow rate	$\pm$ 0.86 kg/h

As a result of these experiments, the amounts of distilled water obtained from the systems and the efficiencies of these systems were calculated, and then compared to each other. The efficiency of a solar distillation system was the proportion of thermal energy used for obtaining water to solar radiation on the glass cover of the system within a certain time interval (Tiwari et al., 2003). It can be expressed as follows;

$$\eta = q_{ew} / I(t) \qquad (2)$$

where, η is the efficiency, q_{ew} is thermal energy used for distilled water, I (t) is solar radiation falling on a glass cover. This expression can also be stated as below (Sodhaet al.,1980), in form of the portion of heat, which is transferred to transparent cover from water surface via vaporization, to the amplitude of radiation on the effective collector surface:

$$\eta = \left[(h_{ew} + h_{sg}) / (h_{gw} + h_{sg}) \right] (T_w - T_a) \qquad (3)$$

where, the coefficient of heat transfer via vaporization (h_{ew}) (Malik et al.,1982);

$$h_{ew} = 16.273 \times 10^{-3} h_{cw} (P_w - P_g) / (T_w - T_g) \qquad (4)$$

coefficient of heat transfer via convection from water to cover (h_{cw}) (Dunkle et al., 1961);

$$h_{cw} = 0.884 [(T_w - T_g) + (P_w - P_g)(T_w + 273)/(268.9 \times 10^3 - P_w)]^{1/3} \qquad (5)$$

coefficient of heat transfer from glass cover to the environment (Duffie et al., 1980);

$$h_{sg} = 5.7 + 3.8V \qquad (6)$$

coefficient of heat transfer to water surface to transparent cover (Malik et al.,1982);

$$h_{gw} = h_{cw} + h_{rw} + h_{ew} \qquad (7)$$

and coefficient of heat transfer via radiation from water surface to cover (h_{rw}) (Sharma et al., 1991);

$$h_{rw} = \varepsilon_{eff} \sigma \left[(T_w + 273)^2 + (T_g + 273)^2 \right] \left[T_w + T_g + 546 \right] \qquad (8)$$

The amount of distilled water obtained hourly from the distiller is calculated according to the formula below.

$$m_{ew} = \frac{h_{ew} (T_w - T_g) 3600}{L_w} \qquad (9)$$

where L_w is the latent heat of vaporization of water and calculated using the following correlation;

$$L_w = 3044205.5 - 1670.1109 \, T_w - 1.14258 \, T_w^2 \qquad (10)$$

Accordingly, the efficiency of system based on the amount of distilled water is,

$$\eta = \frac{m_{ew}L}{IA3600} \qquad (11)$$

The efficiency in the system using the pump is calculated via the following equation;

$$\eta = \frac{m_{ew}L}{IA3600 + Wp.\Delta t} \qquad (12)$$

RESULTS AND DISCUSSION

The experiments of solar still integrated with solar water heating collectors were performed on 2 October 2012 under climatic conditions of Elazığ city. The radiation and wind speed values for that day are given in Fig. 6. Conventional solar still (Type 1), conventional solar still integrated with solar water heating collector (Type 2), and the distiller integrated with tubular heat exchanger (Type 3) and with plate heat exchanger (Type 4) were used with natural convection. In addition, the experiment was performed with Type-4 by using forced convection. Throughout the experiments, the temperature measurements were performed on the glass surface of condenser, outer surface of glass, basement, water and vapor, and then expressed via graphics.
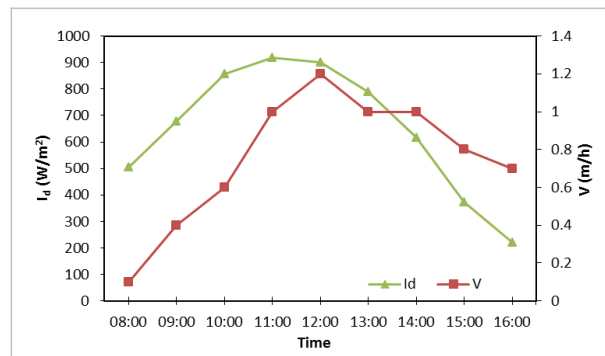

Figure 6. Time-dependent change of the radiation and wind speed values

<u>Type 1 :</u>

For the conventional solar still, as defined in Figure 4, the bottom temperature (T_b), water temperatures (T_w), vapor temperature (T_v), internal surface of glass (T_{ig}), and outer surface of glass (T_{og}) are presented in Figure 7.

As seen in Figure 7, the glass temperatures increased till 12:00 and then declined. The highest temperature of glass surfaces was measured at 12:00, when the internal temperature was 59.3 ˚C and glass surface temperature was 56.6 ˚C. In distillation systems, it has been observed that the amount of distilled water production increased as the glass temperatures decreased. Bottom and water temperatures showed continuous increase during the day, while vapor temperature increased until 12:00 and then decreased. The highest vapor temperature was measured at 12:00 to be 64.1˚. In performance measurements, it has

been observed that the temperatures of bottom and water were close to each other.
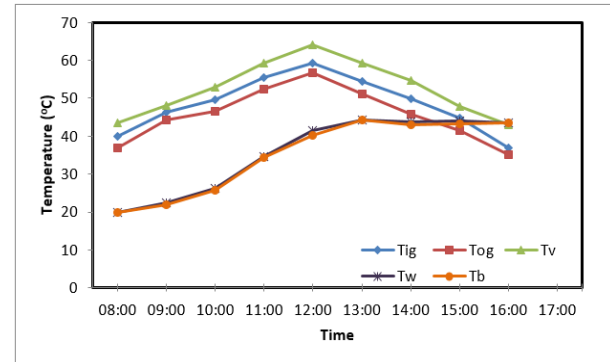

Figure 7. Time-dependent change of temperatures in conventional solar still

In Figure 8, the amount of distilled water obtained by conventional solar still was expressed as m, while the amount of water was expressed as mt. In performed measurements, it was found that the temperature of distilled water continuously increased until 15.00 and then decreased. The highest water production throughout the measurement periods was determined to be 210 ml between 14.00 and 15.00. At the end of the day, a total of 844 mL distilled water was obtained. By means of heat storage within the water inside the tank, the distillation that was slow during daytime continued after the sunset, even during the night-time. One of the most important factors was the exterior temperature decreasing during night-time due to atmospheric conditions. The heat stored in pool during daytime maintained the continuance of distillation until the water temperature decreased to external temperature. The amount of distilled water obtained in the night-time was found to be 1545 ml. The total amount of distilled water obtained in this system in a day was found to be 2389 ml.
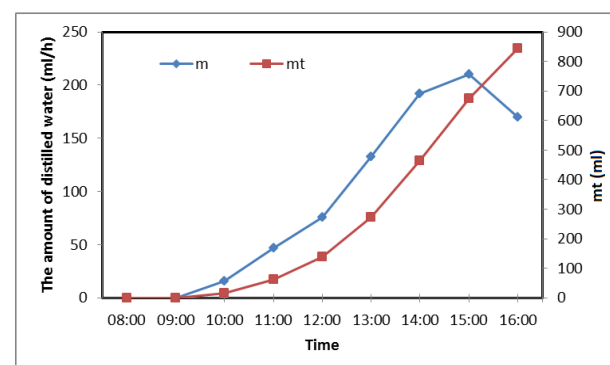
Figure 8. Amount of water distilled in conventional solar still

The distillation of water started with the increase of thermal capacity of distillation pool by the solar radiation intensity. This value was approximately 3-4 MJ/m². It was determined in pools manufactured in different shapes that the distillation continued after the sunset. It was observed that evaporation in the distillation system was minimal in the morning hours and reached maximum between 12: 00-15: 30.

Type 2:

In this system, the solar still was integrated with solar water heating collector. The water within the distiller was transferred via natural convection, and its temperature increased while passing through solar water heating collector. The system temperatures measured in experiments are presented in Figure 9.
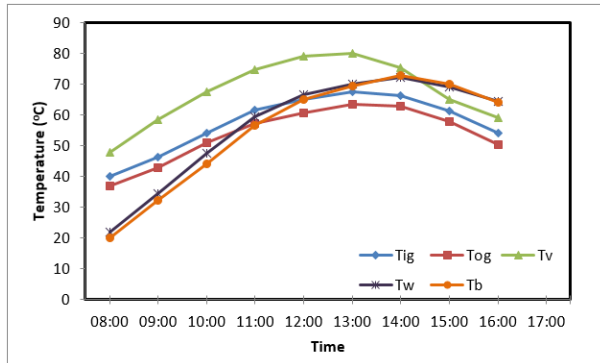
Figure 9. Time-dependent change of temperatures in conventional solar still integrated with solar water heating collector

As seen in Figure 9, the glass temperatures increased till 13:00 and then declined. The highest temperature of glass surfaces was measured at 13:00, when the internal temperature was 67.6 ˚C and glass surface temperature was 63.5 ˚C. Bottom and water temperatures showed continuous increase until 14:00 and 13:00, respectively, and then decreased. The highest vapor temperature was measured at 13:00 to be 80˚C. In performance measurements, an increase was observed in measured temperatures in proportion to the conventional solar still.

The highest water production was achieved between 14:00 and 15:00 as 688 ml. At the end of day, a total of 2582 ml distilled water was obtained. The amount of distilled water obtained during the night-time was measured to be 2630 ml. The total amount of daily production of distilled water in this system was found to be 5212 ml (Figure 10).

Type 3:

In this system, tubular heat exchanger was placed into the conventional solar still integrated with solar water heating collector. Through the natural convection, the water that was heated in solar water heating collector was let to pass through the tubular heat exchanger within the distiller, and the temperature of the water within the distiller increased.

As seen in Figure 11, the glass temperatures increased till 13:00 and then declined. The highest temperature of glass surfaces was measured at 13:00, when the internal temperature was 69.0 ˚C and glass surface temperature was 65.0˚C. Bottom and water temperatures showed continuous increase until 14:00 and 13:00, respectively, and then decreased. The highest vapor temperature was measured at 13:00 to be 81.0˚C. In performance

measurements, an increase was observed in measured temperatures in proportion to the conventional solar still.

Figure 10. The amount of distilled water distilled in conventional solar still integrated with solar water heating collector

It was observed that the hourly amount of distilled water production in solar still integrated with tubular heat exchanger increased continuously until 15.00 and then decreased.
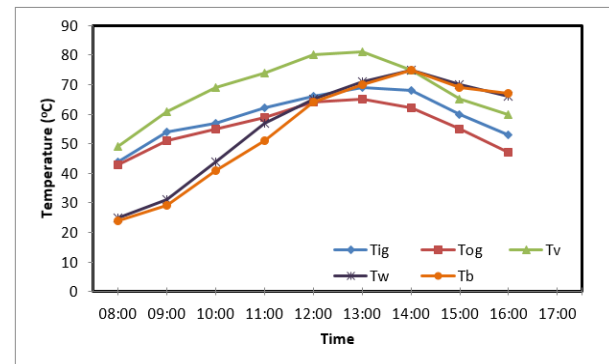
Figure 11. Time-dependent change of temperatures in conventional solar still integrated with tubular heat exchanger

As a result of hourly measurements, the highest amount of water production was obtained between 14:00 and 15:00 (a total of 654 ml). At the end of the day, a total of 2502 ml of distilled water was obtained (Figure 12). The amount of water obtained during the night-time was determined to be 2520 ml. With this system, the total amount of water obtained in a day was found to be 5022 ml.
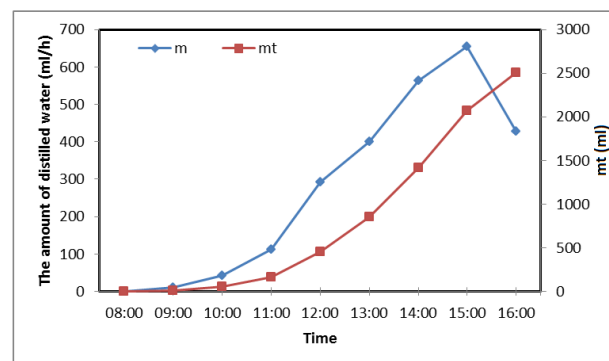
Figure 12. The amount of distilled water distilled in conventional solar still integrated with tubular heat exchanger

Type 4 :

In this system, plate heat exchanger was placed into the conventional solar still integrated with solar water heating collector. Through the natural convection, the water that was heated in solar water heating collector was let to pass through the plate heat exchanger within the distiller, and the temperature of the water within the distiller increased. As seen in Figure 13, the glass temperatures increased till 13:00 and then declined. The highest temperature of glass surfaces was measured at 13:00, when the internal temperature was 73.2 °C and glass surface temperature was 70.1 °C. Bottom and water temperatures and vapor temperature showed continuous increase until 14:00 and 13:00, respectively, and then decreased. The highest vapor temperature was measured at 13:00 to be 85.8°. In performance measurements, an increase was observed in measured temperatures in proportion to the conventional solar still integrated with tubular heat exchanger.
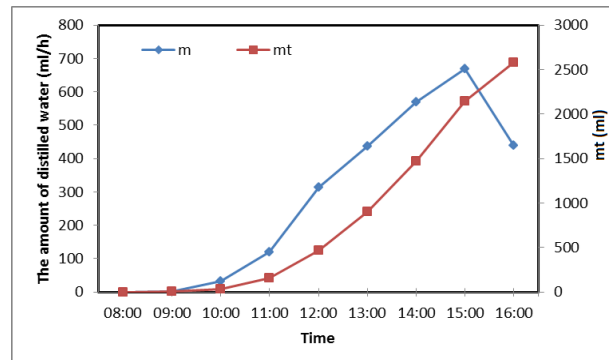

Figure 13. Time-dependent change of temperatures in conventional solar still integrated with plate heat exchanger

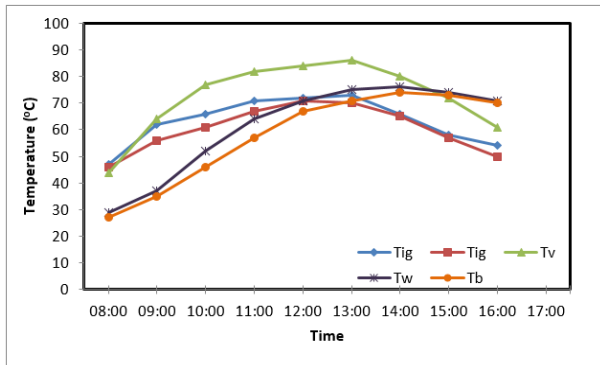It was observed that the hourly amount of distilled water production in solar still integrated with plate heat exchanger increased continuously until 15.00 and then decreased. As a result of hourly measurements, the highest amount of water production was obtained between 14:00 and 15:00 (a total of 692 ml). At the end of the day, a total of 3066 ml of distilled water was obtained (Figure 14). The amount of water obtained during the night-time was determined to be 2722 ml. With this system, the total amount of water obtained in a day was found to be 5788 ml.

Figure 14. The amount of distilled water distilled in conventional solar still integrated with plate heat exchanger

The efficiency values obtained via natural convection are presented in Figure 15 (η_1 for Type 1, η_2 for Type 2, η_3 for Type 3, and η_4 for Type 4).

As seen in Figure 15, it was determined that the solar still integrated with plate heat exchanger was the one having the highest efficiency value. In natural convection systems, it was observed that the efficiency generally increased throughout the day and peaked at the end of daytime. The maximum efficiency values calculated as a result of measurements were 51.47% for conventional solar still, 46.73% for conventional solar still integrated with solar water heating collector, 45.38% for conventional solar still integrated with tubular heat exchanger, and 55.91% for conventional solar still integrated with plate heat exchanger.
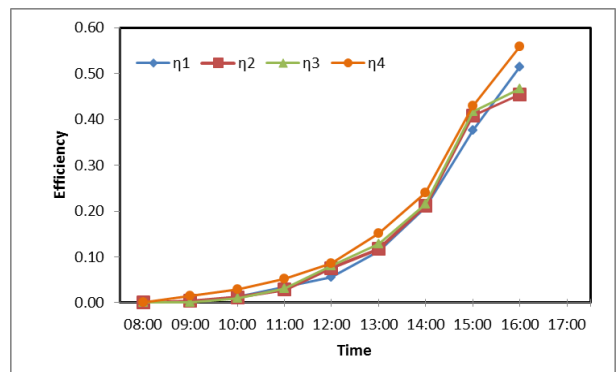
Figure 15. Time-dependent changes of system efficiencies

Type 5 :

In this experiment, the plate heat exchanger was placed into the conventional solar still integrated with solar water heating collector and then run via forced convection.

For the experiment carried out in October, the bottom temperature (Tb), water temperature (Tw), vapor temperature (Tv), internal surface of glass (Tig), outer surface of glass (Tog) temperatures are presented in Figure 16.

Figure 16. Time-dependent change of temperatures in conventional solar still integrated with plate heat exchanger (forced convection)

As seen in Figure 16, the glass temperatures increased till 13:00 and then declined. The highest temperature of glass surfaces was measured at 13:00, when the internal temperature was 74.2 ˚C and glass surface temperature was 71.0 ˚C. Bottom and water temperatures and vapor temperature showed continuous increase until 14:00 and 13:00, respectively, and then decreased. The highest vapor temperature was measured at 13:00 to be 86.3˚. In performance measurements, an increase was observed in measured temperatures in proportion to the conventional solar still integrated with tubular heat exchanger.

It was observed that the hourly amount of distilled water production in forced convection solar still integrated with plate heat exchanger increased continuously until 15.00 and then decreased. At the end of the day, a total of 3278 ml of distilled water was obtained (Figure 17). The amount of water obtained during the night-time was determined to be 2790 ml. With this system, the total amount of water obtained in a day was found to be 6068 ml.
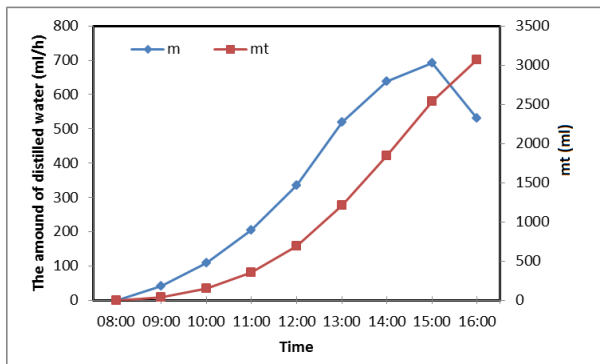
The results of experiments carried out with solar still integrated with plate heat exchanger via natural and forced convection are presented in Figure 18.

Figure 17. The amount of distilled water distilled in conventional solar still integrated with plate heat exchanger (forced convection)

Figure 18. Natural and forced convection system efficiencies

In natural and forced convection systems, it was observed that the efficiency generally increased throughout the day and peaked at the end of the day. The maximum efficiency values calculated as a result of measurements were 55.91% for conventional solar still integrated with plate heat exchanger (natural convection), and 55.91%

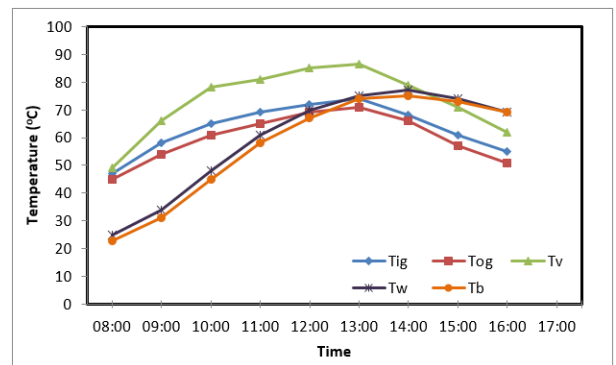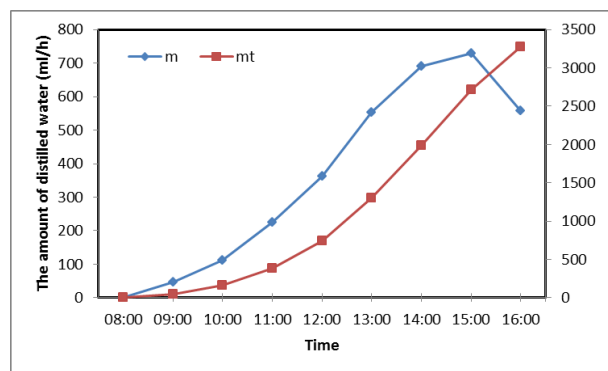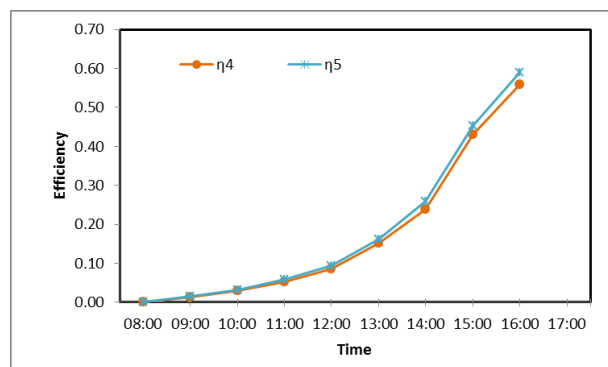for conventional solar still integrated with plate heat exchanger (forced convection at 50 kg/h). Accordingly, the productivity of forced convection system was found to be the highest one. There is a harmony between distillers' efficiency and air temperature, received solar energy and water temperature. The air temperature, received solar energy and mean water temperature are the variables depending on each other, and the increase in any of them increases the efficiency of distiller.

CONCLUSIONS

In this study, the experimental research was carried out on the performance of traditional solar still and, by placing different types of heat exchangers within the distiller integrated with solar collector in order to improve performance; the effects of these heat exchangers were also examined.

The results obtained from the analyses of performed experiences are summarized below;
- It was observed that the vaporization peaked between 12:00 and 15:00 in distillation systems. For this reason, the amount of distilled water obtained in morning hours was higher than those obtained in afternoon.
- It was found that the amount of distilled water obtained between 11:00 and 12:00, when the solar radiation peaked, was less than the amount of distilled water obtained between 14:00 and 15:00. This was because most of the energy received between 11.00 and 12.00 was spent on increasing the temperature of the water within distiller. Moreover, since the temperature of transparent cover was high, the level of condensation decreased.
- It was observed that the temperature of transparent cover is of significant importance for the performance of distiller. It was also determined that decreasing the temperature of transparent cover or keeping it constant may improve the efficiency of distiller.
- The maximum amount of distilled water production in conventional solar still integrated with solar water heating collector was measured to be 688 ml between 14.00 and 15.00. At the end of the day, a total of 2582 ml was obtained. The amount of distilled water obtained during the night-time was determined to be 2630 ml, and the total amount of distilled water obtained in a day was calculated to be 5212 ml.
- The maximum amount of distilled water obtained hourly with solar still integrated with tubular heat exchanger was achieved between 14:00 and 15:00 (654 ml). 2502 and 2520 ml of distilled water was obtained during daytime and night-time, respectively, while the total amount of distilled water obtained throughout the day was 5022 ml.
- The maximum amount of distilled water obtained hourly with solar still integrated with plate heat exchanger was achieved between 14:00 and 15:00 (692 ml). 3066 and 2722 ml of distilled water was obtained during daytime and night-time, respectively,

while the total amount of distilled water obtained throughout the day was 5788 ml.

- As a result of the measurements, it was determined that the calculated efficiency value of conventional solar still was 51.47%. In natural convection systems, the efficiency of solar still integrated with solar water heating collector was 46.73%, while that of solar still integrated with tubular heat exchanger was 45.38% and the efficiency of solar still integrated with plate heat exchanger was found to be 55.91%.
- The reason for obtaining lower efficiency from solar still integrated with tubular heat exchanger in proportion to that of solar still integrated with plate heat exchanger was the increase in both heat transfer surface area and absorber surface area by means of plate heat exchanger placed into the solar still distiller. So, the temperature of water within the distiller increased to higher temperatures, and an increase was obtained in vaporization level.
- For solar still systems integrated with solar water heating collector, it was determined that the efficiency of the system integrated with plate heat exchanger was higher than the efficiency values of system integrated with tubular heat exchanger and than that of the conventional system. Moreover, it was observed that the value of 58.99% could be achieved via forced convection system.

ACKNOWLEDGMENTS

REFERENCES

Alaudeen A., Johnson K., Ganasundar P., Syed Abuthahir A., Srithar K., 2014, Study on stepped type basin in a solar still distiller, Journal of King Saud University – *Engineering Sciences,* 26, 176–183.

Appadurai M., Velmurugan V., 2015, Performance analysis of fin type solar still integrated with fin type mini solar pond, *Sustainable Energy Technologies and Assessments*, 9, 30–36.

Duffie J., Backman W.A., 1980, *Solar Engineering Thermal Processes,* Wiley, New York.

Dunkle R.V., 1961, Solar water distillation, the roof still and multiple effect diffusion still, International Development in Heat Transfer, *ASME, Proc. International Heat Transfer, Part V,* University of Colorado.

Holman, J.P. (1971). *Experimental Methods for Engineers,* McGrawHill Book Company, 37-52.

Malik, M.A.S., Tiwari, G.N., Kumar, A. and Sodha, M.S. 1982, *Solar Distillation: A Practical Study of a Wide Range of Stills and Their Optimum Design, Construction and Performance,* Pergamon Press, Oxford.

Morad M.M., El-Maghawry H.A.M., Wasfy K.I., 2015, Improving the double slope solar still performance by using flat-plate solar collector and cooling glass cover, *Desalination*, 373, 1–9.

Rajaseenivasan T., Nelson Raja P., and Srithar K., 2014, An experimental investigation on a solar still with an integrated flat plate collector, *Desalination*, 347, 131-137.

Sampathkumar K., Arjunan T.V., Pitchandi P., and Senthilkumar P., 2010, Active solar distillation A detailed review, *Renewable and Sustainable Energy Reviews,* 14, 1503–1526.

Sharma V.B., Mallick S.C., 1991, Estimation of heat transfer coefficients, upward heat flow and evaporation in a solar still distiller, *Trans. ASME (Solar Energy),* 113, 36-41.

Sodha M.S., Singh U., Kumar A., Tiwari G.N., 1980, Transient analysis of solar still distiller, *Energy Conversion and Management,* 20, 191-195.

Tiwari G.N., Shukla S.K., Singh I.P, 2003, Computer modeling of passive/active solar still distillers by using internal glass temperature, *Desalination*, 154, 171-185.

Xiong J., Xie G., Zheng H., 2013, Experimental and numerical study on a new multi-effect solar stillwith enhanced condensation surface, *Energy Conversion and Management*, 73, 176–185.

Emin EL, He was born in 1985 Diyarbakır. He earned his undergraduate degree from the Department of Mechanical Engineering of Dicle University in 2008. In 2010, he started his graduate program in the Department of Mechanical Engineering of the Faculty of Engineering, Fırat University, Department of Thermodynamics and completed his master's degree in 2013. She has been working as a lecturer in Bitlis Eren University since 2013.

Assoc. Prof. Gülşah ÇAKMAK was born in 1977 in Elazığ. She earned her undergraduate degree from the Department of Mechanical Engineering of Fırat University (FU) in 1998. She continued M.S. and Ph.D. studies in the same department. She worked as a research assistant in Fırat University between 2000 and 2011. She received her Ph. D. degree with her work on " Design of solar dryer system with swirling flow for drying seeded grape".She has been working as an associate professor since 2014. Gülşah ÇAKMAK's primary field of interest is heat exchangers, drying and thermodynamics.

Assoc. Prof. Zeki ARGUNHAN. He was born in 1966 in Batman. Bachelor of Science in Mechanical Engineering Middle east Technical University, in 1987. After serving in various positions within General Directorate of Highways he moved to the Dicle University Batman Vocational High School as a lecturer in 1995. He get PhD. from Fırat University in 2003. He has PhD in Thermodynamic and Energy. He is Associate Professor in the Department of Mechanical Engineering at Batman University. His research interests are in Thermodynamic, Energy, Solar, Heat exchanger and Fuel. He has 37 publications, 16 in international and national scientific journals.

Prof. Dr. Cengiz YILDIZ. He was born in Elazığ in 1962. He completed his Bachelor Degree in 1985, Master's Degree in 1987 and received his Ph.D. from Fırat University in 1990. He started his academic career as Research Assistant in Department of Mechanical Engineering of Fırat University, Engineering Faculty in 1986. He was promoted to the rank of Assistant Professor in 1991, Associate Professor in 1997 and Professor in 2003. He served as Department Chair in Department of Mechanical Engineering between 2005 and 2007 and as Dean of Fırat University Faculty of Engineering between 2007 and 2011. His research interests are thermodynamics, heat transfer, heat exchangers, drying and renewable energy sources.

NUMERICAL INVESTIGATION OF BUOYANCY DRIVEN HEAT TRANSFER OF WATER-BASED CuO NANOFLUIDS IN A RECTANGULAR ENCLOSURE WITH AN OFFCENTER SOLID CONDUCTING BODY

Çiğdem SUSANTEZ* and Kamil KAHVECİ*
*Trakya University Engineering Faculty Mechanical Engineering Department
22030 Edirne, cigdemsusantez@trakya.edu.tr, kamilk@trakya.edu.tr

Abstract: In this study, buoyancy driven heat transfer of water-based CuO nanofluid in a rectangular enclosure with a solid cylinder was investigated numerically for different values of aspect ratio, location and diameter of solid cylinder, solid volume fraction and Rayleigh number. While bottom and upper walls of enclosure are adiabatic, sidewalls are isothermal. Thermal conductivity of solid cylinder was assumed to be equal to that of the base fluid. Governing equations were solved numerically by Comsol Multiphysics finite element modeling and simulation software. Results show that heat transfer rate increases considerably with an increase in the Rayleigh number and solid volume fraction and with a decrease in the solid cylinder diameter. Results also show that heat transfer rate shows an increase with an increase of aspect ratio for low values of Rayleigh number. Finally, results show that heat transfer rate gets its highest value for square enclosure case for high values of Rayleigh number.
Keywords: Nanofluid, Enclosure, Convective heat transfer, Rayleigh number, Nusselt number

MERKEZ DIŞI KATI İLETKEN BİR CİSİM İÇEREN DİKDÖRTGEN KAPALI BİR ORTAMDA SU BAZLI CuO NANOAKIŞKANLAR İÇİN KALDIRMA KUVVETİ ETKİLİ ISI TRANSFERİNİN NÜMERİK İNCELENMESİ

Özet: Bu çalışmada, katı bir silindir içeren dikdörtgensel kapalı bir ortamda su bazlı CuO nanoakışkanlar için kaldırma kuvveti etkili ısı transferi farklı yükseklik genişlik oranı, katı silindirin yeri ve çapı, nanoparçacık hacim oranı ve Rayleigh sayısı değerleri için nümerik olarak incelenmiştir. Kapalı ortamın alt ve üst duvarları adyabatik iken, yan duvarları izotermaldir. Silindirin ısı iletim katsayısının baz akışkanınkine eşit olduğu varsayılmıştır. Yönetici denklemler Comsol Multiphysics sonlu eleman modelleme ve simülasyon yazılımı kullanılarak nümerik olarak çözülmüştür. Sonuçlar, ısı transferinin Rayleigh sayısı ve nanoparçacık hacim oranının artışı ve katı silindir çapının düşüşü ile önemli ölçüde arttığını göstermiştir. Sonuçlar aynı zamanda Rayleigh sayısının düşük değerleri için ısı transferinin yükseklik genişlik oranının artışı ile arttığını göstermiştir. Sonuçlar ayrıca ısı transferinin en yüksek değerlerini Rayleigh sayısının yüksek değerleri ve karesel kapalı ortam durumu için aldığını göstermiştir.
Anahtar Kelimeler: Nanoakışkan, Kapalı ortam, Taşınımla ısı transferi, Rayleigh sayısı, Nusselt sayısı

NOMENCLATURE

ar: aspect ratio [ar = H/L]
c_p: specific heat at constant pressure [Jkg^{-1}K^{-1}]
D: diameter of the solid cylinder [m]
g: gravitational acceleration [ms^{-2}]
H: height of the enclosure [m]
k: thermal conductivity [WmK^{-1}]
k^*: ratio of the thermal conductivity of the solid cylinder to that of the base fluid
L: width of the enclosure [m]
Nu: Nusselt number $[-\frac{k_{eff}}{k_f}\frac{\partial T^*}{\partial x^*}\big|_{x^*=0}]$
n: shape factor [$= 3/\Psi$]
$\vec{n}$: unit normal vector
P: pressure [Pa]
Pr: Prandtl number [$= \frac{\nu_f}{\alpha_f}$]

$\dot{q}$: heat flux [Wm^{-2}]
Ra: Rayleigh number [$= \frac{g\beta_{T,f}L^3\Delta T}{\nu_f\alpha_f}$]
T: temperature [K]
u: velocity component in x direction [ms^{-1}]
v: velocity component in y direction [ms^{-1}]
x: horizontal coordinate [m]
y: vertical coordinate [m]

Greek symbols
α: thermal diffusivity [m^{2}s^{-1}]
β: ratio of the liquid nanolayer thickness to the original particle radius
β_T: thermal expansion coefficient [K^{-1}]
ΔT: temperature difference [K]
μ: dynamic viscosity [Pa s]
ν: kinematic viscosity [m^{2}s^{-1}]

φ: solid volume fraction
Ψ: sphericity
ρ: density [kgm^{-3}]

Subscripts
a: average
c: cylinder
C: cold
eff: effective
f: fluid
H: hot
S: surface
s: solid
1: outside of the solid cylinder
2: inside of the solid cylinder

Superscripts
*: dimensionless variable

INTRODUCTION

Conventional heat transfer fluids have relatively low thermal conductivity and this is the main drawback in enhancing the heat transfer performance of many engineering devices. In the past, micron-sized particles with high thermal conductivities were tried to be used within the base fluid to eliminate this drawback. However, it was observed that using micron-sized particles have some other drawbacks such as clogging, sedimentation and high pressure drop. These drawbacks have been overcome by the production of solid particles in nano size with the advancement in technology. Ag, Al, Au, Cu, Fe, diamond, Al_2O_3, CuO, Fe_3O_4, TiO_2 and carbon nano tubes have been used as nanoparticles within the base fluid. Nanofluids have a wide variety of applications in the fields of heat transfer (industrial cooling applications, smart fluids, nuclear reactors, extraction of geothermal power and other energy sources), automotive (nanofluid coolant, nanofluid in fuel, brake nanofluids), electronic (cooling of microchips, microscale fluidic applications), biomedical (nanodrug delivery, cryopreservation, nanocryosurgery, …) (Wong and Leon, 2010). Therefore, over the last decades, nanofluids have been the subject of many studies. Wang et al. (1999) measured the effective thermal conductivity of nanofluids by steady state parallel plate method. They used Al_2O_3 and CuO as nanoparticles and water, vacuum pump fluid, engine oil and ethylene glycol as the base fluid. Their results show that adding 8% Al_2O_3 increases the thermal conductivity of ethylene glycol 40%. They also observed that the measured thermal conductivity of nanofluids is much higher than that of the predicted value by existing models. Xuan and Li (2000) performed a study on the thermal conductivity of nanofluids and developed Nusselt number correlations. They used hot wire method to measure the thermal conductivity of water-based Cu nanofluids. They found that increasing the volume fraction of Cu nanoparticles from 2.5% to 7.5% increases the ratio of the thermal conductivity of nanofluid to that of the base liquid from 1.24 to 1.78. Choi et al. (2001) added nanotubes to oil and found that the thermal conductivity of nanofluid with 1.0

vol. % nanotubes is 160 times greater than that of the oil. They also found that the measured thermal conductivities are significantly higher than the predictions of conventional models. Their study also shows that the measured thermal conductivity shows a non-linear increase with nanotube volume fraction. Xuan and Li (2003) performed an experimental study on the convective heat transfer of water-based Cu nanofluids in a tube. They suggested a Nusselt correlation including the effects of microconvection and microdiffusion of nanoparticles. They also found that the friction factor of water-based Cu nanofluids and water are almost the same. Kang et al. (2006) made an experimental study to measure the thermal conductivity of nanofluids and observed that adding 1% ultra-dispersed diamond increases the effective thermal conductivity of ethylene glycol more than 70%. In another study, Murshed et al. (2008) found that increase in the thermal conductivity of ethylene glycol-based nanofluids is 18% for 5% volumetric loading of TiO_2 particles and 45% for 5% volumetric loading of Al particles. They also found that increase of thermal conductivity of nanofluids with temperature is linear. Li and Peterson (2006) conducted an experimental study to investigate the effects of temperature and volume fraction on the thermal conductivity of nanofluids. Their results show that adding 6% CuO and 10% Al_2O_3 enhances the thermal conductivity of water 1.52 and 1.3 times, respectively. Jang and Choi (2004) suggested a theoretical model accounting the effect of Brownian motion of nanoparticles on the thermal behavior of nanofluids. Murshed et al. (2009) developed a new model combining the static and dynamic effects of thermal conductivity of nanofluids. Cianfrini et al. (2011) performed a theoretical study on natural convection heat transfer of nanofluids in annular spaces between horizontal concentric cylinders. They observed that heat transfer can be enhanced considerably with an optimum particle addition, which depends on temperature and nanoparticle size. Oztop and Abu-Nada (2008) investigated natural convection heat transfer and fluid flow in a partially heated enclosure filled with nanofluids. They observed that heat transfer increases with an increase in Rayleigh number and heater size. Kahveci (2010) investigated buoyancy driven heat transfer of nanofluids in a tilted enclosure for different values of Rayleigh number, solid volume fraction, ratio of nanolayer thickness to the original particle radius and inclination angle. The results show that maximum heat transfer takes place at 45 deg. for Ra=10^4 and at 30 deg. for Ra=10^5, 10^6. Pak and Choi (1998) conducted an experimental investigation on the turbulent flow of nanofluids with metallic oxide particles in a circular pipe. They found that the convective heat transfer coefficient of nanofluid with 3% solid volume fraction is 12% smaller than that of water for a given average fluid velocity. Lai and Yang (2011) found that heat transfer shows an increase with the increase of particle volume fraction and Rayleigh number for the water-based Al_2O_3 nanofluid in a square enclosure. They also found that heat transfer rate of nanofluid is lower than that of water at a fixed temperature difference because of relatively high dynamic viscosity of nanofluids. Yu et al. (2011) made a numerical

study on the laminar natural convection of water-based CuO nanofluids in a horizontal triangular enclosure. Their results show that, when the Grashof number is greater than a critical value, a pitchfork bifurcation is observed. Rahman et al. (2011) numerically investigated the mixed convection of nanofluids in an inclined lid-driven triangular enclosure. They observed that the effect of the solid volume fraction on the flow field is greater than its effect on the thermal field. Susantez et al. (2012) investigated buoyancy driven heat transfer of nanofluids in a square enclosure with a heat conducting solid circular body at the center for various values of the ratio of the thermal conductivity of the solid cylinder to that of the base fluid. The results show that the effect of the ratio of thermal conductivity of the solid cylinder to that of the base fluid on heat transfer rate is negligible. Cihan et al. (2012) investigated convective heat transfer in an inclined square enclosure with a solid cylinder at the center and found that maximum heat transfer takes place at 45° for Ra=10^4 and 30° for Ra=10^5 and Ra=10^6.

From the literature given above, it can be seen that there is a limited number of studies on heat transfer and fluid flow of nanofluids in an enclosure with a conducting solid body and the effects of the several parameters such as aspect ratio of the enclosure, cylinder diameter and location on flow and heat transfer have not been studied yet. Accordingly, heat transfer enhancement of water-based CuO nanofluids in a rectangular enclosure with a solid conducting body was investigated numerically in this study for different values of aspect ratio, diameter and location of the solid cylinder, solid volume fraction, and Rayleigh number.

ANALYSIS

The schematic view of the enclosure geometry used in the study is seen in Fig. 1. While sidewalls of the enclosure are at constant temperature, upper and bottom walls are in adiabatic conditions.
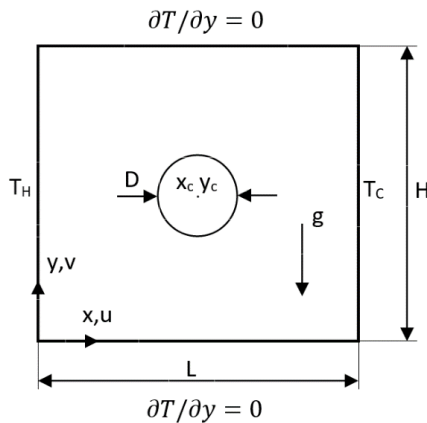

Figure 1. Geometry and coordinate system

Under the assumption of two dimensional, Newtonian, steady and incompressible flow with constant thermophysical properties, the governing equations take the following form:

Continuity equation:

$$\frac{\partial u}{\partial x} + \frac{\partial v}{\partial y} = 0 \tag{1}$$

Momentum equations:

$$u\frac{\partial u}{\partial x} + v\frac{\partial u}{\partial y} = -\frac{1}{\rho_{eff}}\frac{\partial P}{\partial x} + \frac{\mu_{eff}}{\rho_{eff}}\left[\frac{\partial^2 u}{\partial x^2} + \frac{\partial^2 u}{\partial y^2}\right] \tag{2}$$

$$u\frac{\partial v}{\partial x} + v\frac{\partial v}{\partial y} = -\frac{1}{\rho_{eff}}\frac{\partial P}{\partial y} + \frac{\mu_{eff}}{\rho_{eff}}\left[\frac{\partial^2 v}{\partial x^2} + \frac{\partial^2 v}{\partial y^2}\right]$$
$$+ g\beta_{T,eff}(T - T_c) \tag{3}$$

Energy equation:

$$u\frac{\partial T}{\partial x} + v\frac{\partial T}{\partial y} = \frac{k_{eff}}{(\rho c_p)_{eff}}\left[\frac{\partial^2 T}{\partial x^2} + \frac{\partial^2 T}{\partial y^2}\right] \tag{4}$$

Energy equation for the solid cylinder:

$$\frac{\partial^2 T}{\partial x^2} + \frac{\partial^2 T}{\partial y^2} = 0 \tag{5}$$

The governing equations are nondimensionalized by the following nondimensional variables:

$$x^* = \frac{x}{L}, y^* = \frac{y}{L}, u^* = \frac{u}{\frac{\alpha_f}{L}}, v^* = \frac{v}{\frac{\alpha_f}{L}},$$

$$P^* = \frac{L^2}{\rho_f \alpha_f^2}P, \quad T^* = \frac{T - T_C}{T_H - T_C} \tag{6}$$

where u^* and v^* dimensionless velocity components, P^* is dimensionless pressure, T^* is dimensionless temperature, α_f and ρ_f are thermal difusivity and densitiy of the base fluid, respectively.

The corresponding nondimensional form of the governing equations are as follows:

$$\frac{\partial u^*}{\partial x^*} + \frac{\partial v^*}{\partial y^*} = 0 \tag{7}$$

$$\frac{\rho_{eff}}{\rho_f}u^*\frac{\partial u^*}{\partial x^*} + \frac{\rho_{eff}}{\rho_f}v^*\frac{\partial u^*}{\partial y^*} =$$
$$-\frac{\partial P^*}{\partial x^*} + \frac{\rho_{eff}}{\rho_f}\frac{v_{eff}}{v_f}Pr\left[\frac{\partial^2 u^*}{\partial x^{*2}} + \frac{\partial^2 u^*}{\partial y^{*2}}\right] \tag{8}$$

$$\frac{\rho_{eff}}{\rho_f}u^*\frac{\partial v^*}{\partial x^*} + \frac{\rho_{eff}}{\rho_f}v^*\frac{\partial v^*}{\partial y^*} =$$
$$-\frac{\partial P^*}{\partial y^*} + \frac{\rho_{eff}}{\rho_f}\frac{v_{eff}}{v_f}Pr\left[\frac{\partial^2 v^*}{\partial x^{*2}} + \frac{\partial^2 v^*}{\partial y^{*2}}\right] \tag{9}$$
$$+RaPr\frac{(\rho\beta_T)_{eff}}{(\rho\beta_T)_f}T^*$$

$$u^*\frac{\partial T^*}{\partial x^*} + v^*\frac{\partial T^*}{\partial y^*} = \frac{\alpha_{eff}}{\alpha_f}\left[\frac{\partial^2 T^*}{\partial x^{*2}} + \frac{\partial^2 T^*}{\partial y^{*2}}\right] \tag{10}$$

$$\frac{\partial^2 T^*}{\partial x^{*2}} + \frac{\partial^2 T^*}{\partial y^{*2}} = 0 \tag{11}$$

where aspect ratio, Prandtl and Rayleigh numbers are defined as:

$$ar = \frac{H}{L}, \quad Pr = \frac{v_f}{\alpha_f}, \quad Ra = \frac{g\beta_{T,f}L^3\Delta T}{v_f\alpha_f} \tag{12}$$

where g is gravitational acceleration, ΔT is the temperature difference between the isothermal walls of the enclosure, $\beta_{T,f}$ and v_f are thermal expansion coefficiet and kinematic viscosity of the base fluid, respectively.

The governing equations are subjected to the following boundary conditions:

$$T^*|_{0,y^*} = 1, \quad T^*|_{1,y^*} = 0,$$
$$\left.\frac{dT^*}{dy}\right|_{x^*,0} = 0, \quad \left.\frac{dT^*}{dy}\right|_{x^*,ar} = 0 \qquad (13)$$
$$u^*|_{0,y^*} = 0, \quad u^*|_{1,y^*} = 0,$$
$$u^*|_{x^*,0} = 0, \quad u^*|_{x^*,ar} = 0, \quad u^*|_S = 0 \qquad (14)$$
$$v^*|_{0,y^*} = 0, \quad v^*|_{1,y^*} = 0,$$
$$v^*|_{x^*,0} = 0, \quad v^*|_{x^*,ar} = 0, \quad v^*|_S = 0 \qquad (15)$$

The thermal boundary conditions for the surface of the solid cylinder are based on the continuity of heat flux and thermal equilibrium:
$$\vec{n} \cdot (\vec{q}_1 - \vec{q}_2) = 0 \qquad (16)$$
$$T_1 = T_2 \qquad (17)$$

where $\vec{n}$ is unit normal vector. The subscripts 1 and 2 represent nanofluid and solid cylinder, respectively. From the heat flux continuity equation an extra parameter k^*, which is the ratio of the thermal conductivity of the solid cylinder to that of the base fluid, emerges. In this study, it was assumed that the thermal conductivity of the solid cylinder is equal to that of the base fluid.

Thermal conductivity of the nanofluid is one of the most important parameters related to the heat transfer performance of nanofluids. As there is not a theoretical model for the thermal conductivity of nanofluids, models for solid-liquid mixtures are generally used for this purpose. One of these types of model is Maxwell model (Maxwell, 1873) defined as:
$$\frac{k_{eff}}{k_f} = \frac{k_s + 2k_f + 2(k_s - k_f)\phi}{k_s + 2k_f - (k_s - k_f)\phi} \qquad (18)$$

where k_s and k_f are the thermal conductivity of solid particles and base fluid, respectively, and ϕ is the nanoparticle volume fraction.

Another model proposed by Hamilton and Crosser (1962) for two component mixtures with nonspherical particles takes into account the effect of the shape of particles.
$$\frac{k_{eff}}{k_f} = \frac{k_s + (n-1)k_f + (n-1)(k_s - k_f)\phi}{k_s + (n-1)k_f - (k_s - k_f)\phi} \qquad (19)$$
The shape factor n is defined as a function of sphericity Ψ as $n = 3/\Psi$.

Yu and Choi (2003) proposed a thermal conductivity model based on liquid layering around solid particles. With the assumption of $k_{layer} = k_s$ this model for spherical particles takes the following form:
$$\frac{k_{eff}}{k_f} = \frac{k_s + 2k_f + 2(k_s - k_f)(1 + \beta)^3 \phi}{k_s + 2k_f - (k_s - k_f)(1 + \beta)^3 \phi} \qquad (20)$$
where, β is the ratio of the liquid layering thickness to the original particle radius. This model was used in the present study for the effective thermal conductivity of nanofluids by assuming that $\beta = 0.1$, which is a value that produces good agreements with experimental thermal conductivity data.

To estimate the effective viscosity of nanofluid, the Brinkman model (Brinkman, 1952) was used in this study.
$$\mu_{eff} = \mu_f / (1 - \phi)^{2.5} \qquad (21)$$

The other effective properties of nanofluids can be defined as follows:
$$(\rho c_p)_{eff} = (1 - \phi)(\rho c_p)_f + \phi(\rho c_p)_s \qquad (22)$$
$$(\rho \beta_T)_{eff} = (1 - \phi)(\rho \beta_T)_f + \phi(\rho \beta_T)_s \qquad (23)$$
$$\rho_{eff} = (1 - \phi)\rho_f + \phi \rho_s \qquad (24)$$

The local and average Nusselt number along the hot isothermal wall of the enclosure can be defined as follows:
$$Nu = -\frac{k_{eff}}{k_f} \left.\frac{\partial T^*}{\partial x^*}\right|_{x^*=0} \qquad (25)$$
$$Nu_a = \frac{1}{ar} \int_0^{ar} Nu \, dy^* \qquad (26)$$

RESULTS AND DISCUSSION

Numerical simulations were performed by Comsol Multiphysics finite element modeling and simulation software. The parallel direct sparse solver (Pardiso), which is a high performance and memory efficient solver, was used for the solutions.

The thermophysical properties of the base fluid and nanoparticle used in the study were given in Table 1. The Prandtl number of the base fluid is 6.2.

Table 1. The thermophysical properties of the base fluid and nanoparticle

Property	Water	CuO
$\rho(kg/m^3)$	997.1	6500
$c_p(J/kg\,K)$	4179	536
$k(W/m\,K)$	0.613	20
$\alpha \cdot 10^7 (m^2/s)$	1.47	57.4
$\beta_T \cdot 10^6 (1/K)$	210	51
Pr	6.2	-

A mesh dependency test was also carried out in this study (see Table 2 and 3). The average Nusselt number on the hot wall was obtained for each mesh case. It is seen from Table 2 that the case 5 is appropriate to have mesh independent results. Therefore, it was used in the simulations in the study.

Table 2. The number of mesh elements used in mesh dependency study

Case	Number of elements	Edge elements	Number of degrees of freedom
1	1114	116	2231
2	2224	196	4611
3	6194	350	12724
4	17362	440	34859
5	27908	594	55660

Table 3. Average Nusselt numbers for ar = 0.5, D/L = 0.125, $x_c^* = 0.5$, $y_c^* = 0.25$, $\emptyset = 0$

Case	Ra=10^4	Ra=10^6
1	1.2277	8.5768
2	1.2354	9.0693
3	1.2386	9.1663
4	1.2406	9.1979
5	1.2409	9.2062

Numerical results were validated by comparing the results of this study with the results of Khanafer et al. (2003) and Kahveci (2010) (see Tables 4 and 5). An acceptable agreement is seen between the results. The main reason of relatively higher difference between the results of this study and Khanafer et al. (2003) is different thermal effective conductivity models used for the nanofluid.

Table 4. Validation of the results for water-based Cu nanofluid

	Gr/∅	0	0.04	0.08	0.12	0.16	0.2
Present	10^3	1.934	2.053	2.167	2.282	2.408	2.560
Khanafer et al. (2003)	10^3	1.948	2.100	2.251	2.418	2.584	2.766
Present	10^4	4.078	4.367	4.645	4.916	5.182	5.446
Khanafer et al. (2003)	10^4	4.089	4.375	4.705	5.035	5.365	5.710

Table 5. Validation of the results for water-based CuO nanofluid

	Ra/∅	0.05	0.10	0.15	0.20
Present	10^4	2.466	2.650	2.828	3.005
Kahveci (2010)	10^4	2.466	2.651	2.829	3.005
Present	10^5	5.163	5.597	6.025	6.450
Kahveci (2010)	10^5	5.165	5.599	6.027	6.452
Present	10^6	10.143	11.074	12.008	12.953
Kahveci (2010)	10^6	10.160	11.089	12.022	12.966

Temperature distribution and velocity field in the enclosure are seen in Figs. 2, 3 and 4 for various values of the parameters considered in this study. As it can be observed from the figures that a clockwise rotating circulation is formed in the flow field. Circulation intensity increases considerably with an increase in the Rayleigh number as a result of strengthening convection. As it can also be seen from the temperature distribution that flow regime evolves to the boundary layer flow regime with an increase in the Rayleigh number. As the Rayleigh number increases, the thickness of the thermal boundary layer decreases. As it can be observed from the figures that circulation intensity generally shows a small decrease with an increase in the solid volume fraction for low values of the Rayleigh number as a result of increase in the viscosity. On the other hand, circulation intensity shows an increase with an increase in the solid volume fraction for high values of the Rayleigh number. This can be attributed to the relatively weak viscous forces in high Rayleigh numbers. With an increase in solid volume fraction, both thermal conductivity and viscosity of the nanofluid increases. For low values of Rayleigh number, the effect of viscosity increase on flow is in important levels as a result of relatively significant viscous forces. The effect of viscosity on flow decreases with an increase in the Rayleigh number as a result of relatively lower viscous forces. Therefore, circulation weakens for low Rayleigh number and strengthens for high Rayleigh numbers with an increase in the solid volume fraction. As it can be seen from Fig. 3 that circulation intensity shows a considerable decrease with an increase in the diameter of the cylinder especially for low values of Rayleigh number. As it can also be seen from Figure 3 that maximum velocity shows a decrease or increase with a change of cylinder location depending on the obstruction level of the cylinder on flow and depending on the decrease in flow cross section. It can also be concluded from Figs. 2-4 that circulation intensity shows an increase with an increase in the aspect ratio as a result of higher heat transfer surface area.

The variation of the average Nusselt number with the solid volume fraction is seen in Figs. 5-7 for various values of the parameters considered in this study. As it can be seen from these figures that the average Nusselt number shows a linear increase with the solid volume fraction. It can also be observed that the average Nusselt number shows a significant increase with the Rayleigh number. The average heat transfer rate shows a decrease with an increase in the diameter of the solid cylinder inside the enclosure. As it can be seen from Figs. 5-7 that the heat transfer rate shows an increase with an increase of aspect ratio for low values of Rayleigh number. Highest value of heat transfer rate is for square enclosure case for high values of Rayleigh number.
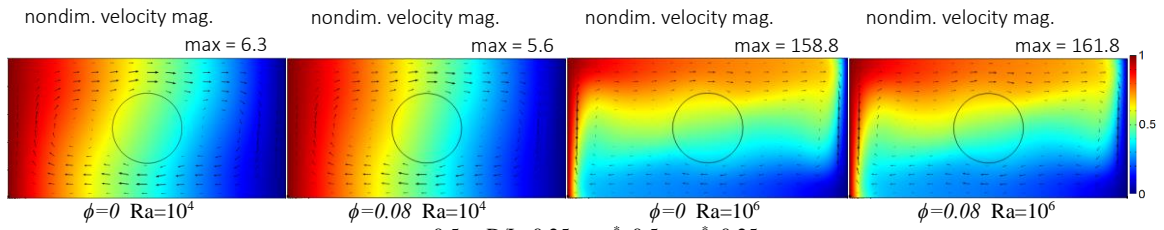
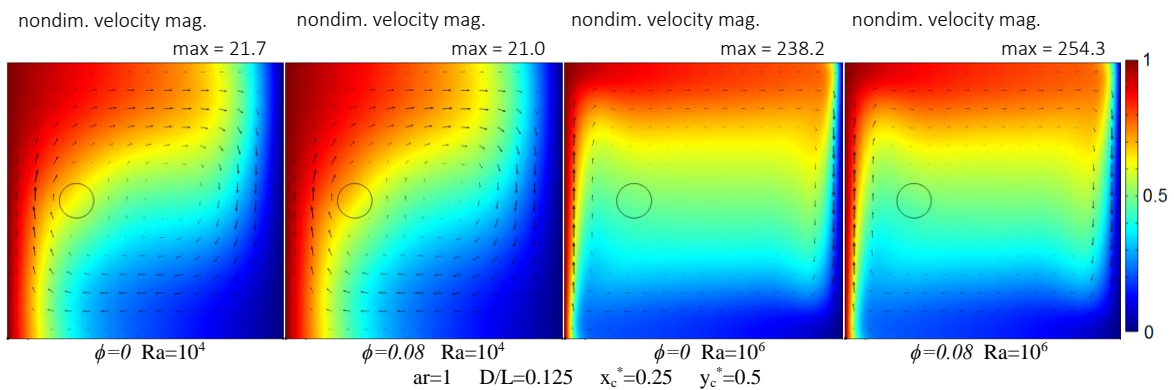**Figure 2.** Temperature distribution and velocity field of water-based CuO nanofluid for ar =0.5

Figure 3a. Temperature distribution and velocity field of water-based CuO nanofluid for ar =1

nondim. velocity mag. max = 18.8   nondim. velocity mag. max = 18.6   nondim. velocity mag. max = 239.2   nondim. velocity mag. max = 255.1

$\phi=0$ Ra=10^4 $\phi=0.08$ Ra=10^4 $\phi=0$ Ra=10^6 $\phi=0.08$ Ra=10^6

ar=1   D/L=0.125 x_c^*=0.25 y_c^*=0.75

nondim. velocity mag. max = 17.3   nondim. velocity mag. max = 17.8   nondim. velocity mag. max = 238.3   nondim. velocity mag. max = 253.2

$\phi=0$ Ra=10^4 $\phi=0.08$ Ra=10^4 $\phi=0$ Ra=10^6 $\phi=0.08$ Ra=10^6

ar=1   D/L=0.125 x_c^*=0.5 y_c^*=0.75

nondim. velocity mag. max = 18.2   nondim. velocity mag. max = 17.9   nondim. velocity mag. max = 237.8   nondim. velocity mag. max = 252.8

$\phi=0$ Ra=10^4 $\phi=0.08$ Ra=10^4 $\phi=0$ Ra=10^6 $\phi=0.08$ Ra=10^6

ar=1   D/L=0.125 x_c^*=0.75 y_c^*=0.75

nondim. velocity mag. max = 21.7   nondim. velocity mag. max = 21.0   nondim. velocity mag. max = 238.2   nondim. velocity mag. max = 254.2

$\phi=0$ Ra=10^4 $\phi=0.08$ Ra=10^4 $\phi=0$ Ra=10^6 $\phi=0.08$ Ra=10^6

ar=1   D/L=0.125 x_c^*=0.75 y_c^*=0.5

Figure 3b. Temperature distribution and velocity field of water-based CuO nanofluid for ar =1

nondim. velocity mag.
max = 18.8

nondim. velocity mag.
max = 18.6

nondim. velocity mag.
max = 239.3

nondim. velocity mag.
max = 255.1

$\phi=0$ Ra=10^4 $\phi=0.08$ Ra=10^4 $\phi=0$ Ra=10^6 $\phi=0.08$ Ra=10^6

ar=1   D/L=0.125 x_c^*=0.75 y_c^*=0.25

nondim. velocity mag.
max = 17.3

nondim. velocity mag.
max = 17.8

nondim. velocity mag.
max = 238.3

nondim. velocity mag.
max = 253.2

$\phi=0$ Ra=10^4 $\phi=0.08$ Ra=10^4 $\phi=0$ Ra=10^6 $\phi=0.08$ Ra=10^6

ar=1   D/L=0.125 x_c^*=0.5 y_c^*=0.25

nondim. velocity mag.
max = 18.9

nondim. velocity mag.
max = 18.8

nondim. velocity mag.
max = 237.2

nondim. velocity mag.
max = 252.6

$\phi=0$ Ra=10^4 $\phi=0.08$ Ra=10^4 $\phi=0$ Ra=10^6 $\phi=0.08$ Ra=10^6

ar=1   D/L=0.25 x_c^*=0.5 y_c^*=0.5

nondim. velocity mag.
max = 15.8

nondim. velocity mag.
max = 15.5

nondim. velocity mag.
max = 236.8

nondim. velocity mag.
max = 250.2

$\phi=0$ Ra=10^4 $\phi=0.08$ Ra=10^4 $\phi=0$ Ra=10^6 $\phi=0.08$ Ra=10^6

ar=1   D/L=0.25 x_c^*=0.25 y_c^*=0.25

Figure 3c. Temperature distribution and velocity field of water-based CuO nanofluid for ar =1

nondim. velocity mag.
max = 19.1

nondim. velocity mag.
max = 17.4

nondim. velocity mag.
max = 238.6

nondim. velocity mag.
max = 262.6

$\phi=0$ Ra=10^4 $\phi=0.08$ Ra=10^4 $\phi=0$ Ra=10^6 $\phi=0.08$ Ra=10^6

ar=1   D/L=0.25 x_c^*=0.25 y_c^*=0.5

nondim. velocity mag.
max = 17.6

nondim. velocity mag.
max = 17.0

nondim. velocity mag.
max = 241.2

nondim. velocity mag.
max = 256.1

$\phi=0$ Ra=10^4 $\phi=0.08$ Ra=10^4 $\phi=0$ Ra=10^6 $\phi=0.08$ Ra=10^6

ar=1   D/L=0.25 x_c^*=0.25 y_c^*=0.75

nondim. velocity mag.
max = 15.4

nondim. velocity mag.
max = 15.0

nondim. velocity mag.
max = 238.3

nondim. velocity mag.
max = 251.8

$\phi=0$ Ra=10^4 $\phi=0.08$ Ra=10^4 $\phi=0$ Ra=10^6 $\phi=0.08$ Ra=10^6

ar=1   D/L=0.25 x_c^*=0.5 y_c^*=0.75

nondim. velocity mag.
max = 15.8

nondim. velocity mag.
max = 15.5

nondim. velocity mag.
max = 236.8

nondim. velocity mag.
max = 250.1

$\phi=0$ Ra=10^4 $\phi=0.08$ Ra=10^4 $\phi=0$ Ra=10^6 $\phi=0.08$ Ra=10^6

ar=1   D/L=0.25 x_c^*=0.75 y_c^*=0.75

Figure 3d. Temperature distribution and velocity field of water-based CuO nanofluid for ar =1

nondim. velocity mag.   nondim. velocity mag.   nondim. velocity mag.   nondim. velocity mag.
max = 19.1   max = 17.4   max = 238.5   max = 262.6

$\phi=0$ Ra=10^4 $\phi=0.08$ Ra=10^4 $\phi=0$ Ra=10^6 $\phi=0.08$ Ra=10^6
ar=1   D/L=0.25 x_c^*=0.75 y_c^*=0.5

nondim. velocity mag.   nondim. velocity mag.   nondim. velocity mag.   nondim. velocity mag.
max = 17.6   max = 17.0   max = 241.2   max = 256.2

$\phi=0$ Ra=10^4 $\phi=0.08$ Ra=10^4 $\phi=0$ Ra=10^6 $\phi=0.08$ Ra=10^6
ar=1   D/L=0.25 x_c^*=0.75 y_c^*=0.25

nondim. velocity mag.   nondim. velocity mag.   nondim. velocity mag.   nondim. velocity mag.
max = 15.4   max = 15.0   max = 238.3   max = 251.7

$\phi=0$ Ra=10^4 $\phi=0.08$ Ra=10^4 $\phi=0$ Ra=10^6 $\phi=0.08$ Ra=10^6
ar=1   D/L=0.25 x_c^*=0.5 y_c^*=0.25

nondim. velocity mag.   nondim. velocity mag.   nondim. velocity mag.   nondim. velocity mag.
max = 17.5   max = 17.2   max = 235.3   max = 249.6

$\phi=0$ Ra=10^4 $\phi=0.08$ Ra=10^4 $\phi=0$ Ra=10^6 $\phi=0.08$ Ra=10^6
ar=1   D/L=0.375 x_c^*=0.5 y_c^*=0.5

Figure 3e. Temperature distribution and velocity field of water-based CuO nanofluid for ar =1

118

Figure 3f. Temperature distribution and velocity field of water-based CuO nanofluid for ar =1

nondim. velocity mag.   max = 13.5   nondim. velocity mag.   max = 13.0   nondim. velocity mag.   max = 228.2   nondim. velocity mag.   max = 237.4

$\phi=0$ Ra=10^4 $\phi=0.08$ Ra=10^4 $\phi=0$ Ra=10^6 $\phi=0.08$ Ra=10^6

ar=1   D/L=0.375 x_c^*=0.75 y_c^*=0.75

nondim. velocity mag.   max = 12.0   nondim. velocity mag.   max = 11.1   nondim. velocity mag.   max = 313.6   nondim. velocity mag.   max = 337.7

$\phi=0$ Ra=10^4 $\phi=0.08$ Ra=10^4 $\phi=0$ Ra=10^6 $\phi=0.08$ Ra=10^6

ar=1   D/L=0.375 x_c^*=0.75 y_c^*=0.5

nondim. velocity mag.   max = 16.8   nondim. velocity mag.   max = 16.3   nondim. velocity mag.   max = 242.6   nondim. velocity mag.   max = 253.6

$\phi=0$ Ra=10^4 $\phi=0.08$ Ra=10^4 $\phi=0$ Ra=10^6 $\phi=0.08$ Ra=10^6

ar=1   D/L=0.375 x_c^*=0.75 y_c^*=0.25

nondim. velocity mag.   max = 11.7   nondim. velocity mag.   max = 11.3   nondim. velocity mag.   max = 235.2   nondim. velocity mag.   max = 245.0

$\phi=0$ Ra=10^4 $\phi=0.08$ Ra=10^4 $\phi=0$ Ra=10^6 $\phi=0.08$ Ra=10^6

ar=1   D/L=0.375 x_c^*=0.5 y_c^*=0.25

Figure 3g. Temperature distribution and velocity field of water-based CuO nanofluid for ar =1
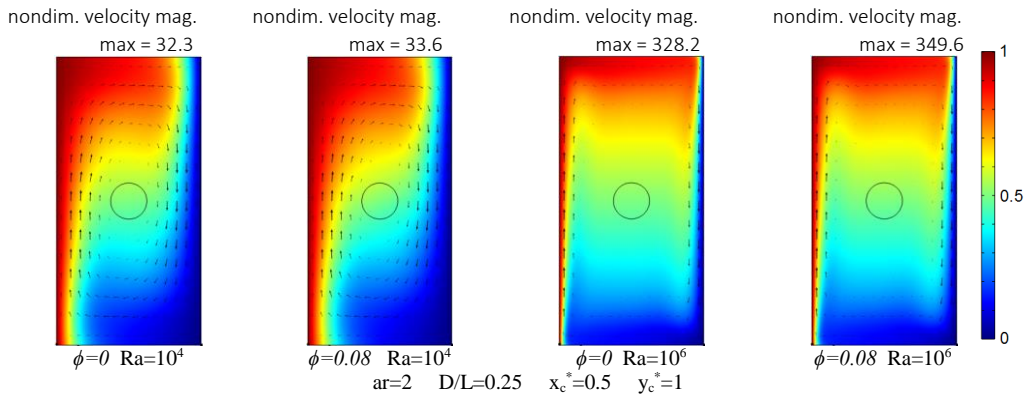
Figure 4. Temperature distribution and velocity field of water-based CuO nanofluid for ar =2
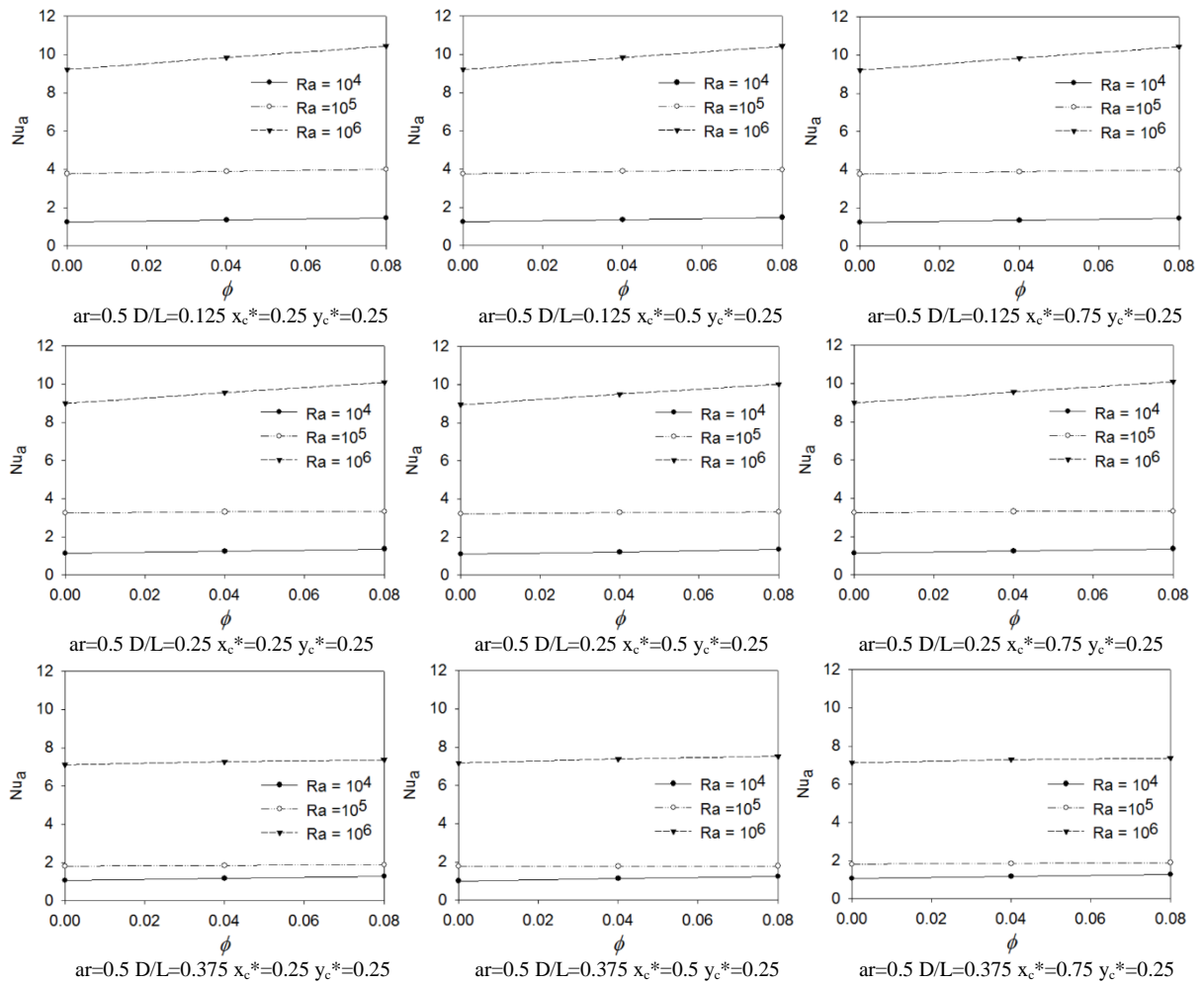
Figure 5. Average Nusselt number for ar = 0.5
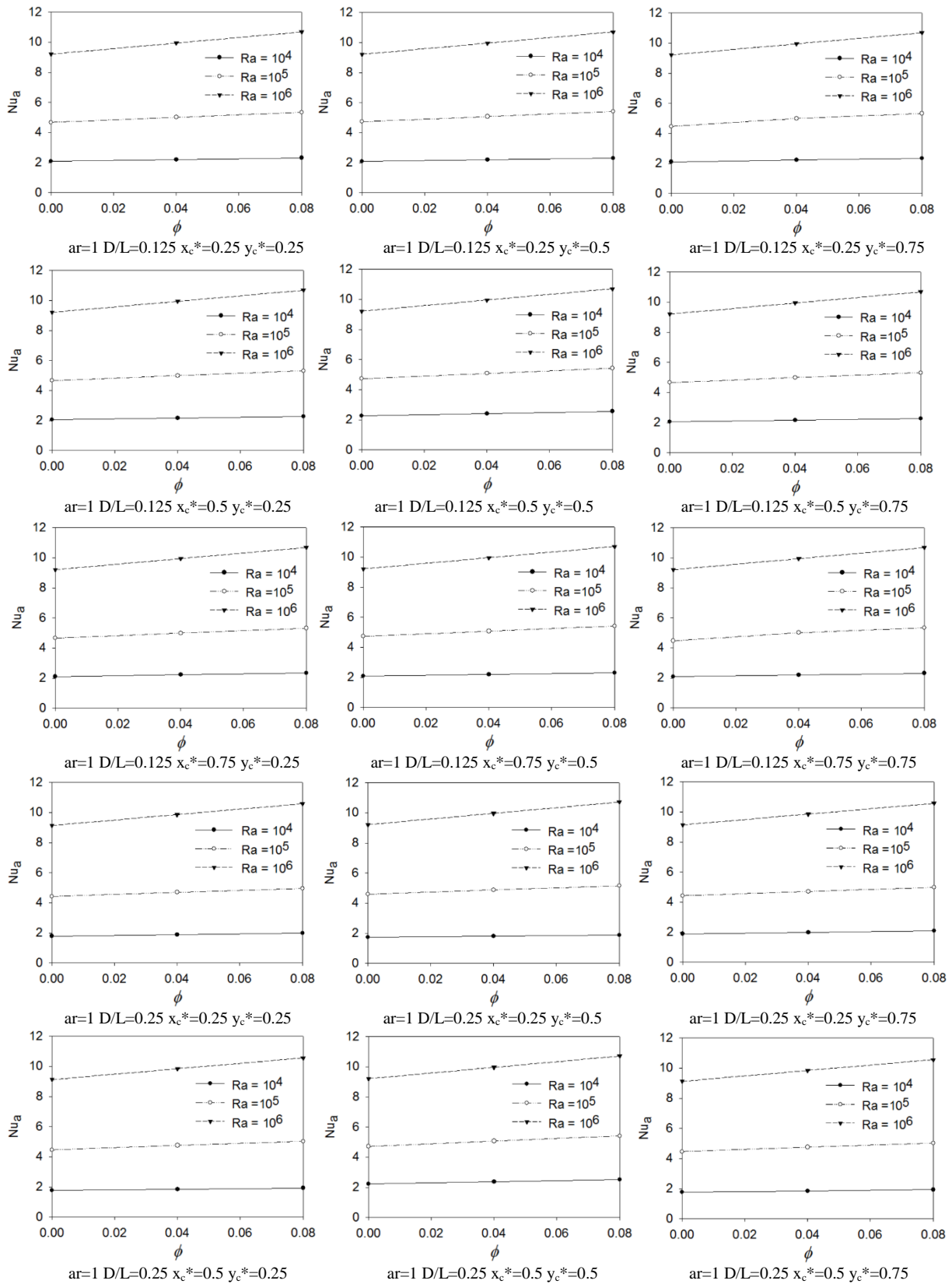
Figure 6a. Average Nusselt number for ar = 1
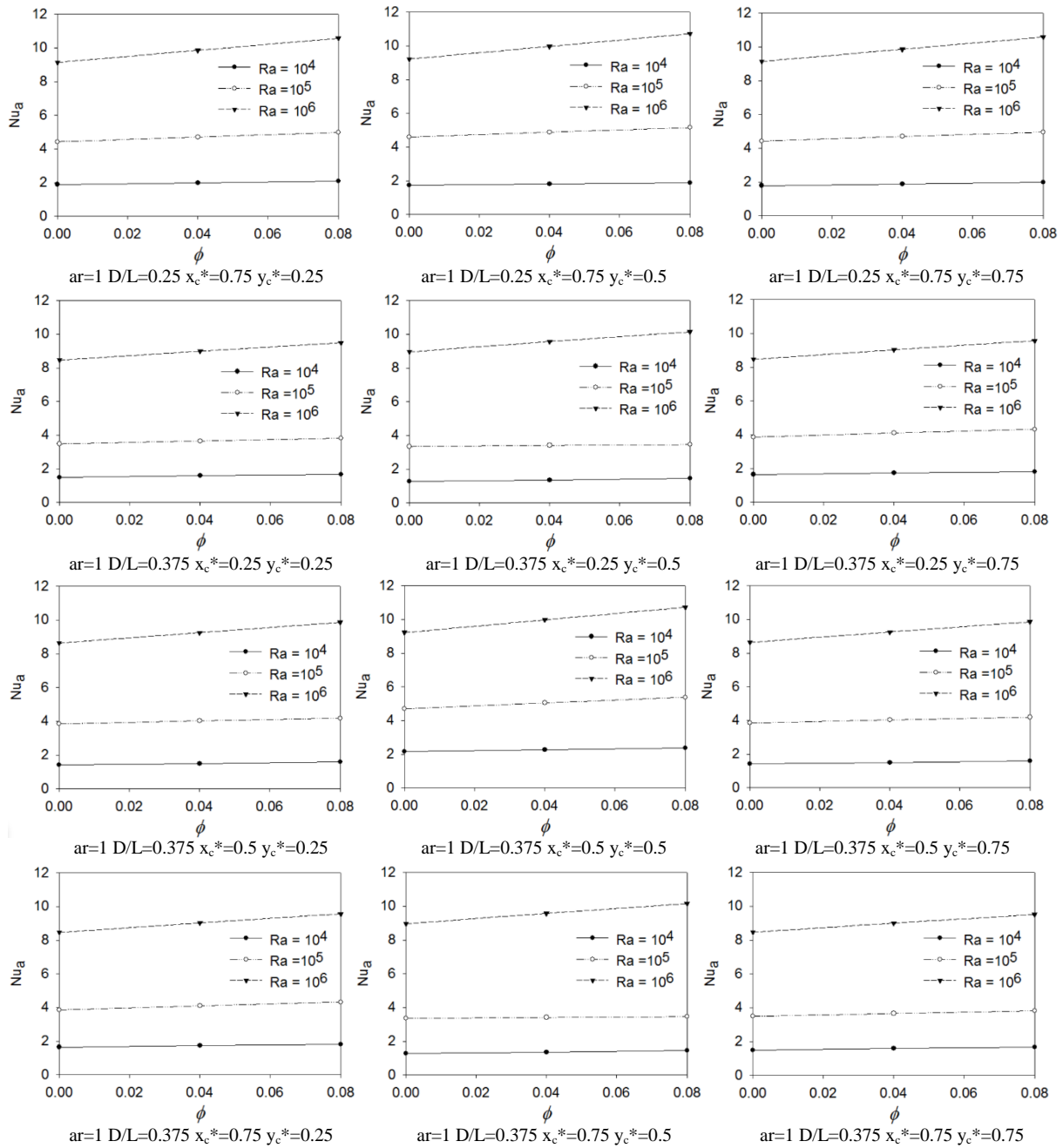
Figure 6b. Average Nusselt number for ar = 1
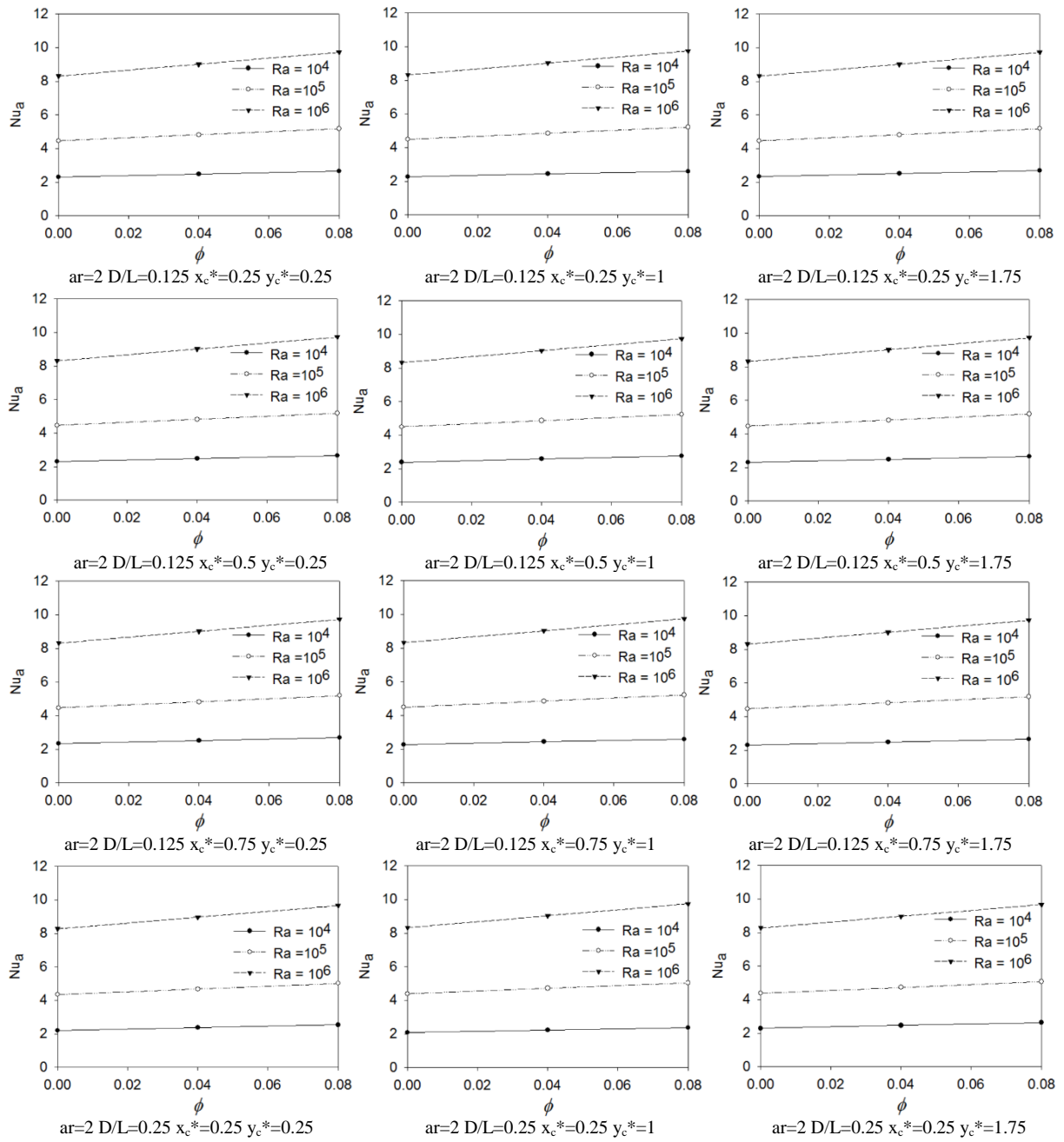
Figure 7a. Average Nusselt number for ar = 2
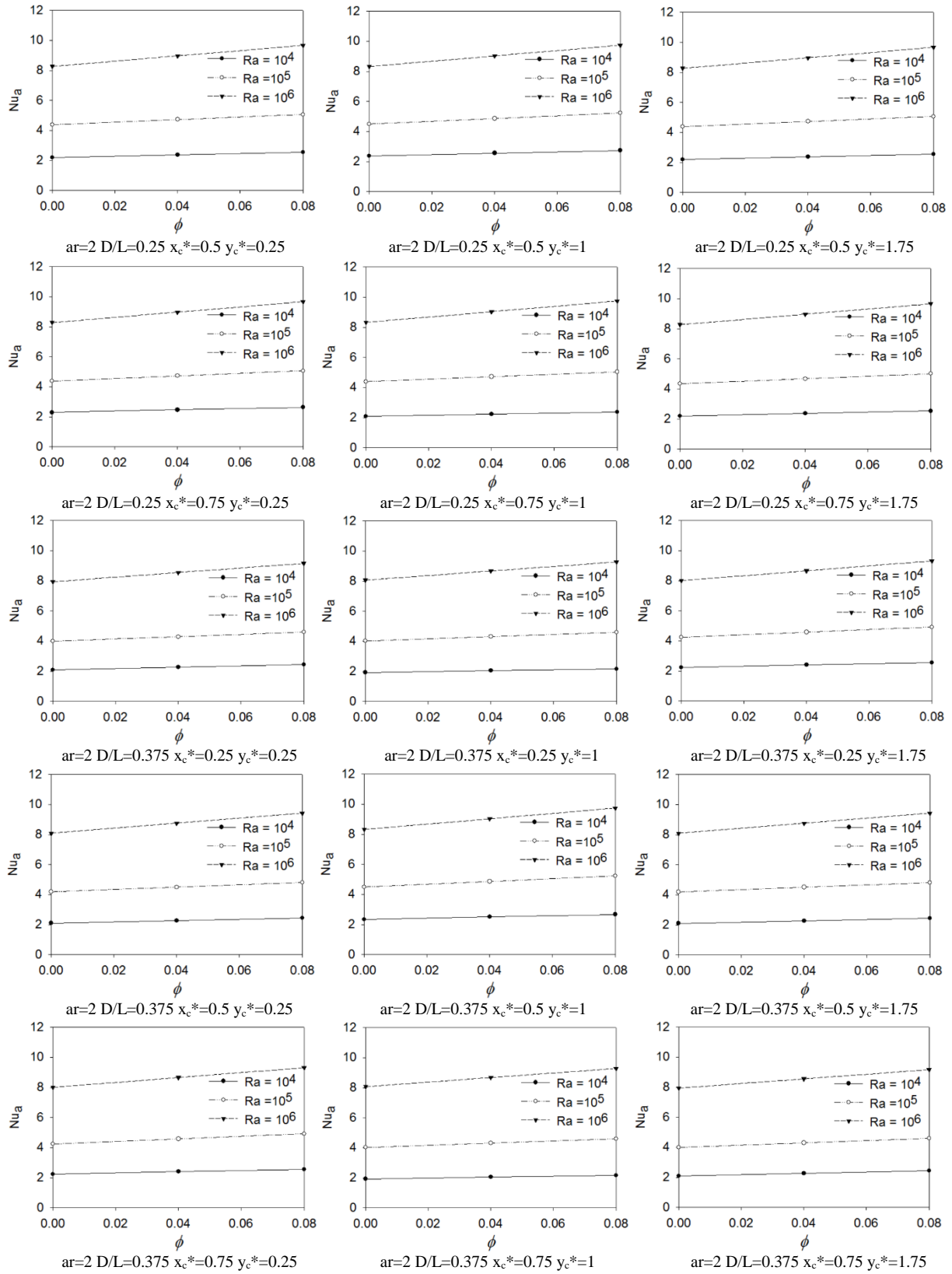
Figure 7b. Average Nusselt number for ar = 2

CONCLUSION

In this paper, heat transfer enhancement of water-based CuO nanofluids in an enclosure with a solid conducting body was investigated numerically by Comsol Multiphysics finite element modeling and simulation software. Computational results were obtained for various values of aspect ratio of the enclosure, diameter and location of the solid cylinder, Rayleigh number and solid volume fraction. It was observed that adding nanoparticles causes an increase in heat transfer rate. The effect of Rayleigh number on heat transfer rate is more significant than that of the solid volume fraction. With an increase of the diameter of cylinder inside the enclosure, heat transfer rate gets lower values. Heat transfer rate shows an increase with an increase of aspect ratio for low values of Rayleigh number. On the other hand, heat transfer rate gets its highest value for square enclosure case for high values of Rayleigh number.

REFERENCES

Brinkman H. C., 1952, The Viscosity of Concentrated Suspensions and Solutions, *J. Chem. Phys.,* 20, 571-581.

Choi S. U. S., Zhang Z. G., Yu W., Lockwood F. E. and Grulke E. A., 2001, Anomalous Thermal Conductivity Enhancement in Nanotube Suspensions, *Appl. Phys. Lett.*, 79(14), 2252–2254.

Cianfrini M., Corcione M. and Quintino A., 2011, Natural Convection Heat Transfer of Nanofluids in Annular Spaces Between Horizontal Concentric Cylinders, *Appl. Therm. Eng.*, 31(17-18), 4055–4063.

Cihan A., Kahveci K. and Susantez Ç., 2012, Buoyancy Driven Heat Transfer of Water-Based CuO Nanofluids in a Tilted Enclosure with a Heat Conducting Solid Cylinder on Its Center, *World Congress on Engineering*, London, 1750-1754.

Hamilton R. L., and Crosser O. K., 1962, Thermal Conductivity of Heterogeneous Two-Component Systems, *Ind. Eng. Chem. Fundam.*, 1(3), 187–191.

Jang S. P. and Choi S. U. S., 2004, Role of Brownian Motion in the Enhanced Thermal Conductivity of Nanofluids, *Appl. Phys. Lett.*, 84(21), 4316–4318.

Kahveci K., 2010, Buoyancy Driven Heat Transfer of Nanofluids in a Tilted Enclosure, *J. Heat Transfer*, 132(6), 062501.

Kang H. U., Kim S. H. and Oh J. M., 2006, Estimation of Thermal Conductivity of Nanofluid Using Experimental Effective Particle Volume, *Exp. Heat Transfer*, 19(3), 181–191.

Khanafer K., Vafai K. and Lightstone M., 2003, Buoyancy-driven heat transfer enhancement in a two-dimensional enclosure utilizing nanofluids, *Int. J. Heat Mass Tran.,* 46, 3639-3653.

Lai F. H. and Yang Y. T., 2011, Lattice Boltzmann Simulation of Natural Convection Heat Transfer of Al$_2$O$_3$/water Nanofluids in a Square Enclosure, *Int. J. Therm. Sci.*, 50(10), 1930–1941.

Li C. H. and Peterson G. P., 2006, Experimental Investigation of Temperature and Volume Fraction Variations on the Effective Thermal Conductivity of Nanoparticle Suspensions (Nanofluids), *J. Appl. Phys.*, 99(8), 084314.

Maxwell J. C., 1873, *A Treatise on Electricity and Magnetism* (Vol.II), Clarendon Press, Oxford, 54.

Murshed S. M. S., Leong K.C. and Yang C., 2008, Investigations of Thermal Conductivity and Viscosity of Nanofluids, *Int. J. Therm. Sci.*, 47(5), 560–568.

Murshed S. M. S., Leong K.C. and Yang C., 2009, A Combined Model for the Effective Thermal Conductivity of Nanofluids, *Appl. Therm. Eng.*, 29(11-12), 2477–2483.

Oztop H. F. and Abu-Nada E., 2008, Numerical Study of Natural Convection in Partially Heated Rectangular Enclosures Filled with Nanofluids, *Int. J. Heat Fluid Flow*, 29(5), 1326–1336.

Pak B.C. and Cho Y. I., 1998, Hydrodynamic and Heat Transfer Study of Dispersed Fluids with Submicron Metallic Oxide Particles, *Exp. Heat Transfer*, 11(2), 151–170.

Rahman M. M., Billah M. M., Rahman A. T. M. M., Kalam M. A., Ahsan A., 2011, Numerical Investigation of Heat Transfer Enhancement of Nanofluids in an Inclined Lid-Driven Triangular Enclosure, *Int. Commun. Heat Mass Transfer*, 38(10), 1360–1367.

Susantez Ç., Kahveci K., Cihan A. and Hacihafızoğlu O. 2012, Natural Convection of Water-Based CuO Nanofluids in an Enclosure with a Heat Conducting Solid Circular Cylinder at the Center. *6th International Ege Energy Symposium & Exhibition*, İzmir, 653-664.

Wang X., Xu X. and Choi S. U. S., 1999, Thermal Conductivity of Nanoparticle–Fluid Mixture, *J. Thermophys Heat Transfer*, 13(4), 474–480.

Wong K. V. and Leon O., 2010, Applications of Nanofluids: Current and Future (Review Article), *Advances in Mechanical Engineering,* 2, 1-11.

Xuan Y. and Li Q., 2000, Heat Transfer Enhancement of Nanofuids, *Int. J. Heat Fluid Flow*, 21(1), 58–64.

Xuan Y. and Li Q., 2003, Investigation on Convective Heat Transfer and Flow Features of Nanofluids, *J. Heat Transfer*, 125(1), 151–155.

Yu W., and Choi S. U. S., 2003, The Role of Interfacial Layers in the Enhanced Thermal Conductivity of Nanofluids: A Renovated Maxwell Model, *J. Nanopart. Res.*, 5(1), 167–171.

Yu Z. T., Xu X., Hu Y. C., Fan L. W. and Cen K. F., 2011, Numerical Study of Transient Buoyancy-Driven Convective Heat Transfer of Water-Based Nanofluids in a Bottom-Heated Isosceles Triangular Enclosure, *Int. J. Heat Mass Transfer*, 54(1-3), 526–532.

Çiğdem SUSANTEZ was born in İstanbul-Turkey in 1982. She graduated from the Mechanical Engineering Department of Trakya University in 2007 as a highest ranking student of the department and faculty. She worked as a research assistant between 2009 and 2016. She obtained her PhD degree in 2015 from Trakya University. She has been working as an Assistant Professor at Mechanical Engineering Department of Trakya University since 2016. Her main research fields are heat transfer and fluid mechanics.

Kamil KAHVECİ was born in Bayburt-Turkey in 1971. He graduated from the Mechanical Engineering Department of Trakya University in 1993. He obtained his MSc degree in 1995 and PhD degree in 1998 from Trakya University. He has been working as a Professor at Trakya University since 2015. His main research fields are heat transfer and fluid mechanics.

INVESTIGATION OF AN SI-CAI ENGINE FUELLED WITH METHANE-HYDROGEN MIXTURES FOR DIFFERENT EXHAUST VALVE LIFTS

Bilge ALBAYRAK ÇEPER* and Emin BORLU*
* Erciyes University Faculty of Engineering Mechanical Engineering Dept
38039 Melikgazi, Kayseri,
balbayrak@erciyes.edu.tr, borluemin@gmail.com

Abstract: In this study, a spark-assisted controlled auto-ignition (SI-CAI) engine with different Methane-Hydrogen blends was numerically and experimentally investigated under different excess air ratio and valve lift value conditions. Experimental results were used to validate the numerical study. GT-Power simulation tool was used for the numerical studies. The valve lifts were created ranging from 3.0 to 5.0 mm with 0.5 increments. The excess air ratio (λ) values were considered as 1.0, 1.1, 1.2, 1.3 and 1.4. Besides, Methane-Hydrogen blends were constituted as 100% Methane (100M), 90% Methane-10% Hydrogen (90M10H), 80% Methane-20% Hydrogen (80M20H) and 70% Methane-30% Hydrogen (70M30H) by volume. Results revealed that the peak pressure values increase when the valve lift increases. The pressure and temperature values tend to reduce with the increasing of λ values. Increasing the volume fraction of Hydrogen in Methane–Hydrogen blend contributes to pressure development earlier. As a conclusion increasing of the volume fraction of Hydrogen in the Methane-Hydrogen blend causes a reduction in the indicated thermal efficiency and mean effective pressure, and a lower specific fuel consumption.
Keywords: Methane-Hydrogen blends, GT-Power, valve lift, excess air ratio, cylinder pressure.

FARKLI EGZOZ VALF YÜKSEKLİKLERİ İÇİN BİR SI-CAI MOTORDA METAN-HİDROJEN KARIŞIMLARININ İNCELENMESİ

Özet: Bu çalışmada, farklı metan-hidrojen karışımlarının buji ateşlemeli kontrollü kendi kendine tutuşmalı bir motorda (SI-CAI) farklı hava fazlalık katsayısı ve valf yükseklik değerlerinde sayısal ve deneysel inceleme yapılmıştır. Deneysel sonuçlar sayısal çalışmanın doğruluğu için kullanılmıştır. Sayısal çalışma için GT-Power simülasyon programı kullanılmıştır. Valf yükseklikleri 0.5 mm artış değeri ile 3.0-5.0 mm arasında ele alınmıştır. Hava fazlalık katsayısı (λ) değerleri 1.0, 1.1, 1.2, 1.3 ve 1,4 olarak dikkate alınmıştır. Bununla birlikte, metan-hidrojen karışımları hacimsel olarak %100 Metan (100M), %90 Metan-%10 Hidrojen (90M10H), %80 Metan-%20 Hidrojen (80M20H) ve %70 Metan-%30 Hidrojen (70M30H) olacak şekilde incelenmiştir. Sonuçlar valf yüksekliklerinin artması ile maksimum basınç değerlerinin arttığını göstermiştir. Hava fazlalık katsayısının artması ile basınç ve sıcaklık değerlerinde azalma eğilimi görülmüştür. Metan-hidrojen karışımlarında hidrojenin hacimsel oranının artırılması ile basınç gelişimlerinin erken gerçekleştiği görülmüştür. Sonuç olarak, metan hidrojen karışımlarındaki hidrojenin hacimsel oranının artışı indike ısıl verimde ve ortalama efektif basınçta azalmaya ve daha düşük özgül yakıt tüketimine neden olmuştur.
Anahtar Kelimeler: Metan-hidrojen karışımları, GT-Power, valf yüksekliği, hava fazlalık katsayısı, silindir basıncı.

ABBREVIATIONS

$BSCO_2$	brake specific carbon dioxide
BSCO	brake specific carbon monoxide
BSHC	brake specific hydrocarbon
BSFC	brake specific fuel consumption
CA	crankshaft angles
CAI	controlled auto ignition
CFD	computational fluid dynamics
CH_4	methane
CI	compression ignition
CO_2	carbon dioxide
CO	carbon monoxide
EGR	exhaust gas recirculation
GDI	gasoline direct injection
HC	hydrocarbon
HCCI	homogeneous charged compression ignition
HRR	heat release rate
IC	internal combustion
LPG	Liquid petroleum gas
NO	nitric oxide
NVO	negative valve overlap
ppm	part per million
SI	spark ignition
SI-CAI	spark assisted controlled auto ignition
VVL	various valve lifts
λ	excess air ratio

INTRODUCTION

Concerns about the increase in emissions emitted from IC engines, and increasing fuel prices due to the reduction of fossil fuel reserves lead researchers to work the incentive studies on the combustion technology of IC engines. In this regard, CAI combustion is one of the most promising alternative combustion methods in comparison with conventional spark ignition (SI) and compression ignition (CI) combustion engines. The CAI concept is based on the auto-ignition of a fuel mixture highly diluted gasses in order to achieve high indicated efficiency and low NOx and soot emissions through low-temperature combustion (Knop et al., 2009). In CAI combustion, the chemical kinetics of the mixture in a cylinder play a key role in combustion characteristics, since CAI combustion is achieved through auto-ignition of the mixture (Ebrahimi and Desmet, 2010, Yao et al., 2009). Therefore, CAI combustion is influenced by intake air temperature, air-fuel ratio, compression ratio, exhaust gas rate, auto-ignitable of a fuel. Several methods such as heating intake air, higher compression ratios, exhaust gas recirculation (EGR) and more ignitable fuels, has been investigated to achieve CAI combustion (Lee and Lee, 2007; Bai et al., 2010; Guo and Neill, 2013; Lee et al., 2013; Zhang and Wu, 2012). However, CAI combustion restricts the operating range of an engine due to challenges in the ignition timing and combustion phase control.

One of the most effective and practical means of achieving CAI combustion in an engine is EGR or exhaust trapping by negative valve overlap (NVO) (Hunicz and Kordos, 2011). EGR are used not only to initiate but also to control CAI combustion (Chen et al., 2003). The valve events are the main strategy to trap a certain rate of exhaust gas for CAI combustion. A number of studies have been performed by using various valve timing over CAI combustion. Kalian et al. (2008), studied on a modified engine for CAI combustion mode using a cam profile switching mechanism that can switch between high and low lift cam profiles for SI-CAI mode transition. Yeom et al. (2007), investigated the emissions and combustion characteristics of HCCI engine fuelled with LPG and gasoline by using variable valve timing to control the amount of residual gas in the cylinder. The characteristics of the LPG HCCI combustion mode was compared with those of the gasoline HCCI engine in their study. Cinar et al. (2015), studied on a single cylinder HCCI engine using four different cams to change valve lift. They reported that HCCI operating range can be extended by low lift cams.

Chen et al. (2014), carried out numerical and experimental studies on a single cylinder equipped with variable valve lifts and timings devices to expand the engine's operation range from low load limit to idle operation under HCCI combustion. During the engine operation, the valve lifts were adjusted from 0.3 mm to 9.5 mm with negative valve overlap strategy. In their study, it was stated that the intake backflow becomes greater and the highest temperature region occurs on the exhaust valve side when the intake valve opens earlier with a higher lift. The interaction between intake flow and residual gasses was considered as a possible means for the extended operation range of diluted HCCI combustion.

Mahrous et al. (2009), investigated 4-valve direct injection HCCI by using a 1D fluid-dynamic engine cycle simulation tool to determine the effects of variable valve timing strategy on the gas exchange process and the engine's performance. They used various valve timings and compared the results with using typical valve timing used for SI and HCCI engine. One of the results of this study is that the optimum engine performance could be achieved by actuating the intake valve at the symmetric crank angle position relative to the timing of exhaust valve closing.

CAI/HCCI combustion is achieved by controlling the temperature, pressure, and composition of the fuel and air mixture, so that it spontaneously ignites the air/fuel mixture in the engine. This special characteristic of CAI/HCCI allows the combustion to occur within very lean or diluted mixtures, it causes to achieve low exhaust temperatures that dramatically reduce engine NOx emissions. Similar to an SI engine the charge is well mixed which minimizes the particulate emissions, also inheriting the advantages of a CI engine being no throttling losses, therefore an overall higher efficiency can be achieved (Cao et al., 2005).

The use of natural gas as fuel in SI engines presents several positive aspects. The natural gas as a fuel provides high indicated thermal efficiency, low knock probability, and reduced NOx emissions. However, some problems such as low flame velocity and the rise of cyclic variability. One way to avoid these problems is Hydrogen addition to natural gas (Karim et al., 1996). Moderated concentrations of Hydrogen don't affect excellent on knock resistance properties of natural gas. Nevertheless, when the amount of Hydrogen fraction increases, the knock is observed earlier (Moreno et al., 2010).

Previous studies have been performed focusing on SI and CAI engine mode. Unlike these studies, SI-CAI combustion mode was investigated for various valve lifts (VVL), excess air ratio (λ) values and Methane-Hydrogen blends at full load. 1D cycle simulation tool, GT-power, as used for the numerical analyses. The 1D mode was generated for the numerical analyses, and numerical results were validated used experimental data. The experimental study was carried out by using a Lombardini LGW 523 two-cylinder engine, 505 cc with the compression ratio of 10:7. After the accuracy of the model was proven GT-power was used to explore the abilities of SI-CAI engines. This study reveals that the ability of the model for SI-CAI combustion model shows a good agreement with experimental studies.

NUMERICAL METHOD

Numerical studies instead of experimental studies have been shown to be useful both in terms of cost and time. Numerical solution can work faster in terms of adjusting the valve lift in an experimental system. GT-Power is software that is used to perform the engine simulation by Gamma Technologies. GT-Power calculates the flow motion in time using many different models for all parts of the engine (Fjallman, 2014). Figure 1 shows the engine simulation model as built in GT-power. The characteristic features of the used engine model used are given in Table 1. Exhaust gasses were taken from ex-port1 and ex-port2 line and send EGR valve. After that, EGR mixture was given in both manifolds.
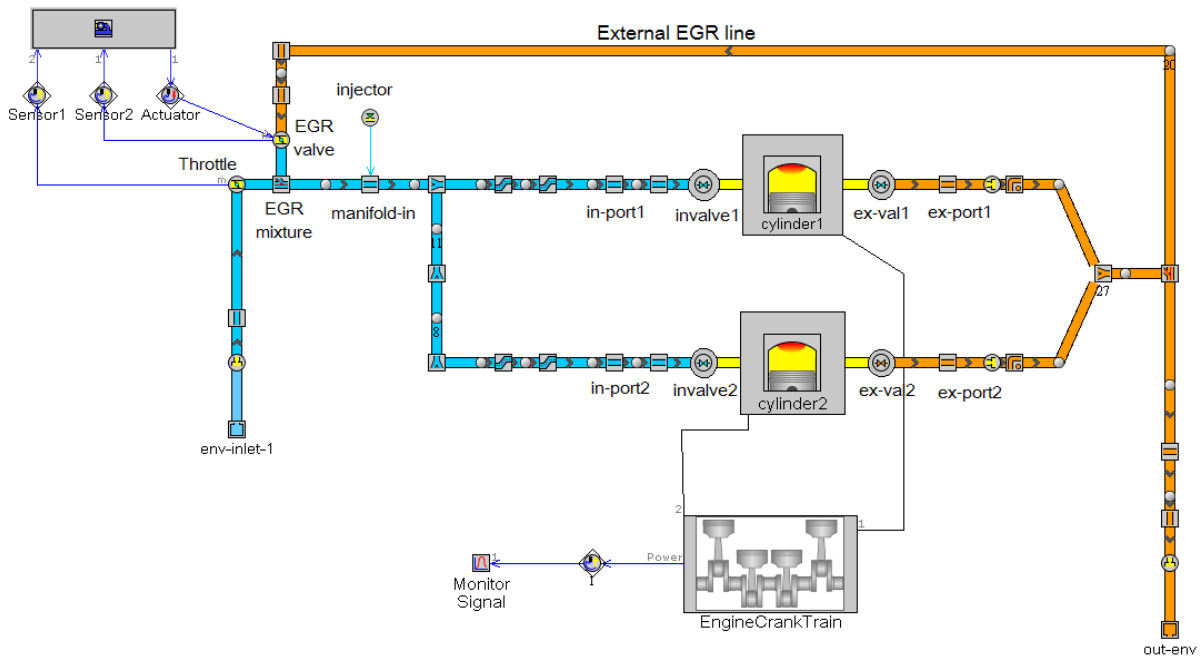
Figure 1. GT-POWER simulation model.

Table 1. The engine specifications

Description	Unit	Value
Cylinder bore	[mm]	71.5
Stroke	[mm]	62
Displacement volume	[cc]	505
Compression ratio	[-]	10.7
Intake valve diameter	[mm]	32
Exhaust valve diameter	[mm]	27

The cam profiles are defined the sub-module VT-Design of GT-Power which is a software to design camshaft and rocker mechanism for engines. The valve profiles are defined depending on valve lifts and exhaust valve opening duration. Polynomial model with the full-cam-16 method, in which the polynomial equation is divided into 16 regions, which was used in the design of cams. Valve train model is shown in Figure 2. The valve lifts based on the parameters defined in Table 2 are set to 3, 3.5, 4, 4.5 and 5 mm from this program. Figure 3 shows the valve opening width versus crank angle degree. Especially exhaust valve lifts were changed in this study.
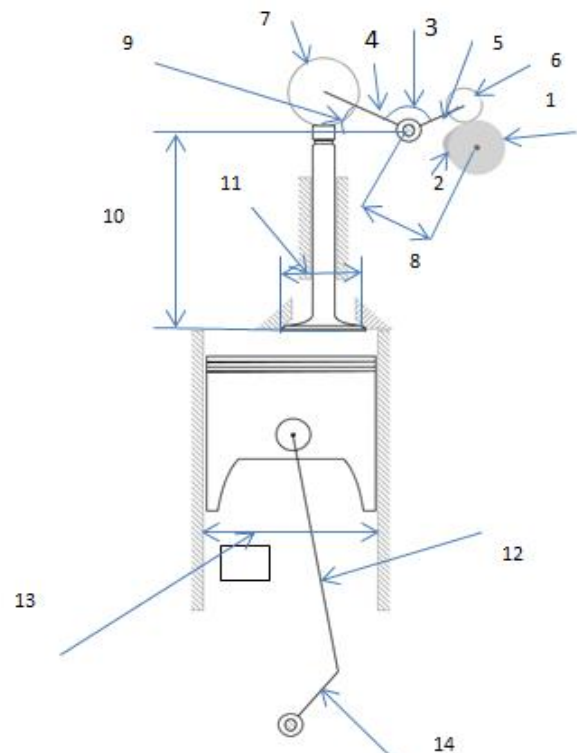
Figure 2. Valve train model.

Table 2. Valve train characteristics.

1	Base Radius	12 mm
2	Cam width	5 mm
3	Included Angle	130°
4	Valve Side Arm Length	40 mm
5	Cam Side Arm Length	26 mm
6	Roller or Contract Radius	7.5 mm
7	Valve Side Contract Radius	15 mm
8	Pivot-Cam Distance	30 mm
9	Valve Side Arm Angle	25° degree
10	Valve Height	90 mm
11	Valve Diameter	36 mm
12	Connection Rod Length	107 mm
13	Piston Bore	71.8 mm
14	Crank Throw Radius	31 mm

EXPERIMENTAL APPARATUS AND PROCEDURE

Experiments were performed to validate the numerical model developed for SI-CAI combustion mode. The experimental studies were carried out for 5 mm valve lift by reducing the cam width illustrated as corresponding to number 2 in Figure 2, from the original dimension, 7 mm. For SI-CAI operation, the engine was equipped with an air pre-heating system of 1.2 kW that can control the intake air temperature in the range 90–110 °C.

A water-cooled piezo-electric pressure transducer (Kistler 6041A) was used with connected to a charge amplifier for the in-cylinder pressure measurements; absolute pressure was calculated considering the mean intake manifold pressure. The power output of the test engine was measured by Baturalp Tayland model hydrokinetic dynamometer. The experimental setup is depicted in Figure 4. The engine was previously operated with gasoline for SI mode and after experiments were repeated for SI-CAI engine mode. All experiments were performed at full-load and steady-state conditions. For SI-CAI engine mode, intake air temperature, and EGR were used with the adjusted valve lift, 5 mm. The experiments were performed at an engine speed of 2000 rpm with Methane fuel for a stoichiometric mixture. The study was run at 2000 rpm engine speed that is one of the most common driving ranges. Methane-Hydrogen blends were used at different excess air ratio values for the other experiments.
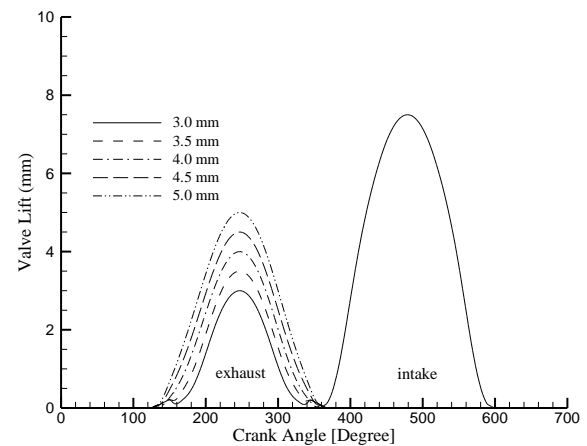
Figure 3. The amount of opening with the opening duration of the intake and exhaust valves at different valve lifts.
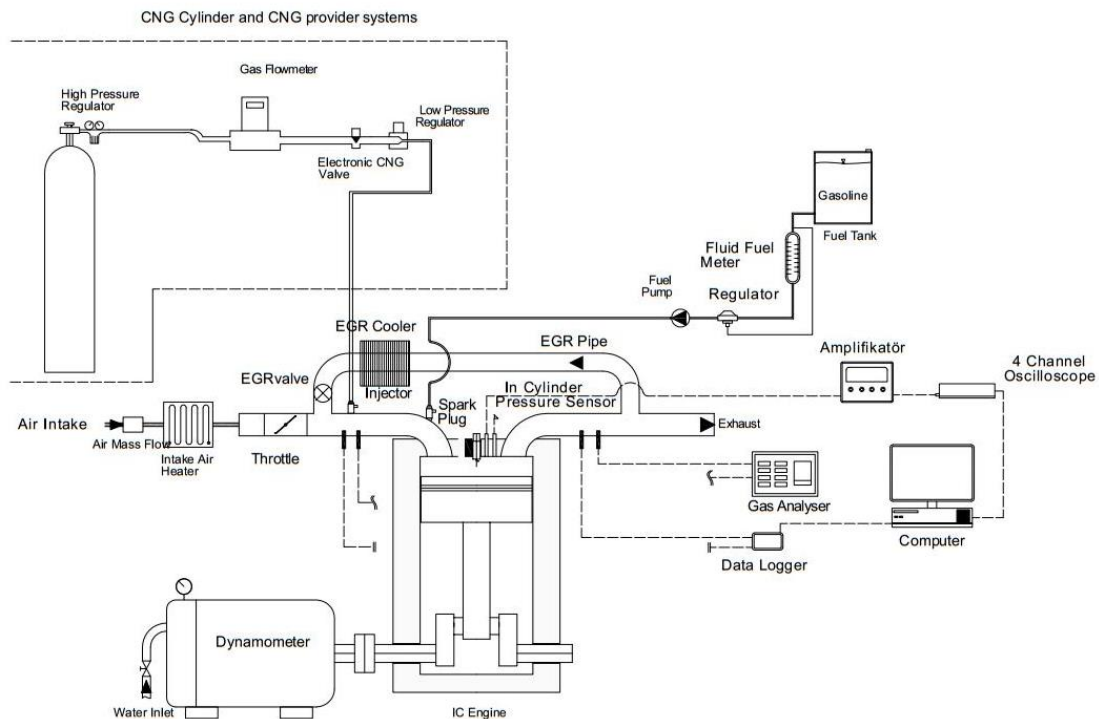
Figure 4. Experimental setup

RESULTS AND DISCUSSION

Model Validation

In order to prove the accuracy of the numerical model, pressure results of the experimental and numerical study were compared with each other. Figure 5 shows the comparison of the numerical and experimental results for both SI and SI-CAI combustion mode at 2000 rpm with a stoichiometric mixture of Methane fuel. Valve lifts were taken as 5 mm for both cases.

As seen in Figure 5, the numerical results show a good agreement with experimental data (within ± 5%). Maximum pressure values are obtained as 41 bar and 39.2 bar for numerical and experimental studies, respectively, for SI mode. For the case of SI-CAI mode, the maximum pressure values are obtained as about 30.8 and 30.2 bar for numerical and experimental studies respectively. Therefore, the based on the model was used to predict the effects of different parameters (valve lifts, λ, methane -hydrogen blends) on in-cylinder pressure and temperature development, engine performance and emissions.
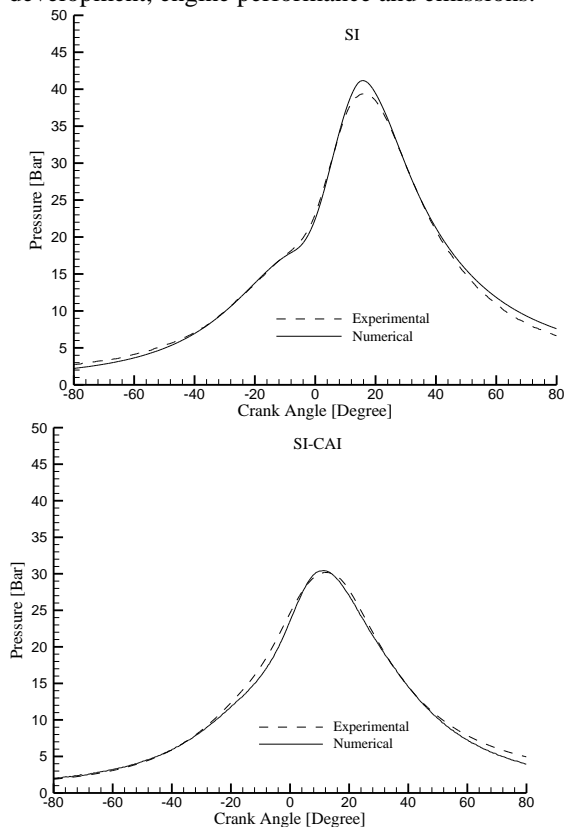
Figure 5. Comparison of experimental and numerical results of SI and SI-CAI engine mode.

Pressure development

Figure 6 illustrates the in-cylinder pressure and temperature values against crank angle for Methane fuel at 2000 rpm and stoichiometric mixture (λ=1.0). Maximum pressure values are observed about 29.0 and 27.5 bar for 5.0 and 3.0 mm valve lifts, respectively. As seen in this figure, the cylinder pressure and temperature value tend to increase, the valve lift value increase.

The temperature values have a similar trend to the pressure value which tends to rise with increasing of valve lift. SI-CAI mode has a low temperature due to the fact that EGR includes the compounds such as CO_2 and H_2O that have a higher value of heat capacity. It can also be seen that the effects of valve lifts on temperature development are in the form of an increase.
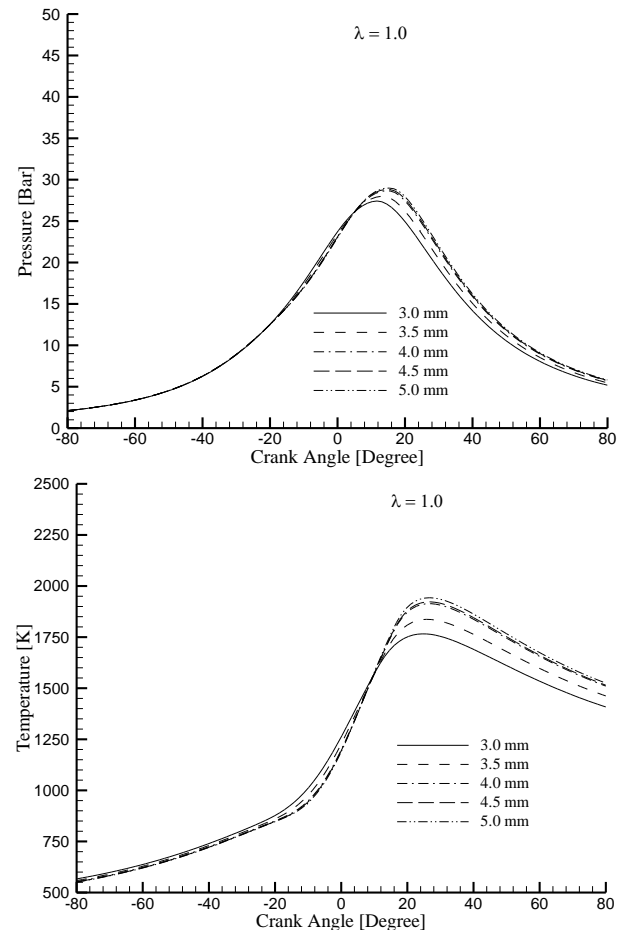
Figure 6. Pressure and temperature values versus crank angle for different valve lifts

Figure 7 shows the pressure values of Methane fuel for considered λ values and valve lifts at 2000 rpm. When the valve lift values increase from 3 to 5 mm, it is seen that the pressure values increase. The peak pressure values are 27.0, 26.0, 24.5 and 23.0 bar for 5 mm valve lift at λ values of 1.1, 1.2, 1.3 and 1.4, respectively. With the increasing of excess air ratio values, the peak pressure values decrease because of less amount of fuel mixture, in turn, in-cylinder pressure developed in a lower value.

Similarly, temperature values inside the cylinder tend to decrease when the λ increases (Fig. 8). For λ value of 1.1, 1.2, 1.3, 1.4 at 5.0 mm valve lift, the temperature values are obtained as 1875 K, 1800 K, 1720 K, 1648 K, respectively. As seen in the figures, the temperature
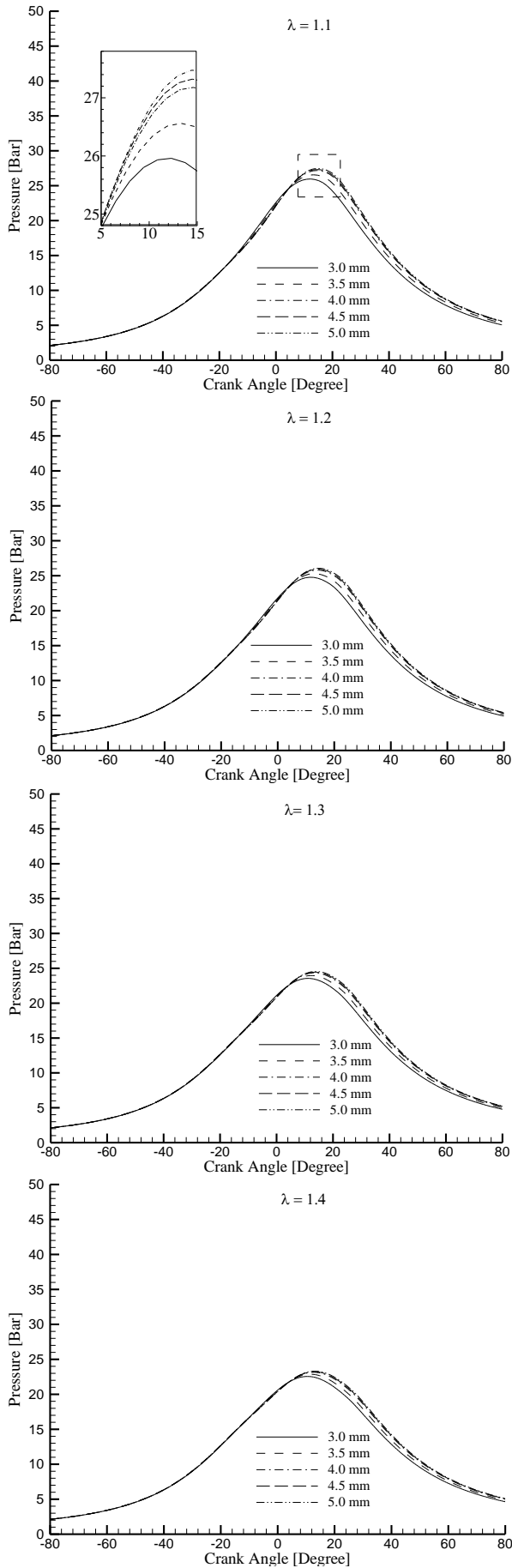
Figure 7. Pressure values of Methane fuel versus crank angle for the different exhaust valve lifts at 2000 rpm
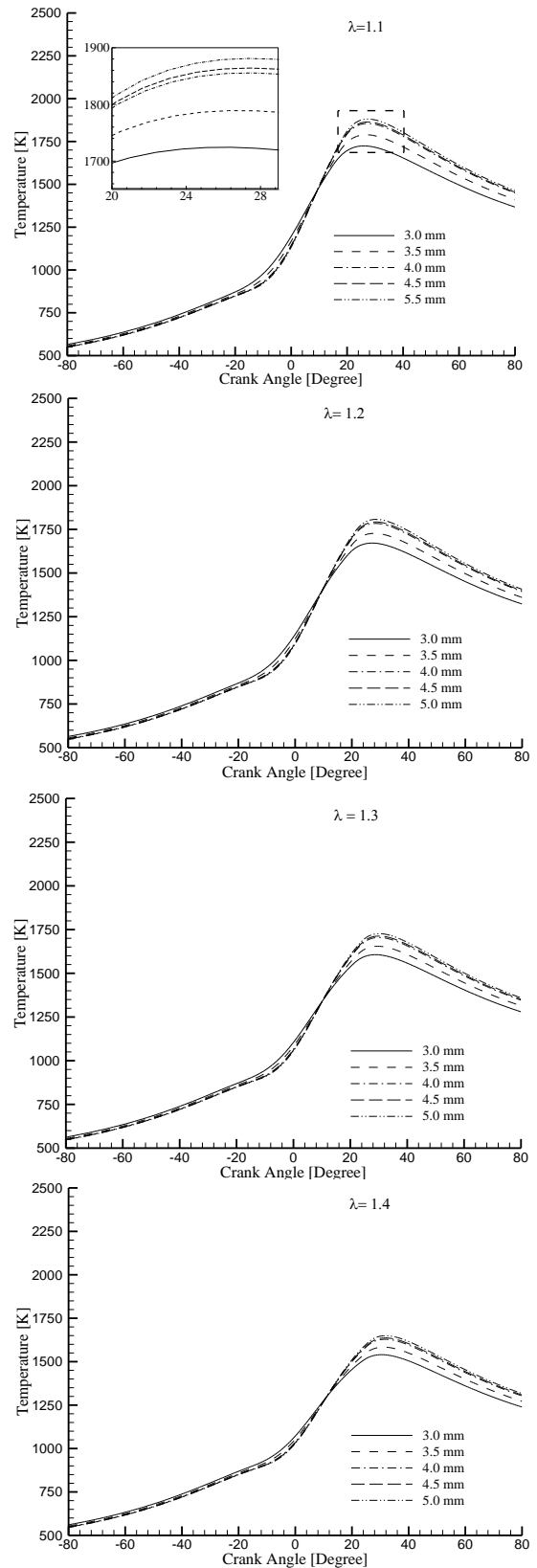

Figure 8. Temperature values versus crank angle for the different exhaust valve lifts at SI-CAI mode

The pressure and temperature values of different Methane-Hydrogen blends at 2000 rpm for λ=1.0 and 5 mm valve lift are presented in Figure 9 and 10. With the addition of Hydrogen to Methane, in-cylinder pressure values increase. The maximum pressure values are

obtained as 48 bar at 70M30H mixture. The reason of this is that with Hydrogen addition to Methane, heat release, which leads to pressure development, occurs earlier, as seen in this Figure.
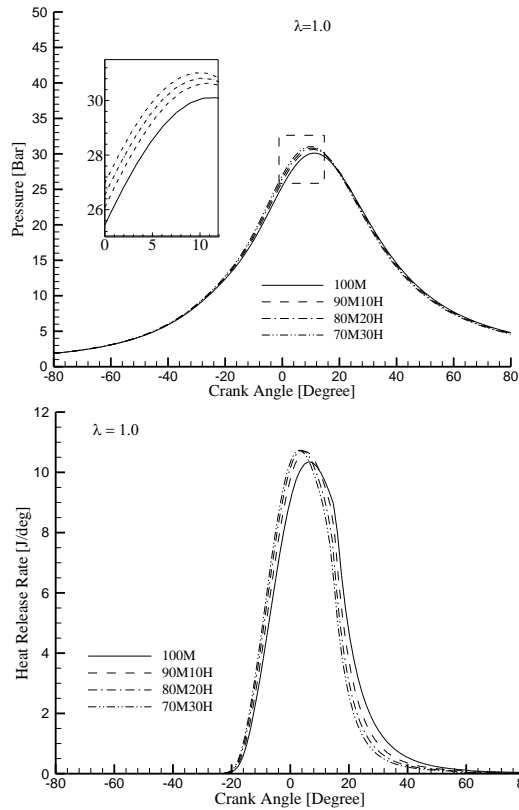
Figure 9. Pressure values and heat release rate versus crank angle for the different fuel blends at
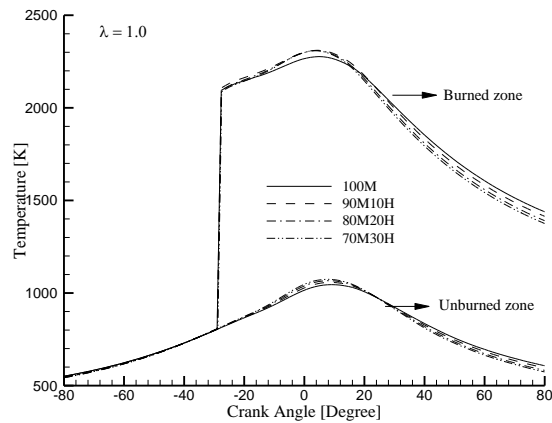
Figure 10. Temperature traces versus crank angle for the different fuel blends

Heat release rate (HRR) is a measure of how fast the chemical energy of the fuel is converted to thermal energy. Therefore, it directly affects the pressure rise rate (dP/dt). The heat release rate was calculated using the first law of thermodynamics as stated by Stone (1999) and Yildiz et al. (2015). In order to calculate heat transfer from gas to the wall, Woschni heat transfer model was used. Thus, the temperature in the cylinder was estimated from the energy balance (Heywood, 1988).

Figure 11 shows also the pressure traces depending on excess air ratio for the different fuel blends. As seen in this figure, the peak pressure values decrease with the increase of λ. It can also be noted that the effect of Hydrogen addition on pressure development decreases with the increase of λ.
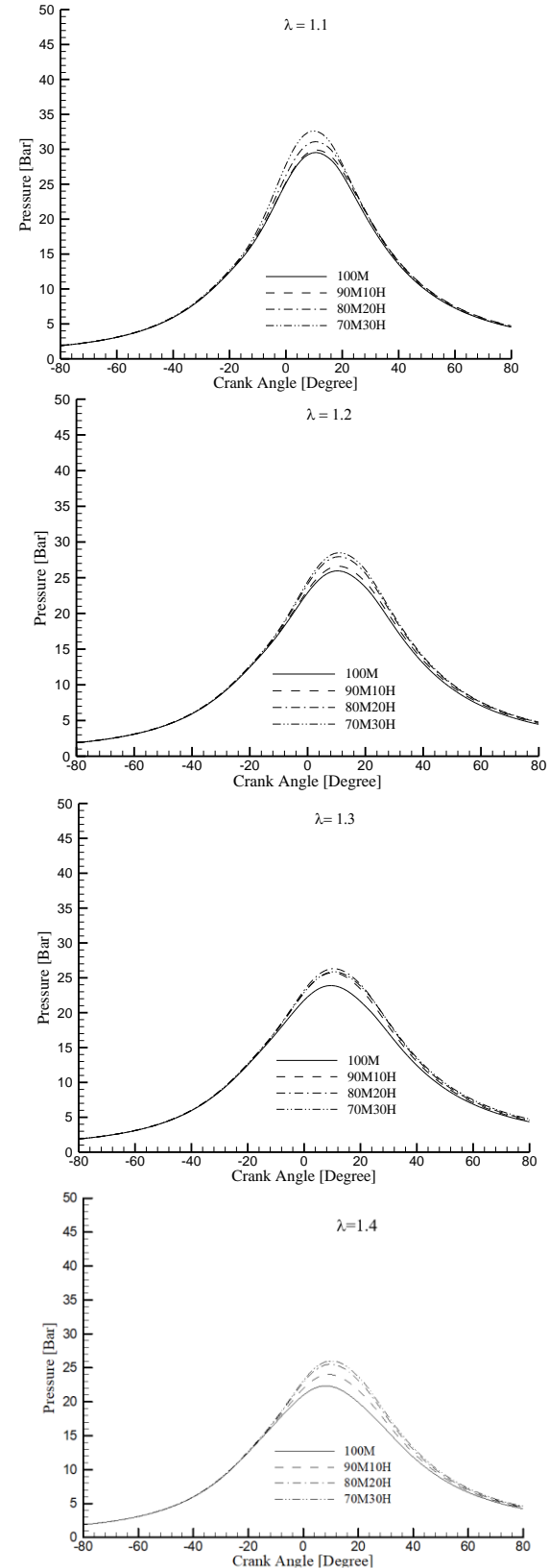
Figure 11. Pressure values versus crank angle for the different Methane-Hydrogen blends at various λ values.

The results of indicated thermal efficiency, brake specific fuel consumption (BSFC) and indicated mean effect pressure (IMEP) for different Methane-Hydrogen blends and λ values at 2000 rpm are given in Figure 12. On considered the results with regard to Hydrogen addition to Methane, the increase of Hydrogen addition lowered indicated thermal efficiency and IMEP considerably at λ value of 1.0.

This can be attributed to early pressure development which leads to an increase in the compression work during the cycle, although peak pressure values increase (Figure 11). However, the results except for BSFC of Methane-Hydrogen blends are in an upward trend up to λ value of 1.1. After λ value of 1.2, the change in indicated thermal efficiency and BSFC are not remarkable for Methane-Hydrogen blends.
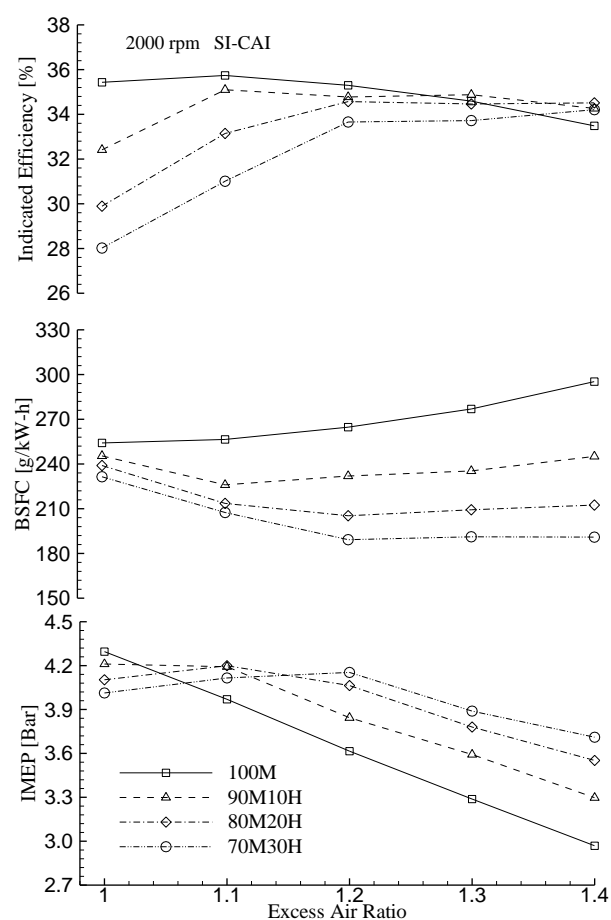
Figure 12. Changes in indicated efficiency, BSFC and IMEP with λ value and fuel blends

The results of indicated thermal efficiency, brake specific fuel consumption (BSFC) and indicated mean effect pressure (IMEP) for different Methane-Hydrogen blends and λ values at 2000 rpm are given in Figure 12. On considered the results with regard to Hydrogen addition to Methane, the increase of Hydrogen addition lowered indicated thermal efficiency and IMEP considerably at λ value of 1.0. This can be attributed to early pressure development which leads to an increase in the compression work during the cycle, although

peak pressure values increase (Figure 11). It can also be seen that there is a decrease in BSFC with the increment of excess air ratio from 1.0 to around 1.2 for all blends. But the further increase of excess air ratio leads to the increasing of BSFC due to a reduction in combustion efficiency (Syed et al., 2012). As volume fraction of Hydrogen in the mixture increases, BSFC values decreases. Besides, BSFC values reach to the minimum value when excess air ratio is about 1.1 and 70M30H.

Figure 13 shows brake specific emissions of CO, CO_2, and HC at the exhaust line without an after-treatment system against λ value for Methane-Hydrogen fuel blends at 5mm exhaust valve lift. As seen in the figure, BSCO emissions increase with increasing of Hydrogen addition. On the other hand, when the λ value reaches 1.3 value, there is not any effect of Hydrogen addition on BSCO because its values are already so low. $BSCO_2$ emissions reduce with increasing of Hydrogen addition rate due to reducing the content of carbon in the fuel blends, as expected. BSHC emission reaches its minimum value when λ is slightly greater than nearly 1.0. BSHC emission increases with the increased λ values. However, Hydrogen addition provides lower BSHC emissions. Because of the increase of excess air ratio, lean mixture and the decrease of peak temperature in the cylinder, incomplete combustion occurs easier to happen and burning velocity becomes slow, so the amount of unburned hydrocarbons increase (Zhang et al., 2011). HC emission for combustion process composes mainly due to incomplete combustion and wall quenching effect (Naeve et al., 2011).
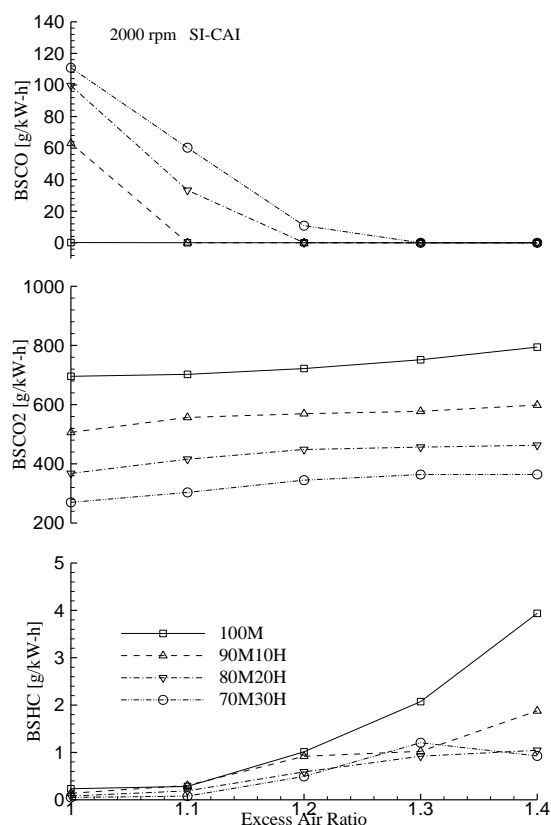

Figure 13. Changes in the specific emissions of.CO, CO_2, HC with λ value and fuel blends

136

CONCLUSIONS

In this study, numerical and experimental studies were performed for an engine model of Lombardini LGW-523 engine using GT-Power analysis tool. SI-CAI engine mode was investigated at 2000 rpm engine speed for different excess air ratios, valve lifts and, Methane-Hydrogen blends. The main conclusions are ordered at below:

- The numerical engine model was accomplished in good agreement with experimental results.
- The effect of the valve lifts (3 to 5 mm) on pressure development were investigated under SI-CAI combustion mode. When the considered valve lift values increased, the peak pressure and temperature values increased. Furthermore, the higher peak pressure values were obtained at 5 mm valve lift.
- The effect of valve lifts (3 to 5 mm) on pressure development with different λ were investigated under SI-CAI mode. It is observed that greater than a valve lift value of 3.5, the change in the pressure developments are very close to each other for each λ value.
- It was also investigated the Hydrogen addition to Methane for different λ values at 5 mm valve lift. The addition of Hydrogen influenced on the peak pressure in an increasing trend. Moreover; in terms of engine performance, the lowest BSFC and BSHC emission values were obtained at 70M30H blends.

Since the accuracy of the numerical procedure is proved, different parameters on an SI-CAI engine can be investigated in next studies.

ACKNOWLEDGEMENTS

REFERENCES

Bai Y, Wang Z, Wang J., 2010, Part-load characteristics of direct injection spark ignition engine using exhaust gas trap. Applied Energy, 87, 2640-46.

Cao L., Zhao H., Jiang X. and Kalian N., 2005, Numerical Study of Effects of Fuel Injection Timings on CAI/HCCI Combustion in a Four-Stroke GDI Engine, SAE International, 2005-01-0144.

Chen R, Milovanovic N, Turner J, Blundell D., 2003, The thermal effect of internal exhaust gas recirculation on controlled auto ignition. SAE paper 2003-01-0751.

Chen T, Xie H, Li L, Zhang L, Wang X, Zhao H., 2014, Methods to achieve HCCI/CAI combustion at idle operation in 4VVAS gasoline engine. Applied Energy, 116, 41-51.

Cinar C, Uyumaz A, Solmaz H, Topgul T., 2015, Effects of valve lift on the combustion and emissions of a HCCI gasoline engine. Energy Conversion and Management, 94, 159-68.

Ebrahimi R, Desmet B., 2010, An experimental investigation on engine speed and cyclic dispersion in an HCCI engine. Fuel, 89, 2149-56.

Fjallman J., 2014, GT-Power Report, KTH Mechanics, SE-100-44 Stockholm, Sweden, https://www.diva-portal.org/smash/get/diva2:624472/FULLTEXT01.pdf
Guo H, S.Neill W., 2013, The effect of Hydrogen addition on combustion and emission characteristics of an n-heptane fuelled HCCI engine. Int J Hydrogen Energy, 38, 11429-37.

Heywood, J. B.(1988). Internal Combustion Engine Fundamentals. McGraw-Hill, Newyork, USA.

Hunicz J, Kordos P., 2011, An experimental study of fuel injection strategies in CAI gasoline engine. Experimental Thermal and Fluid Science, 35, 243-52.

Kalian N, Zhao H, Qiao J., 2008, Investigation of transition between spark ignition and controlled auto-ignition combustion in a V6 direct-injection engine with cam profile switching. Proc. IMechE, Part D: Journal of Automobile Engineering, 222, 1911-26.

Karim G.A., Wierzba I. and Al-Alousi Y., 1996, Methane-Hydrogen mixtures as fuels. Int J of Hydrogen Energy, 21(7), 625-31.

Knop V, Francqueville L, Duffour F, Vangraefschèpe, F., 2009, Influence of the valve-lift strategy in a CAI engine using exhaust gas re-breathing -Part 2: Optical Diagnostics and 3D CFD Results. SAE Int. J. Engines, 2(1), 271-88.

Lee C.H, Lee K.H., 2007, An experimental study of the combustion characteristics in SCCI and CAI based on direct-injection gasoline engine. Experimental Thermal and Fluid Science, 31, 1121-32.

Lee K, Kim Y, Byun C, Lee J., 2013, Feasibility of compression ignition for Hydrogen fueled engine with neat Hydrogen-air pre-mixture by using high compression. Int J Hydrogen Energy, 38, 255-64.

Mahrous A.F.M, Potrzebowski A, Wyszynski M.L, Xu H.M, Tsolakis A, Luszcz P., 2009, A modeling study into effects of variable valve timing on the gas exchange process and performance of a 4-valve DI homogeneous charge compression ignition (HCCI) engine. Energy Conversion and Management, 50, 393-98.

Moreno1 F., Muñoz M., Magén O., Monné C., Arroyo J., 2010, Modifications of a spark ignition engine to

operate with Hydrogen and Methane blends, International Conference on Renewable Energies and Power Quality (ICREPQ'10) Granada (Spain), 23th to 25th March.

Naeve N, He YT, Deng J., 2011, Waste coke oven gas used as a potential fuel for engines, SAE Technical Paper; SAE 2011-01-0920.

Stone R., 1999, Introduction to Internal Combustion Engines, Third Edition. Society of Automotive Engineers Inc., Warrendale, 641 pp.

Syed Y., Venkateswarlu K. and Khan N., 2012, Effect of Ignition Timing and Equivalence Ratio on the Performance of an Engine Running at Various Speeds Fuelled with Gasoline and Natural Gas, International Journal of Advanced Science and Technology Vol. 43, June.

Yao M, Zheng Z, Liu H., 2009, Progress and recent trends in homogeneous charge compression. Progress in Energy and Combustion Science, 35, 398-437.

Yeom K, Jang J, Bae C., 2007, Homogeneous charge compression ignition of LPG and gasoline using variable valve timing in an engine. Fuel, 86, 494-03.

Yildiz M., Akansu S.O., Albayrak Çeper B., 2015, Computational Study of EGR and Excess Air Ratio Effects on a Methane Fueled CAI Engine, International Journal of Automotive Engineering and Technologies, vol.4, 152-161.

Zhang C, Wu H., 2012, The simulation based on Chemkin for homogeneous charge compression ignition combustion with on-board fuel reformation in the chamber. Int J Hydrogen Energy, 37, 4467-75.

Zhang C., Pan J., Tong J., Li J., 2011, Effects of Intake Temperature and Excessive Air Coefficient on Combustion Characteristics and Emissions of HCCI Combustion, Procedia Environmental Sciences, 11:1119-1127.

NATURAL CONVECTION OF NANOFLUIDS IN AN INCLINED SQUARE CAVITY WITH SIDE WAVY WALLS

Elif Büyük ÖĞÜT*, Metin AKYOL** and Müslüm ARICI***

*Vocational School of Hereke, Kocaeli University, 41800, Hereke, Kocaeli, elif.ogut@kocaeli.edu.tr
**Turkish Coast Guard Command, TCSG-103 Command, Akdeniz, Mersin, metin199tr@gmail.com
***Kocaeli University, Engineering Faculty, Mechanical Engineering Department, Umuttepe Campus, Kocaeli, muslumarici@gmail.com

Abstract: In this study, a numerical simulation is performed to study natural convection of water based nanofluid in an inclined square side wavy walls cavity. The the top and bottom walls of the cavity are assumed to be adiabatic and the side walls are at different constant temperatures. Three different nanoparticles, Cu, CuO and Al_2O_3 are used in the study. The computations are conducted for solid volume fractions of 0%, 5% and 10% and for Rayleigh number of 10^4, 10^5 and 10^6**.** The analyses were conducted for $0°$, 45^0 and $90°$ inclination angle for enclosed cavity, 0.05, 0.075, and 0.1 amplitude and 1 and 3 undulation numbers. The results show that heat transfer rate increases with the increase in nanoparticle volume fraction and Rayleigh number. Additionally, it is observed that increasing undulation number increases heat transfer rate significantly.
Keywords: Natural convection, nanofluid, inclination cavity, wavy wall.

YAN DUVARLARI DALGALI EĞİK BİR KARE KAVİTE İÇİNDEKİ NANOAKIŞKANLARIN DOĞAL KONVEKSİYONU

Özet: Bu çalışmada yan duvarları dalgalı, eğik kare bir kavite içindeki, su bazlı nanoakışkanın doğal konveksiyonu nümerik olarak incelenmiştir. Kapalı bölgenin üst ve alt duvarları adyabatik, yan duvarları ise farklı sabit sıcaklıkta tutulmuştur. Bu çalışmada Cu, CuO ve Al_2O_3 olarak üç farklı nanaopartikül kullanılmıştır.Kapalı bölgenin eğim açısı saat ibresi yönünde $0°$, 45^0 and $90°$ olarak seçilmiş olup, genlik değerleri 0.05,0.075, and 0.1 için tek ve üç dalgalı duvarlara sahip kavite için analizler yapılmıştır. Sonuçlara göre, nanopartikül hacimsel konsantrasyonu ve Rayleigh sayısının artmasıyla ısı transfer oranı artmaktadır. Ayrıca, dalga sayısındaki artışla beraber ısı transfer miktarı önemli ölçüde artmaktadır.
Anahtar Kelimeler: Doğal konveksiyon, nanoakışkan, eğik kavite, dalgalı duvar

NOMENCLATURE

c_p	specific heat at constant pressure
g	acceleration due to gravity
k	thermal conductivity
L	length of the cavity
n	undulation number
Nu	Nusselt number
p	pressure
Pr	Prandtl number
Ra	Rayleigh number
T	temperature
u	velocity component in the x direction
v	velocity component in the y direction
x	cartesian coordinates
y	cartesian coordinates

Greek symbols

α	thermal diffusity
β	thermal expansion coefficient
λ	amplitude
ϕ	solid volume fraction
μ	viscosity
ρ	density
Φ	inclination angle

Superscripts

*	dimensional variable

Subscripts

c	cold
f	fluid
h	hot
nf	nanofluid
s	solid

INTRODUCTION

Natural convection heat transfer in enclosed cavities has many important applications in engineering systems, including electronic cooling devices, heat exchangers, MEMS devices, electric machinery and solar energy collectors (Ostrach, 1988). However, the traditional working fluids used in such systems (e.g., water, oil or

ethylene glycol) have a low thermal conductivity, thus their heat transfer performance is inevitably limited. Therefore, a requirement appeared for new working fluids with a higher thermal conductivity.

Nanofluids, consisting of nanoparticles with high thermal conductivity (e.g., Cu, Ag, CuO, Al$_2$O$_3$, or TiO$_2$) suspended in a base fluid with low thermal conductivity (e.g., water, oil or ethylene glycol) provide an effective means of improving the heat transfer performance in many engineering systems. The heat transfer enhancement achieved by such fluids was first investigated by Choi (1995). Since then, the thermophysical properties of many different nanofluids have been examined and various models have been proposed for estimating their heat transfer performance (Das *et al.*, 2006; Wang and Mujumdar, 2007). It has been shown that nanofluids yield an effective improvement in the heat transfer performance compared to traditional working fluids. However, the extent of the heat transfer enhancement depends on the size, shape, concentration and thermal properties of the nanoparticles used. More specifically, the heat transfer performance improves with an increasing nanoparticle volume fraction, a reducing nanoparticle size, and an increasing thermal conductivity.

In recent years, the problem of natural convection heat transfer in square or rectangular cavities filled with nanofluid has attracted significant attention. Khanafer *et al.* (2003) investigated the problem of buoyancy-driven heat transfer enhancement in a two dimensional square enclosure filled with Cu-water nanofluid. Hwang *et al.* (2007) studied the problem of buoyancy-driven heat transfer within a rectangular cavity filled with water-based Al$_2$O$_3$ nanofluid. Oztop and Abu-Nada (2008) investigated heat transfer and fluid flow due to buoyancy forces in a partially heated enclosure using nanofluids using various types of nanoparticles. It was found that the heat transfer enhancement due to using a nanofluid is more pronounced at a low aspect ratio than at a high aspect ratio. Ghasemi and Aminossadati (2009) investigated the natural convection heat transfer performance of water-CuO nanofluid in an inclined enclosure, while Kahveci (2010) examined the heat transfer performance of various buoyancy driven nanofluids in a differentially-heated tilted enclosure. Ogut (2009) numerically investigated the heat transfer enhancement of water-based nanofluids in a two-dimensional inclined enclosure with a constant flux heater for a range of inclination angles, nanoparticles, solid volume fractions, heat source lengths and Rayleigh numbers. The results show that the presence of nanoparticles causes a substantial increase in the heat transfer rate. The length of the heater also affects heat transfer, the latter decreasing with an increase in the length of the heater. While the heater length is increased, the average heat transfer rate actually starts to decrease for smaller inclination angles.

The studies that investigate enclosed cavity with wavy wall filled with nanofluid are not so common, but recently researchers have started to focus on it. Abu Nada and Oztop (2011) investigated heat transfer enhancement of Al$_2$O$_3$-water nanofluids in differentially heated wavy cavities numerically. They concluded that heat transfer increases with increasing of geometry parameter for the same Rayleigh number and nanoparticle fraction. Nikfar and Mahmoodi (2012) investigated natural convection heat transfer in complex cavity having wavy side walls with MLPG (Meshless Local Petrov) method. The results show that significant differences exist between the rates of heat transfer in the cavity for the two viscosity models employed. At Ra=10^3 the average Nusselt number of the hot wall increases with increase in the volume fraction of the nanoparticles for both considered viscosity models. At other Rayleigh numbers the average Nusselt number estimated for Brinkman formula increases with increase in volume fraction of the nanoparticles while it decreases for Maiga's correlation. Nasrin *et al.* (2013) studied the numerical modeling of steady laminar combined convection flow in a vertical triangular wavy enclosure filled with water–CuO nanofluid. The left and right vertical walls of the cavity take the form of a triangular wavy pattern. Mansour and Bakier (2013) studied heat transfer by natural convection in a differentially and wavy walled enclosure with uniform internal heat generation numerically. Both the flow field and heat transfer characteristics were affected due to changes in the values of Rayleigh number and the amplitude of the wavy-wall. Cho *et al.* (2013) numerically investigated natural convection heat transfer characteristics and entropy generation of water-based nanofluids in an enclosure bounded by wavy vertical walls and flat upper and lower surfaces. Cho *et al.* (2012) studied natural convection heat transfer performance of Al$_2$O$_3$-water nanofluid in an enclosed cavity bounded by vertical isothermal walls with a complex-wavy-surface and straight upper and lower walls with adiabatic conditions. Esmaeilpour and Abdollahzadeh (2012) numerically investigated the effect of adding ultra fine metallic nanoparticles to pure fluid on heat transfer rate and the entropy generation distribution within an enclosure with vertical wavy wall. It was found that the entropy generation increases with increasing Grashof number and also decreases with increasing surface waviness. Ogut (2010) numerically investigated laminar natural convection flow of water based nanofluids in an inclined square enclosure, where adjacent walls heated in a different way and other walls were insulated, using polynom based differential quadrature (PDQ) method. Ogut *et al.* (2014) numerically investigated heat transfer enhancement by natural convection in a two dimensional enclosed cavity that has hot left wall and cold and wavy right wall filled with water based nanofluid. According to the obtained results, the Rayleigh number and the solid volume fraction have considerable effect on flow and heat transfer. When comparing the nanofluid and the water, heat transfer rate is higher in nanofluid due to adding the solid particles that have high thermal conductivity in water. The heat transfer rate increases by intensifying circulation due to increasing Rayleigh number.

In the literature, cases where single wall is wavy, just one amplitude value is used, single nanofluid is considered and inclination angle has no affect as cavity, have been studied in literature. This study differs than others in such a manner that, how flow and heat transfer characteristics affected by factors of number of waves, amplitude value, nano particle usage, inclination angle of cavity and Rayleigh number all together. The present study therefore aims to investigate natural convection in an inclined square cavity with side wavy walls and find the effects of varying the solid volume fraction (Φ), nanoparticle type, Rayleigh number (Ra), inclination angle, undulation number and amplitude on flow and heat transfer.

MATHEMATICAL FORMULATIONS

The cavity with side wavy walls is depicted in Fig. 1. The height of cavity is L. The enclosed cavity rotated clockwise and inclination angle represented with φ. The problem is considered to be two dimensional. The top and bottom walls of the cavity are assumed to be adiabatic and the vertical walls are at different constant temperatures.
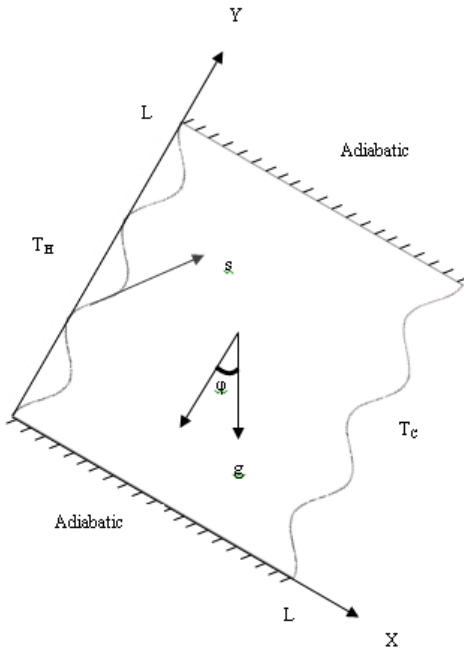
Figure 1. Physical geometry and boundary conditions

The undulation equation is expressed as follows:

$x_{left}=f(y)=\lambda(1-\cos(2\pi ny))$,
$x_{right}=f(y)=[1-\lambda+\lambda(\cos(2\pi ny)]$ (1)

where n and λ are the number of undulations and the amplitude, respectively.

The top and the bottom walls are insulated and the fluid is isothermally heated and cooled by the left and the right side walls at uniform temperatures of T_H and T_C, respectively. Cavity is considered to be filled with Cu, CuO and Al_2O_3 mixture of water. The nanofluid is assumed to be incompressible. It is also assumed that the base fluid and the nanoparticles are in thermodynamic equilibrium and that they flow at the same velocity. The thermophysical properties of the base fluid and the nanoparticles are given in Table 1. The thermophysical properties of the nanofluid are assumed to be constant except for the density variation in the buoyancy force, for which the Boussinesq approximation was used. The viscous dissipation terms and the thermal radiation are also assumed to be negligible.

Table 1. Thermophysical properties of water and nanoparticles

Property	Water	Cu	CuO	Al_2O_3
ρ(kg/m^3)	997.1	8933	6500	3970
c_p (j/kg K)	4179	385	535.6	765
k (W/m K)	0.613	400	20	40
αx10^7 (m^2/s)	1.47	1163.1	57.45	131.7
β(K^{-1})	0.00021	0.000051	0.000051	0.000024

The governing equations for laminar, steady-state, natural convection in an enclosure filled with a nanofluid in terms of the Navier–Stokes formulation are given as,

The continuity equation;

$$\frac{\partial u^*}{\partial x^*} + \frac{\partial v^*}{\partial y^*} = 0 \tag{2}$$

x-momentum equation;

$$\left(u^*\frac{\partial u^*}{\partial x^*} + v^*\frac{\partial u^*}{\partial y^*}\right) = -\frac{1}{\rho_{nf}}\frac{\partial p^*}{\partial x^*} + \frac{\mu_{nf}}{\rho_{nf}}\left(\frac{\partial^2 u^*}{\partial x^{*2}} + \frac{\partial^2 u^*}{\partial y^{*2}}\right) + \frac{1}{\rho_{nf}}(\rho\beta)_{nf}\ g\ (T-T_C)\sin\varphi \tag{3}$$

y-momentum equation;

$$\left(u^*\frac{\partial v^*}{\partial x^*} + v^*\frac{\partial v^*}{\partial y^*}\right) = -\frac{1}{\rho_{nf}}\frac{\partial p^*}{\partial y^*} + \frac{\mu_{nf}}{\rho_{nf}}\left(\frac{\partial^2 v^*}{\partial x^{*2}} + \frac{\partial^2 v^*}{\partial y^{*2}}\right) + \frac{1}{\rho_{nf}}(\rho\beta)_{nf}\ g(T-T_C)\cos\varphi \tag{4}$$

Energy equation;

$$\left(u^*\frac{\partial T}{\partial x^*} + v^*\frac{\partial T}{\partial y^*}\right) = \alpha_{nf}\left(\frac{\partial^2 T}{\partial x^{*2}} + \frac{\partial^2 T}{\partial y^{*2}}\right) \tag{5}$$

The α_{nf} is the thermal diffusion coefficient of the nanofluid and described as follow;

$$\alpha_{nf} = \frac{k_{nf}}{(\rho c_p)_{nf}} \tag{6}$$

To convert governing equation into dimensionless form, the following parameters are used;

$$x = \frac{x^*}{L} \ , \ y = \frac{y^*}{L} \ , \ u = \frac{u^*}{\alpha_f/L} \ , \ v = \frac{v^*}{\alpha_f/L} \ , \ p = \frac{L^2}{\rho_f \alpha_f^2} p^* ,$$

$$\theta = \frac{T^* - T_C}{T_H - T_C} \tag{7}$$

In this equations u^* and v^* are dimensional form of the velocity component, p^* is dimensional pressure component, T^* is dimensional temperature, ρ_f is fluid density at T_C, α_f is the thermal diffusity of fluid.

$$Pr = \frac{\gamma_f}{\alpha_f} \ , \ Ra = \frac{g\beta_f L^3 \Delta T}{\gamma_f \alpha_f} \tag{8}$$

In these equations g is the acceleration of gravity, β is the thermal expansion coefficient, γ is kinematic viscosity, ΔT is the temperature difference between side walls.

The effective dynamic viscosity of the nanofluid can be presented by models for two phases mixture. In this study the Brinkman (1952) model for nanofluid with spherical particle is used.

$$\mu_{nf} = \frac{\mu_f}{(1-\phi)^{2.5}} \tag{9}$$

The density, heat capacity and thermal expansion coefficient of the nanofluid are as follows, respectively:

$$\rho_{nf} = (1-\phi)\rho_f + \phi\rho_s \tag{10}$$

$$(\rho c_p)_{nf} = (1-\phi)\rho_f c_{pf} + \phi\rho_s c_{ps} \tag{11}$$

$$(\rho\beta)_{nf} = (1-\phi)\rho_f \beta_f + \phi\rho_s \beta_s \tag{12}$$

In this equation Φ is the volume fraction and "nf", "f", and "s" subscripts are presents nanofluid, fluid and solid particles, respectively.

For effective thermal conductivity Yu and Choi (2003) model is used;

$$\frac{k_{nf}}{k_f} = \frac{k_s + 2k_f + 2(k_s - k_f)(1+\eta)^3 \phi}{k_s + 2k_f - (k_s - k_f)(1+\eta)^3 \phi} \tag{13}$$

In this model, η, which is the ratio of fluid layer thickness to the original particle radius, is fixed to 0.1.

The Nusselt number is evaluated from the following relation:

$$Nu = \frac{h_{nf} L}{k_f} \tag{14}$$

The heat transfer coefficient, h_{nf}, is obtained from

$$h_{nf} = \frac{q}{(T_H - T_C)} \tag{15}$$

The wall heat flux per unit area, q, can be written as

$$q = -k_{nf} \frac{(T_H - T_C)}{L} \frac{\partial\theta}{\partial\zeta} \tag{16}$$

where k_{nf} is thermal conductivity of nanofluid and ζ is normal direction to the wall. Substituting Eqs. (16) and (15) into Eq.(14) yields the following relation for the local Nusselt number:

$$Nu = -\frac{k_{nf}}{k_f} \left.\frac{\partial\theta}{\partial\zeta}\right|_{wall} \tag{17}$$

The average Nusselt number (Nu_a) is obtained by integrating the local Nusselt number along the left wavy surface and is defined by

$$Nu_a = \frac{1}{S}\int_0^s Nu \, ds \tag{18}$$

where S is the total chord length of the wavy surface and s is the coordinate along the wavy surface.

NUMERICAL SOLUTION

In the study ANSYS Fluent 14.0 is used to solve the governing equations. Momentum and energy equations are discretized by second order upwind scheme, the pressure-velocity equation is coupled by SIMPLE algorithm.

To investigate mesh independency, the analysis conducted for 0.1 amplitude and 3 undulation cavity with Cu-water nanofluid for Ra=10^6, 0.05 volume fraction. Average Nusselt numbers compared for 41x41, 61x61 81x81 101x101 mesh sized cavity. The results show that from 81x81 mesh size the mean Nusselt number doesn't distribute to any remarkable change. Therefore analyses were conducted with 81x81 mesh points.

The numerical code is validated with the study of Khanafer et al. (2003) where heat transfer enhancement in a two-dimensional enclosed cavity filled with nanofluid by different Grashof numbers and volume fractions is investigated. The results are compared in Table 2. According to the Table 2, there is a very good agreement between results of present study and that of Khanafer.

Table 2. Comparison of average Nusselt numbers

	Gr/ Φ	0	0.04	0.08	0.12	0.16	0.20
Present Study	10^3	1.9	2.1	2.2	2.3	2.4	2.6
Khanafer et al.	10^3	1.9	2.1	2.3	2.4	2.5	2.7
Present Study	10^4	4.1	4.4	4.7	5	5.2	5.5
Khanafer et al.	10^4	4.1	4.4	4.7	5	5.3	5.7
Present Study	10^5	8.1	8.7	9.3	10	10.1	11.2
Khanafer et al.	10^5	8.4	8.9	9.6	10.2	10.9	11.6

RESULTS AND DISCUSSION

Streamlines and isotherms for wavy walls that has one and three undulations are presented for various values of the Rayleigh number (Ra=10^4, 10^5 and 10^6) and the solid volume fraction (Φ=0%, 5%, 10%) with fixed Prandtl number (Pr=6.2). In addition, the values of the average Nusselt number are presented for different Rayleigh numbers and amplitudes (0.05, 0.75, 0.1), inclination angles (0°, 45°, 90°) for both Cu-water , CuO-water and Al$_2$O$_3$-water nanofluids.

Streamlines for φ=0° inclination angle, 1 undulation and 0.05 amplitude cavity are given in Fig. 2. The cavity is filled with Cu-water nanofluid. As seen in the figure, an eddy was formed at the center of flow region which rotates in clockwise direction . It has been observed that, an elliptical flow cell occurs at the center of cavity in the cases for low values Rayleigh number. With the increasing of Rayleigh number circular/elliptic flow cell transforms into the rectangular form. Increasing the nanoparticle volume fraction does not affect flow curves significantly. The high values of stream functions show that the circulation and vortex are getting stronger with increasing Rayleigh numbers.

Isotherms for φ=0^0 inclination angle, 1 undulation and 0.05 amplitude cavity with Cu-water nanofluid are given in Fig. 3. For low values of Rayleigh number, convection is so weak that isotherms are similar with those of pure conduction situation. With increasing Rayleigh numbers, convection becomes dominant and circulation gets stronger. Fluid particles heated near hot wall, moves upward through left side wall and cold fluid particles move down through right side wall. With the increase in flow rate due to increase in Rayleigh number, isotherms moves to center of cavity and reach to a parallel view. Additionally, thermal boundary layers appear at side walls with increasing Rayleigh number. Heat transfer increases and thermal boundary layers get thinner, with increasing flow rate due to increasing Rayleigh number. Streamlines for φ=0^0 inclination angle, 3 undulations and 0.05 amplitude cavity with Cu-water nanofluid are given in Fig. 4. In the graphs for different Rayleigh numbers, an elliptic fluid cell forms in the middle of the cavity. Due to increasing Rayleigh number, fluid circulation scales up and elliptic fluid cell transforms into rectangular form and quadratic form eventually. Increase in the volume fraction does not have a significant effect on the circulation region in the cavity.

Isotherm contours for φ=0^0 inclination angle, 3 undulations and 0.05 amplitude cavity with Cu-water nanofluid are given in Fig. 5. When isotherms were analyzed, fluid expands upward along the hot wall (left wall) and falls down along the cold wall. With increasing fluid circulation due to increasing Rayleigh number, the isotherm contours come into parallel with each other in the middle of the cavity. With increasing Rayleigh number, the convection becomes stronger and boundary layer grows along the wavy walls. Increasing volume fraction doesn't effect isotherms contours considerably. The heat transfer rate increases, due to surface area increasing with augmenting number of undulation number.
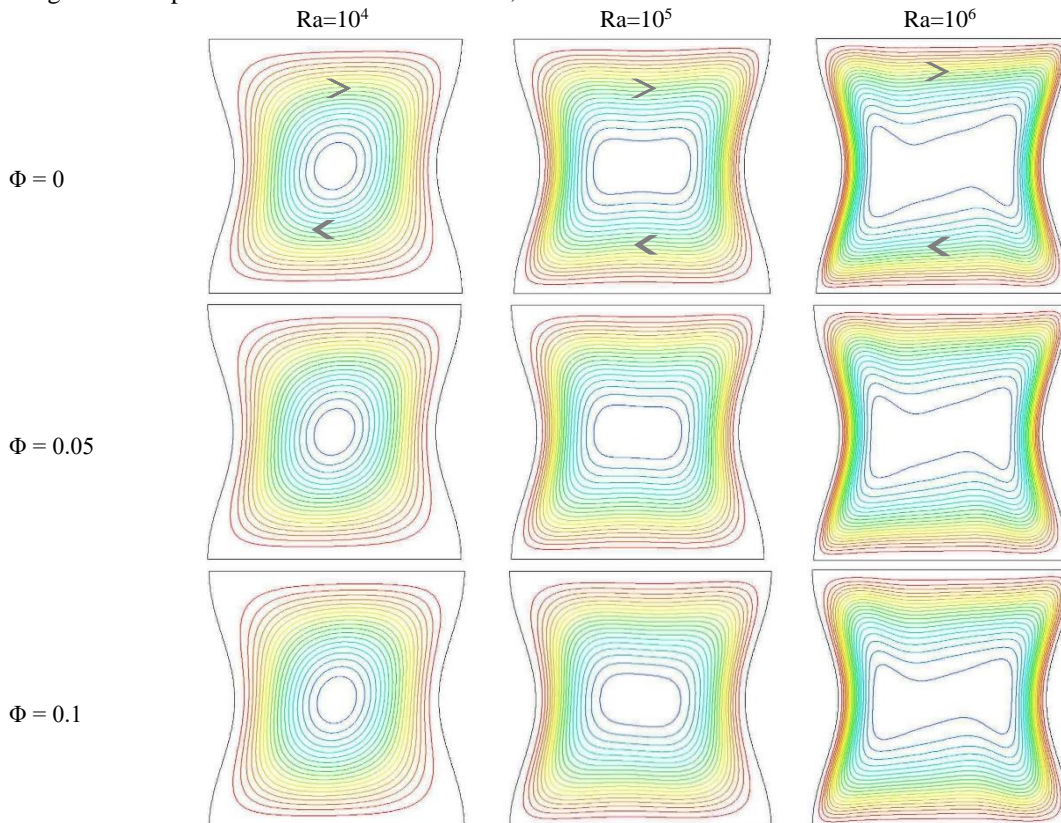

Figure 2. Streamlines for Cu-water nanofluid in cavity with one undulation for λ=0.05 and φ=0° .

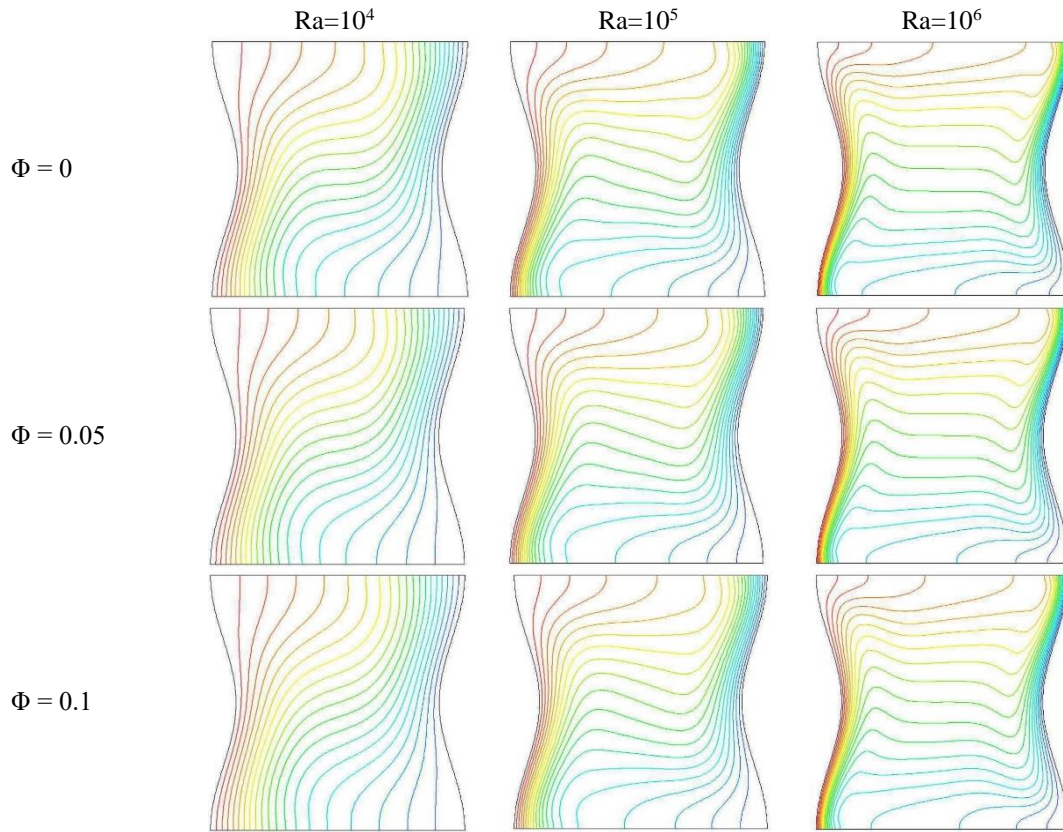**Figure 3.** Isotherms for Cu-water nanofluid in cavity with one undulations for λ=0.05 and φ=0°

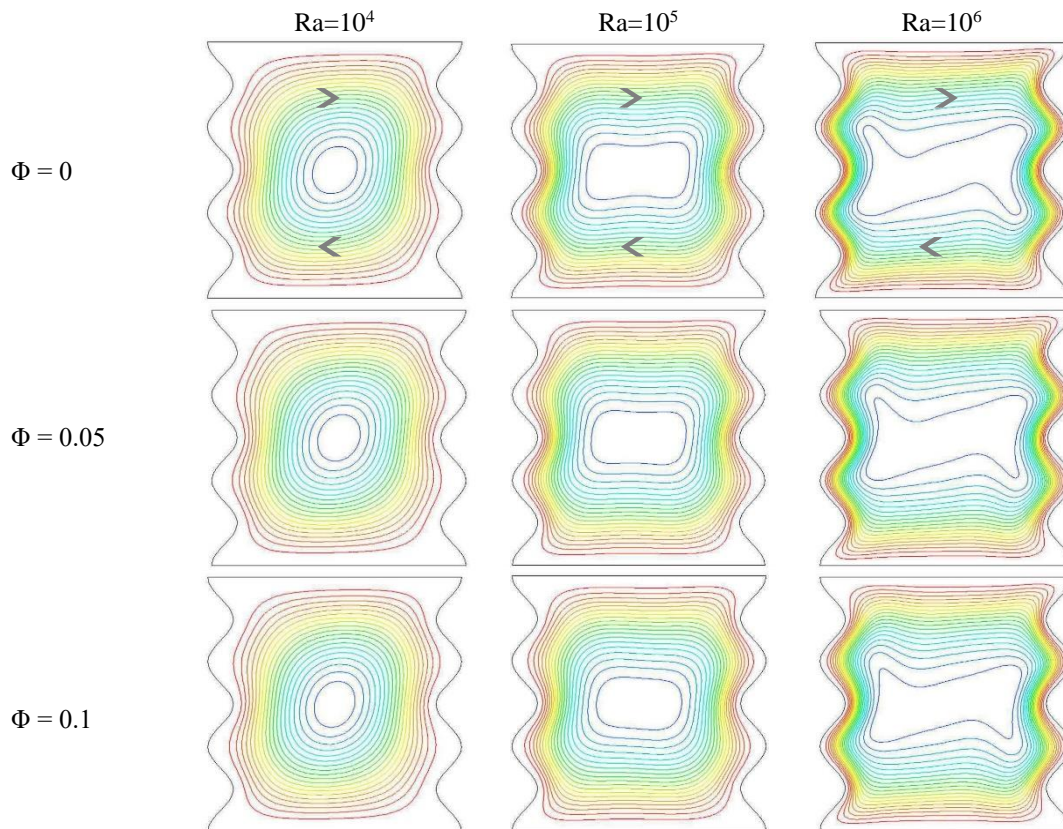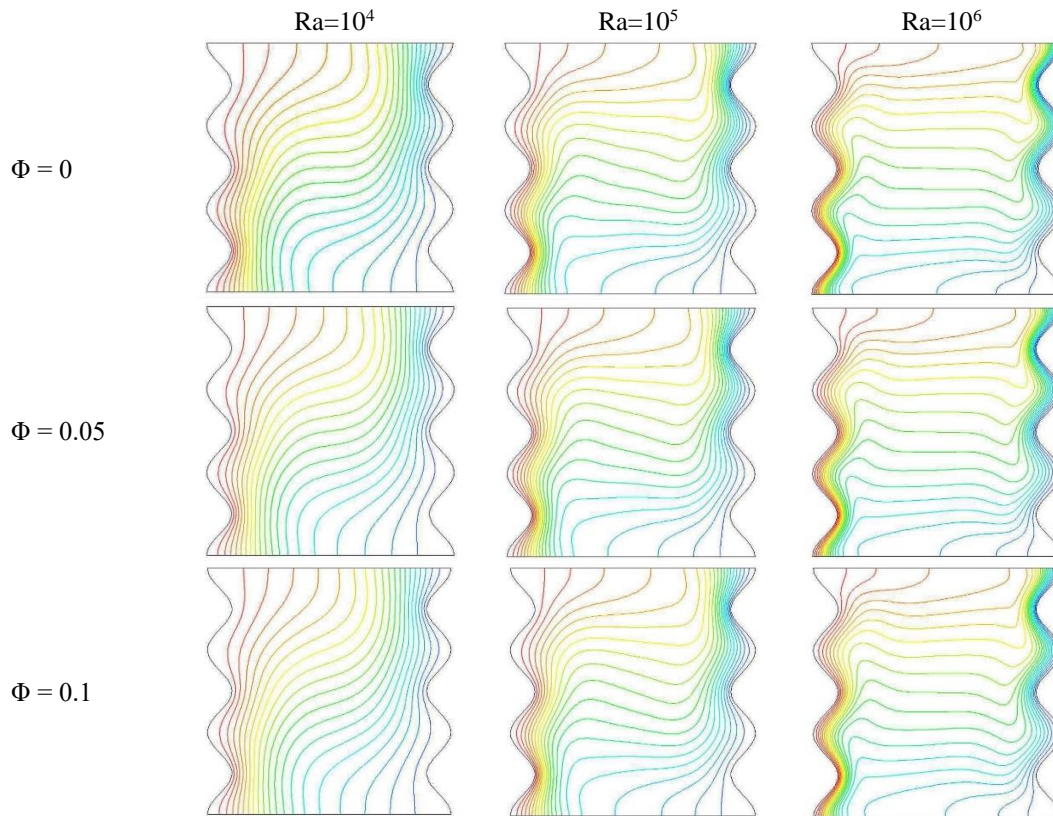**Figure 4.** Streamlines for Cu-water nanofluid in cavity with three undulations for λ=0.05 and φ=0° .

Figure 5. Isotherms for Cu-water nanofluid in cavity with three undulations for λ=0.05 and φ=0° .

Effects of Different Parameters on The Local Nusselt Number

Effect of Rayleigh number

Fig. 6 shows variation of local Nusselt number along hot wall for a) 0°, b) 45° and c) 90° inclination angle, 1 undulation, 0.05 volume fractions, 0.05 amplitude cavity filled Cu-water nanofluid. As shown for 0° inclination angle cavity, isotherms at the bottom of hot wall are more intense, while the temperature gradient is higher, to the upward, distance between curves increase and temperature gradient declines. As a result, the local Nusselt number takes a maximum value at the bottom of hot wall, while it decreases toward upper wall. Local Nusselt value is increasing by increasing of Rayleigh number as a result of increasing convective heat transfer rate. For φ=45° inclination angle cavity local Nusselt value is lower comparing to the 0° inclination angle cavity.

The reason is that, for φ=45° inclination angle, the hot wall affects temperature gradient negatively, with the effect of gravity, and get closer to the up side so the circulation gets weaker in the enclosed cavity. Increase in Rayleigh number causes higher differences in local Nusselt number at the bottom of the hot wall while this difference decreases to the upward. For φ=90° inclination angle, the convective heat transfer rate decreases because of hot wall moving to upside. In this case, heat transfer occurs by conduction. For that reason, local Nusselt value
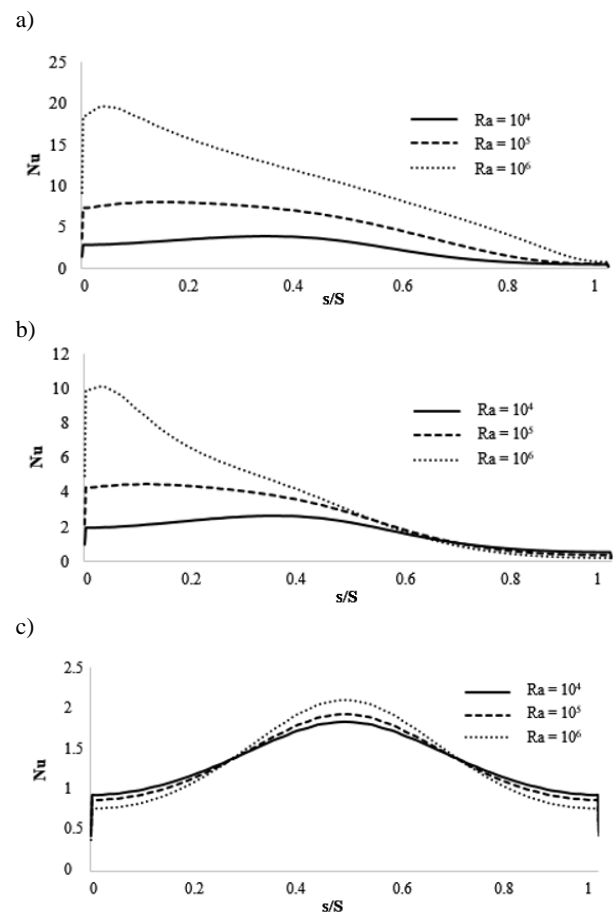
Figure 6. Variations of the local Nusselt number along the hot wavy wall for different Rayleigh numbers for λ=0.05,Φ=0.05, n=1 and a) φ=0° ,b)φ=45° and c) φ =90° (Cu-water nanofluid)

145

takes minimum value comparing to the other cases. Therefore, increasing Rayleigh number shows its effect in the middle of the wall and causes local Nusselt value to increase.

Effect of the amplitude

Fig. 7 shows variation of local Nusselt number for a) φ=0°, b) φ=45° and c) φ=90° inclination angle, 1 undulation, 0.05 volume fractions, varying amplitude cavity filled Cu-water nanofluid along hot wall. With increasing amplitude value local Nusselt number decreases at the bottom of the hot wall, at the peak of the wave with increasing amplitude local Nusselt number increases. At upside of the hot wall again local Nusselt number values decreases by increasing amplitude. At the closer upside area of the hot wall local Nusselt numbers are under 1, it means heat transfer rate is weaker than heat transfer rate with conduction. While comparing φ=45° with φ=0°, it can be noted that, the difference occurs at the bottom of the hot wall, reoccurs at the top the wave, vanishes to the upward. Local Nusselt number takes minimum value at the top of the hot wall as an indicator of isotherms behaviours. For φ=90°, at the bottom of the hot wall, increasing amplitude causes local Nusselt number to decrease, to the top of the wave increasing of amplitude causes significant increase for local Nusselt number. At the highest level of hot wall, a similar behavior is observed as bottom wall.

a)

b)

c)
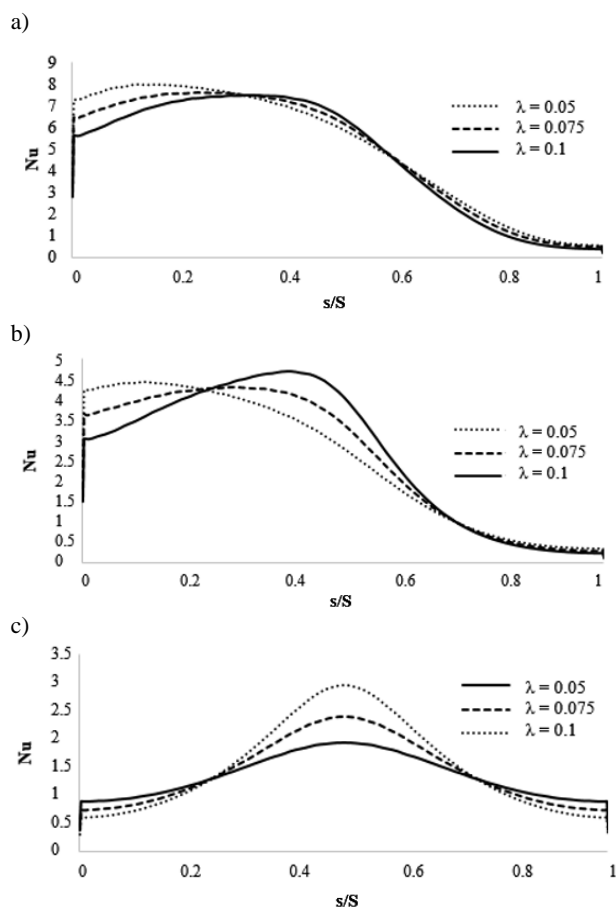
Figure 7. Variations of the local Nusselt number along the hot wavy wall for different amplitude for Ra= 10^5, Φ=0.05, n=1 and a) φ=0°, b) φ=45° and c) φ =90° (Cu-water nanofluid)

Effect of the volume fraction

Fig. 8 shows variation of local Nusselt number for 0°, 45° and 90° inclination angle, 1 undulation, 0.05 volume fractions, 0.05 amplitude cavity filled with Cu-water nanofluid along hot wall. Compared to pure fluid, using nanoparticles that have high thermal conductivity, depending to the increasing volume fractions, increases heat transfer rate. Due to increase in heat transfer rate, local Nusselt number increases along the hot wall. With increasing inclination angle, local Nusselt number decreases. For 90° of inclination angle, local Nusselt number takes maximum value in the middle of the hot wall, at the top of the wave.
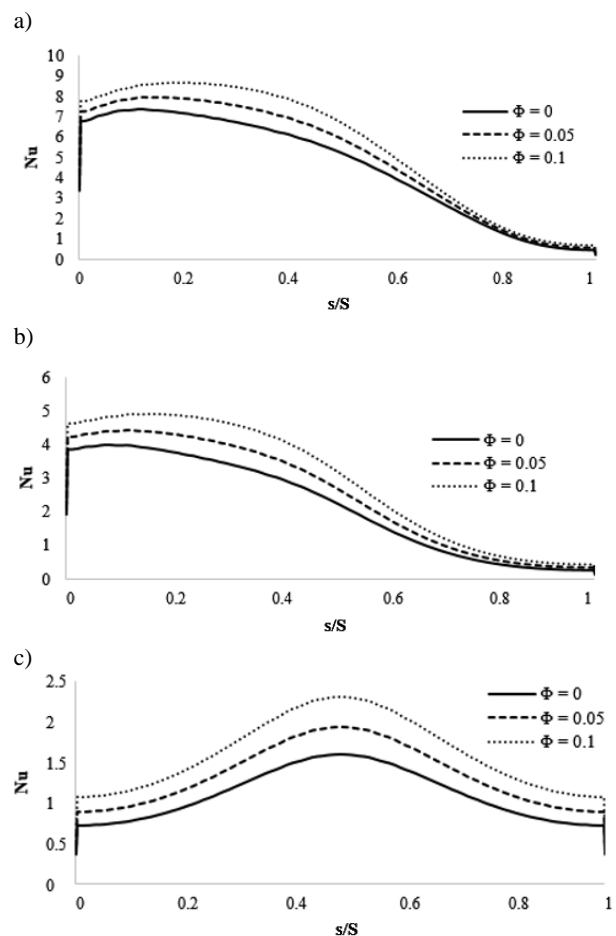
a)

b)

c)

Figure 8. Variations of the local Nusselt number along the hot wavy wall for different volume fractions for Ra= 10^5, Φ=0.05, n=1 and a) φ=0°, b) φ=45° and c) φ =90° (Cu-water nanofluid)

Effect of the angle of inclination

Fig. 9 shows variation of local Nusselt number for varying inclination angle, 1 and 3 undulations, 0.05 volume fractions, 0.05 amplitude cavity filled with Cu-water nanofluid along hot wall. With increasing inclination angle, the hot wall gets closer to the upside and the nanofluid became warmer, can't carry out circulation, heat transfer occurs by conduction with stable situation. For that reason, the clockwise inclination angles decreases local Nusselt number. For 3 undulation numbers, with increasing inclination angle local Nusselt

number decreases along hot wall similarly with 1 undulation number results. On the other hand, with increasing undulation number heat transfer rate and local Nusselt number values increase.
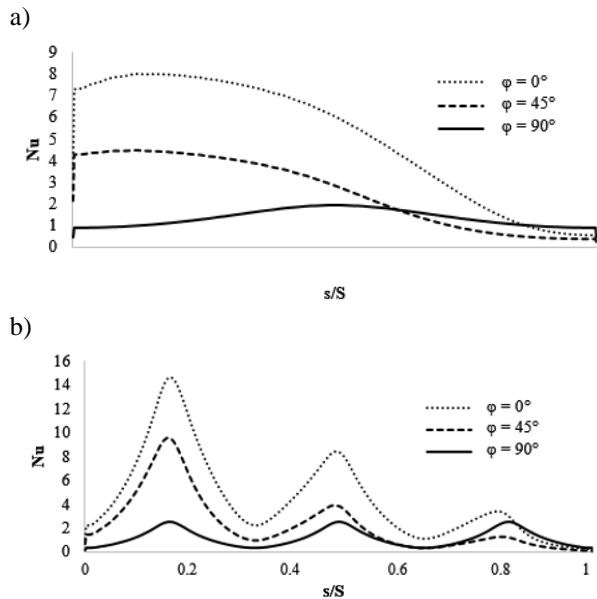
a)

b)

Figure 9. Variations of the local Nusselt number along the hot wavy wall for different inclination angle for Ra= 10^5, λ=0.05 and a) n=1 and b) n=3 (Cu-water nanofluid)

Fig.10 shows variation of average Nusselt number for varying volume fractions for Ra=10^5, 1 undulation, 0.05 amplitude cavity with different nonaparticles. It is noted that, nanofluid with metal nanoparticles have higher Nusselt value and enhance heat transfer rate compared to the nanofluid include oxide nanoparticles. Adding the nanoparticles that have higher thermal conductivity to the pure fluid increases heat transfer rate. While comparing average local Nusselt number for Cu, CuO and Al_2O_3 water nanofluid, the nanofluid that include Cu nanoparticles have higher heat transfer rate since, thermal conductivity for nanoparticles with Cu, is higher compared to Al_2O_3.
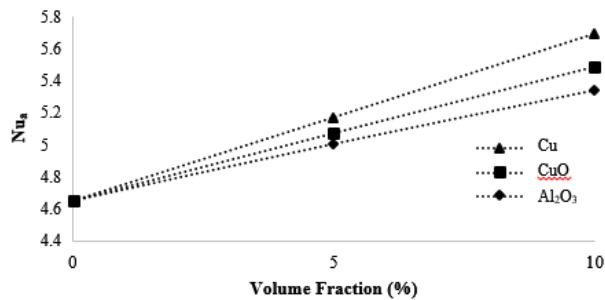
Figure 10. Variation of average Nusselt number with volume fraction for different nanoparticles, and Ra= 10^5, λ=0.05 and n=1

Table 3 shows variation of average Nusselt number for varying volume fractions and Rayleigh numbers for 1 and 3 undulations, 0.05 amplitude cavity filled with Cu-water nanofluid. With increasing Rayleigh number fluid circulation intensifies and average Nusselt number increases. For 3 undulation number average Nusselt

numbers are higher compared to the 1 undulation condition as shown in Table–3. With increasing inclination angle average Nusselt number decreases, since the hot wall gets closer to the upside and the circulation is being suppressed. Also with increasing undulation number average Nusselt number increases too.

Table 3. Average Nusselt numbers for λ=0.05
(Cu-water nanofluid)

		n=1		
	Φ/Ra	10^4	10^5	10^6
φ=0°	0%	2.2386	4.6491	9.2631
	5%	2.4826	5.1673	10.3716
	10%	2.7259	5.6862	11.4913
φ = 45°	0%	1.5204	2.2382	3.1941
	5%	1.7606	2.5960	3.7163
	10%	2.0238	2.9833	4.2841
φ =90°	0%	1.1307	1.1335	1.1389
	5%	1.3713	1.3742	1.3804
	10%	1.6487	1.6516	1.6585
		n=3		
	Φ/Ra	10^4	10^5	10^6
φ=0°	0%	2.3175	4.6755	9.3501
	5%	2.5747	5.2133	10.4180
	10%	2.8305	5.7582	11.4951
φ = 45°	0%	1.5834	2.3742	3.4804
	5%	1.8305	2.7468	4.0336
	10%	2.1008	3.1488	4.6320
φ =90°	0%	1.1622	1.1623	1.1639
	5%	1.4096	1.4098	1.4112
	10%	1.6948	1.6949	1.6963

Variation of average Nusselt number for different amplitude and Rayleigh number values, at 0.05 volume fraction, for 0° inclination angle and 1 and 3 wave cavities has been shown in Table 4. For low values of Rayleigh numbers, increasing amplitude doesn't effect average Nusselt number and circulation structure significantly. For higher Rayleigh numbers, at Ra=10^6, with increasing amplitude average Nusselt number increases significantly.

Table 4. Average Nusselt numbers for Φ=0.05 and φ=0°
(Cu-water nanofluid)

	n=1			n=3		
λ/Ra	10^4	10^5	10^6	10^4	10^5	10^6
0.05	2.4826	5.1673	10.3716	2.5747	5.2133	10.4180
0.075	2.4668	5.1429	10.4459	2.6029	5.2107	10.5981
0.1	2.4461	5.1467	10.5576	2.6281	5.2480	10.8119

Average Nusselt numbers between Cu-water based nanofluid in square cavity by Kahveci (2010) and wavy cavities has been compared in Table 5. Heat transfer rate increases up to 6 % with the increase in number of waves. Nusselt value increases by usage of nanoparticles and considering above mentioned affect there is an increase in heat transfer rate up to 28 %.

Table 5. Comparison of average Nusselt numbers for square cavity and wavy wall cavity for λ =0.1

	Ra	Square cavity (Kahveci, 2010)	n=1	n=3
Φ = 0	10^4	2.27	2.31	2.36
	10^5	4.72	4.73	4.74
	10^6	9.23	9.32	9.68
Φ = 0.05	10^4	2.48	2.55	2.63
	10^5	5.20	5.22	5.25
	10^6	10.24	10.41	10.71
Φ = 0.1	10^4	2.68	2.79	2.90
	10^5	5.66	5.72	5.81
	10^6	11.23	11.49	11.84

CONCLUSIONS

In this study, a numerical simulation is performed to study natural convection of water based nanofluid in an inclined square side wavy walls cavity. The top and bottom walls of the cavity were assumed to be adiabatic. The left wall of the cavity is hot where right wall of the cavity is cold. According to the results, Rayleigh number, volume fraction, nanoparticle type, amplitude, undulation number and inclination angle have significant effect on the circulation structure and heat transfer rate. Heat transfer rate increases, with increasing fluid circulation due to Rayleigh number. Heat transfer is arised by conduction for for low values of Rayleigh numbers, while it is arised by convection for high values of Rayleigh numbers.

It can be seen from the study that, nanofluids with nanoparticles having high heat conductivity, increases heat transfer rate compared to pure fluids. Average Nusselt number is higher for nanofluids with Copper nanoparticles. Heat transfer rate increases, while increasing volume fraction of nanofluids.

Although there is no significant effect on average Nusselt number by changing amplitude it is noted that, for Ra= 10^6 , heat transfer rate increases by increasing amplitude. While examining effect of the inclination angle of the enclosed cavity, it can be seen that heat transfer rate significantly decreases, while heated wall approaches to upside, due to inclinations applied in clockwise direction.

Considering the undulation number effect, while comparing square, 1 undulation and 3 undulation cavities, it is noted that, with increasing undulation numbers heat transfer rate increases significantly. Wavy form of the cavity increases average Nusselt values up to

6%, and with consideration of the nanofluid usage, this value rises up to 28%.

REFERENCES

Abu-Nada E., Oztop H.F., 2011, Numerical Analysis of Al_2O_3/Water Nanofluids Natural Convection in a Wavy Walled Cavity, *Numerical Heat Transfer, Part A,* 59, 403–419.

Brinkman H.C., 1952, The viscosity of Concentrated Suspensions and Solutions, *J. Chem. Phys.*, 20, 571–581.

Cho C.C., Chen C.L., Chen C.K., 2012, Natural Convection Heat Transfer Performance in Complex-Wavy-Wall Enclosed Cavity Filled with Nanofluid, *Int. J. of Thermal Sciences* 60, 255-263.

Cho C.C., Chen C.L., Chen C.K., 2013, Natural Convection Heat Transfer and Entropy Generation in Wavy-Wall Enclosure Containing Water-Based Nanofluid, *Int. J. of Heat and Mass Transfer*, 61,749–758.

Choi S.U.S., 1995, Enhancing Thermal Conductivity of Fluids with Nanoparticles, FED 231/MD-66, in: D.A. Siginer, H.P. Wang (Eds.), *Developments and Applications of Non Newtonian Flows, ASME*, 99-105.

Das S.K., Choi S.U.S., Patel H.E.., 2006, Heat Transfer in Nanofluids - a Review, *Heat Transfer Engineering*, 27, 3-19.

Esmaeilpoura M., Abdollahzadeh M., 2012, Free Convection and Entropy Generation of Nanofluid Inside an Enclosure With Different Patterns of Vertical Wavy Walls, *Int. J. of Thermal Sciences*, 52, 127-136.

Ghasemi B., Aminossadati S.M., 2009, Natural Convection Heat Transfer in an Inclined Enclosure Filled with a Water-CuO Nanofluid, *Numerical Heat Transfer Part A – Applications*, 55, 807-823.

Hwang KS., Lee J.H., Jang S.P., 2007, Buoyancy-Driven Heat Transfer of Water-Based Al_2O_3 Nanofluids in a Rectangular Cavity, *International Journal of Heat and Mass Transfer*, 50, 4003-4010.

Kahveci K., 2010, Buoyancy Driven Heat Transfer of Nanofluids in a Tilted Enclosure, *ASME Journal of Heat Transfer*, 132, 062501-062512.

Khanafer K., Vafai K., Lightstone M., 2003, Buoyancy-Driven Heat Transfer Enhancement in a Two-Dimensional Enclosure Utilizing Nanofluids, *International Journal of Heat and Mass Transfer* 46,.3639-3653.

Mansour, M.A., Bakier, M.A.Y., Free convection heat transfer in complex-wavy-wall enclosed cavity filled with nanofluid, *Int. Comm. in Heat and Mass Transfer*, 44 (2013) pp.108–115

Nasrin R., Alim M.A., Chamkha A. J., 2012, Combined Convection Flow in Triangular Wavy Chamber Filled with Water–CuONanofluid: Effect of Viscosity Models, *International Communications in Heat and Mass Transfer,* 39, 1226–1236.

Nikfar M., Mahmoodi M., 2012, Meshless Local Petrov–Galerkin Analysis of Free Convection of Nanofluid in a Cavity With Wavy Side Walls, *Engineering Analysis with Boundary Elements*, 36, 433–445.

Ogut E.B., 2009, Natural Convection of Water-Based Nanofluids in an Inclined Enclosure with a Heat Source, *International Journal of Thermal Sciences,* 48, 2063–2073.

Ogut E.B., 2010, Heat transfer of water-based nanofluids with natural convection in an inclined square enclosure (Eğik Kare Kapalı bir Bölge İçindeki Su bazlı Nanoakışkanların Doğal Taşınımla Isı Transferi), J. of Thermal Science and Technology (Isı Bilimi ve Tekniği Dergisi, 30, 23-33.

Ogut E.B., Arıcı M, Akyol M., 2014, Natural Convection of Nanofluids in a Square with One Side Wavy Wall Cavity, *7th International Ege Energy Symposium and Exhibition, Uşak, Türkiye,*905-916.

Ostrach S., 1988, Natural Convection in Enclosures, *ASME Journal of Heat Transfer,* 110, 1175-1190.
Brinkman, H.C.,1952, The Viscosity of Concentrated Suspensions and Solutions, *J. Chem. Phys.*, 20, 571–581.

Oztop H.F., Abu-Nada E., 2008, Numerical Study of Natural Convection in Partially Heated Rectangular Enclosures Filled with Nanofluids, *International Journal of Heat and Fluid Flow*, 29, 1326-1336.

Wang X.Q., Mujumdar A.S., 2007, Heat Transfer Characteristics of Nanofluids: a Review, *International Journal of Thermal Sciences*, 46,.1-19.

Yu W., Choi S.U.S., 2003, The role of interfacial layers in the enhanced thermal conductivity of nanofluids: a renovated Maxwell model, *J. Nanoparticle Res.,* 5, 167-171.

Elif Büyük ÖĞÜT graduated from Trakya University with a BS and PhD in Mechanical Engineering. She is currently an Associate Professor in the Vocational School of Hereke at Kocaeli University. Her research interests include Computational Fluid Dynamic, MHD, Natural and Mixed Convection in Enclosure and Heat Transfer in Nanofluids.

Metin AKYOL graduated from Turkish Naval Academy with a BS in Mechanical Engineering and rank of Ensign. He received his MSc from Kocaeli University in Mechanical Engineering. He worked as Executive Officer in TCSG-121 Command between 2009-2011. After his promotion to Lieutenant JuniorGrade he worked as Communication Officer in TCSG YasamCommand between 2011-2015. Also he commanded TCSG-103 Command between 2015-2016. He is currently working in Turkish Coast Guard Command HQ in Ankara/Turkeywith rank of Lieutenant. His research interests include CFD, Natural Convectionin Enclosure and Heat Transfer in Nanofluids.

Müslüm ARICI is a faculty member in Mechanical Engineering Department of Kocaeli University, Turkey. He received BS, MSc and PhD degree from the same university in 2000, 2004 and 2010, respectively. He completed Diploma Course at von Karman Institute, Belgium in 2007. His research fields of interest are Numerical Heat Transfer, Computational Fluid Dynamics, Thermal Energy Storage Systems, Nanofluids and Energy-Efficient Buildings.

ISI BİLİMİ VE TEKNİĞİ DERGİSİ İÇİN MAKALE HAZIRLAMA ESASLARI

Isı Bilimi ve Tekniği Dergisi'nde, ısı bilimi alanındaki özgün teorik ve deneysel çalışmaların sonuçlarının sunulduğu makaleler ve yeterli sayıda makaleyi tarayarak hazırlanmış olan literatür özeti makaleler yayınlanmaktadır. Makaleler, Türkçe veya İngilizce olarak kabul edilmektedir. Makaleler ilk sunumda serbest formatta hazırlanabilir. Ancak yayın için kabul edilmiş olan makaleler dergimizin basım formatına tam uygun olarak yazarlar tarfından hazırlanmalıdır. Aşağıda, ilk sunuş ve basıma hazır formatta makale hazırlamak için uyulması gereken esaslar detaylı olarak açıklanmıştır.

İLK SUNUŞ FORMATI

İlk sunuşta, makale A4 boyutundaki kağıda tek sütun düzeninde, 1.5 satır aralıklı ve sayfa kenarlarından 25'er mm boşluk bırakılarak yazılmalıdır. Yazı boyutu 11 punto olmalı ve **Times New Roman** karakter kullanılmalıdır. Şekiller, tablolar ve fotograflar makale içinde **olmaları gereken yerlere** yerleştirilmelidir. Makale, elektronik olarak editörün e-posta adresine gönderilmelidir.

BASIMA HAZIR MAKALE FORMATI

Hakem değerlendirmelerinden sonra, yayın için kabul edilmiş olan makaleler, dergimizin basım formatına tam uygun olarak yazarlar tarafından hazırlanmalıdır. Makaleler yazarların hazırladığı haliyle basıldığı için, yazarların makalelerini basım için hazır formatta hazırlarken burada belirtilen esasları titizlikle takip etmeleri çok önemlidir. Aşağıda, basıma hazır formatta makale hazırlamak için uyulması gereken esaslar detaylı olarak açıklanmıştır.

Genel Esaslar

Makaleler genel olarak şu başlıklar altında düzenlenmelidir: Makale başlığı (title), yazar(lar)ın ad(lar)ı, yazar(lar)ın adres(ler)i, özet (abstract), anahtar kelimeler (keywords), semboller, giriş, materyal ve metod, araştırma sonuçları, tartışma ve sonuçlar, teşekkür, kaynaklar, yazarların fotoğrafları ve kısa özgeçmişleri ve ekler. Yazılar bilgisayarda tek satır aralıklı olarak, 10 punto Times New Roman karakteri kullanılarak Microsoft Office Word ile iki sütun düzeninde yazılmalıdır. Sayfalar, üst kenardan 25 mm, sol kenardan 23 mm, sağ ve alt kenarlardan 20 mm boşluk bırakılarak düzenlenmelidir. İki sutun arasındaki boşluk 7 mm olmalıdır. Paragraf başları, sütunun sol kenarına yaslanmalı ve paragraflar arasında bir satır boşluk olmalıdır.

Birinci seviye başlıklar büyük harflerle kalın olarak, ikinci seviye başlıklar bold ve kelimelerin ilk harfleri büyük harf olarak ve üçüncü seviye başlıklar sadece ilk harfi büyük olarak yazılır. Bütün başlıklar sutunun sol kenarı ile aynı hizadan başlamalıdır ve takip eden paragrafla başlık arasında bir satır boşluk olmalıdır. Şekiller, tablolar, fotoğraflar v.b. metin içinde ilk atıf yapılan yerden hemen sonra uygun şekilde yerleştirilmelidir. İlk ana bölüm başlığı, Özetten (Abstract'tan) sonra iki satır boşluk bırakılarak birinci sutuna yazılır.

Başlık, Yazarların Adresi, Özet, Abstract ve Anahtar Kelimeler

Yazılar Türkçe veya Ingilizce olarak hazırlanabilir. Her iki durumda da makale özeti, başlığı ve anahtar kelimeler her iki dilde de yazılmalıdır. Eğer makale Türkçe olarak kaleme alınmışsa, Türkçe başlık ve özet önce, İngilizce başlık ve Özet (Abstract) sonra yazılır. Eğer makale İngilizce olarak kaleme alınmışsa önce İngilizce başlık ve özet (abstract) sonra Türkçe başlık ve özet yazılır. Başlık, sayfanın üst kenarından 50 mm aşağıdan başlar ve kalın olarak 12 punto büyüklüğünde, büyük harflerle bütün sayfayı ortalayacak şekilde yazılır. Yazar(lar)ın adı, adresi ve elektronik posta adresi başlıktan sonra bir satır boşluk bırakılarak yazılmalıdır. Yazarların adı küçük, soyadı büyük harflerle yazılmalı ve bold olmalıdır. Yazarların adresinden sonra üç satır boşluk bırakılarak, Özet ve Abstract 10 punto büyüklüğünde bütün sayfa genişliğinde yazılır. Özet ve Abstractan sonra anahtar kelimeler (Keywords) yazılır.

Birimler

Yazılarda SI birim sistemi kullanılmalıdır.

Denklemler

Denklemler, 10 punto karakter boyutu ile bir sütuna (8 cm) sığacak şekilde düzenlenmelidir. Veriliş sırasına göre yazı alanının sağ kenarına yaslanacak şekilde parantez içinde numaralanmalıdır. Metin içinde, denklemlere **'Eş. (numara)'** şeklinde atıfta bulunulmalıdır.

Şekiller

Şekiller 8 cm (bir sütun) veya 16 cm (iki sütun) genişliğinde olmalıdır ve makale içerisinde olmaları gereken yerlere bilgisayar ortamında sutunu (veya bütün sayfa genişliğini) ortalayacak şekilde yerleştirilmelidir. Şekil numaraları (sıra ile) ve isimleri şekil **altına, 9 punto büyüklüğünde** yazılmalıdır.

Tablolar

Tablolar 8 cm (bir sütun) veya 16 cm (iki sütun) genişliğinde olmalıdır. Makale içerisinde olmaları gereken yerlere bilgisayar ortamında sutunu (veya bütün sayfa genişliğini) ortalayacak şekilde yerleştirilmelidir. Tablo numaraları (sıra ile) ve isimleri tablo **üstüne, 9 punto büyüklüğünde** yazılmalıdır.

Fotograflar

Fotograflar, siyah/beyaz ve 8 cm (bir sütun) veya 16 cm (iki sütun) genişliğinde olmalıdır. Fotograflar digitize edilerek, makale içinde bulunmaları gereken yerlere bilgisayar ortamında sutunu (veya bütün sayfa genişliğini) ortalayacak şekilde yerleştirilmelidir ve şekil gibi numaralandırılmalı ve adlandırılmalıdır.

Yazar(lar)ın Fotograf ve Kısa Özgeçmişleri

Yazarların fotografları digitize edilerek, makalenin en sonuna özgeçmişleri ile birlikte uygun bir şekilde yerleştirilmelidir.

SEMBOLLER

Makale içinde kullanılan bütün semboller alfabetik sırada Özetten sonra liste halinde tek sütun düzeninde yazılmalıdır. Boyutlu büyüklükler birimleri ile birlikte ve boyutsuz sayılar (Re, Nu, vb.) tanımları ile birlikte verilmelidir.

KAYNAKLAR

Kaynaklar metin sonunda, ilk yazarın soyadına göre alfabetik sırada listelenmelidir. Kaynaklara, yazı içinde, yazar(lar)ın soyad(lar)ı ve yayın yılı belirtilerek atıfta bulunulmalıdır. Bir ve iki yazarlı kaynaklara, her iki yazarın soyadları ve yayın yılı belirtilerek (Bejan, 1988; Türkoğlu ve Farouk, 1993), ikiden çok yazarlı kaynaklara ise birinci yazarın soyadı ve "*vd.*" eki ve yayın yılı ile atıfta bulunulmalıdır (Ataer *vd*, 1995). Aşağıda makale, kitap ve bildirilerin kaynaklar listesine yazım formatı için örnekler verilmiştir.

Ataer Ö. E., Ileri A. and Göğüş, Y. A., 1995, Transient Behaviour of Finned-Tube Cross-Flow Heat Exchangers, *Int. J. Refrigeration,* 18, 153-160.

Bejan A., 1998, *Advanced Engineering Thermodynamics* (First Ed.), Wiley, New York.

Türkoğlu H. and Farouk B., 1993, Modeling of Interfacial Transport Processes in a Direct-Contact Condenser for Metal Recovery, *Proc. of 73rd Steel Making Conference*, Detroit, 571-578.

Türkoğlu H., 1990, *Transport Processes in Gas-Injected Liquid Baths*, Ph.D. Thesis, Drexel University, Philadelphia, PA, USA.

İnternet, 2004, Türkiye İstatistik Kurumu, *Atıksu İstatistikleri*, http://www.tuik.gov.tr/HaberBulteni.

DİĞER HUSUSLAR

Hakem değerlendirmesinden sonra kabul edilen makaleler, yukarıda açıklandığı şekilde dizilerek basıma hazırlandıktan sonra, bir elektronik kopyası editöre gönderilmelidir. Makalenin basıma hazır kopyası ile birlikte, "Telif Hakkı Devri Formu" da doldurularak göderilmelidir. Telif Hakkı Devir Formu'na ve bu yazım klavuzuna www.tibtd.org.tr adresinden ulaşılabilir.

FOTOĞRAFINIZ

TÜRK ISI BİLİMİ VE TEKNİĞİ DERNEĞİ
ÜYELİK BAŞVURU FORMU

A. Adınız Soyadınız :

Ünvanınız :

Doğum yeri : :   Doğum tarihi: /   / 19   T.C. Kimlik No:

İş Adresiniz :

Ev adresiniz :

Telefonunuz : İş   Ev   Cep

E-posta :

B. *Derneğe   □Asil üye   □Fahri üye   olmak istiyorum.

1. Sizi tanıyan dernek üyesi (Üyelik için) :

2. Mezun olduğunuz
   <u>Yüksek Okullar</u>   <u>Yıl</u>   <u>Branşınız</u>   <u>Ünvanınız</u>

3. İlgilendiğiniz konular :

2015 yılı aidatı olarak toplam 25 YTL (Yirmibeş Milyon TL) derneğin

   İş Bankası Maltepe Şubesi Hesap No: 42120867567
   IBAN: TR08 0006 4000 0014 2120 8675 67

   hesabına yatırılmıştır.

                                        Tarih :   İmza :

* Asil üye olmak için beş yıllık deneyim gereklidir.
  Fahri üyelik için yüksekokul mezunu olma şartı yoktur.

Türk Isı Bilimi ve Tekniği Derneği
Gazi Üniversitesi
Mühendislik Fakültesi
Makina Mühendisliği Bölümü
06570 Maltepe/ ANKARA

İÇİNDEKİLER / CONTENTS